Segregation-Assisted Creep in Nickel-based Superalloys: Experiments, Theory and Modelling

Daniel Barba Cancho

St. Edmund Hall College

University of Oxford

A thesis submitted for the degree of

Doctor of Philosophy

Submitted: Michaelmas Term 2017

Wings are a constraint that makes

it possible to fly.

— Robert Bringhurst

A mis padres y abuelos...

Abstract

Mid-temperature creep deformation in the range of 600 to 850°C is assuming greater importance in Ni-based superalloys. This is because the design operating temperature of the combustion cycle is increasing as the new generations turbofan engines become more efficient. The temperature at the rim of turbine disks and the root of turbine blades can be in this critical range of temperatures for significant portions of the mission cycle, leading to a complex time-dependent mode of plasticity called "microtwinning". Unfortunately this kind of coupled displacive-diffusive deformation mechanism is not yet well understood, and even the range of temperatures and stresses where microtwinning occurs is not clearly defined.

This work explores the fundamentals of this phenomenon, from the kinetics of microtwinning to its influence on the mechanical behaviour of the material. To achieve this objective, coupled computational-experimental studies have been carried out. First, the contribution of microtwinning mechanism to the creep deformation of a single crystal superalloy is studied. The accumulated creep strain computed from quantitative stereology of the tested samples supports the role of this mechanism in conferring plastic deformation. Second, the chemical composition of the microtwins is analysed by means of atomic-resolution characterisation techniques (APT and TEM). Segregation of γ'-stabilisers to the growing faults is found to be

crucial for the understanding of the creep mechanisms in this range of temperatures. Third, a model for diffusion-controlled growth of microtwins is proposed and used to recover the experimental creep strain rates. This then provides the basis for a thermodynamically consistent constitutive model developed on the basis of crystal plasticity theory. The constitutive model is subsequently implemented into a finite element code to study the activation of the different plastic mechanisms within single crystal and polycrystalline aggregates depending on the crystal orientation. With the support of this model, a relation between the rotations of the crystal and the creep life of the different crystal orientations is established. The numerical and experimental results ultimately reveal the critical role of the microtwinning on the asymmetric behaviour of the alloy and thus, its influence on the mechanical performance.

Key words: creep, superalloys, segregation, microtwinning, continuum mechanics, crystal plasticity

Declaration

I declare that this thesis is entirely my own work, and except where otherwise stated, that it describes my own research.

D. Barba Cancho,

Preface

Notation

The following general scheme of notation is used in the present work:

- Scalars are written as italic light-face letters or Greek light-face letters (e.g. J, ψ_0 or e_0).
- Vectors and second-order tensors are written as bold-face minuscules or majuscules (e.g. $\mathbf{n}$, $\mathbf{m}$, $\mathbf{L}$, $\mathbf{l}$ or $\mathbf{F}$).
- Fourth-order tensors are written as blackboard bold-face letters (e.g. $\mathbb{C}$).

The indicial notation for the Cartesian components of the second-order and fourth-order tensors is using the similar typesetting except without the bold-face style, e.g. b_i, F_{ij} and $\mathbb{C}_{ijkl}$ denote a vector, second-order tensor and fourth-order tensor, respectively.

In terms of mathematical operations, some symbols are listed in the following. The tensor (or dyadic) product between two vectors is denoted as $\mathbf{a} \otimes \mathbf{b}$ ($a_i b_j$). Single contraction of vector (or internal product) is indicated as $\mathbf{a}\,\mathbf{b}(a_i b_i)$. Double contraction of tensors (internal product of second order tensors) is indicated by a double dot, such as $\mathbf{A} : \mathbf{B}$ ($A_{ij}B_{ij}$). For fourth order tensors, the internal product is indicated as $\mathbb{A} :: \mathbb{B}$ ($A_{ijkl}B_{ijkl}$). Common mathematical symbols are adopted as

well, e.g. transpose is denoted by superscript "T", an inverse by superscript "-1", etc. Arguments of functions are enclosed in {} brackets.

Published Work

The research in this thesis has been published in the following papers:

- D. Barba, S. Pedrazzini, A. Vilalta-Clemente, A.J. Wilkinson, M.P. Moody, P.A.J. Bagot, A. Jérusalem and R.C. Reed. *On the composition of microtwins in a single crystal Nickel-based superalloy* Scripta Materialia, 127:37-40, 2016.

- D. Barba, E. Alabort, S. Pedrazzini, D.M. Collins, A.J. Wilkinson, P.A.J. Bagot, M.P. Moody, A. Jérusalem, and R.C. Reed. *On the microtwinning mechanism in a single crystal superalloy* Acta Materialia 135:314-329, 2017

- D. Barba, T.M. Smith, J. Miao, M.J. Mills, R.C. Reed, *Segregation-assisted plasticity in Ni-based superalloys.* Metallurgical Transactions A (Under review).

- D. Barba, D. Garcia-Gonzalez, E. Alabort, R.C. Reed., A. Jérusalem *A thermodynamically consistent constitutive model for diffusion-assisted plasticity in Ni-based superalloys.* International Journal of Plasticity (Under review).

Acknowledgements

This research project has been made possible through the help and support of many people to whom I am immensely thankful. Especially, please allow me to dedicate my acknowledgment of gratitude toward the following significant advisors and contributors:

First and foremost, I would like to thank my advisors Prof. Roger C. Reed and Prof. Antoine Jérusalem for their support and encouragement during my PhD. Their combined knowledge on physical metallurgy and continuum mechanics has provided me with invaluable help. Their advice, guiding and motivation have been inestimable.

Besides my advisors, I would like to especially grate the support of Dr. Enrique Alabort, Dr. Paraskevas Kontis and Dr. García-González for introducing me to the harsh world of research and for complementing the role of my advisors. Special mention to Dr. Stella Pedrazzini for her support and advice on the experimental characterisation part of my thesis. I wish also to thank Prof. Mike Mills and Dr. Tim Smith for their hospitality during my stay at the Ohio State University and for their indispensable knowledge on physical metallurgy of superalloys. I am also especially grateful to André Nemeth, Emily Kwong, Dongli Li, Lili Zhang, David Collins and many of my colleages in the Solid Mechanics group.

Finally, and most importantly, I sincerely thank my family and friends, for their

love, advice and support. Especially, I would like to thank my parents Agustin Barba and Inés Maria Cancho for teach me, raise me up and love me. This thesis would not be possible without all their help.

Oxford, 24 October 2017 D. B.

a	lattice parameter
A	area of stacking fault
$\overline{\overline{\mathbf{b}}}$	condensed deformation vector associated with the phase transformation
$\mathbf{b}$	Burgers vector
$\mathbf{C}^{\mathrm{e}}$	elastic right Cauchy-Green tensor
$\mathbb{C}$	elastic stiffness matrix in Ω_0
$\mathbb{C}_{\mathrm{crys}}$	elastic stiffness matrix in the crystal reference frame
c	chemical concentration
c_{tr}	chemical concentration of the transformed phase in Ω_0
$c_{\mathrm{pa\text{-}}\infty}$, c_{pa}	chemical concentration in the parent phase far from the pa-tr interface in Ω_0
$c_{\mathrm{pa\text{-}int}}$	chemical concentration in the parent phase at the interface
$\overline{\overline{\mathbf{D}}}^{\mathrm{p:s}}$	symmetric part of the plastic slip velocity gradient tensor in $\overline{\overline{\Omega}}$
$\overline{\overline{\mathbf{D}}}^{\mathrm{p:tr}}$	symmetric part of the plastic transformation velocity gradient tensor in $\overline{overline\Omega}$
$\mathbf{d}^{\mathrm{e}}$	symmetric part of the elastic velocity gradient tensor in Ω
$\dot{\mathcal{D}}$	global dissipation rate per unit of reference volume
$\dot{\overline{\overline{\mathcal{D}}}}_{\mathrm{slip}}$	dissipation rate due to slip deformation per unit volume in $\overline{\overline{\Omega}}$
$\dot{\overline{\overline{\mathcal{D}}}}_{\mathrm{transformation}}$	dissipation rate due to phase transformation
D_{eff}	effective diffusivity
D_{Co}	Co diffusivity
D_{Cr}	Cr diffusivity
$\delta_{\mathrm{tr}:\beta}$	transformation dilatational strain per unit volume of system β
$\mathbf{E}^{\mathrm{e}}$	elastic Green-Lagrange strain tensor
e_0, e	specific internal energy per unit volume in Ω_0 and Ω
η_0, η	specific entropy per unit volume in Ω_0 and Ω
ε	macroscopic strain
$\mathbf{F}$	deformation gradient tensor
$\mathbf{F}^{\mathrm{e}}$	elastic deformation gradient tensor
$\mathbf{F}^{\mathrm{p:s}}$	plastic slip deformation gradient tensor
$\mathbf{F}^{\mathrm{p:tr}}$	plastic transformation deformation gradient tensor
$\mathbf{F}_{\Delta V}$	volumetric deformation gradient associated with the phase transformation produced per unit volume of slip system α
F_{rep}	force due to dislocation elastic repulsion
F_{fault}	force due to the change of fault energy
F_{partial}	total force on the partial dislocation
F_τ	external force
f_0	volumetric transformed phase fraction in Ω_0
f	volumetric transformed phase fraction in Ω
$f_{0:\beta}$	volumetric transformed fraction of system β in Ω_0
$f_{\gamma'}$	fraction of γ' precipitates
f_{twin}	twin fraction
γ_{tr}	transformation shear strain per unit volume
γ_α	shear strain of slip system α
$\dot{\gamma}_0$	reference strain rate
γ_{twin}	twin shear strain
γ_{SF}	stacking fault energy
γ_{SESF}	SESF stacking fault energy
γ_{CISF}	CISF stacking fault energy
γ_{APB}	APB stacking fault energy
G	specific Gibbs free energy
ΔG_0	activation Gibbs free energy at zero stress
ΔG	activation Gibbs free energy
H	height of the specimen
h	hardening moduli parameter
h_{t}	height of the twin ledge
$\mathbf{I}$	identity matrix
J	determinant of the deformation gradient
J^{tr}	determinant of the transformation deformation gradient
$\mathcal{J}$	chemical flux
K_0	zero order Bessel function
$\mathbf{L}_0^{\mathrm{p:s}}$, $\overline{\overline{\mathbf{L}}}^{\mathrm{p:s}}$	plastic slip velocity gradient tensor in Ω_0 and $\overline{\overline{\Omega}}$
$\mathbf{L}_0^{\mathrm{p:tr}}$,$\overline{\overline{\mathbf{L}}}^{\mathrm{p:tr}}$	plastic transformation velocity gradient tensor in Ω_0 and $\overline{\overline{\Omega}}$
$\mathbf{l}$	velocity gradient tensor
$\mathbf{l}^{\mathrm{e}}$	elastic velocity gradient tensor
L	length of the specimen
l	dislocation length/twin front length
l_{char}	characteristic length of the diffusion problem

$\overline{\overline{\mathbf{M}}}$	Mandel stress tensor in $\overline{\overline{\Omega}}$
$\overline{\overline{\mathbf{m}}}$	slip direction
$m_{\alpha/\beta}$	rate sensitivity parameter of system α/β
μ_{tr}	specific chemical potential of the transformed phase in Ω_0
μ_{pa}	specific chemical potential of the parent phase in Ω_0
μ_0	interface mobility
$\overline{\overline{\mathbf{n}}}$	slip plane normal
ν	vibrational frequency
$\nabla_{\mathbf{X}}$	gradient with respect to Ω_0
$\nabla_{\mathbf{x}}$	gradient with respect to Ω
Ω_0, $\overline{\Omega}$, $\overline{\overline{\Omega}}$, Ω	initial, first intermediate, second intermediate relaxed and deformed configurations
Ω_0	adimensionalised concentration
p	pressure/Péclet number
ψ_0, ψ	Helmholtz free energy per unit volume in Ω_0 and Ω
ψ_0^{pa}	parent phase Helmholtz free energy per unit volume in Ω_0
ψ_0^{tr}	transformed phase Helmholtz free energy per unit volume in Ω_0
$\psi_{0:\mathrm{chem}}$	chemical term of the specific Helmholtz free energy per unit volume in Ω_0
$\psi_{0:\mathrm{mech}}$	mechanical term of the specific Helmholtz free energy per unit volume in Ω_0
ψ, λ	Schmid angles
ϕ	plastic function
q	heat flux per unit volume in Ω/interaction hardening parameter/non-dimensional interface mobility
$\mathbf{R}_{\mathrm{crys}\to\Omega_0}$	rotation matrix between crystal reference frame and Ω_0
$\mathbf{R}_{\mathrm{twin}}$	rotation matrix between the parent crystal reference frame and the twin crystal reference frame
r	radial distance in the diffusion problem/heat generation per unit volume
$\mathbf{S}_0$, $\overline{\mathbf{S}}$, $\overline{\overline{\mathbf{S}}}$	second Piola-Kirchhoff stress tensor in Ω_0, $\overline{\Omega}$ and $\overline{\overline{\Omega}}$
$s_{\alpha/\beta}$	resistance for slip/phase transformation of system α/β
s	shear produced by a whole twinned crystal
$\mathrm{SF}_{\mathrm{twin}}$	twin partial Schmid factor
$\mathrm{SF}_{\mathrm{partial}}$	trailing partial Schmid factor
σ_{cri}	critical stress for twin nucleation
$\boldsymbol{\sigma}$	Cauchy stress tensor
$\boldsymbol{\sigma}_{\mathrm{pa}}$	parent phase Cauchy stress tensor
$\boldsymbol{\sigma}_{\mathrm{tr}}$	transformed phase Cauchy stress tensor
T	absolute temperature
τ	resolved shear stress
$\mathbf{v}$	velocity tensor
v_{tr}	twin ledge velocity within the γ'
$\overline{v}_{\mathrm{tr}}$	average twin ledge velocity
V_0, V	volume of material in Ω_0 and Ω
$\overline{\overline{\mathbf{W}}}^{\mathrm{p:s}}$	skew part of the plastic slip velocity gradient tensor in $\overline{\overline{\Omega}}$
$\overline{\overline{\overline{\mathbf{W}}}}^{\mathrm{p:tr}}$	skew part of the plastic transformation velocity gradient tensor in $\overline{\overline{\Omega}}$
W	width of the specimen
X, Y	Cartesian coordinates in the diffusion problem
x, y	non-dimensional coordinates in the diffusion problem

Contents

1 Introduction

1.1 Efficient design of aero engines

Gas turbines in aircraft gain thrust by transforming the chemical energy of fuel to acceleration of the surrounding fluid (air). The temperature and pressure evolutions along the cycle of a typical aeroengine are illustrated in Fig. 1.1. Since the first turbojet in the late 1930s, engineers have been seeking to increase the efficiency of this cycle in order to reduce fuel costs and CO_2 fingerprint. The cycle efficiency increases as the system operates at higher temperatures, a tendency historically followed as observed in Fig. 1.2.

The materials used for each section of the cycle are mainly chosen by consideration of the temperature reached in every stage. The aforementioned increase of temperature in turbines could not be possible without the development of new Ni-based superalloys with higher temperature capabilities. These metals are used extensively in the most critical hot parts of the turbine engine, especially in the first stages of the turbine section.

However, with increasing in-service temperatures, these alloys are now facing the activation of new deformation mechanisms. These mechanisms present a complex

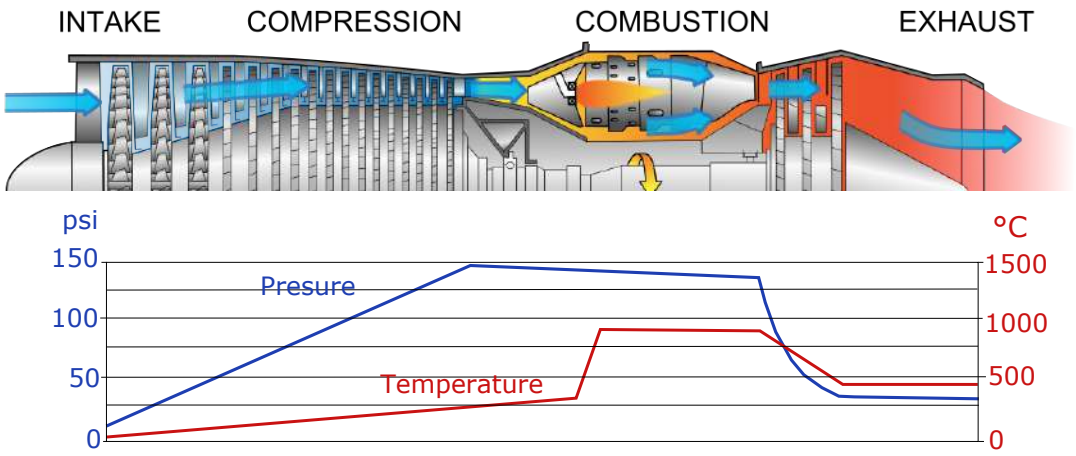

Figure 1.1 – Different stages in a commercial turbine engine cycle (top) and temperature and pressure evolution of the air flow through the different stages of the turbine engine cycle (bottom). Adapted from [1]

coupling between chemistry and plasticity that is still not fully understood; let alone their effects on the component performance. These complex creep mechanisms are introduced next.

1.2 Mid-temperature mechanisms in Ni-based superalloys

The creep deformation behaviour of the Ni-based superalloys controls the service life of most turbine components used in modern aeroengines [2]. The micromechanics in service of these materials are not entirely understood, but it is known that there is a strong dependence upon temperature, orientation and the magnitude of the applied stress [3].

This strong dependence is due to the wide variety of deformation mechanisms observed in these metals as illustrated Fig. 1.3. At high temperatures, thermally activated climb of dislocations has been observed to be the dominating deformation mechanism [5, 6]. When the temperature is low enough to prevent the domination

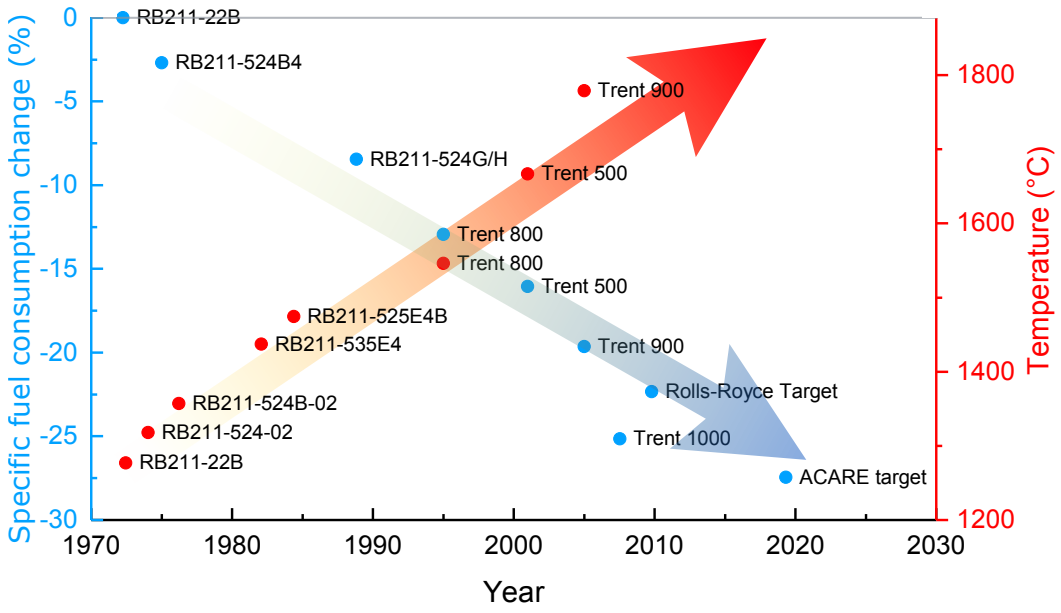

Figure 1.2 – Historical evolution of the turbine entry temperature and the specific fuel consumption of aeroengines [1]. ACARE - Advisory Council for Aviation Research and innovation in Europe.

of thermally activated diffusive processes, paired dislocations can shear the γ' precipitates creating a defect called antiphase boundary (APB), or bypass them by the Orowan looping mechanism [7, 8]. Less fully understood is the region at mid-temperature and lower stresses where the time-dependent process called microtwinning has been observed. In turbine disks of aircraft engines, where middle region temperatures (600-850°C) are present, microtwinning has been reported to be an important deformation mechanism [9, 10, 11].

The consequences of this deformation mechanism on the mechanical behaviour and microstructure of these superalloys are poorly understood. Undesirable re-crystallisation associated with the twin growth has been observed in single crystal superalloys by Moverare et al. [2]. They also discovered that microtwin bands enhance the fast propagation of cracks, leading to a catastrophic failure of the material. Some authors also reported segregation of heavy elements to the twin boundaries [10, 3].

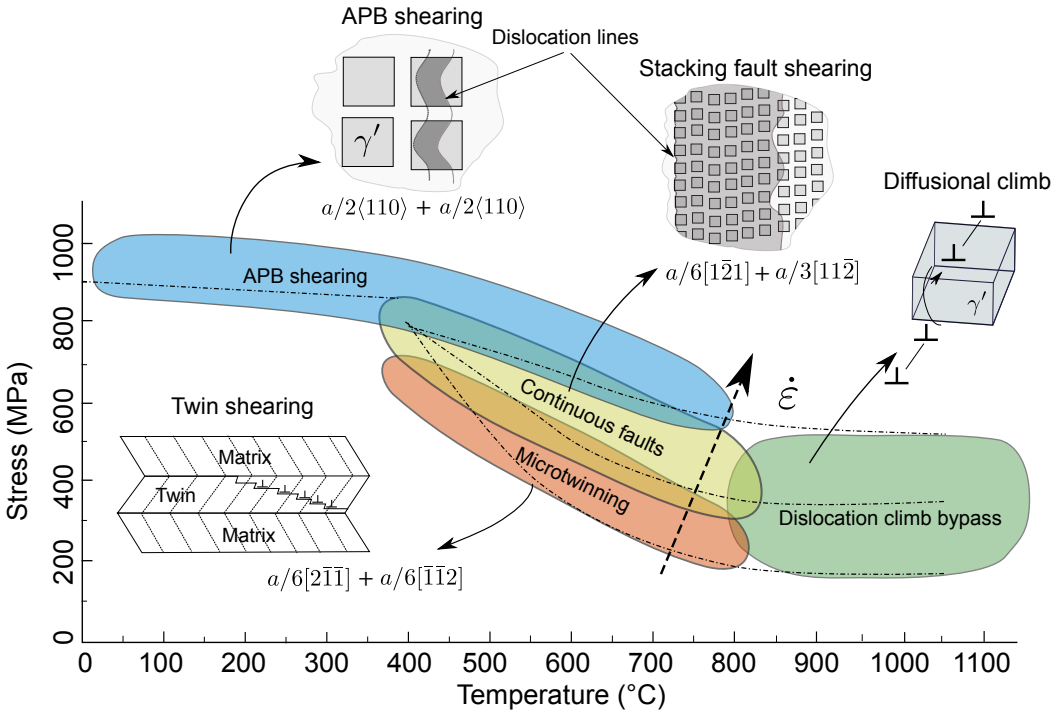

Figure 1.3 – Deformation map for a polycrystalline superalloy illustrating the dependence on stress, temperature and strain rate. Adapted from Smith et al. [4]. For single crystal superalloys the map is also dependent on the crystal orientation.

Traditionally, mechanical twinning has been described as an almost instantaneous displacive process that occurs at low temperatures when the number of active linear independent shearing systems is reduced thus promoting the activation of other deformation mechanisms [12, 13]. This is not the case for Ni-based superalloys, where a diffusive step is coupled with the time-independent shearing of partial dislocations making this phenomenon present only at high temperatures [10, 11]. This special link between the diffusive phenomena and the displacive dislocation shearing requires a completely new understanding of the twinning problem in Ni-based superalloys. Despite some previous research efforts [9, 10], the mechanism remains largely unknown.

1.3 Aim of the current research and thesis structure

In order to continue improving the capabilities of Ni-based superalloys, more fundamental research of these new active mechanisms is needed. First, a greater understanding of the underlying physics, i.e. segregation assisted plasticity or dislocation systems, is needed, for example to elucidate the temperature and stress dependence of the mechanisms and the competition among them (stacking faults vs. antiphase boundaries). Second, for design purposes, this understanding needs to be scaled up into thermomechanical consistent continuum models which can capture the relevant phenomena while retaining the dependence on the lower scales accurately. Finally, simulations of the relevant microstructures are needed to predict the mechanical behaviour of the alloy including these mechanisms which might be active during service. This work aims at linking the different scales of the problem in order to provide a deep understanding of the microtwinning mechanism, see Fig. 1.4.

1.3.1 Contributions of the current work

The contributions of this work to the field can be summarised in five major points:

1. Identification of the microtwinning regime conditions for a commercial single crystal superalloy MD2. The mechanism mapping is done by a systematic campaign of creep tests to study the influence of temperature, stress and orientation on the activation of the microtwinning mechanism. First, the influence of the orientation is studied by fixing the temperature at 800°C. The three main high symmetry orientations are tested: $\langle 001 \rangle$, $\langle 011 \rangle$ and $\langle 111 \rangle$.

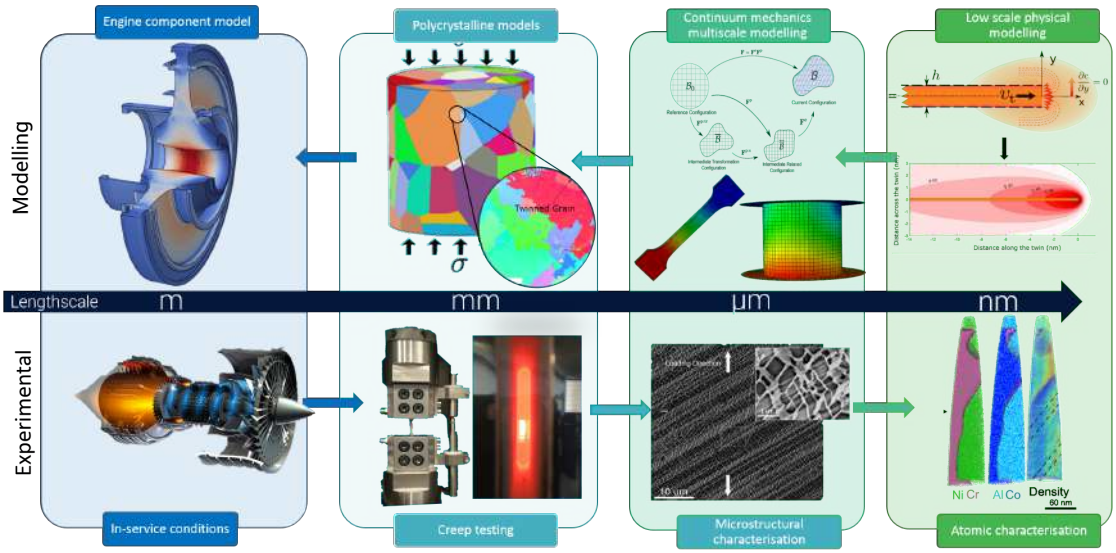

Figure 1.4 – Multiscale experimental and modelling framework.

Second, the orientation is fixed to ⟨011⟩ and tests at different temperatures and tensile stresses are performed. This allows to understand and identify the dependence of stress and temperature on microtwin formation.

2. Multiscale characterisation of the deformation mechanism occurring in the mid-temperature range. This includes:

   - **Macroscale (optical microscopy):** Fractographic studies are performed on the tested specimens to elucidate the role of microwinning on fracture damage. A clear connection between microtwin formation and embrittlement of the fracture is found.
   - **Microscale (scanning electron microscopy – SEM, and electron backscattered diffraction – EBSD):** A combination of SEM and EBSD techniques are used to identify the operative deformation mechanisms and to quantify the twin fraction formed during the creep tests. Additionally, EBSD analyses on the deformed regions are performed to study the distribution of microstrains around the microtwins.

These results are used to understand the link between microtwins and the embrittlement of the materials in the studied regime.

- **Atomic scale (transmission electron microscopy – TEM and atom probe tomography – APT):** TEM characterisation is used to elucidate the deformation mechanisms occurring during creep and the related physical phenomena, i.e. solute atmosphere around the growing faults and segregation assisted shearing. Furthermore, APT studies are used to quantify the chemical composition of the faults.

3. Modelling of the experimentally observed deformation mechanisms. This includes:

   - **Physical model of the diffusion micromechanics:** The observations made in the APT and TEM studies are incorporated in a ledge-fault type growth model. By solving the diffusion field around the fault front tip, the growth velocities can be calculated and eventually the experimental macroscopic creep rates can be predicted.
   - **A continuum mechanics theory which links the lower scale mechanisms to the macroscopic behaviour:** A phase transformation formulation for microtwinning is developed from the First and Second Principles of Thermodynamics, thus assuring the energetic consistency of the model. A multiscale approach is used to link the influence of the chemical composition at the atomistic scale with the flow rule at the macroscale through the free energy function of the system.
   - **A crystal plasticity-finite element (CP-FE) framework applying the continuum mechanics theory to model the mechanical**

behaviour of Ni-based superalloys: A series of FE simulations for different creep conditions at 800°C are performed to validate the proposed constitutive model. The framework is used to elucidate the influence of orientation and load direction on the activation of the different creep mechanisms. Additionally, the computational model is extended to the study of polycrystalline aggregates for validation purposes.

1.3.2 Thesis structure

For this purpose, the work presented in this thesis is structured as presented in Fig. 1.5:

Chapter 2 provides a complete review of the topic from two different points of view: physical metallurgy and continuum mechanics. First, the previous experimental observations of creep microtwinning related mechanisms are reviewed along with the different physical metallurgy theories to explain them. Second, an overview of the continuum mechanics and the crystal plasticity foundations is presented. The different approaches developed historically to tackle computationally the creep deformation problem in superalloys and the mechanical twinning are also reviewed. Chapter 3 focusses on the mechanical characterisation of the single crystal superalloy MD2 at mid-temperature. Tension and compression creep tests are presented in the relevant range of temperatures (750-850°C) and stresses (625-700 MPa) for microtwinning. The study is structured in two sections. First, the effect of orientation on the mechanical performance at 800°C is studied. Then, the orientation is fixed and the study is focussed on the effect of temperature and stress on microtwin formation. These results are used to quantify the role of the microtwinning mode in conferring deformation by means of quantitative stereology

measurements of the twin fraction. Finally, the embrittlement associated with microtwins formation is studied.

In Chapter 4, atomic resolution microscopy techniques are used elucidate the diffusion processes associated with the plastic deformation during creep. TEM and APT are used combined to characterise the chemical changes around the different deformation faults responsible for the creep deformation. The experimental observations are rationalised, focussing on the different diffusion scales present during twin extension.

In Chapter 5, this rationalisation is incorporated into a model for diffusion-controlled growth of segregated faults. From this emerge estimations of the twin lengthening/thickening kinetics. Finally, the model is used to recover the macroscopically-observed creep rates. The work provides the basis for the thermo-mechanical constitutive model developed in the next chapter.

In Chapter 6, the modelling is scaled up to the continuum scale. A general constitutive framework is proposed for phase transformation problems. This is then particularised for the case of microtwin formation in a multiscale fashion. This model has been developed under the assumptions of large deformation and thermodynamic consistency. The model couples the kinetics of the phase transformation with changes of the chemical composition and, therefore, diffusion between phases in a CP framework

In Chapter 7, the developed model is used for the study of creep deformation of the single crystal MD2 superalloy. The constitutive framework is implemented into a CP-FE code to study the orientation dependence of the activation of the different plastic mechanisms. The results are used to rationalised the tension/compression asymmetry and the distinct creep lives observed experimentally in Chaper 2. Finally,

the model is extended to the study the creep deformation of the polycrystalline version of MD2 superalloy as a validation of the proposed framework.

Finally, Chapter 8 summarises the main findings of this thesis and its contribution to the field. The link between the different scales is emphasised and the implications of the thesis findings on the future alloy design are detailed. The future research lines are also identified for further investigation.

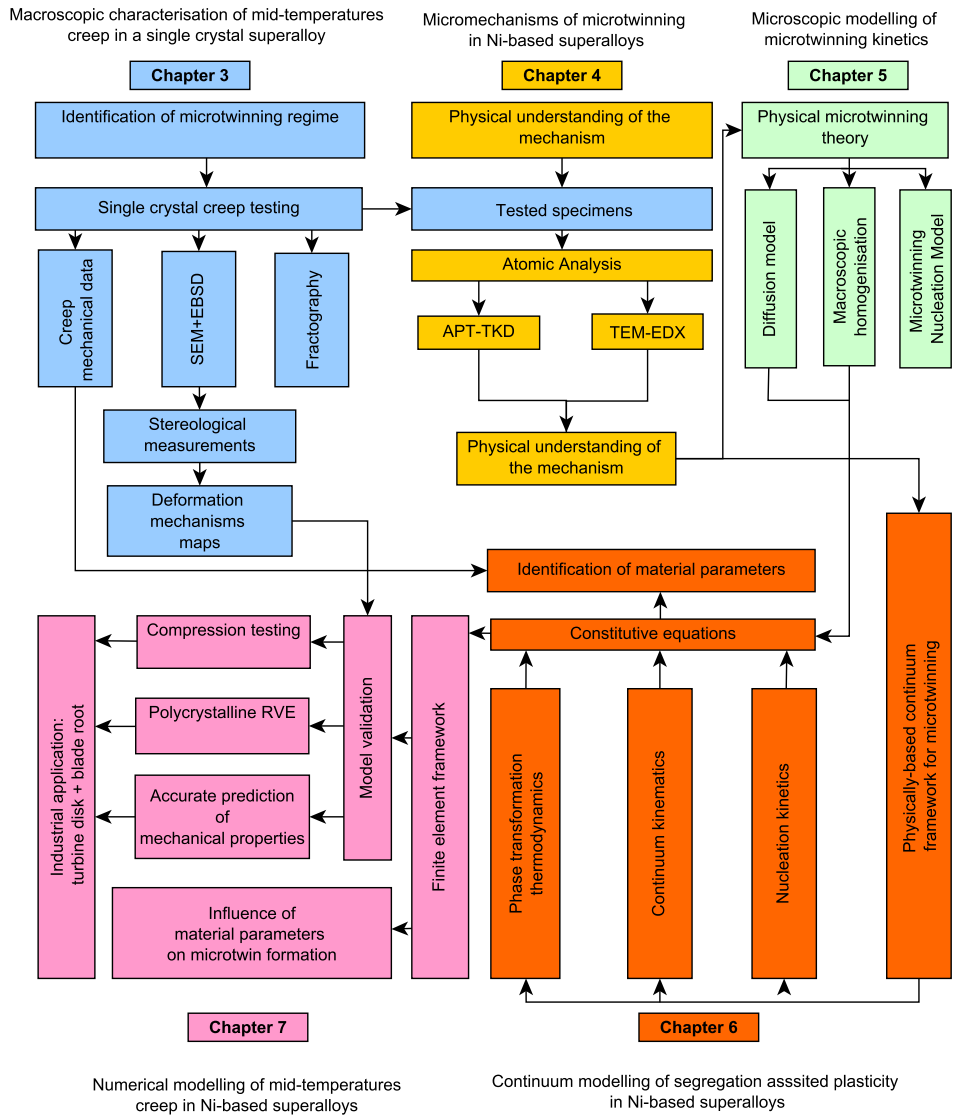

Figure 1.5 – Thesis structure showing key research activities divided by chapter.

2 Literature review

The first section in this chapter presents the work done to date on the physical aspects of microtwinning in Ni-based superalloys. This provides the basis for the review presented in the second section on the different approaches that have been developed to tackle the problems of creep in Ni-based superalloys and twinning in metals.

2.1 Physical metallurgy of metals: microtwinning

Metals are well known for undergoing large amounts of plastic deformation before failing. Plastic deformation of these materials is caused by several mechanisms such as slip, twinning, phase transformation or shear banding. The deformation mechanisms studied in this thesis are confined to a mix of slip, twinning, phase transformation coupled together. The basic concepts of the plastic slip and twinning mechanics are explained next. For a further review of the topic, the reader is referred to the work of Honeycombe [14].

2.1.1 Crystallography of plastic deformation

Crystalline metals are formed by atoms arranged in a pattern that repeats itself periodically in space [14]. In order to deform a metal plastically, these atoms need to move relative to each other along certain planes. This requires the rupture of atomic bondings leading to theoretical stresses tens or hundred times higher than the observed ones [14]. The discrepancy between the theoretical stresses and the experimentally observed ones is explained by the presence of dislocations.

Dislocations are structural defects in the crystal lattice allowing the metal atomic planes to glide by reducing drastically the stress required for such gliding [15, 16]. The process of dislocation gliding is explained in Fig. 2.1. Structurally, dislocations represent an extra half plane of atoms in the lattice. The intersection of the half plane and the glide plane (GP) is referred as a dislocation line. A dislocation is defined by its dislocation line vector and the Burgers vector. The Burgers vector **b** quantifies the difference between the distorted lattice around the dislocation and the perfect lattice, see Fig. 2.1.

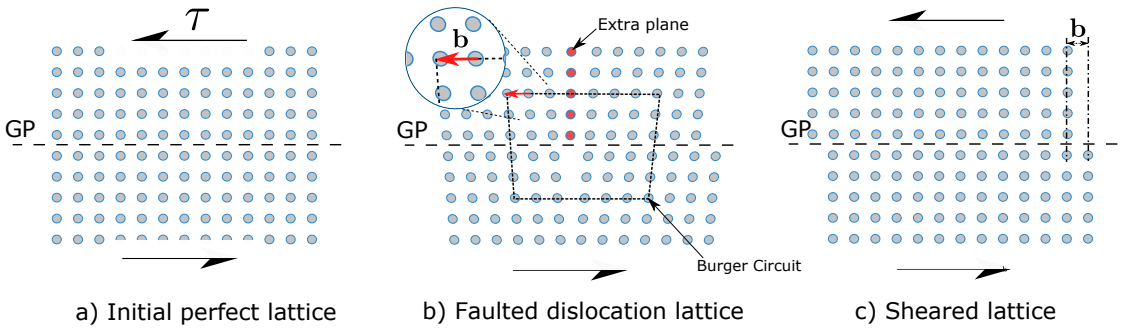

Figure 2.1 – a) Initial atomic arrangement under a shear stress τ; b) dislocation defect structure with a Burgers vector **b**. The circuit detailed around the dislocation defines the Burgers vector; c) final perfect atomic sheared structure.

Dislocations glide along well-defined crystallographic planes. Such crystallographic planes are referred to as slip planes, while the glide direction is defined as the slip

direction. The combination of a particular slip plane and slip direction is defined as the slip system. In FCC metals such as Ni, slip dislocations move primarily along one of the six closed-packed $\langle 110 \rangle$ directions, lying on four $\{111\}$ planes. These are illustrated in Fig. 2.2.

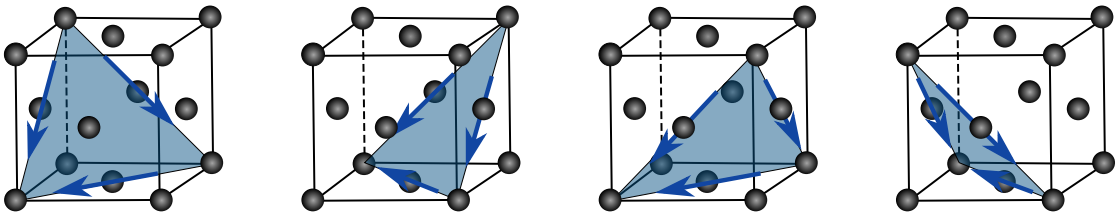

Figure 2.2 – Six different sliding systems in FCC metals.

2.1.2 Slip, stacking faults and twinning

The stacking sequence of $\{111\}$ planes in a FCC metal is ABCABCABC so the fourth layer relative position coincides with the first as shown in Fig. 2.3a. A full dislocation of Burgers vector $\mathbf{b} = a/2\langle 110 \rangle$ (a is the lattice parameter) translates the atoms in the B layer to other adjacent B lattice sites as observed in Fig. 2.3a. The shear produced by a full glide event leaves the final $\{111\}$ stacking sequence unaltered. In this movement, the atoms in the B layer need to overcome the blue atoms below making this path energetically unfavorable. In order to avoid this, the full shear can be split into two partial shears as indicated in Fig. 2.3a. In order for this to happen, the full dislocation needs to dissociate into two smaller ones; these are referred to as partial dislocations.

2.1.3 Stacking faults

The energy of a dislocation is proportional to the square of its Burgers vector $E \propto Gb^2$. This makes the dissociation process energetically favourable in this sense. However, the shear of a partial dislocation transforms the stacking sequence as

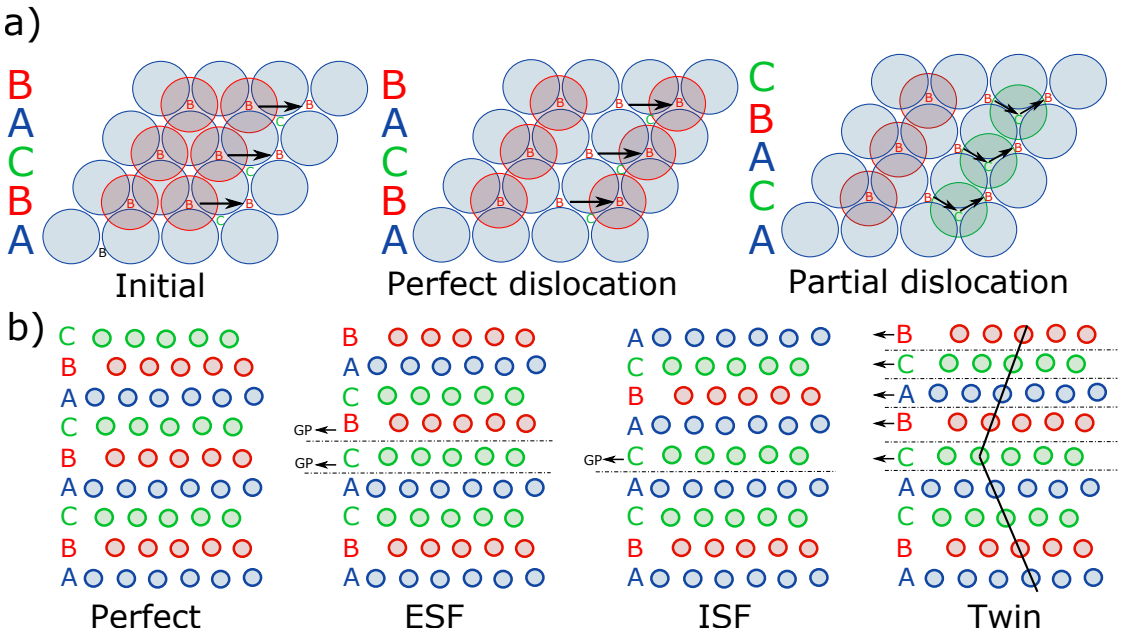

Figure 2.3 – a) Atomic path for a perfect dislocation (left). The staking sequence remain unaltered (center). The full dislocation can split into two partials creating a fault in the stacking sequence among them (right); b) stacking sequences for the different type of faults in FCC metals.

indicated in Fig. 2.3a (right). This is referred as a stacking fault (SF) and it has an associated fault energy measured in J/m^2. In monoatomic FCC metals two different types of stacking faults can be found: extrinsic stacking faults (ESF) and intrinsic (ISF). The first occurs when an extra plane is inserted in the sequence (ABC<u>B</u>ABC) and the second one when a plane is removed (ABCBC). The stacking sequences for the different faults are summarised in Fig. 2.3b. In intermetallic compounds such as superalloys, where the atomic structure is more complicated, the ESF and ISF ramificates into a wide variety of complex stacking faults [3]. These faults are usually of higher energy due to the near atomic neighbour violations formed.

2.1.4 Twinning

The creation of stacking faults is intimately related to the formation of twins. Twins are formed by the continuous shear of partial dislocations on consecutive

gliding planes as indicated in Fig. 2.3b. Twinning can be considered as a slip shearing coupled with crystal rotation [17]. This deformation mechanism has been historically associated with low temperature modes of deformations [18, 19]. However, in the case of Ni-based superalloys this phenomenon is observed at relative high temperatures (above 600°C) suggesting that its kinetics are somewhat different from the low temperature phenomenon.

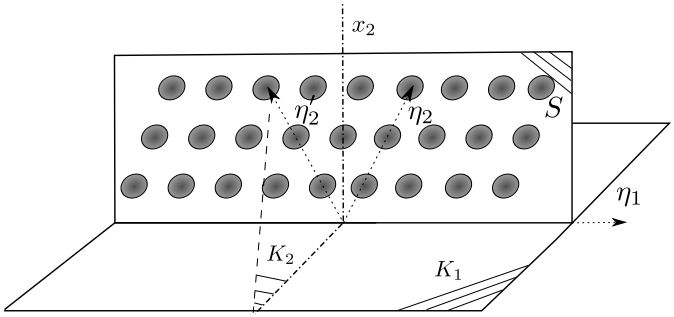

Figure 2.4 – Schema of twinning geometric elements.

Four important geometrical elements define any twin system (Fig. 2.4): the shearing plane $\mathbf{K}_1$, the shearing direction $\boldsymbol{\eta}_1$, the second undistorted plane $\mathbf{K}_2$ and the second undistorted vector $\boldsymbol{\eta}_2$. All the atoms above the shearing plane are displaced proportionally to its distance to $\mathbf{K_1}$ [20]. Depending on whether the Miller indexes of these four elements $(\boldsymbol{\eta}_1, \boldsymbol{\eta}_2, \mathbf{K}_1, \mathbf{K}_2)$ are rational numbers or not, two kind of twins can be defined: type I twins ($\mathbf{K}_1$ and $\boldsymbol{\eta}_1$ rational) and type II twins ($\mathbf{K}_2$ and $\boldsymbol{\eta}_2$ rational) [21]. When the Miller indexes of all the geometrical vectors are rational numbers, both types merge to compound twins (mixture of type I and II). Most FCC metals, due to their high symmetry, belong to this latter group [21] with Ni-based superalloys not being an exception [10].

2.1.5 Creep and time-dependent plastic deformation

At high temperatures ($T \geq 0.4\,T_m$), the deformation of metals is governed by thermally activated deformation mechanism for which diffusive processes are rate controlling. This regime where plastic deformation occurs even when the stresses are below the yield strength is referred to as creep. The mechanisms include long range diffusion creep, dislocation climbing of precipitates or short range fault reordering among others. This work is focussed on the deformation mechanisms that include dislocations gliding within their forming processes. The relation between the observed macroscopic deformation and the microscopic shearing of the dislocations is usually modelled by the Orowan equation:

$$\dot{\gamma} = \rho_{\mathrm{m}}\, b\, v \tag{2.1}$$

which simply states that the deformation rate $\dot{\gamma}$ is the result of the product of the gliding dislocation density ρ_{m}, the average dislocation velocity v and the Burgers vector magnitude b. This law was originally postulated for standard dislocation glide but can be used also for the case of dislocation climb [22]. Following statistical thermodynamics [22] the average dislocation velocity can be expressed as:

$$v \propto \nu\, \lambda \exp\left\{\frac{-\Delta G}{kT}\right\} \tag{2.2}$$

where ν is the vibration frequency of the dislocation, λ is the average distance advanced on every successful event, k is the Boltzmann constant and T is the temperature. The activation energy ΔG is used to characterised the barrier process limiting the dislocation shearing (climb of the precipitates, atomic reshuffling, etc.).

The energy barrier ΔG includes the work produced by the external stress acting over the dislocation during the thermally activated event and can be written as:

$$\Delta G = \Delta G_0 - V\tau \tag{2.3}$$

where ΔG_0 is the activation energy under zero stress, τ is the resolved shear stress produced by the external load and $V = -\frac{\partial G}{\partial \tau}\Big|_{T=\text{cte.}}$ is the activation volume, which is related to material volume involved during the thermally activated event. The experimental determination of V is of great importance because it represents a faithful fingerprint of the deformation mechanism. This characteristic volume presents small values for short range reordering processes and larger ones for dislocation solute interactions.

The general concepts of plastic deformation introduced here are considered in the next section for the case of mid-temperature deformation mechanisms in Ni-based superalloys.

2.1.6 Ni-based superalloys

Ni-based superalloys are biphasic alloys composed of an arrangement of γ'–Ni-Al(Ti) precipitates embedded coherently in a Ni-γ matrix as illustrated in Fig. 2.5. This unique combination is intimately related to the anomalous yield strength increase with temperature ("yield anomaly"). This phenomenon has been exploited in most of the turbine components in the last 60 years.

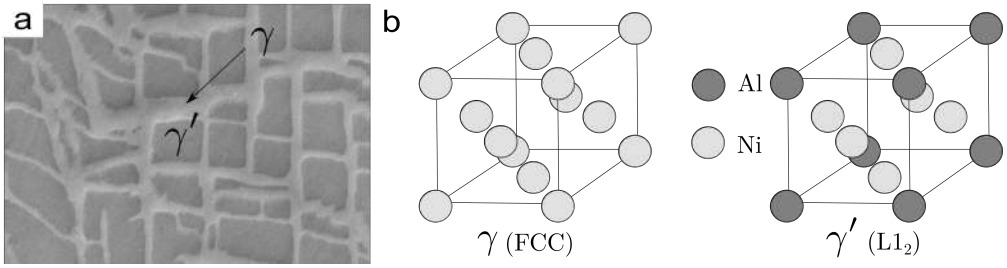

Figure 2.5 – a) Typical microstructure in a Ni-based superalloy (MD2) with an array of cubic γ' precipitates embedded coherently in a γ matrix; b) atomic structure of γ and γ' phases.

Considerable research has been carried out to develop an understanding of the wide variety of deformation mechanisms prevalent in single crystal superalloys. At the highest temperatures of approximately 850°C or beyond, climb-assisted glide of dislocations around the strengthening γ' precipitates is accepted to be the dominant deformation mechanism [5, 6]. When the temperature is sufficiently low (below around 600°C) the traditional view is that pairs of dislocations can shear the γ' precipitates, creating an antiphase boundary (APB), or else bypass them by the Orowan looping mechanism [7, 8] if the γ' fraction is low enough. More controversial is the region between 600 and 850°C where a range of different mechanisms have been reported [10]. An example is the stacking fault shear in which strongly coupled dislocations separated by intrinsic/extrinsic faults shear the γ' precipitates. But it is also within this temperature regime that a rather different deformation mode is found: deformation by microtwinning [9]. This deformation mechanism consists of thin bands of up to a few microns of rotated lattice running through the γ matrix and γ' precipitates [10]. Although the physics of this phenomenon differs from the low temperature mechanical twinning, the geometrical and mechanical consequences stated before in Section 2.1.4 persist in microtwinning.

2.1.6.1 Microtwinning observations in Ni-based superalloys

The microtwinning mechanism was first postulated by Kear et al. [23] in the 1970s as a viable mode of deformation in superalloys. Since then, several authors have reported the formation of microtwins in both single and polycrystalline superalloys at many different temperatures and stresses, see Fig. 2.6 and Table 2.1 which summarise the information in the literature so far. One notices that microtwinning has been reported at rather lower temperatures in polycrystalline alloys (between 650 and 750°C) than in single crystals, where it has been observed generally in the range 750 to 850°C. Moreover, the stress needed to activate it varies from superalloy to superalloy: it has been found to vary between stresses of 500 and 850 MPa, see Fig. 2.6. At this stage, it seems reasonable to believe that the kinetics of the microtwinning mechanism depend strongly upon alloy chemistry but also on microstructural features such as precipitate size or alloy type: e.g. single or polycrystalline systems.

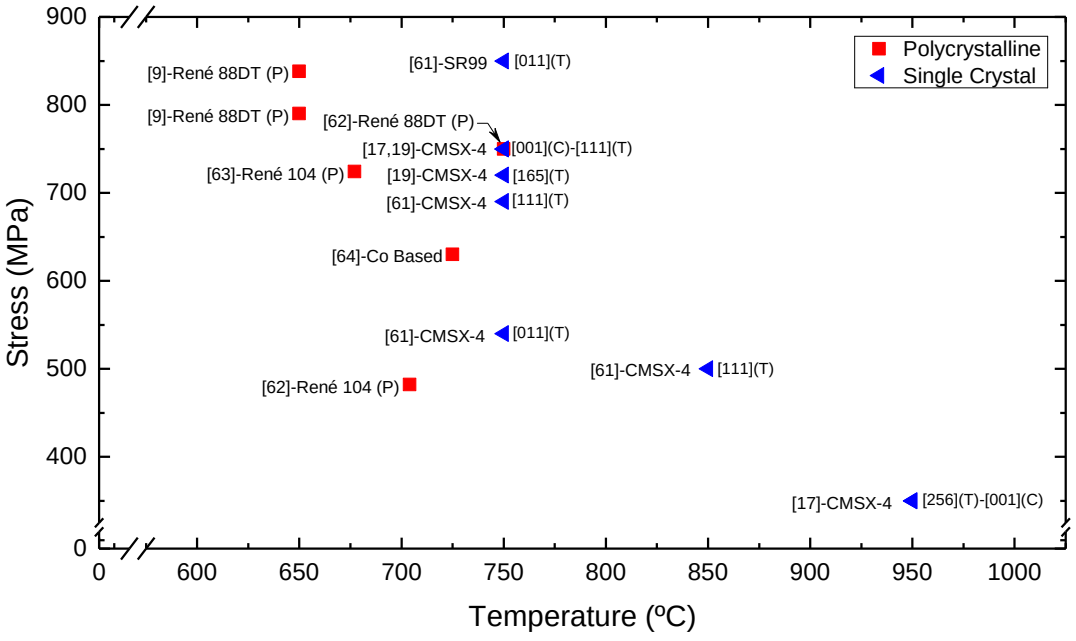

Figure 2.6 – Microtwinning conditions observed in the literature [24, 25, 26, 27, 28, 29, 6].

Table 2.1 – Experimental tests for which twinning was observed as a major deformation mechanism in Ni-based superalloys. S refers to single crystal alloy whereas P refers to polycrystalline alloys. T refers to tensile stress while C refers to compression test.

Reference	Alloy	Stress (MPa)	Temp (°C)	Direction
Ardakani et al. [24]	1-CMSX-4 (S)	690 (T)	750	<111>
	2-CMSX-4 (S)	500 (T)	850	<111>
	3-CMSX-4 (S)	540 (T)	750	<011>
	4-SRR90 (S)	850 (T)	750	<011>
Knowles and Gunturi [26]	5-CMSX-4 (S)	350 (C)	950	<001>
	6-CMSX-4 (S)	750 (C)	750	<001>
	7-CMSX-4 (S)	350 (T)	950	<256>
Knowles and Chen [25]	8-CMSX-4 (S)	720 (T)	750	<165>
	9-CMSX-4 (S)	750 (T)	750	<111>
Viswanathan et al. [6]	10-René 88DT (P)	838 (T)	650	-
	11-René 88DT (P)	790 (T)	650	-
Unocic et al. [28]	12-René 88DT (P)	750 (T)	750	-
	13-René 104 (P)	482 (T)	704	-
Unocic et al. [29]	14-René 104 (P)	724 (T)	677	-
Tian et al. [27]	15-Co-Based (P)	630 (T)	725	-

2.1.6.2 Microtwinning Mechanics

In parallel to these observations, rationalisation of the micromechanics of deformation has become increasingly possible as new experimental observations have emerged [23, 25, 10]. Originally, Kear et al. [23] assumed that the formation of microtwins occurs as a consequence of the formation of isolated superlattice intrinsic stacking faults (SISFs) in γ' which coalesce at high values of strain as illustrated in Fig. 2.7a. This was believed to be driven by the annihilation of dislocation pile-ups of opposite signs. Later, Knowles and Chen [25] called into question the need for the annihilation process. Instead, an autonomous system of dislocations was assumed to create a twin band behind them. A somewhat different mechanism was proposed first by Kolbe et al. [9] and then later adapted by Kovarik et al. [10], in which the need for localised atomic diffusion was emphasised as indicated in

Fig. 2.7b. In this model, the set of proposed dislocations leads to a high-energy faulted structure within the γ' phase (the so-called complex stacking fault – CSF) within the γ' phase which, after a four-step atomic reordering process, regresses to a perfect crystal structure with an effective rotation of 60° with respect to the parent phase. Kovarik et al. [10] estimated the energy barrier for the reordering process to be close to the self-diffusion energy for Ni in the γ' phase, justifying their assumption with atomistic simulations. This theory is supported by the experimental observations of Legros et al. [30]. They observed that dislocations slow down when they go from the γ matrix to the γ' precipitates due to the diffusion step only present in the γ' phase (no Al wrong-neighbour structure is formed in the γ phase).

It should be stated that the relatively high value of this energy barrier contrasts with the lower activation energy for twinning and stacking fault-mediated shear found in other FCC alloys. Unfortunately, even though these models successfully explain the atomic deformation path leading to the final rotated configuration, they offer an unsatisfactory explanation for how the dislocations overcome the initial energy barrier imposed by the CSF which is very high, of the order of $300\,\mathrm{mJ/m^2}$. The latest findings which make use of atomic-resolution analysis techniques on single crystal superalloys offer some suggestions which address this conundrum. Chemical fluctuations have been linked experimentally to the formation of faulted structures after mid-temperature deformation (650-850°C). In a series of Co-based superalloys, Titus et al. [31] reported partitioning of heavy elements such as Co, Cr, W and Ta to stacking faults (SFs), both SESFs and SISFs. Furthermore, Smith et al. [32] observed the segregation of Co, Nb, Ti and Ta along the SFs using interrupted creep tests in a single crystal version of the polycrystalline superalloy

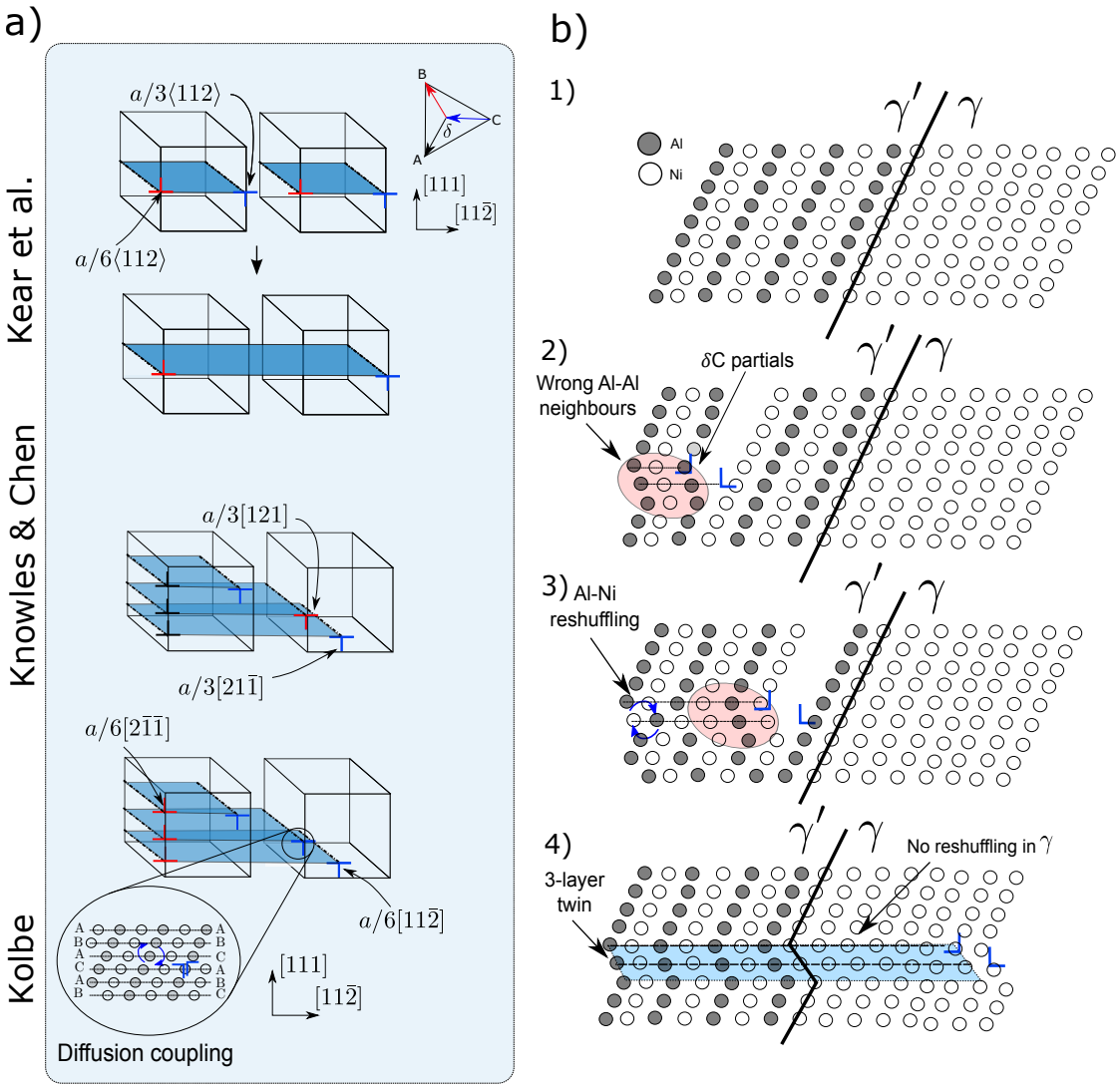

Figure 2.7 – a) Dislocation diagrams for the different microtwinning theories proposed in the literature: Kear et al. [23], Knowles and Chen [25] and Kolbe/Kovarik et al.[9, 10]; b) detailed diagram of the microtwinning model proposed by Kolbe [9].

ME3, later extended to its polycrystalline version [4]. Furthermore, the latter revealed the formation of a high-density Co/Cr atmosphere which encloses the SF tip. Despite these experimental observations, the understanding of the segregation processes and its coupling with the deformation kinetics is far from being complete. Some of the attempts to explain the process are reviewed next.

2.1.6.3 Physical models for microtwinning

Although significant efforts have been aimed at explaining microtwinning in superalloys [10, 9], many aspects of the process remain to be understood; twin nucleation, propagation and coupling with other diffusional processes are controversial. There is little work focussed on these aspects which are crucial to eventually developing faithful continuum models. The physical study of the nucleation and propagation of microtwins can be reduced to the work of Knowles and Chen [25] for the nucleation and the work of Karthikeyan et al. [33] for the propagation of the microtwins.

Supported by energetic balances, Knowles and Chen [25] proposed a twin nucleation criterion based on the critical radius of a twin nucleus r_c:

$$r_c = \frac{1}{2}\frac{\mu n^2 b^2}{nb\tau - \gamma_{SF}} \quad \text{where} \begin{cases} n & - \text{ number of layers in the nucleation process} \\ \mu & - \text{ shear modulus of } \gamma' \\ \gamma_{SF} & - \text{ stacking fault energy} \end{cases}$$

For SISFs, $\mathbf{b}_{SISF} = a/3\langle 112\rangle$ whereas for SESFs defects, $\mathbf{b}_{SESF} = a/6\langle 112\rangle$. According to this model, r_c for a SESF defect is half the value of r_c for a SISF one, making a twin more likely to be formed after a SESF than after a SISF defect. This is confirmed by experiments where the microtwins are always related with the appearance of SESFs [9, 11]. These defects can be observed under compression in the $\langle 001\rangle$ direction and in tension in the $\langle 011\rangle$ direction [26, 25].

On the other hand, the microtwinning continuum model of Karthikeyan et al. [33] is based on the assumption that the atomic reordering proposed by Kolbe [9] is the time-limiting process for dislocation glide. They assumed an exponential drop of the fault energy from the initial high energy CSF (G_{CSF}) to the completely

reordered low energy SESF (G_{SESF}) promoted by atomic diffusion after the twin shearing (pseudo to real twin transformation):

$$G(t) = (G_{\mathrm{CSF}} - G_{\mathrm{SESF}})e^{-Kt} + G_{\mathrm{SESF}} \tag{2.4}$$

where K is a diffusion constant related to the diffusivity of the atomic reordering D_{ord} and t is the time after shearing. The strain rate produced by microtwinning is then obtained by the energetic balance of the dislocation system:

$$\dot{\gamma} = \frac{\rho\, b\, D_{\mathrm{ord}}(b/x^2)}{\ln\left[f_2(G_{\mathrm{CSF}} - G_{\mathrm{SESF}})/(2\tau_{\mathrm{eff}}b - f_2\, G_{\mathrm{SESF}})\right]} \tag{2.5}$$

where x is the short range diffusion length, f_2 is volume fraction of secondary γ', ρ is the density of partial dislocations and $\tau_{\mathrm{eff}} = \tau - \frac{f_3 \Gamma_{\mathrm{CSF}}}{2b}$ is the effective stress on the dislocation, where f_3 is the fraction of tertiary γ'.

Although the theory shows good accordance with some superalloys (René 104), it fails to take into account dislocation density evolution, thus leading to important errors in other superalloys (René 88). Furthermore, Viswanathan et al. [11] proved that the reordering process occurs over a larger distance, which may explain the overestimation of the dislocation motion reported by Karthikeyan et al. [33].

2.2 Continuum modelling of microtwinning in Ni-based superalloys

Two main challenges arise in the modelling of the microtwinning mechanism in Ni-based superalloys; first the constitutive modelling of the creep response at high temperature and secondly the numerical and constitutive treatment of the rotations

produced by the twin mechanism. The reader is referred to the work of Hozpafel et al. [34] and Roters et al. [35] for further reference on continuum mechanics and crystal plasticity theory.

2.2.1 Crystal plasticity modelling of creep in Ni-based superalloys

Crystal plasticity (CP) has demonstrated the ability to model faithfully the mechanical crystalline response of superalloys at high temperatures [36, 37, 38, 39]. Ghosh et al. [36] proposed a phenomenological CP model for uniaxial creep of single crystal superalloys including the effect of crystallography and tertiary creep. In this approach, slip over octahedral {111} and cubic {001} planes is considered. Brehm et al. [40] extended this study by including a precise description of the dislocation densities for the different slip systems and their interaction. MacLachan et al. [37] proposed a simplified power-law model with a reduced number of parameters including the effect of partial ⟨112⟩ shear on the creep rates, which was assumed to be symmetric. Their results capture with good agreement the creep response for tensile ⟨001⟩ and ⟨111⟩ orientations. The work of Busso et al. [41] accounts for the additional hardening effects associated with dislocation density gradients, which have been proved crucial to cause the γ' strengthening in superalloys. Part of this work is further extended in Zhao et al. [42] in a diffusion-mechanical coupled framework to study the influence of oxidation on the crack initiation in Ni-based superalloys CMSX-4. The work of Kashiro et al. [43] provides a detailed insights into the nucleation mechanisms of ⟨110⟩ superpartials using a coupled FE-dislocation dynamics model. Shenoy et al. [44] developed a rate dependent, microstructure-sensitive CP model of the mechanical behaviour of polycrystalline

IN100 at 650°C. The model is based on the generation of representative volume elements (RVEs) of the actual microstructure and a physically based CP constitutive framework. Ma et al. [39] incorporated the climb mechanism over γ' precipitates in a dislocation based CP model and obtained a good prediction of all stages of creep for $\langle 001 \rangle$ orientation. They further developed the model [45] by including the chemical dependency of the diffusivity on the climbing rates. The work of Kim et al. [46] extended this approach for a wider range of alloys by accounting for the alloy composition in the calculation of the elastic properties. Vorster et al. [47] developed a RVE method for predicting the creep strength of a wide range of single crystal superalloys. In this model, the plastic deformation (in the form of a stochastic viscous law) is constrained to the γ channels, while the γ' precipitates are assumed to deform elastically. This method has been extended by Keshavarz et al. in several studies [38, 48, 49, 50] to a three-scale framework: (i) precipitate level; (ii) single crystal level and (iii) polycrystalline level. The bridge between scales is performed by the identification of the material parameters from the lower scale in a bottom-up approach. In this model they have included the plastic deformation of the γ' phase and non-Schmidian effects. The major limitation of the models developed until now is that their effectiveness is usually proven for a limited set of crystal orientations or loading conditions without accounting for the chemical changes during plastic deformation reported in the literature [51, 52, 53].

Despite all the research described for the case of creep in superalloys, limited work has been done to study the mechanics of microtwinning in superalloys. The work of Keshavrarz et al. [48] is the sole one in the literature that considers this deformation mechanism in a pseudo-twinning model. The twin nucleation criterion is obtained from Unocic et al. [29]: twin partials are nucleated if, after overcoming

a threshold stress, the leading partial undergoes a higher stress than the trailing partial due to differing Schmid factors, leading to dissociation. This model shows good correlation with experimental results for CMSX-4, proving its ability to simulate mid-temperature superalloys behaviour. However, its phenomenological modelling and the fact that twinning is simply a simple shearing prevents the study of some of the microtwinning's effects (crystal reorientation, twin fraction, diffusion coupling, etc.).

2.2.2 Twinning in crystal plasticity models

Twin rotation in computational plasticity models introduces additional difficulties to the standard slip formulations [54, 55]. These challenges arise from the reorientation produced in the twinned element. Two different approaches can be found in the literature regarding the twin rotation treatment as indicated in Fig. 2.8: micromechanical models and continuum mechanics models.

In the first approximation, a twinned element is considered as a new grain, which forms abruptly, thus affecting the convergence of computational models. In these models, the characteristic element size is comparable to the twin thickness for mechanical twins or to the twin step size in the case of diffusion assisted twinning. Several models can be found in the literature which attempt to describe twinning by this approach [56, 57, 58]. To tackle the twinning problem, Van Houtte [56] proposed a crystallographic rotation governed by the volume fraction of the twinned regions; a grain is allowed to reorient if the accumulated twin fraction f reaches a critical value f_{tw}. This scheme has been successfully introduced in visco-plastic self-consistent models [59, 60], and CP-FE models [57, 58].

In the second approximation, the problem is treated on the continuum scale and each

element transfers smoothly from the untwinned state to the twinned state [61, 35]. This means that the mechanical response is the result of the homogenisation within the element. The homogenisation can consider the elastic deformation of each part independently [61]:

$$\mathbf{S} = f\,\mathbf{S}_{\mathrm{tw}} + (1-f)\,\mathbf{S}_{\mathrm{pa}} \tag{2.6}$$

where $\mathbf{S}_{\mathrm{tw}}$ and $\mathbf{S}_{\mathrm{pa}}$ are the second Piola-Kirchhoff stress of the twin phase and the parent phase, respectively.

Alternatively, it can be assumed that both phases undergo the same elastic deformation, being the overall response a combination of the stiffness matrices of both phases:

$$\mathbf{S} = \left[f\,\mathbb{C}_{\mathrm{tw}} + (1-f)\,\mathbb{C}_{\mathrm{pa}}\right] : \mathbf{E}^{\mathrm{e}} \tag{2.7}$$

where $\mathbb{C}_{\mathrm{tw}}$ and $\mathbb{C}_{\mathrm{pa}}$ are the elastic stifness matrix of the twin phase and the parent phase, respectively and $\mathbf{E}^{\mathrm{e}}$ is the Green-Lagrange strain tensor. This last approach is the one considered in this work and will be further extended later.

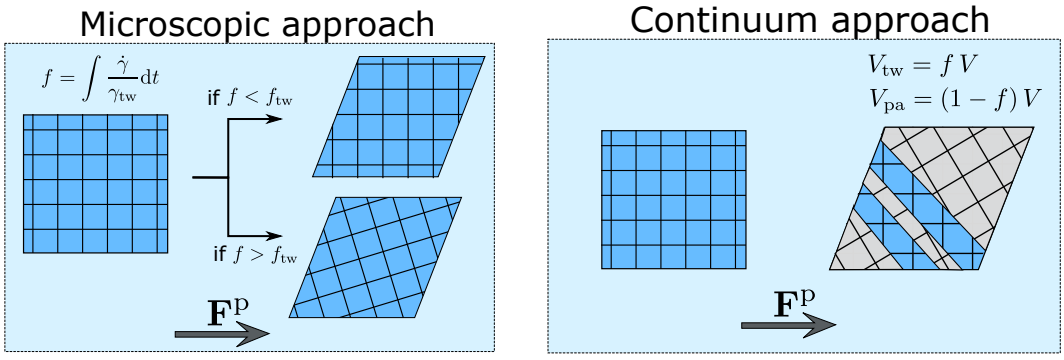

Figure 2.8 – Different modelling approaches for the twin problem. γ_{tw}, $\dot{\gamma}$, f_{tw}, V_{tw} and V_{pa} refers to the reference twin shear, the twin shear rate, the critical twin fraction for crystal rotation and the volume of twin and parent phase, respectively.

The work done to date on the creep deformation of Ni-based superalloys in the studied range of temperatures (650-850°C) is clearly extensive. However, these

models do not include other time-dependent deformation mechanisms, recently observed, such as microtwinning, or their coupling with the chemical changes during deformation. Further insights into the physics of Ni-based superalloys are needed to provide reliable models to predict their mechanical behaviour within this temperature region.

3 Macroscopic characterisation of mid-temperature creep in a single crystal superalloy

3.1 Introduction

Resistance to plasticity is a significant advantage of the Ni-based superalloys, particularly when in single crystal form [62, 2]. But a distinction must be made between the time-dependent mode of deformation – so-called creep deformation – which is prevalent at high temperatures and/or low strain rates [36, 63, 64] and the time-independent – commonly athermal – behaviour [65, 66] which dominates at ambient conditions. Clearly, since many technological applications require the analysis of deformation behaviour, it is important to know which of the two modes is the more likely. This challenge – which has still to be overcome – becomes even more daunting under the loading conditions at which the athermal and creep responses are approximately equal [67, 10, 68, 6, 69, 70].

For the single crystal superalloys the situation is made more acute by the finding that a time-dependent viscous deformation mode involving the propagation of microtwins [26, 9, 10, 30, 71, 6] can occur at this cross-over point. Although these findings confirm the crucial role in conferring plastic deformation of the

microtwinning, many issues need to be addressed. It is known that many variables – i.e. temperature, stress, loading direction, microstructure, alloy composition – play a crucial role in determining the dominant deformation mechanism. To rationalise all the different effects seems a daunting task; it is not surprising therefore that no constitutive modelling of the microtwinning effect accounting for stress and temperature dependence exists as yet. Clearly, what is needed is a controlled experimentation carried out across a range of temperature and stresses, designed in a systematic way. In this chapter, the chemical composition and microstructure are fixed, thus allowing for the influence of temperature, stress and orientation to be studied experimentally.

The present chapter – which is motivated by the above – describes a broad testing experimental campaign to understand the dependence of microtwinning on stress, temperature and crystallographic orientation. The study is organised as follows. The first section is focussed on the effect of the orientation and loading direction on the activation of microtwinning at a fixed temperature. The second section studies the temperature and stress dependence of the microtwin formation for a fixed orientation. Stereological measurements are performed to quantify the changes on the twins population as a function of the stress and temperature. Finally, the consequences of microtwinning on fracture behaviour are discussed.

3.2 Experimental methods

3.2.1 Material

The prototype single crystal Ni-based superalloy MD2 is selected for use in the present study. Its nominal chemical composition is given in Table 3.1. Single crystal castings were produced in rod form using standard investment casting routes and

solution treated for 8 hours at 1275°C, then aged following a two-step process: 6 hours at 1080°C and 16 hours at 870°C to yield a uniform distribution of γ' precipitates.

Table 3.1 – Chemical composition (wt.% and at.%) of Ni-based superalloy MD2.

	Ni	Al	Co	Cr	Hf	Mo	Ta	Si	Ti	W
wt. %	Bal.	5.0	5.1	8.0	0.1	2.1	6.0	0.1	1.3	8.1
at. %	Bal.	11.24	5.25	9.33	0.03	1.33	2.01	0.22	1.65	2.63

3.2.2 Creep testing

3.2.2.1 Tension creep tests

A series of tensile creep tests were performed using an Instron electro-thermal mechanical testing (ETMT) machine. A schematic illustration of the experimental set-up and sample geometry for the tensile tests is presented in Fig. 3.1. For heat application, the system uses the Joule effect with a 400 A DC supply providing electrical current through the sample to generate heat. Miniaturised dog bone specimens of 1.6×1 mm^2 cross section were machined from single crystal cast bars using wire-guided electro-discharge machining (EDM). Specimens were mechanically ground using 1200 grit SiC paper prior to testing to ensure the removal of any induced damaged layer. The testing temperature was controlled by a K-type thermocouple centrally welded onto the specimen. Digital image correlation (DIC) was used to measure the strain within the central 3 mm of the specimen [72]. The tests were performed in air. A constant load was maintained during each test. Creep tests were performed twice in each case to confirm acceptable repeatability.

3.2.2.2 Compression creep tests

Uniaxial compression creep tests were conducted in an Instron servo-electric machine. Fig. 3.1 illustrates the test system and the sample geometry. Cylindrical specimens of $\varnothing 5{\times}5\,\mathrm{mm}^3$ were machined from cast bars using EDM. Custom-made grips were manufactured as illustrated in Fig. 3.1. Silicon carbide plates were used to transfer the load between sample and the grips. A conventional three-zone furnace was used to provide the desired control of the temperature. The temperature was monitored with type K thermocouples at the upper and lower grips. The maximum measured temperature deviation during the tests were confined to within $\pm 3^{\circ}$C. Tests were performed in air and specimens were held for 15 minutes to reach uniform temperature before each test commences. The specimen strain was monitored during the tests using DIC. Boron nitride was used as a lubricant to reduce the friction between the sample and the plates.

3.2.3 Microstructural characterisation

Metallographic examination of the samples was performed using a JEOL 6500F field emission gun scanning electron microscope (FEG-SEM) equipped with a TSL Digiview II EBSD detector.

EBSD maps for geometrically necessary dislocation (GND) density calculations were obtained with the tested sample located at a working distance of 15 mm, tilted 70° and oriented with the rolling direction parallel to the tensile axis of each sample. GND-EBSD diffraction patterns were acquired using a square grid with a 0.05 μm step size, a 30 kV accelerating voltage, 600 pA probe current and a 0.5 s acquisition time at the full 1000×1000 pixel resolution per pattern. A custom Matlab script [73] was then utilised to calculate lattice curvatures identified through the saved

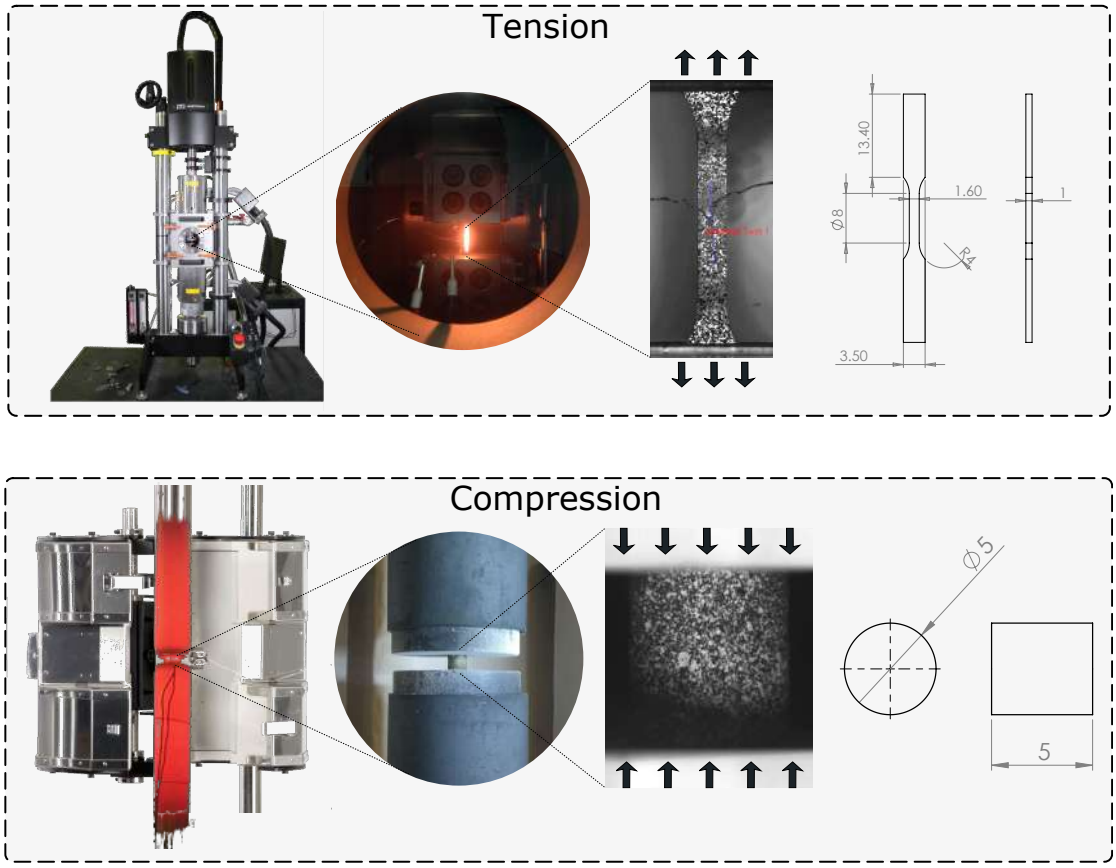

Figure 3.1 – Experimental set-up and sample geometries used for tensile and compressive creep tests (measurements are in mm).

digitised diffraction pattern from each location within the square grid. Measured lattice rotations were subsequently used to calculate the spatially resolved GND content [74].

Backscattered electron images (BEI) of the tested samples were acquired at 10 kV with a 300 pA probe size in order to fully exploit the channelling contrast created by the change in crystallographic orientation of the twins. Images in BEI mode of the twinned structures were used to perform a quantitative stereology assessment of the twin fraction and thickness using image analysis software Image J [75]. Equally spaced micrographs of $20{\times}20\,\mu m^2$ were taken to obtain a representative value of the twin fraction and thickness – starting from the fracture surface and moving

along the tensile direction. The different twin fractions were analysed statistically in order to obtain a mean value for each testing condition within the central 3 mm of the sample. These results were used to map the twinned structure morphology as a function of the stress and the temperature.

Additionally, EBSD low magnification maps of the previously BEI mode imaged regions were obtained to confirm the presence of microtwins using a Zeiss Evo LS1 W-filament SEM equipped with an Oxford Instruments EBSD detector. Finally, the fracture surfaces were characterised using an Alicona optical microscope.

3.3 Influence of the crystal orientation on the microtwinning activation

A series of tension and compression uniaxial creep tests were performed at a fixed temperature in order to study the orientation dependence of the microtwinning mechanism. The stress and temperature conditions of the study were selected carefully by the previous reported microtwinning conditions indicated in Fig. 2.6. A temperature of 800°C was selected for all tests. Different stresses in the range of 625-700 MPa were selected for subsequent model calibration purposes in Chapter 7. Three different high-symmetry orientations were tested: $\langle 001 \rangle$, $\langle 110 \rangle$ and $\langle 111 \rangle$. EBSD was used to measure the deviation of the crystal direction from the ideal nominal orientation, see Table 3.2. The testing conditions for all tests are presented in Table 3.3.

Table 3.2 – Nominal orientations and measured orientations for the single crystal samples used in this study.

Nominal Orientation	$\langle 0\ 0\ 1 \rangle$	$\langle 1\ 1\ 0 \rangle$	$\langle 1\ 1\ 1 \rangle$
Measured Orientation	$\langle 0.02\ -0.07\ 0.99 \rangle$	$\langle 0.73\ 0.67\ -0.08 \rangle$	$\langle 0.66\ 0.53\ 0.54 \rangle$

Table 3.3 – Creep tests conditions for single crystal MD2 at 800°C.

Direction	Tension (MPa)				Compression (MPa)			
⟨001⟩	–	650	675	700	625	650	675	700
⟨011⟩	625	650	675	700	–	650	–	700
⟨111⟩	–	650	–	700	–	650	–	700

The measured tensile and compression behaviours for the different studied orientations are shown in the creep curves in Fig. 3.2. The repeat tests performed for validation are presented in Fig. 3.3 for the specific case of 800°C for the loading direction ⟨011⟩. The creep strain rates computed from the curves in Fig. 3.2 are presented in Fig. 3.4. A strong anisotropy of the creep response is found. Moreover, a tension-compression asymmetric behaviour is observed especially for the crystals oriented along ⟨011⟩ and ⟨001⟩. Further examination of the active deformation mechanisms is presented next.

Post-mortem examination of the samples was carried out to identify the orientations and conditions for which microtwinning occurs. Combined SEM and EBSD techniques were used to identify the deformation features and confirm their twin character. Some examples of these deformed structures are presented in Fig. 3.5a. The activation of microtwins is observed along the ⟨011⟩-direction during tensile deformation and along the ⟨001⟩-direction in compression. The number of active twin systems is found to vary from one direction to another. A single twin system is identified for tensile ⟨011⟩ microtwins while for ⟨001⟩ compression microtwins, two conjugate families of twin systems are observed. This is in agreement with the number of highly stressed twin systems expected for the measured orientations [25]. Although in the SEM image in Fig. 3.5a two twin systems are clearly active for ⟨001⟩ compression, the EBSD image in Fig. 3.5a for the same condition shows only one twin system. This can be explained by the limitation on step size of this

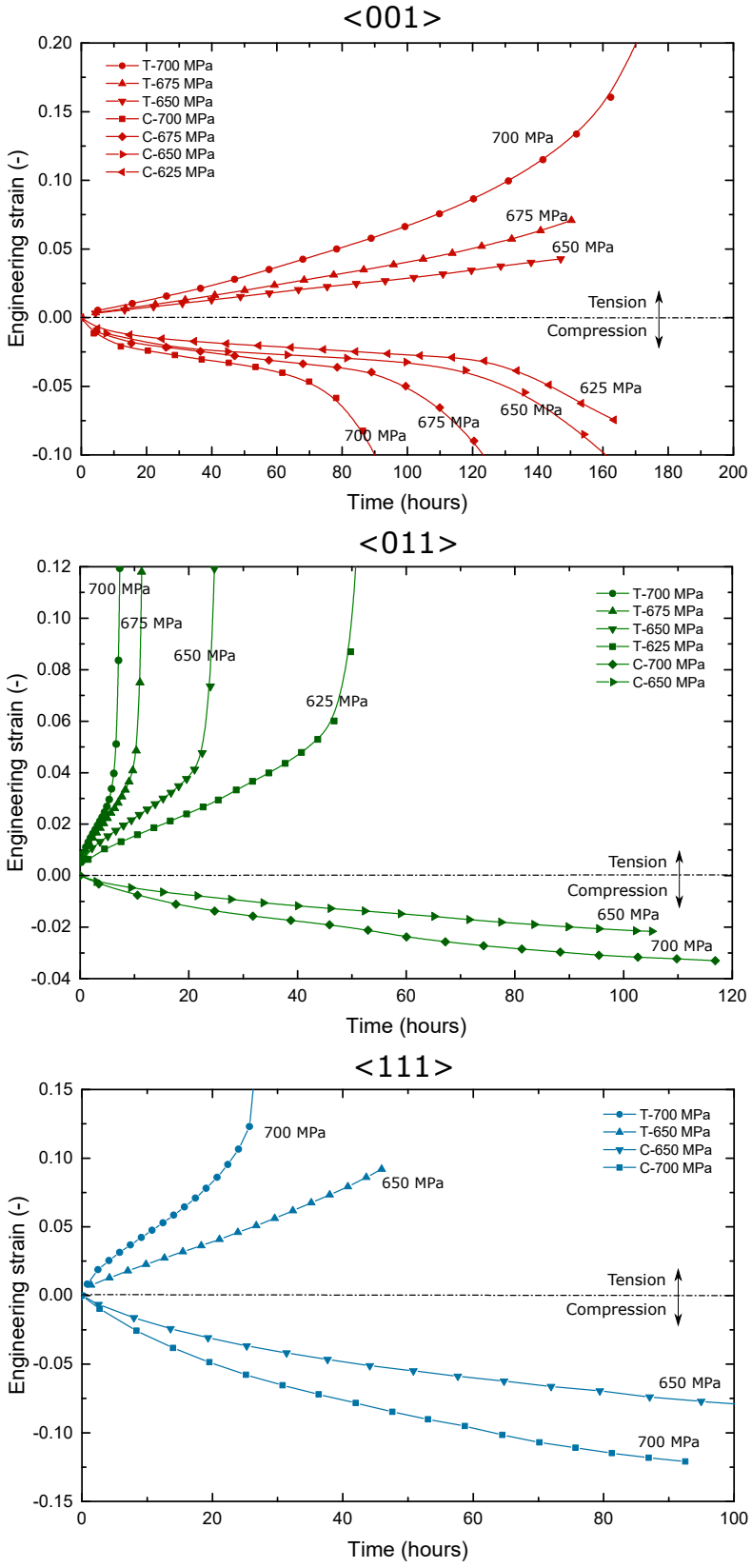

Figure 3.2 – Creep strain curves for MD2 single crystal superalloy at 800°C for the loading directions ⟨001⟩, ⟨011⟩ and ⟨111⟩ and stresses between 625 MPa to 700 MPa

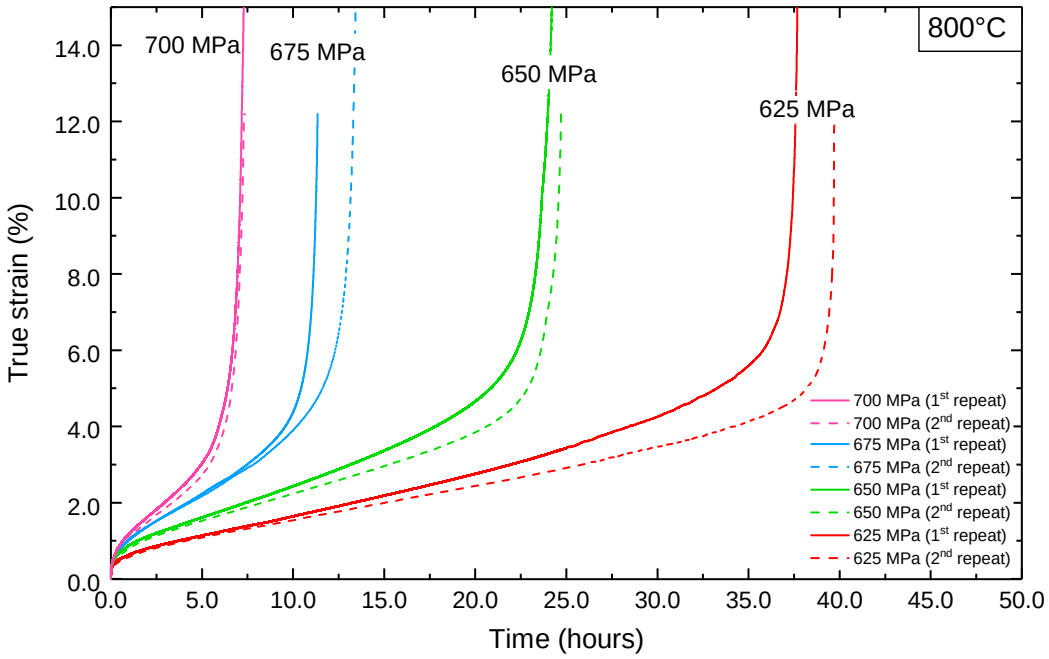

Figure 3.3 – Repetitions for the creep tests of MD2 single crystal superalloy at 800°C for the loading direction ⟨011⟩ and stresses between 625 MPa to 700 MPa

technique. The EBSD misorientation for all cases is 60° consistent with twinning in FCC. Additionally, the fact that formation of these twin bands is not observed in the reversed-load tests (⟨011⟩-compression and ⟨001⟩-tension) implies that the microtwinning formation mechanism is strongly antisymmetric.

The proposed explanation for this behaviour is presented in the atomic model of Fig. 3.5b. In this figure, three adjacent FCC closed packed {111} atomic planes are presented. By sliding the top layer over the bottom and middle layers along the closed packed FCC slip directions ⟨011⟩ and ⟨112⟩, the following different deformation mechanisms take place:

- Slip along ⟨011⟩ directions by a full dislocation (with a Burgers vector $|\mathbf{b}| = a/\sqrt{2}$, where a is the lattice parameter): this leads to a correct stacking sequence but wrong neighbours structure at the shear plane (the local ordering of Al and Ni atoms is corrupted). This shear direction is totally symmetrical

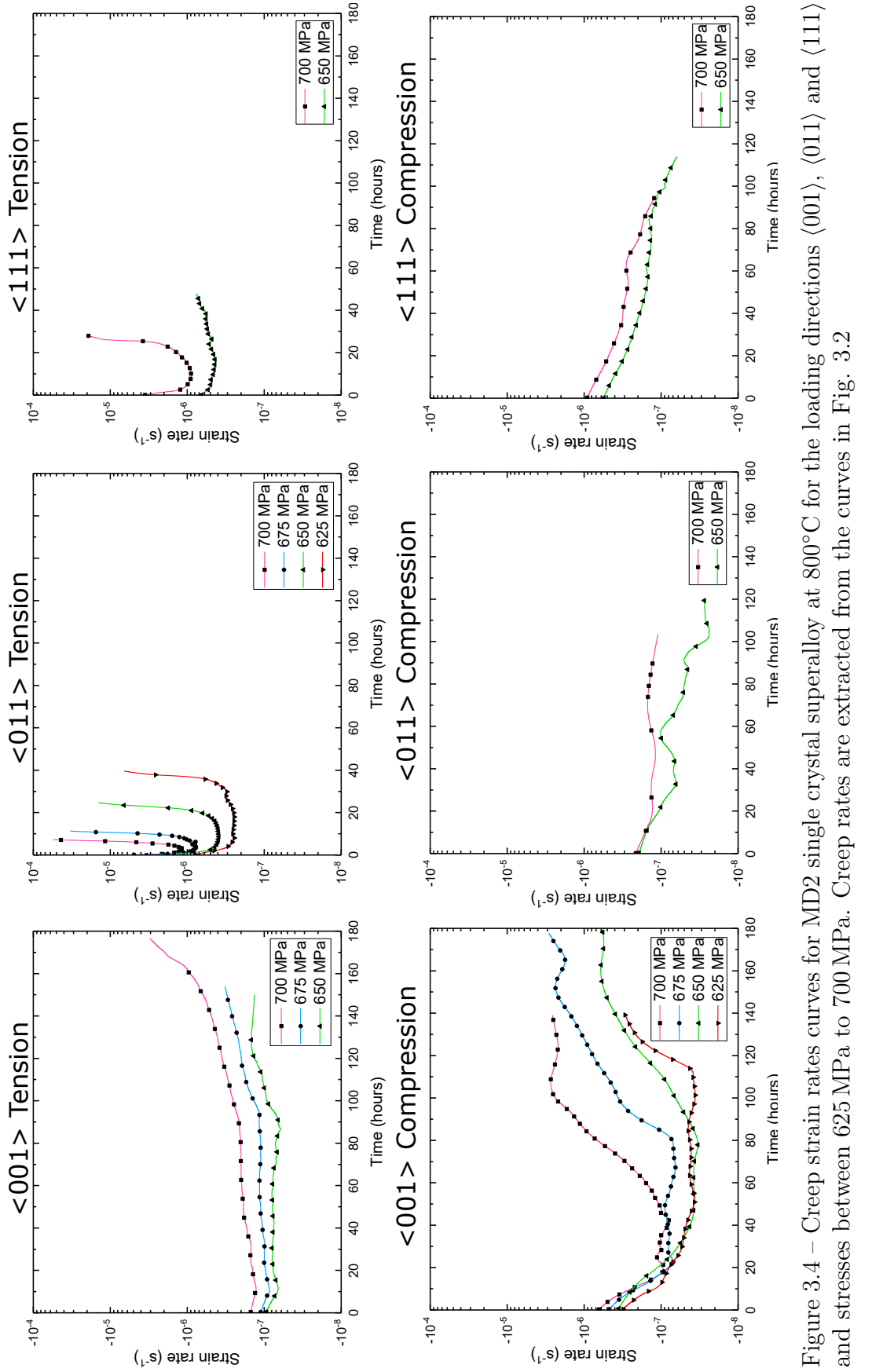

Figure 3.4 – Creep strain rates curves for MD2 single crystal superalloy at 800°C for the loading directions ⟨001⟩, ⟨011⟩ and ⟨111⟩ and stresses between 625 MPa to 700 MPa. Creep rates are extracted from the curves in Fig. 3.2

so it cannot explain by itself the mechanical response observed. Hereafter, this mechanism is referred to as octahedral slip or APB shearing.

- Slip along $\langle 112 \rangle$ directions by a partial dislocation. In this case, two different situations can happen. (i) In a forward positive movement along $\langle 112 \rangle$ (represented as green arrows in Fig. 3.5b and $|\mathbf{b}| = \frac{3\sqrt{6}}{2}$a), a superlattice intrinsic stacking fault (SISF) is created. This configuration is not considered in this work because its large Burgers vector implies a high elastic energy needed for the partial dislocation to form and therefore, it is unlikely to occur [76]. Additionally, the atomic path of the sliding plane is required to overpass the atoms on the subsequent layer, which involves an extra high energy barrier. (ii) However, if the dislocation shear occurs in the opposite direction (red arrows in Fig. 3.5b and $|\mathbf{b}| = \frac{\sqrt{6}}{2}a$), a high energy structure called complex intrinsic stacking fault (CISF) is created. The combination of this type of shear over consecutive layers along with various diffusion processes [52, 51, 53] transforms this high energy fault to a low energy superlattice extrinsic stacking fault (SESF) and, eventually, in the mature state, to microtwins. This process is studied in detail in the next chapter. As the faults extend within the γ' precipitates, the high energy structures created are restored by the segregation of γ stabilizers (Co and Cr). This implies long range diffusion and, therefore, a time-dependent shearing of the γ' precipitates. The stress applied on the dislocation needs to be in equilibrium with the back-stress required to create the new fault or phase. This back-stress is time-dependent and intimately related to the quantity of Co/Cr that is segregated at the growing fault.

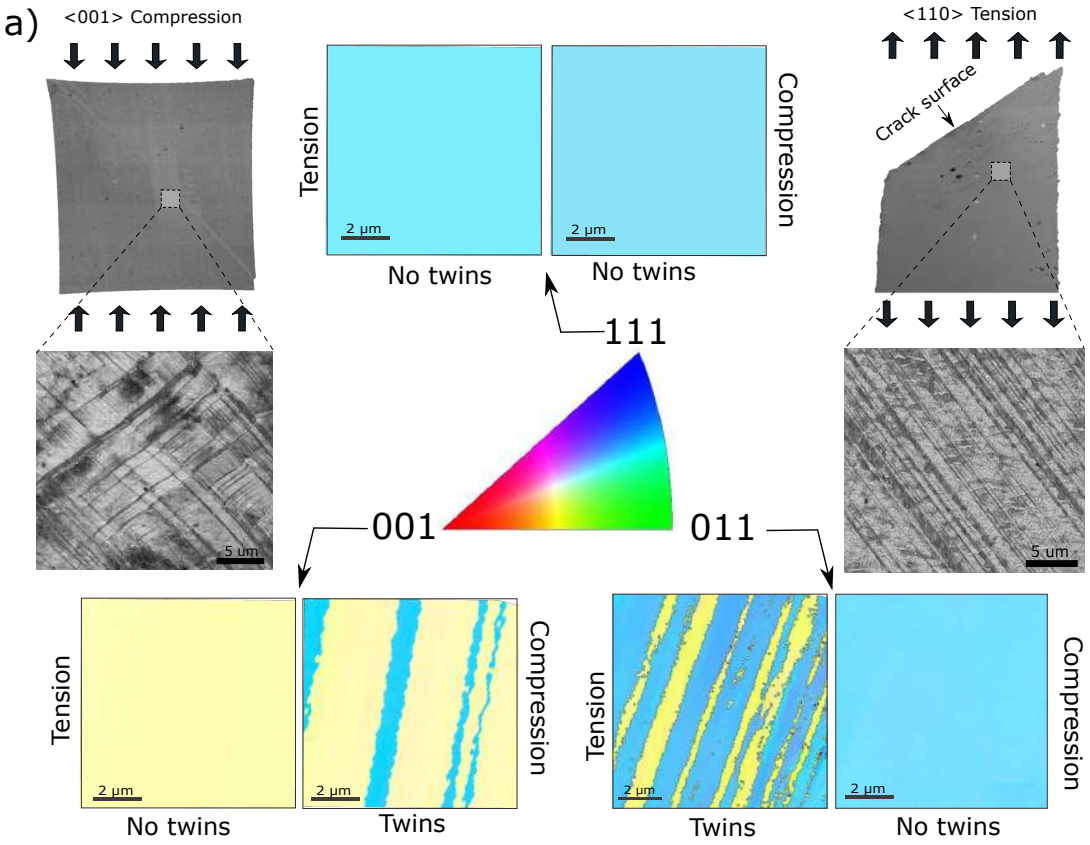

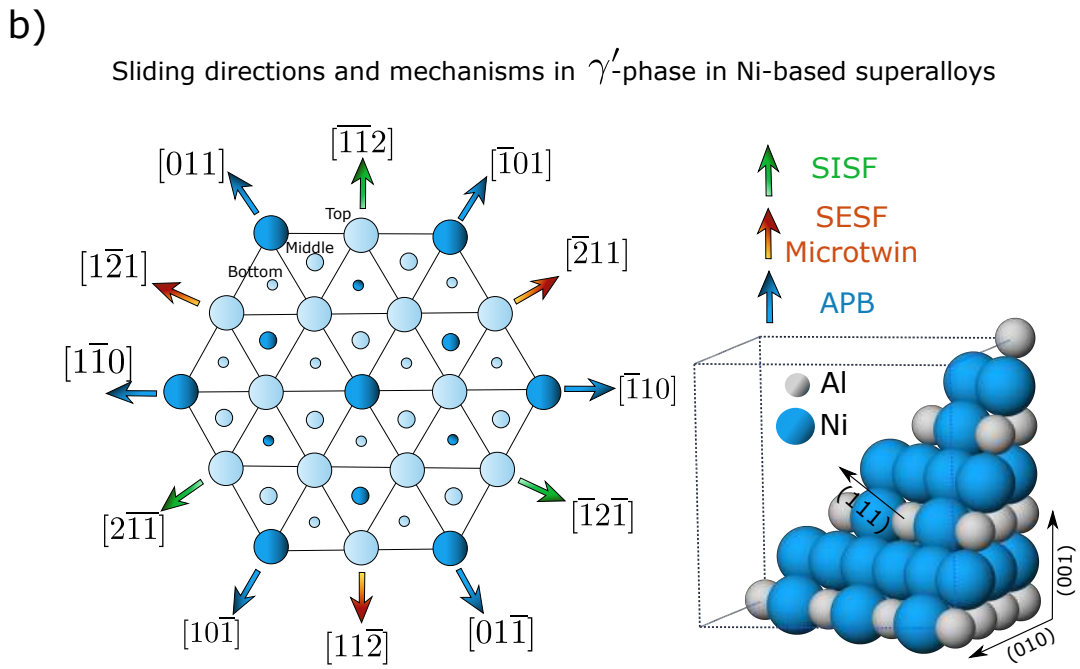

Figure 3.5 – a) EBSD maps of the tested samples at 800°C indicating the conditions for which microtwinning is active: ⟨011⟩ in tension and ⟨001⟩ in compression along with experimental micrographies of the 650 MPa-⟨011⟩-tension and 650 MPa-⟨001⟩-compression specimens containing microtwins after testing; b) crystallography of slip deformation along {111} planes in Ni-based superalloys.

3.4 Influence of the stress and temperature on the microtwinning activation

In this section, the previous study on MD2 is extended for the case of ⟨011⟩ orientation under tension to study the influence of temperature and stress on the microtwinning formation. Guided by the previous reported conditions for microtwinning in Fig. 2.6, a series of creep tests were performed at temperatures between 775 and 850°C with applied tensile stresses of 625, 650, 675 and 700 MPa. The selected testing conditions for mapping the microtwinning mechanism are summarised in Table 3.4.

Table 3.4 – Creep tests conditions for ⟨011⟩ single crystal superalloy MD2 under tension.

Temperature (°C)	Stress (MPa)			
775	625	650	–	–
800	625	650	675	700
825	625	650	675	700
850	625	650	–	–

3.4.1 Identification of temperature/stress regime for microtwinning

The creep results for temperatures of 775°C, 800°C, 825°C and 850°C are shown in Fig. 3.6. The computed strain rates from these curves are presented in Fig. 3.7. The creep curves presented in Fig. 3.6 present the characteristic primary, secondary and tertiary creep regimes from this temperature region [77, 78]. The secondary creep rates used later for the derivation of the activation energy and volume are extracted from the average slope of the stationary stage in the curves from Fig. 3.6. The primary and tertiary creep stages are defined for the subsequent analysis

as the regions where the strain rate is more than double the strain rate in the stationary stage from the curves in Fig. 3.7.

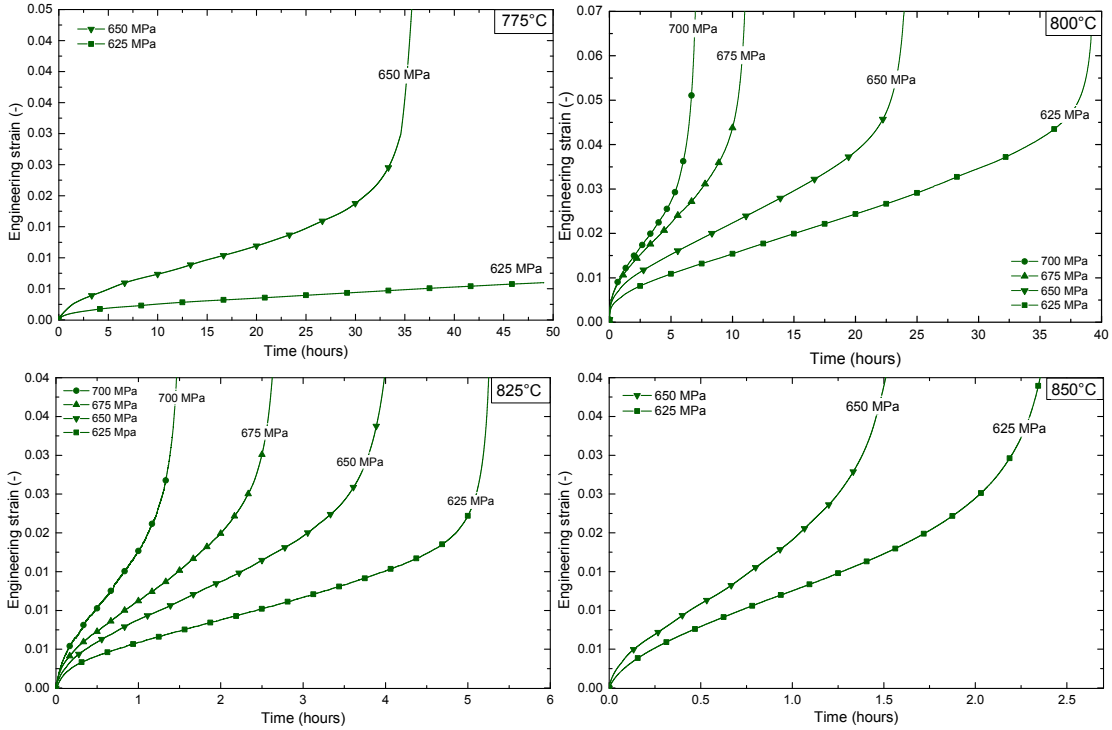

Figure 3.6 – Creep strain curves for ⟨011⟩ single crystal MD2 at 775°C, 800°C, 825°C and 850°C and tensile stresses between 625 MPa to 700 MPa.

EBSD inverse pole figure maps of the deformed regions after testing are shown in Fig. 3.8. Microtwinning is proven to be active at 800°C and 825°C under stress conditions between 625 -675 MPa and at 625 MPa respectively. The microtwins extend across the entire sample width. The misorientation is again 60° between the deformation bands and the matrix confirming that microtwinning occurred In all cases, only one twin system is active during creep. The morphology of the microtwins depends significantly on the testing conditions. This dependency is intimately related to the microtwinning kinetics: both lengthening and thickening. Their kinetics are quantitatively studied in the following chapters.

The steady-state creep stage is now analysed, identifying the type of mechanisms

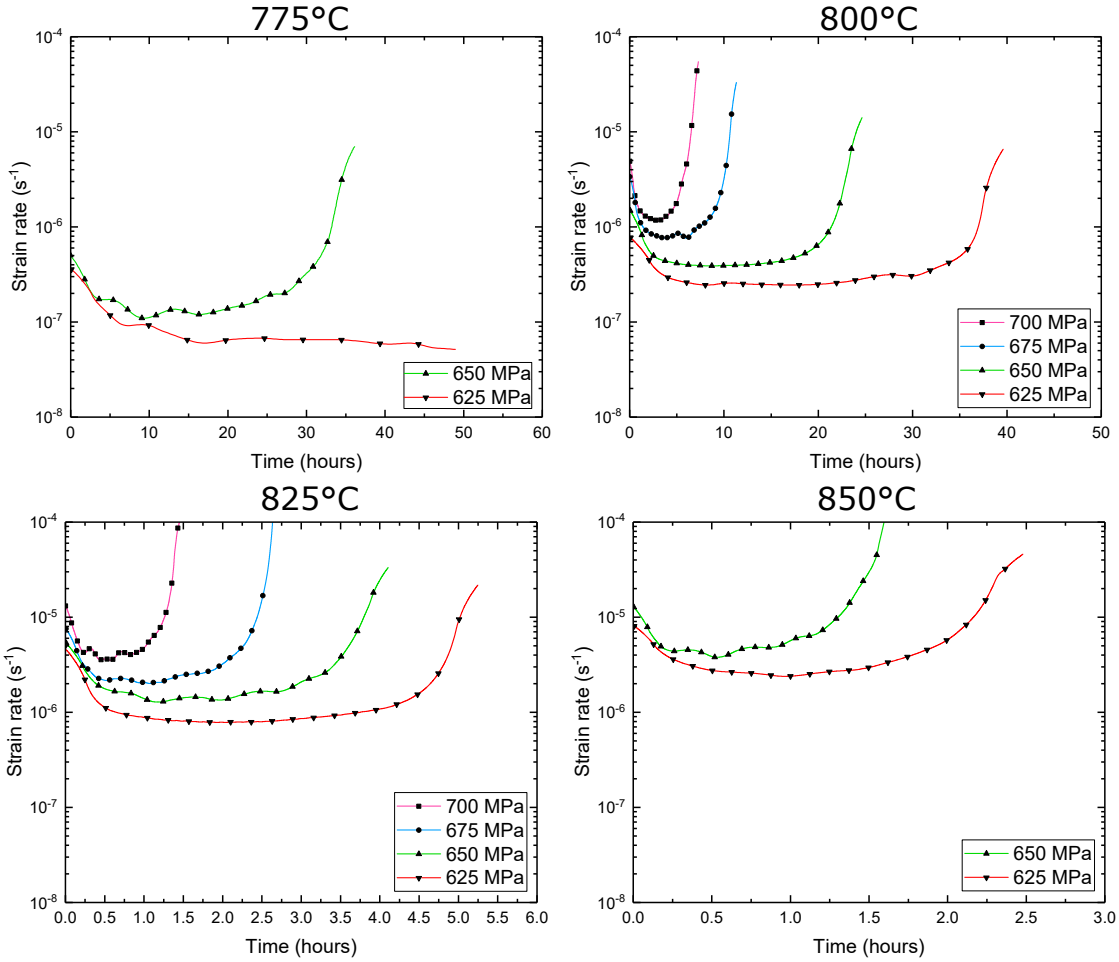

Figure 3.7 – Creep strain rates curves for ⟨011⟩ single crystal MD2 at 775°C, 800°C, 825°C and 850°C and tensile stresses between 625 MPa to 700 MPa. Strain rates are computed from curves in Fig. 3.6

taking place. The secondary creep rates are plotted in Fig. 3.9 differentiating between testing conditions where a microtwinning mechanism is active (red) and conditions where no microtwinning is observed (black). The activation energies ΔG (Fig. 3.9a) and the activation volumes V (Fig. 3.9b) for both cases are indicated as a function of the stress and temperature, respectively. No appreciable change of the apparent activation energies and activation volumes between twin and non-twin conditions is observed. The apparent activation energy values (400-480 kJ/mol) are in agreement with previous studies [79, 80] for the same range of temperatures but substantially higher than the value of self-diffusion of Ni ($Q_{\text{self}} \approx 300\,\text{kJ/mol}$)

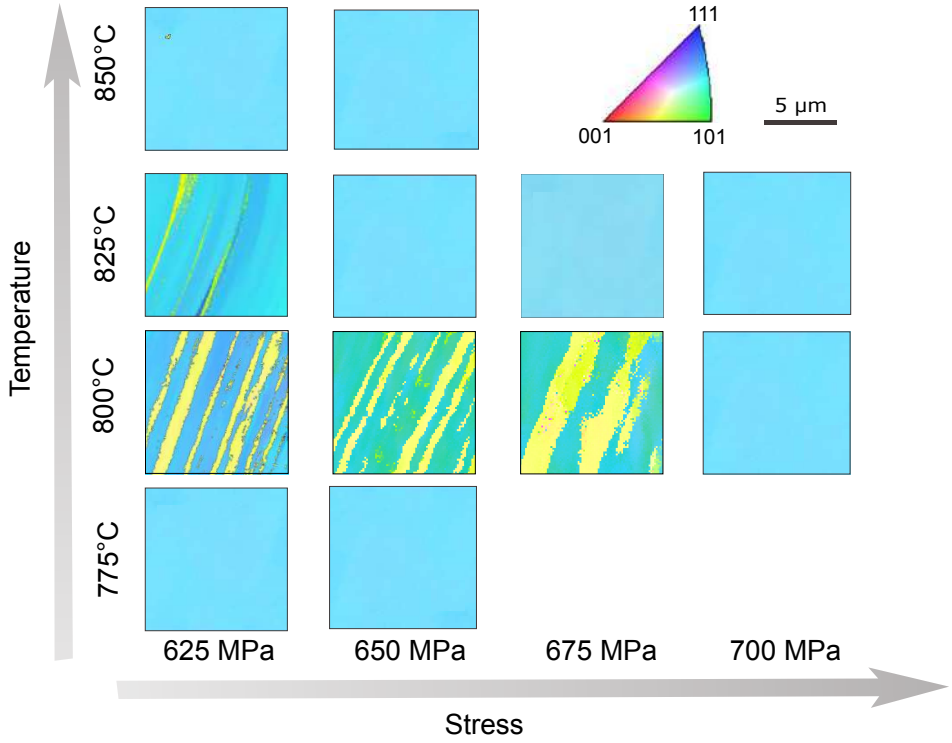

Figure 3.8 – EBSD analysis for ⟨011⟩ single crystal MD2 specimens after creep deformation at the conditions presented in Fig. 3.6. The change of orientation indicates the formation of microtwins.

which suggests that other diffusive processes, different from this, may be taking place. Similarly, the activation volume values (200-300b^3, where $b = 1.4\times10^{-10}$ m) are in agreement with previous studies [64] at similar temperatures.

3.4.2 Estimation of microtwin thickness and fraction, and stress/temperature dependence

The twin bands identified by EBSD analysis are composed of bundles of thinner microtwins which, due to EBSD spot size limitations, appear as a single entity in Fig. 3.8. To overcome this, high-resolution backscattered imaging is used to provide more accurate twin thickness and twin fraction (f_{twin}) measurements, see Fig. 3.10a. Both twin fraction and thickness are found to increase with stress, see

3.4. Influence of the stress and temperature on the microtwinning activation

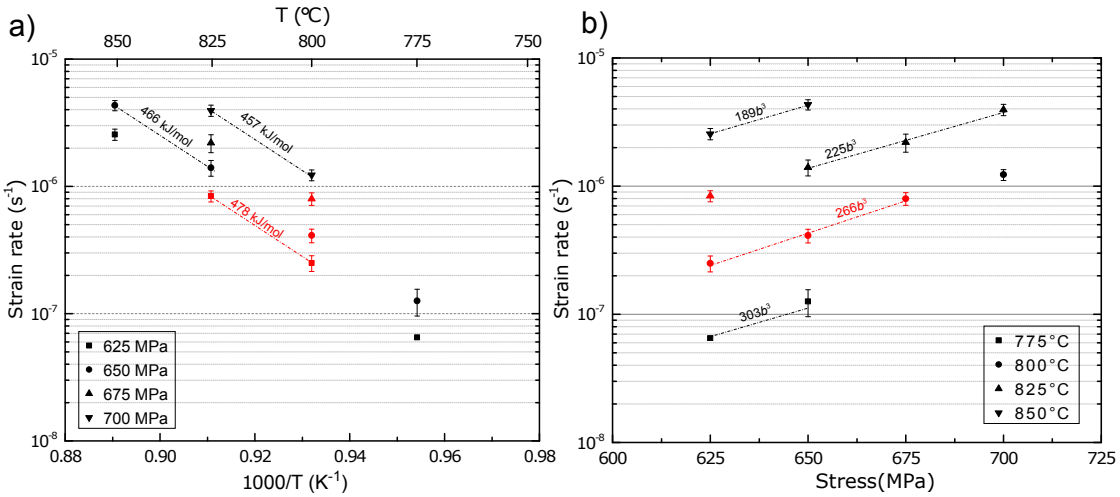

Figure 3.9 – a) Activation energy analysis for ⟨011⟩ MD2 single crystal. Red points represent microtwinning conditions. The activation energy values are indicated as the slope of the linear fit; b) activation volume analysis of the same material. The activation volume values are provided as the slope of the linear fit.

Fig. 3.10b and Fig. 3.11. In contrast, the twins appear in less quantity and are thinner as the temperature increases.

From these experimental results, the following explanations might be inferred: (i) there might be a critical stress for twin partial dislocation nucleation that represents the transition between dislocation climb or fully diffusional creep and the microtwin-stacking fault regime; (ii) as the stress increases, the nucleated partial dislocation population is expected to grows as a direct effect (625-675 MPa at 800°C); (iii) when the stress reaches a critical threshold, dislocation APB shearing might become favourable to the detriment of microtwin formation. This might explain why microtwins are not observed at higher stresses (700 MPa at 800°C) as presented in Fig. 3.10b and Fig. 3.11. Further TEM analysis on the dislocation structures is needed to validate these hypotheses. The evolution of these three stages is consistent with the schematic deformation map proposed in Fig. 1.3.

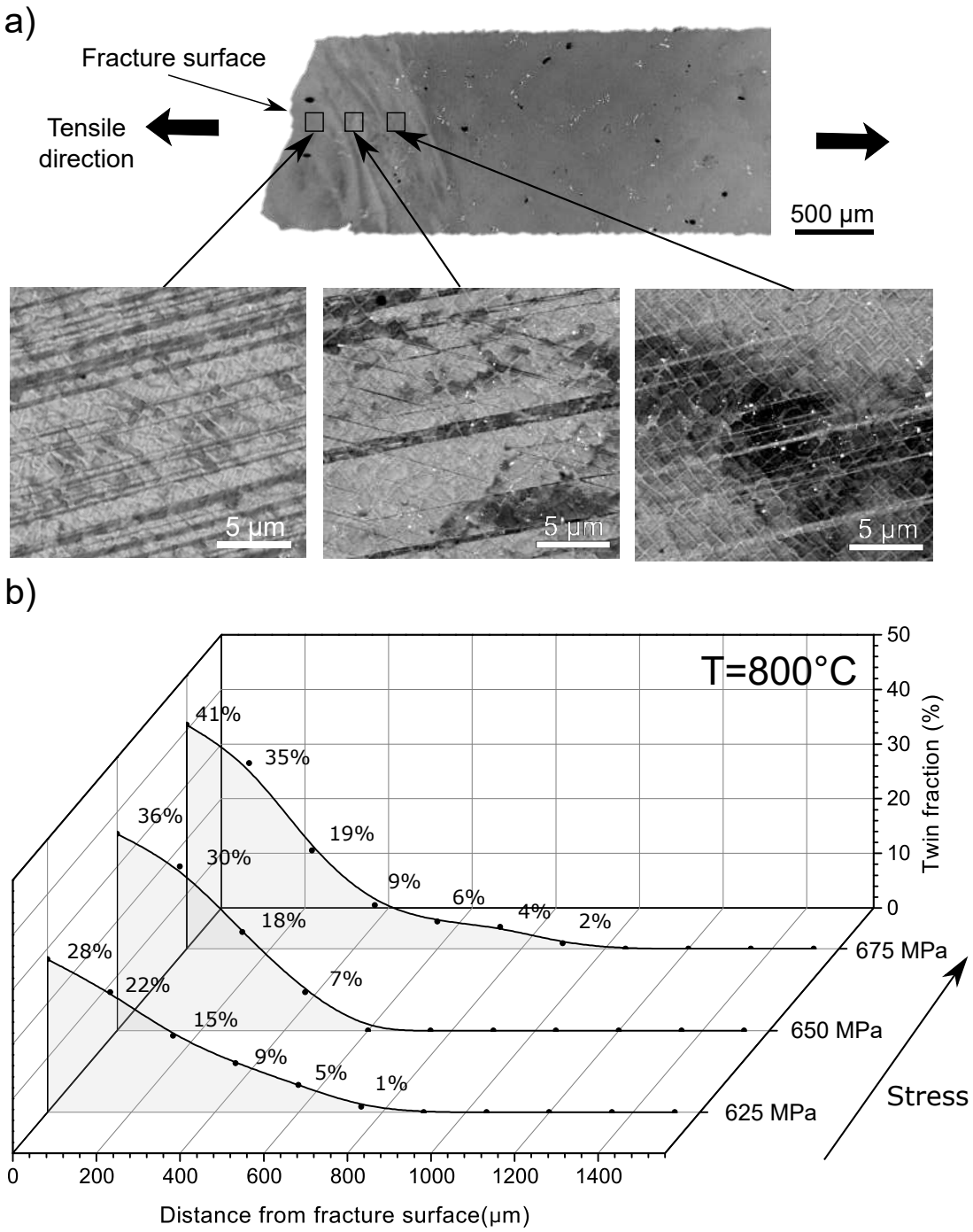

Figure 3.10 – a) ⟨011⟩ specimen tested at 800°C and 650 MPa with detailed micrographs of the twin structures at 150 μm, 300 μm and 450 μm from the cracked surface; b) twin fraction measurements as a function of distance from the fracture surface along the tensile axis of the specimen for ⟨011⟩ samples tested at 800°C.

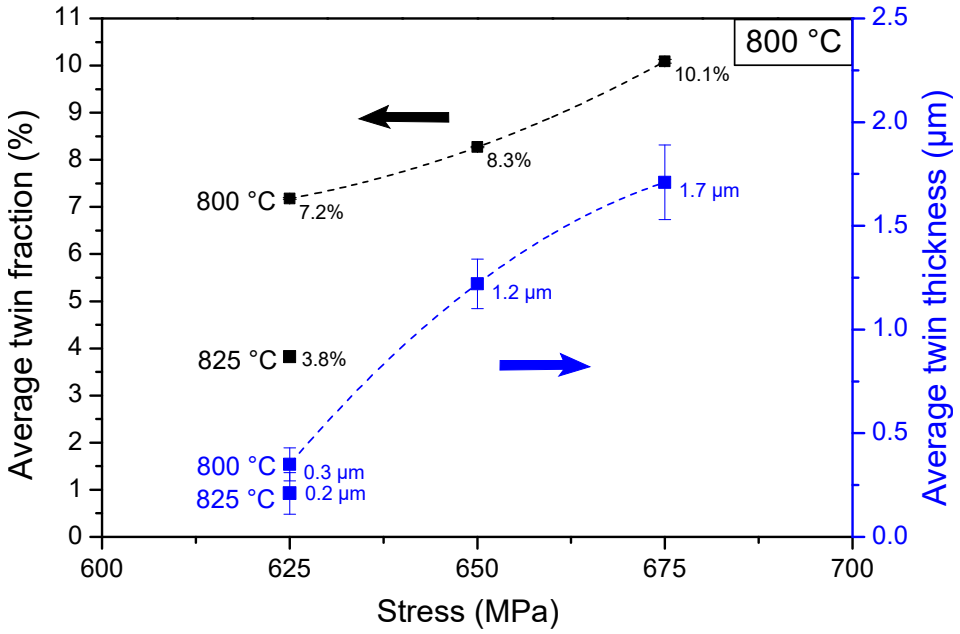

Figure 3.11 – Averaged twin thickness and twin fractions within the central 3 mm of MD2 samples after creep deformation at different temperature and stress levels calculated from results in Fig. 3.10.

3.4.3 Rationalisation of the contribution of the microtwinning mechanism on the overall creep strain

Microtwinning is responsible for the majority of the creep strain at 800°C. The microscopic shear strain produced by microtwinning can be defined as:

$$\gamma_{\text{twin}} = s f_{\text{twin}} \tag{3.1}$$

where f_{twin} is the averaged twin fraction within the gauge length and s is the shear produced by a completely twinned crystal [13]. The average twin fraction f_{twin} within the central 3 mm of each sample is presented in Fig. 3.11. The shear strain s is defined as $s = b/h$, where h is the spacing between the $\{111\}$ shear planes. For the case of the highest Schmid factor $\frac{a}{6}[\bar{2}11]$ twin partial (0.47), $s = \frac{\sqrt{2}}{2}$. The

macroscopic longitudinal twin creep strain $\varepsilon_{\text{twin}}$ can be recovered from [81]:

$$\varepsilon_{\text{twin}} = \sqrt{1 + \gamma_{\text{twin}}^2 \cos^2\phi + 2\gamma_{\text{twin}} \cos\phi \cos\lambda} \tag{3.2}$$

where ϕ and λ are the angles between the tensile axis and the normal to the twin plane and twin direction, respectively [81]. For the $\langle 011 \rangle$ case, $\phi = 35.3°$ and $\lambda = 54.7°$. This strain from microtwinning shearing is presented in Fig. 3.12.

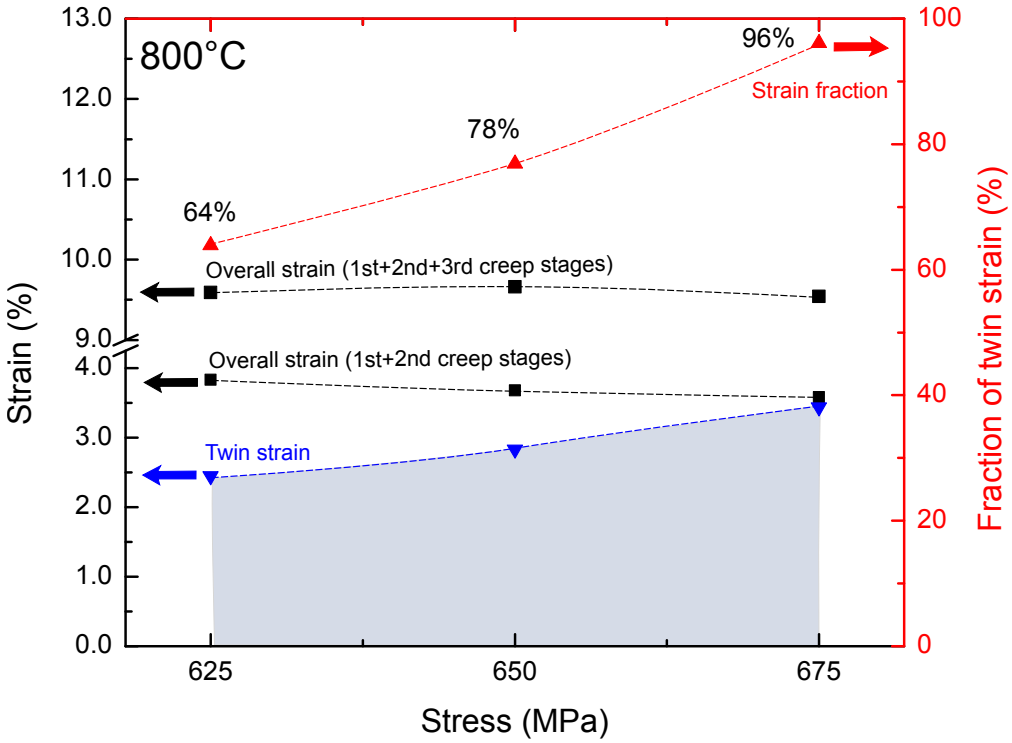

Figure 3.12 – Measured total creep strain and calculated twin strain, both before necking, after creep deformation of $\langle 011 \rangle$ crystals at 800°C. The indicated twin strain fraction is respect to the primary + secondary creep strain.

In order to compare the contribution of the microtwinning shear to the overall creep strain, the primary + secondary and the primary + secondary + tertiary creep strains are displayed in Fig. 3.12. The primary and tertiary creep stages are defined from Fig. 3.7 as the regions where the strain rate is more than double the strain rate in the stationary stage from the curves in Fig. 3.7. During tertiary creep, the

cross-section reduction caused by the necking phenomenon leads to a proportional increase of the stress in the tested sample (constant force test). Because of the high sensitivity of microtwinning to testing conditions as indicated in Fig. 3.8, it seems reasonable to assume that the creep regime where microtwinning is active is constrained to the primary and secondary creep stages of the tests. With this in mind, microtwinning shearing accounts for the majority (64% to 96%) of the total plastic strain, especially at higher stresses (675 MPa), both within the primary and the secondary creep stages. From these results, the confinement of the plastic strain to just one twin system is believed to be accommodated by slip and/or rotations outside the measured gauge length in order to assure compatibility of the sample deformation.

3.5 Influence of microtwinning on the fracture behaviour

One of the most critical requirements for superalloys in turbine engines is the avoidance of brittle behaviour. Several authors have reported fatigue embrittlement in superalloys when microtwins appear during thermo-mechanical fatigue tests [82, 83, 84, 85, 86]. The link between microtwins and crack propagation is still controversial. In our study, a systematic change of the failure event type between twinned conditions and non-twinned conditions is observed, which correlates to the morphology of the fractured surface. A comparative analysis of the tensile creep fracture surfaces is shown in Fig. 3.13a for the case of twinned and twin-free conditions along the $\langle 011 \rangle$ orientation. The fracture mode in the twinned specimens is clearly cleavage-like on the whole fracture surface with small ductile features in localised regions. This is usually associated with a brittle mode of fracture [87].

The fracture facets are oriented along the same {111} plane of the predominant microtwin system. In contrast, the fracture surfaces of the twin-free samples show multiple facets and dimpled regions, typical of ductile failure in single crystals [87]. The fracture surface morphology does not change substantially with testing temperature and stress among the twinned specimens as can be observed in Fig 3.13a. These results support the proposition that crack nucleation and growth in MD2 at 800°C is enhanced due to microtwin formation.

To explain the observed link between microtwins and the embrittlement of the material, the dislocation density distribution around creep twins is studied in detail, see Fig. 3.13b-d. The spatially resolved geometrically necessary dislocation (GND) density is calculated from high resolution (HR)-EBSD data and subsequent evaluation of Nye's dislocation tensor. The GND density distribution is shown in Fig. 3.13c. Higher dislocation density regions can be observed at the twin boundaries and within the twins. This phenomenon is suggested to be caused by dislocation pile-up events at the twin boundaries that can be explained by the abrupt change of Schmid factor at the twin matrix interface ($0.47 \rightarrow -0.57$) which locks the dislocation glide. These dislocations pile-ups can eventually cause stress concentrations which can lead to crack nucleation and propagation along the twin-parent interfaces, see Fig. 3.13d. This mechanism can cause brittle fracture when microtwins appear.

From this research, it follows that if the creep life of these materials is to be improved, consideration must be given to the factors influencing the appearance and thickening of microtwins. This chapter lays a foundation for further studies on the influence of the alloy composition on diffusion-assisted fault formation (i.e. SESFs, SISFs or microtwins).

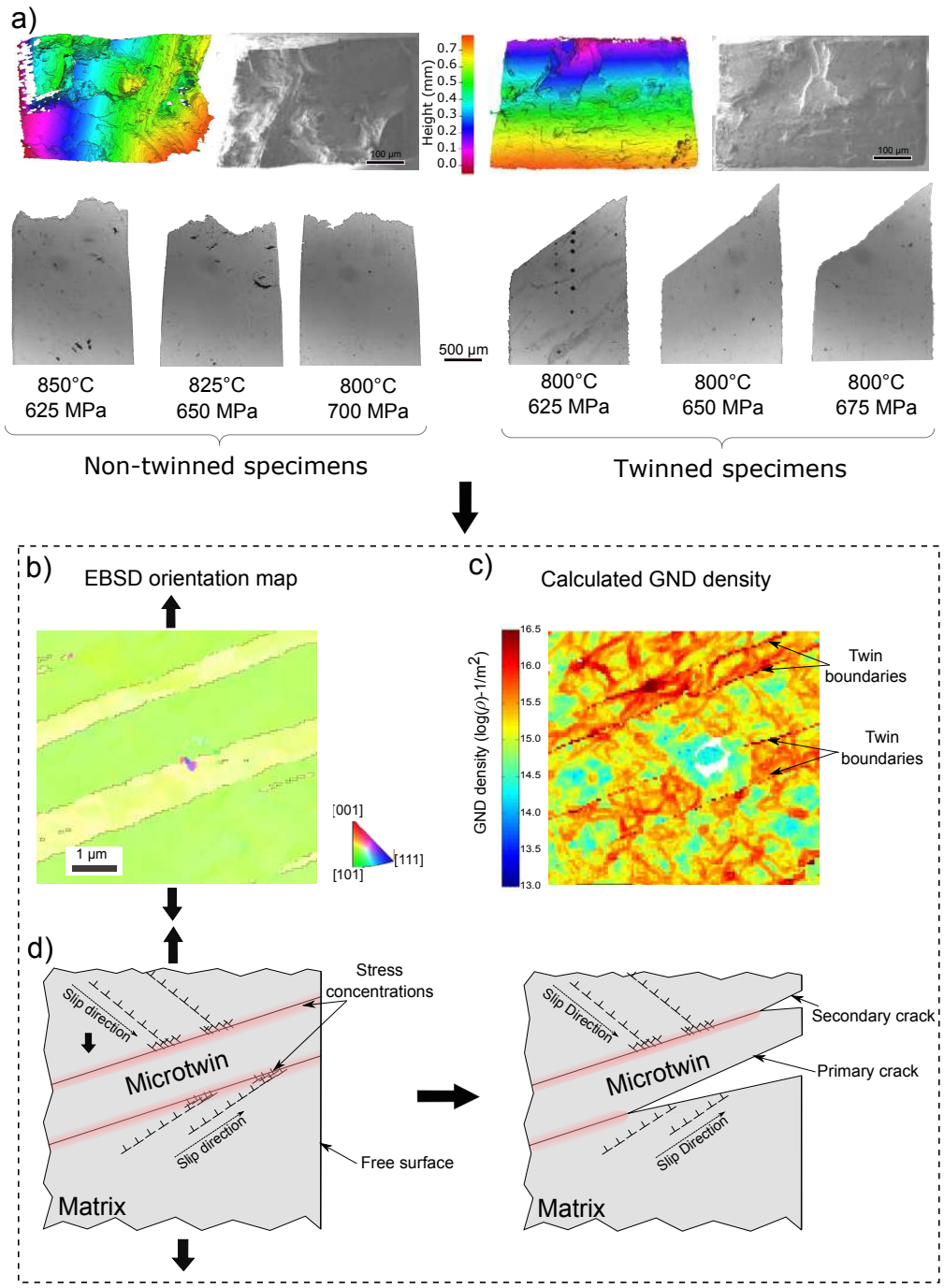

Figure 3.13 – a) Scanning electron micrographs and fracture surface topography analysis are illustrated for the specific cases of non-twinned ⟨011⟩ sample tested at 850°C-625 MPa (top-left) and twinned ⟨011⟩ sample at 825°C-625 MPa (top-right). Images of the fracture sections of twinned and non-twinned ⟨011⟩ samples for several conditions showing the change of fracture mechanism (bottom); b) EBSD map of the twinned region after creep testing along the ⟨011⟩ direction at 800°C and 650 MPa (yellow bands represent microtwins); c) HR-EBSD dislocation density map from the same area; d) micromechanical model of the crack initiation and propagation at the twin boundaries.

3.6 Conclusions

Microtwinning in the single crystal superalloy MD2 has been studied. The following specific conclusions can be drawn:

1. A series of creep tests at 800°C on the prototype single crystal superalloy MD2 was performed for different stresses and orientations to characterise the mechanical response in this microtwinning temperature regime. A strong anisotropy and tension-compression asymmetry along the ⟨001⟩ and ⟨011⟩ orientations have been found. The post-mortem experimental observations elucidate that microtwinning is active only for ⟨001⟩-compression and ⟨110⟩-tension proving the asymmetry of this mechanism.

2. Additionally, the effect of stress and temperature on the microtwinning activation was studied for the single crystal orientation ⟨011⟩ under tension. Microtwinning occurs for tensile stresses between 625-675 MPa and within the temperature interval of 800-825°C. The following observations are made:

   - For this orientation, twin fraction and twin thickness values have been measured by high resolution SEM analysis using electron channelling contrast. Higher stress causes a higher twinned fraction and thicker twins.

   - When microtwins are observed, their fraction and the assumed twinning shear can be used to estimate the twin strain produced, which was shown to account for a significant part of the macroscopic creep strain observed experimentally (64-96% of the primary + secondary creep strain).

3. The microtwinning mechanism alters the fracture mechanism and thus causes

a degree of embrittlement. This observation may be of some practical importance.

4 Micromechanisms of microtwinning in Ni-based superalloys

4.1 Introduction

Plasticity in Ni-based superalloys is most commonly associated with either athermal yielding at temperatures between ambient and ∼700°C, or alternatively time-dependent creep deformation at conditions beyond ∼850°C. The former is mediated by either weakly- or strongly-coupled pairs of dislocations whose motion is controlled by propagation through the γ'-particles [65, 66, 3], whereas the latter depends upon the circumvention of them by climb-assisted glide within the γ matrix [64]. At temperatures between these two limits a mode of deformation has been reported recently [26, 10, 30, 6] involving the propagation of so-called microtwins, by a mechanism which is not completely understood, somewhat controversial but also of significant practical importance.

Microtwins are caused by the propagation of $a/6\,\langle 112\rangle$ twinning partials on every consecutive $\{111\}$ plane [9]. Thus, it was first thought that the diffusion-assisted reordering needed in the vicinity of the leading partials for twin growth could rationalise the time-dependent character of the mechanism. These concepts have been discussed in the literature [33, 10, 6, 88], especially in the work of Kovarik

et al. [10] where the reordering process needed has been studied in detail using *ab initio* atomistic calculations. However, the latest results obtained using high angle annular dark field imaging [89, 32, 31, 90] have revealed a further intriguing aspect of this deformation mode, since the planar faults formed in this region have been found to support segregation of certain important alloying additions. Thus, local enrichment of Co and Cr – and depletion of Ni and Al – at planar faults in the CMSX-4 and ME3 alloys has been reported [90]. Furthermore, the segregation of Ta and W found at superlattice intrinsic stacking faults (SISFs) in a series of Co-based superalloys has been rationalised by means of the phase transformation $\gamma' \rightarrow Co_3Ti$ [31]. Similarly, segregation of Co, Ta, Nb and Ti at superlattice extrinsic stacking faults (SESFs) in ME3 – and again depletion of Ni and Al – have been reported [32]. There, the presence of a solute atmosphere – rich in Cr and Co and lean in Ni and Al – surrounding the leading Shockley partials was detected, suggesting that its diffusive movement in a viscous manner might be associated with the shearing process. A similar phenomenon was observed in a Ni-rich Co-based superalloy by Freund et al. [52]. Thus the idea that the microtwinning process exhibits characteristics of a coupled diffusional-displacive phase transformation has gathered pace in the last few years. But quantitative chemical analysis at atomic resolution is lacking. Hence, further improved high resolution chemical analysis is needed, to better understand the effects occurring and especially to support quantitative theory and modelling of this mechanism.

This chapter is concerned primarily with the chemical segregation at the planar defects introduced by creep deformation in a prototype Ni-based superalloy at 800 °C. In the alloy considered, the role of microtwinning in promoting creep deformation at such temperatures was proven in the previous chapter; nonetheless, the factors

promoting nucleation and propagation of such microtwins need much further clarification. In the present chapter, experimental proof of chemical segregation to microtwins formed in the superalloy is first presented. Second, these findings are extended to other types of faults in superalloys (SISF-SESF-APB). Finally, the different diffusion processes arising from the interpretation of the experimental observations are analysed. This leads to introduce the concept of segregation assisted plasticity.

4.2 Experimental methods

4.2.1 STEM-EDX analysis

Post-mortem SEM examination prior to scanning transmission electron microscopy (STEM) analysis was carried out in order to identify the deformation regions after tensile creep of ⟨011⟩ MD2 single crystal at 650 MPa and 800°C. The samples were prepared by grinding and polishing finished with colloidal silica. The examination plane was carefully selected for subsequent STEM foil extraction, with the extraction plane normal oriented along the ⟨011⟩ axis perpendicular to the tensile direction of the specimen. The preliminary study was performed using a JEOL 6500F field emission gun scanning electron microscope (FEG-SEM) using an accelerating voltage of 10 kV and probe current of 300 pA. Backscattered electron images were acquired in order to reveal the deformed regions within the sample. An overview of the microtwins that formed is shown in Fig. 4.1a.

STEM foils were extracted from these regions normal to an ⟨011⟩ orientation using an FEI Helios Nanolab Dualbeam 600 focussed ion beam (FIB). This assured planar faults are viewed edge-on using high angle annular dark field (HAADF) zone axis imaging as indicated in Fig. 4.1b. Samples were thinned at 5 kV and then further

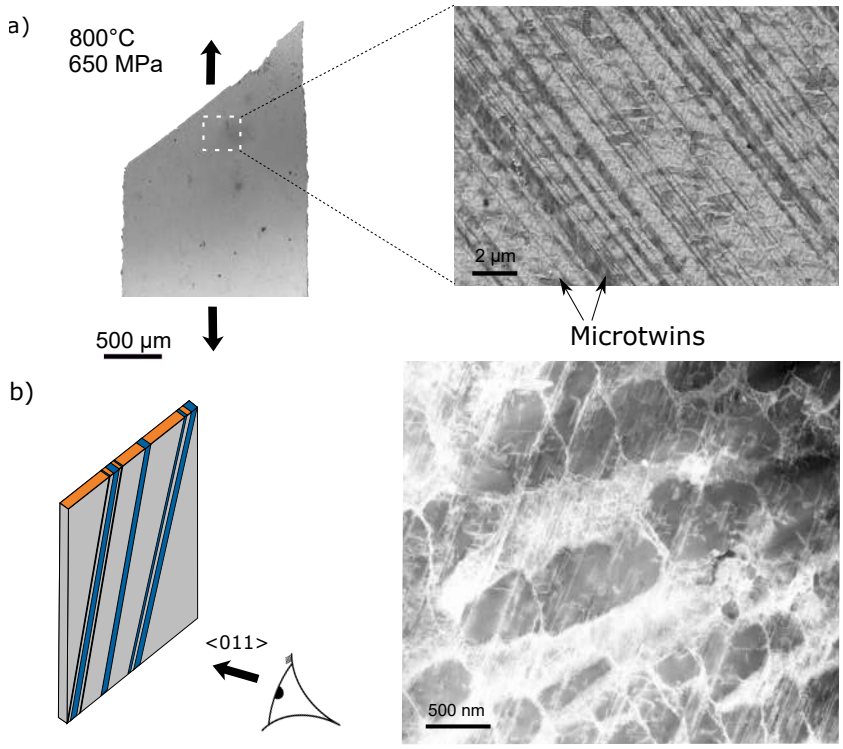

Figure 4.1 – a) Fracture surface of the ⟨011⟩ specimen tested at 800°C and 650 MPa in tension and SEM backscattered electron micrograph detailing the orientation of STEM foil extraction plane perpendicular to the twin bands; b) detailed diagram of STEM foil view angle relative to the crystal orientations and STEM micrograph of the deformed microstructure of the crept specimen.

cleaned using a Fischione Nanomill. Energy dispersive X-ray analysis (EDX) of the foils was performed on an image-corrected Titan3^{TM} 60-300 kV with a Super-X detector utilizing the Bruker Esprit software. Integrated line scans were conducted and quantified through Cliff–Lorimer analysis [91] using experimental K_α energies for Ni, Co, Al, Cr and Ti. L_α was used for the case of Mo. The Cu specimen holder signal was avoided by using the M_α lines for Ta and W since the L_α Ta and W peaks correspond too closely to a Cu peak to be accurately considered. Deconvolution for the W and Ta M_α peaks, as well as background subtraction, was used to reduce the influence of Bremsstrahlung X-rays produced from the inelastic interaction of the beam electrons with the atomic nuclei. For EDS line scan analysis, to reduce the noise and smooth the data, small amounts of averaging

were used. Using these setup, the noise can be reduced and no large effects on the variation of composition along the line scans were observed. Detrimental artifacts from foil thickness to the EDS spectrum like beam spreading or low EDS counts were mitigated by controlling the specimens thickness during the thinning process on the FIB. The FIB foil was thinned to around an estimated 20-50nm where both foil thickness effects were observed to be avoided. Higher atomic resolution STEM analysis was performed using a probe-corrected Titan3^{TM} at 60-300 kV.

4.2.2 APT-TKD analysis

In addition to the TEM study, APT analysis of the tested samples was also performed. Post-mortem examination was carried out after fracture using a Zeiss Merlin field emission gun scanning electron microscope (FEG-SEM) with a Gemini II column using an accelerating voltage of 10 kV and probe current of 300 pA. Backscattered electron images were acquired to identify suitable regions to extract the APT samples from.

Samples were prepared using a Zeiss NVision 40 focussed ion beam microscope (FIB) for correlative atom probe tomography (APT)/transmission Kikuchi diffraction (TKD) analysis. A protective W capping layer was Ga-beam deposited, then a 25×4 μm^2 cantilever was machined out and extracted using a Kleindiek micromanipulator from site specific twinned regions. The cantilever was cut and mounted onto a Cameca standard flat-top Si coupon using W welds and sharpened until the apex of the sample did not exceed 100 nm in diameter. The axis of the needle was perpendicular to the tensile direction of the sample. A 45° pre-angled sample holder was custom made for the present analysis, which enabled the APT coupon to be loaded into a Zeiss Merlin SEM equipped with a Bruker EBSD system for TKD

analysis. TKD was performed at 20 kV with a probe current of 300 pA, following a square grid with a minimum pixel size of 20 nm. Patterns were acquired from rectangular sections 2 μm in length, 80 nm in width following the length of the sample. APT was performed on the samples following TKD, using a Cameca Local Electrode Atom Probe (LEAP) 5000 XR. Samples were run using a UV laser, at evaporation rate of 0.7 % per second, laser energy 100 pJ, frequency 160 kHz, and temperature $-223\,^{\circ}$ C. Reconstructions were performed using IVAS 3.6.12 software.

4.3 Chemical composition of microtwins

The $\langle 011 \rangle$ MD2 specimen tested in tension at 800°C and 650 MPa in the previous chapter was used in this study. The fractured specimen after testing is shown in Fig. 4.1a. Microtwin bands following the fracture plane can be observed along an extensive region of the sample. The γ' precipitates are shown and they are of order 1 μm in size. The microtwins appear as diagonal bands of different contrast; they are arranged in bundles, with thickness varying between 50 nm - 2 μm. Shearing of the γ phase within the microtwin is also clearly visible as the γ' precipitates are rotated inside the twinned regions. A higher detail STEM analysis of the deformed region is presented in Fig. 4.1b. The image shows a high density of continuous faults preferentially along one slip direction. The existence of these faults is a consistent proof of the high activity of partial dislocations shearing at these testing conditions (800°C-650 MPa). This high density of faults contrasts with the relatively cleaner microstructures reported by Smith et al. [53], presumably explained by the higher level of strain imposed here to the samples studied. The complex dislocation structures extend also to the γ-channels where dislocation pile-ups can be observed. Further HR-STEM confirms the presence of CESFs/SESFs, CISFs/SISFs, APBs

and microtwins within the planar faults, with the latter being the most repeated and accounting for most of the plastic deformation. Further STEM and EDX analysis of the microtwins found is presented next.

4.3.1 STEM-EDX analysis

Two different microtwins within the γ' precipitates were analysed using combined STEM and EDX techniques. HAADF-STEM images in the $\langle 011 \rangle$ zone axis of both microtwins are presented in Fig. 4.2-left. The first microtwin is in an early stage of growth, with around 15 $\{111\}$ planes thickness, while the second one is in a mature state extending over the whole field of view. The concentration profiles across the microtwins interfaces are shown in Fig. 4.2-right from vertically integrated EDX line scans. They confirm the segregation of Cr – a well known γ-stabiliser – at the twin interfaces. For the case of the thin twin, the interfaces were also found to be slightly enriched with respect of Mo, although the background noise from the measurements makes this less clear. No conclusive fluctuations for Co were found. No relevant chemical changes associated with Ta, Nb and W elements along faults were observed in any of the two twins.

Nevertheless, the cores of both twins recover the nominal concentration of the γ' precipitate confining the segregation to just the twin interfaces. These observations confirm a local shift of chemistry from $\gamma' \rightarrow \gamma$ at the microtwin interfaces. This is needed to lower the energy of the high-energy faults formed at the twin boundaries, as a result of the partial shearing in the γ' whereas the core of the twin recovers the perfect lattice structure. Further rationalisation of the phenomenon is presented later. The segregation and diffusion processes detailed here are always referred to the shearing process within the γ' precipitates. No segregation was observed at the γ-channels.

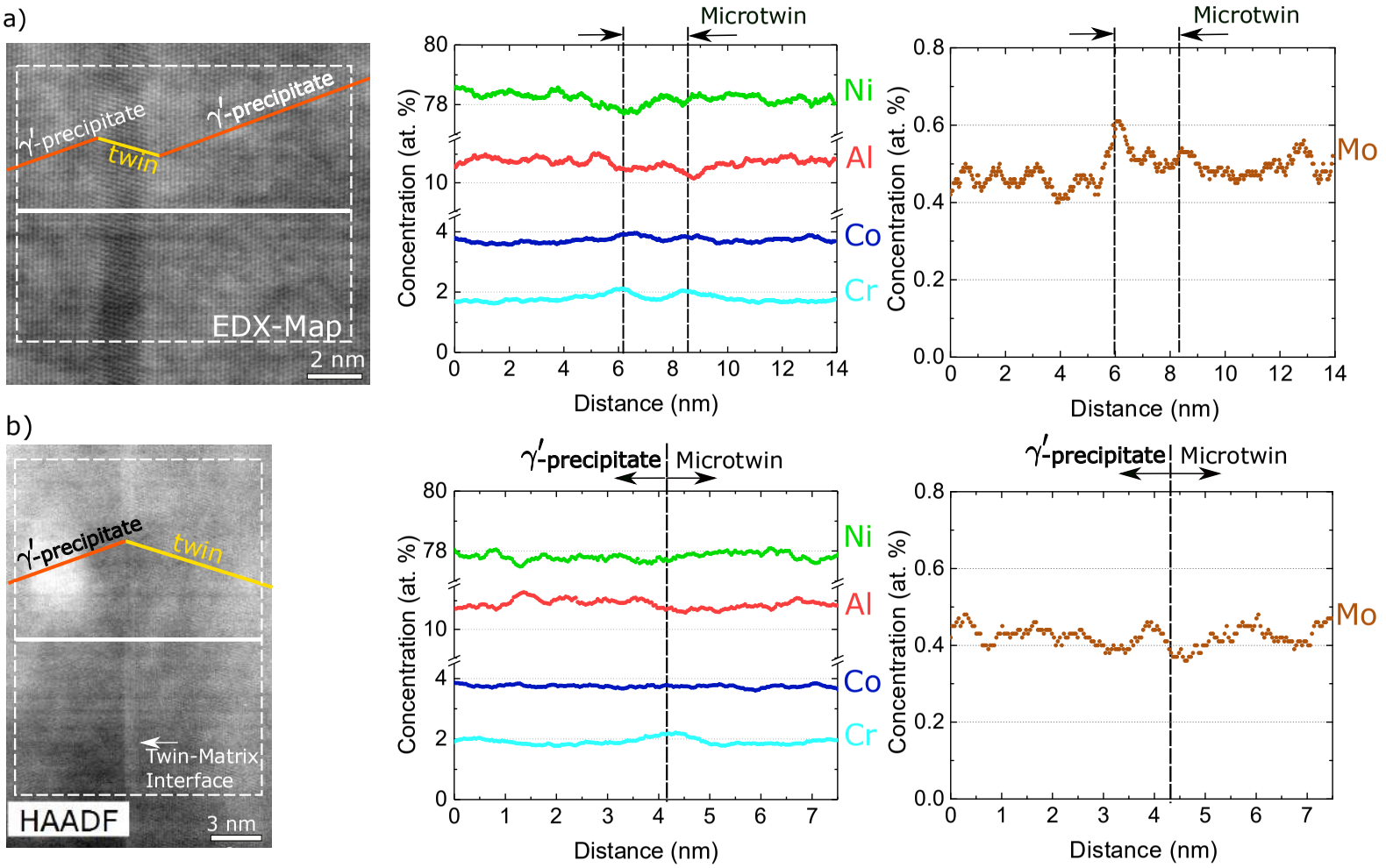

Figure 4.2 – a) Left: HAADF-STEM detail of a microtwin showing the change of lattice orientation between the parent and twinned phase. Right: horizontal integrated EDX line scan across the twin indicated in the HAADF-STEM image; b) left: HAADF-STEM micrograph of a γ'-twin interface showing a higher intensity line microtwin interface. Right: Horizontal integrated EDX line scan across the twin interface. Twin-parent interface is indicated by a dash-line.

4.3.2 Quantification of chemical changes along the microtwins using APT-TKD

The study on the microtwins was extended using combined APT-TKD techniques to quantify the chemical changes around the microtwins. The correlative analysis for a twin containing APT needle is illustrated in Fig. 4.3. The TKD analysis presented here proves conclusively the presence of two microtwins in the atom probe needle prior to APT analysis. Fig. 4.3a illustrates the needle SEM micrograph and its associated TKD inverse pole figure map. Two microtwins are shown in the inverse pole figure map, and the misorientation profile along them is plotted in Fig. 4.3b. Both microtwins exhibit a sharp 60° step, associated with boundaries which are indeed the microtwin-parent interfaces. Only misorientations less than 4° were recorded within the twin and the matrix domains themselves. Fig. 4.3c shows the corresponding APT maps from the needle shown in Fig. 4.3a. Two γ-γ' phase boundaries are shown, and four interfaces were detected within one of the γ' precipitates. The crystallographic information provided by APT is in

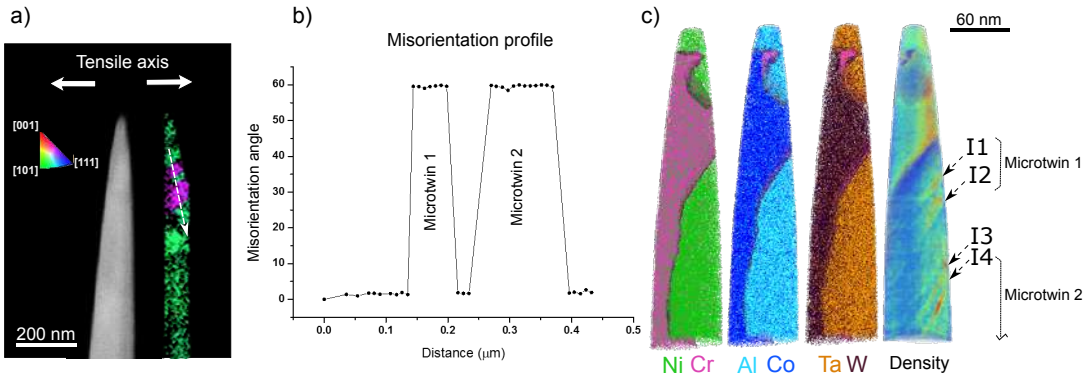

Figure 4.3 – a) SEM secondary electron micrograph showing the atom probe needle and TKD inverse pole figure map plotted along the z-axis; b) two regions displaying 60° misorientation angle corresponding to microtwins are shown to be present in the needle; c) atom maps created through the reconstruction of the APT data set, with γ-γ' phase transitions shown as Ni-Cr, Al-Co and Ta-W partitioning.

general rather limited; usually crystallographic features such as twins and stacking faults are not directly observable. However, their presence in an analysis can be indirectly detected by the observation of local segregation of solute atoms to these features. Furthermore, it is also well documented that such features can also be imaged indirectly in the form of regions of aberrantly high atom density in the 3D reconstruction [92, 93]. These regions arise due to subtle aberrations in the trajectories of the field evaporated ions in the APT experiment itself, instigated by these microstructural features. In Fig. 4.3c, analysis of the atomic density fluctuations through the APT clearly highlights the faults-parent interfaces. Furthermore, a vertical $\langle 011 \rangle$ pole is present along the axis of the needle, coherently with the TKD analysis, and corresponding atomic planes can be resolved within the 2D slice through the APT reconstruction presented in Fig. 4.4a. These planes appear non-continuous within the I1-I2 interfaces, which is further proof of a localised change in crystallographic orientation. Through the aforementioned correlation analysis, the following faulted structure can be inferred in Fig. 4.3c starting from the apex of the needle: first a microtwin is present between I1-I2, then the parent material extends until I3, where a stacking fault might be present and then a second microtwin starts at I4. The segregation at the fault interfaces within the γ' precipitate is shown in Fig. 4.4b as 1D chemical concentration profiles crossing each of the twin boundaries. The Cr content is shown to increase by 2 at.% and Co by 1 at.% at the microtwin-parent interfaces. In contrast, no chemical segregation was observed at the faults within the γ matrix. The peak values for MD2 alloy are consistent with the findings of Smith et al. [32] for ME3 and Viswanthan et al. [90] for CMSX-4.

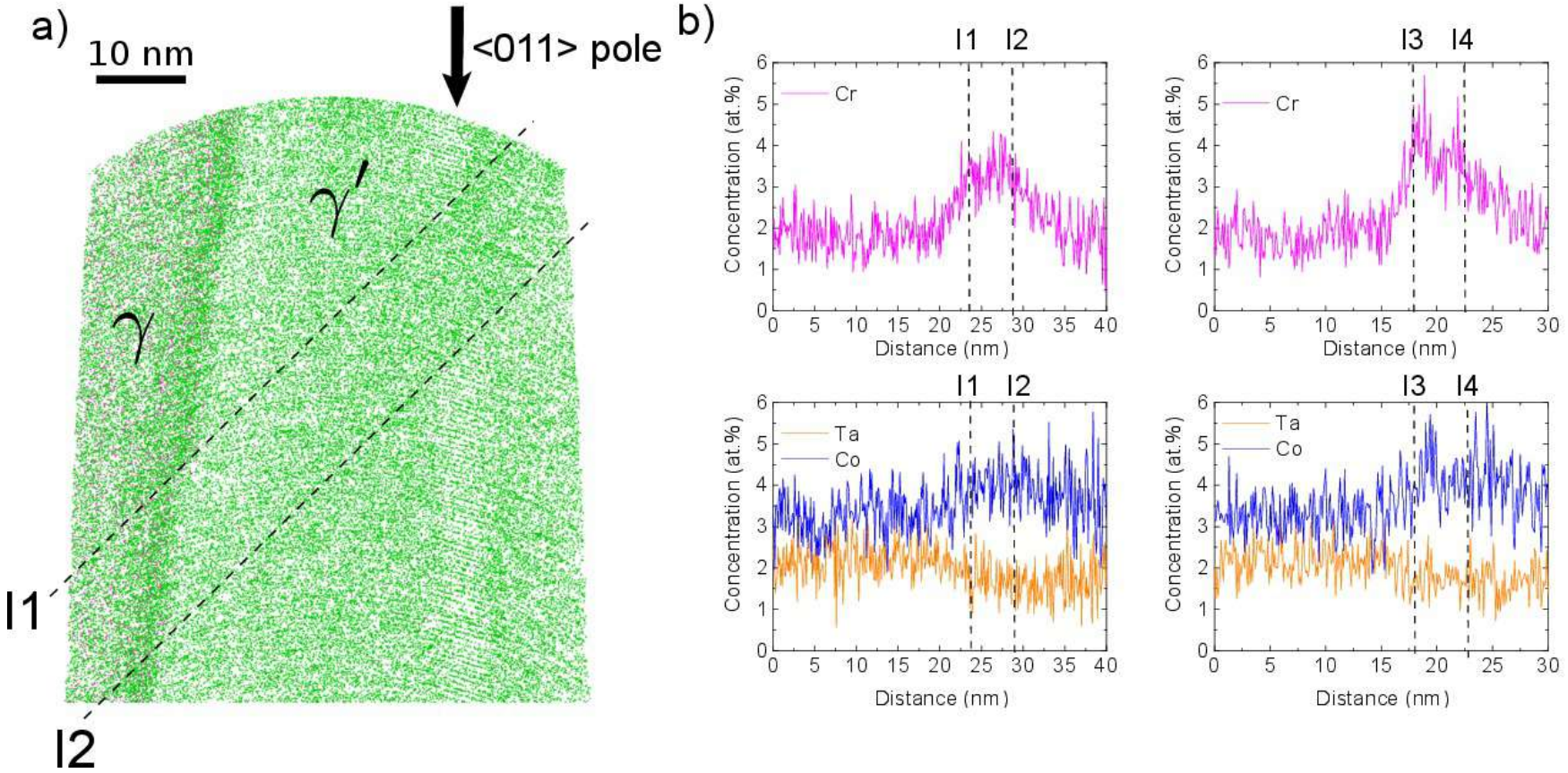

Figure 4.4 – a)Sub-section of the atom probe reconstruction shown in Fig. 4.3. Atomic planes are visible along the indicated ⟨011⟩ pole within the γ' phase and interrupted inside the microtwin; b) segregation of Cr and Co at the microtwin matrix boundaries in the γ' precipitate. No chemical segregation was observed at the faults within the γ matrix.

A second APT needle from the same testing conditions (⟨011⟩ crystal at 800°C-650 MPa) containing fault interfaces is presented in Fig. 4.5. The locations of the interfaces within the needles were identified through apparent localised density variations visible in the form of three parallel planar features as shown in Fig. 4.5a-left. The three-dimensional atom maps of one of these needles are shown in Fig. 4.5a-right. The one-dimensional concentration profiles along a cylindrical region containing the three fault interfaces in the needle are detailed in Fig. 4.5b confirming the previous values for the local enrichment of Cr and Co at the boundaries.

4.4 Extension of compositional changes to other types of faults

The chemical observations presented before for the microtwins are extended here to other type of faults in Ni-based superalloys. Combined STEM-EDX analysis on CISFs/SISFs, CESFs/SESFs and APBs is presented next.

4.4.1 Intrinsic and extrinsic stacking faults

A HAADF-STEM image of a region containing five different planar faults within a γ' precipitate is shown in Fig. 4.6. These correspond to two CESFs/SESFs on a first {111} slip plane and two CESFs/SESFs and a CISF/SISF on a complementary {111} slip system. The faults can be either complex faults (CESF and CISF) or regular faults (SESF and SISF) as the present analysis cannot distinguish between them. The planar faults cut each other presenting interesting interactions and blocking the growth of some of them. Some of the interaction spots and fault ending points present a higher intensity in the HAADF-STEM image which might be related with a higher concentration of heavier elements. This observation is

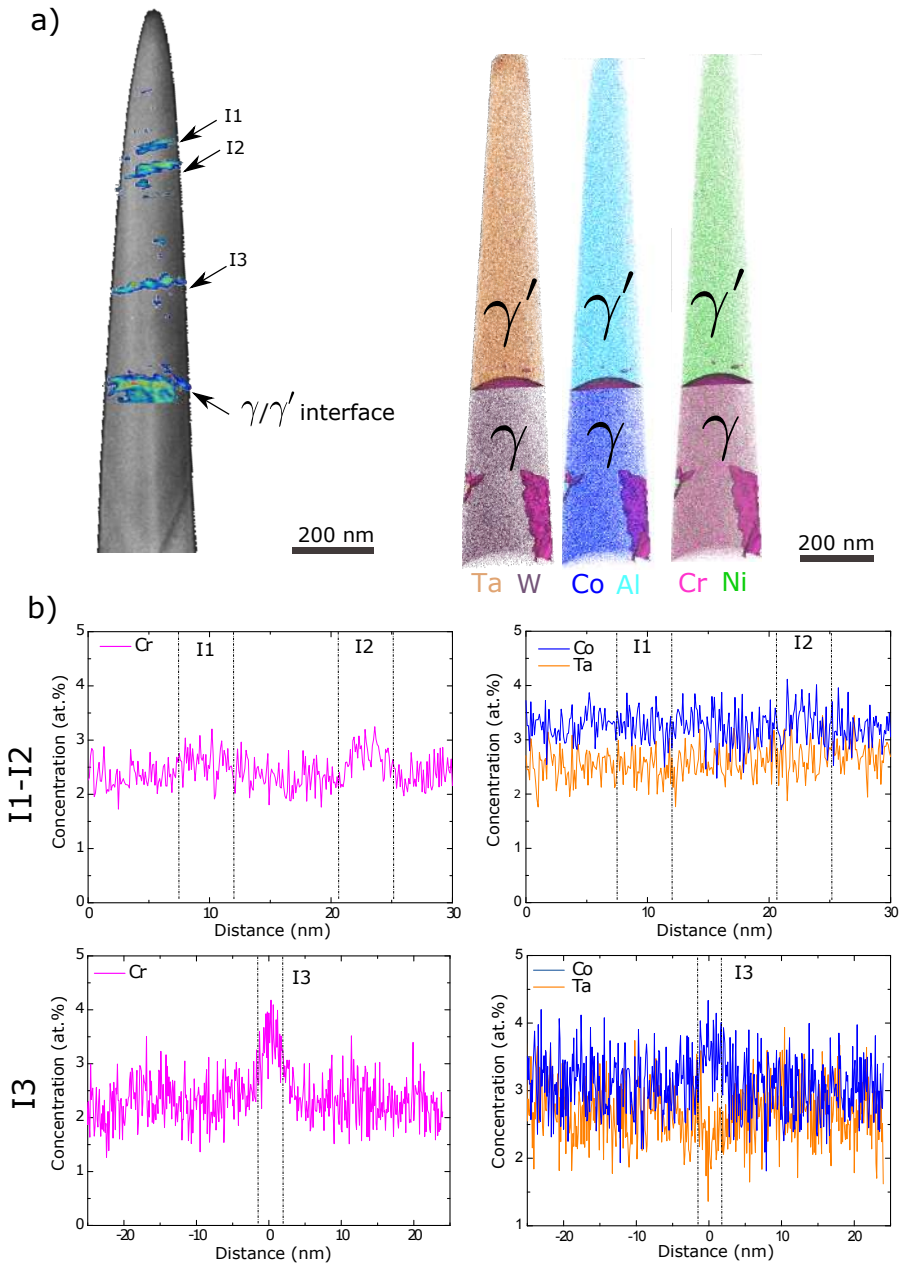

Figure 4.5 – a) Higher atomic density planar features from a tested specimen at 800°C and 650 MPa identifying the position of three fault interfaces within the γ' phase and atom maps with γ-γ' phase transitions; b) 1D concentration profile across the faults interfaces showing segregation of Cr and Co at the interfaces in the γ' phase.

consistent with the previous STEM work in ME3 alloy by Smith et al. [32]. The rationalisation of these higher density regions associated with the fault growth is discussed in the following section.

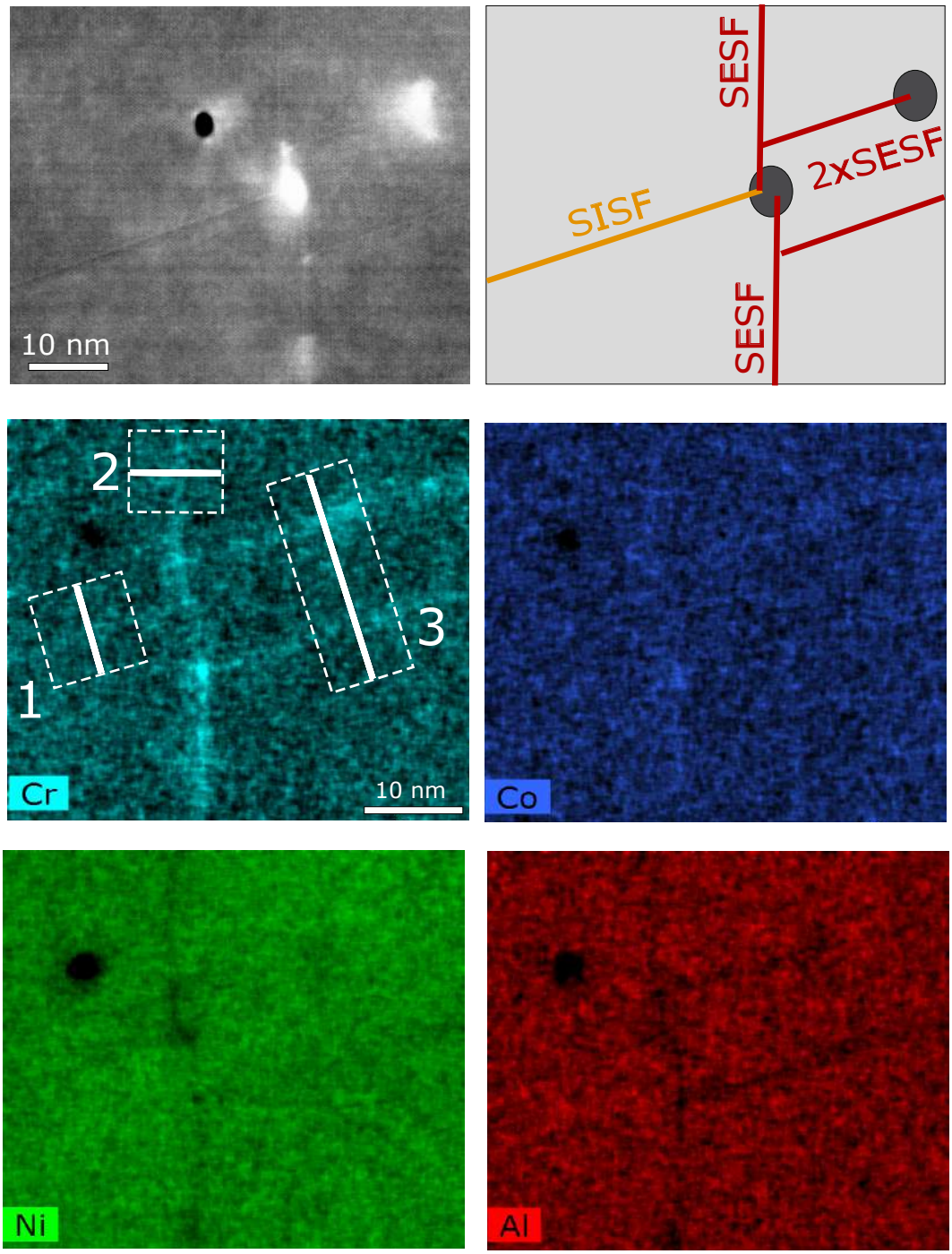

Figure 4.6 – STEM micrograph of a faults structure (CISF/SISF+ CESF/SESF+2xCESF/SESF) and its corresponding elemental EDX maps.

The EDX maps of the faults region are presented in Fig. 4.6. These maps highlight the segregation of Cr and Co along the planar faults. Enhanced Cr fluctuations at the faults are observed to a higher degree than Co in these maps. Conversely, Al

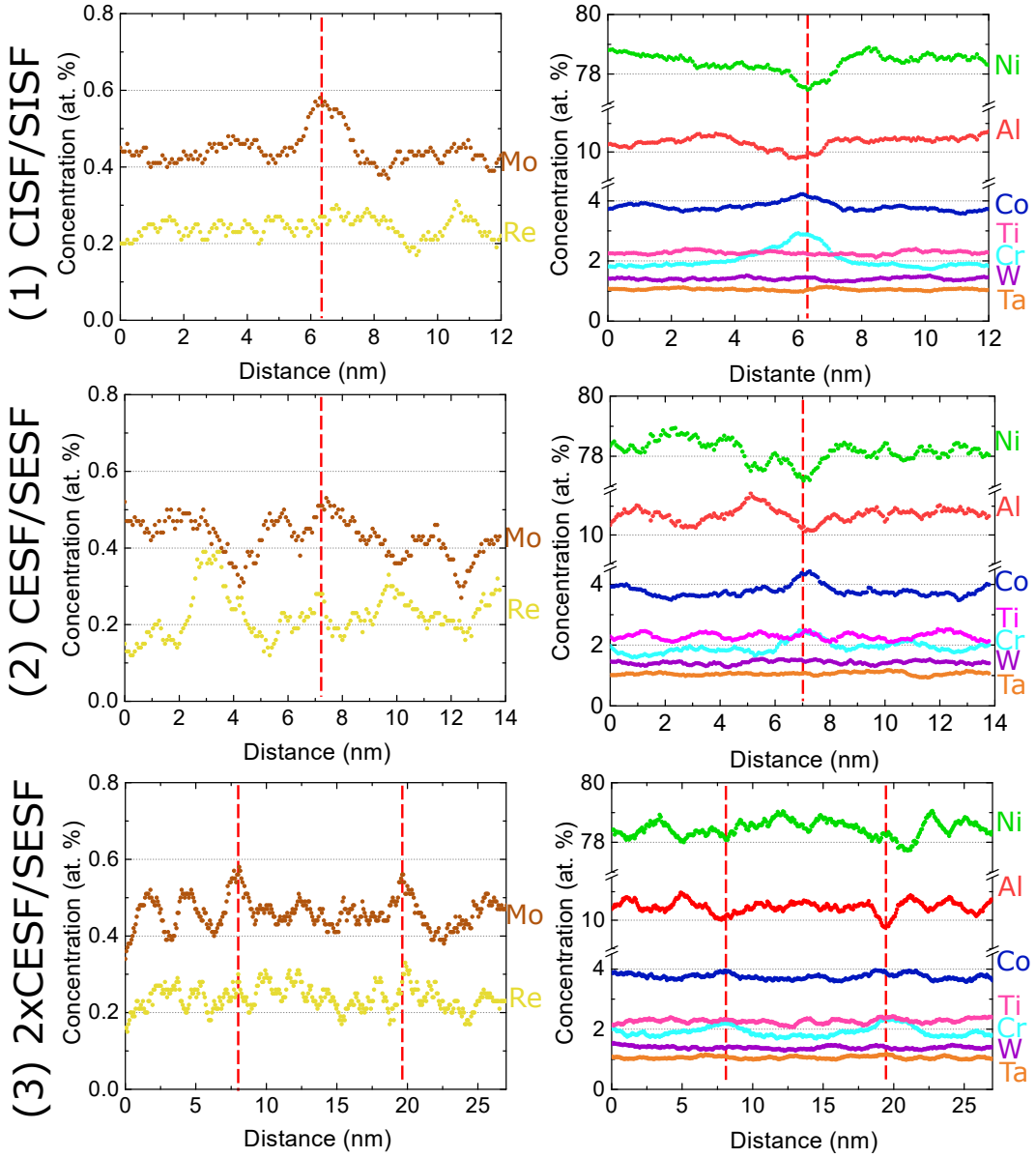

Figure 4.7 – Integrated EDX line scans showing the concentration profiles across the different stacking faults detailed in Fig. 4.6. The positions of the faults are indicated by red lines.

and Ni maps show a slight depletion of these elements along the stacking faults. The compositional changes for each fault were quantified and they are shown as compositional profiles in Fig. 4.7. They are integrated parallel to the plane of each fault as indicated in Fig. 4.6. For the case of the CISF/SISF, the results confirm the segregation of Cr and Mo. Co segregation is much less pronounced. Slight depletion

of Ni and Al from the fault lines is observed. These data confirm the qualitative results of the elemental maps presented before. For the case of the CESFs/SESFs, Co is segregated to a slightly higher intensity for fault (2)-CESF/SESF than in the CISF/SISF. For fault (3)-CESF/SESF the Co segregation is almost negligible. For both CESF/SESF fault, Cr segregation levels are similar to the CISF/SISF case. Non-conclusive data were found for Mo segregation in the case of the CESFs/SESFs. No relevant chemical changes associated with Ta, Nb and W elements along faults were observed.

4.4.2 Anti phase boundary

Finally, an array of planar faults containing an APB within a γ' precipitate was studied. A HAADF-STEM image of the dislocation/fault array is shown in Fig. 4.8a. Several dislocations can be observed coinciding, after atomic resolution fault analysis, with the higher intensity locations observed in the image. These locations have been reported before to be associated with clouds of higher atomic number elements [94].

Analysis of this array of dislocations and SFs indicates that there was an interaction of the primary (horizontal) {111} slip system with the conjugate {111} slip system. It is found that a series of $a/2\langle 110\rangle$ dislocations from the conjugate system was incorporated in the dislocation array of the primary slip plane. This is apparent since Burgers circuits around the individual dislocations configurations produce closure failures containing a component pointing out of the primary glide plane, see Fig. 4.8b. In fact, this is consistent with the presence of $a/2\langle 110\rangle$ dislocations within the array.

The details of these interactions, and the steps leading to this configuration,

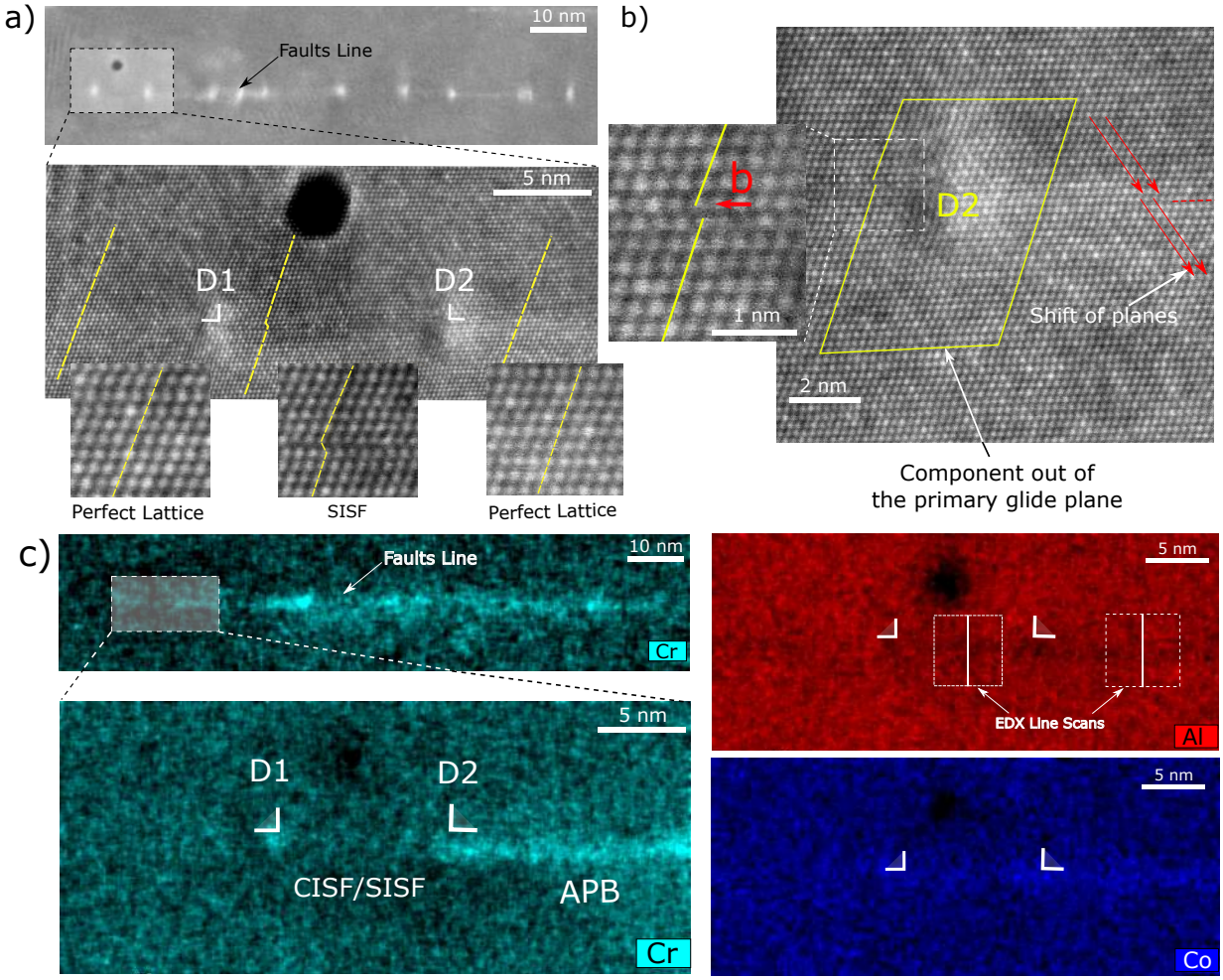

Figure 4.8 – a) HAADF-STEM micrograph of a faults line containing multiple dislocations indicated by brighter spots (top). An atomic resolution STEM micrograph of the first two dislocations area is presented (bottom) with details of the atomic faulted structure. b) Burgers circuit around the dislocation D2 showing the glide component out of the principal slip plane; c) Cr, Co and Al EDX elemental map showing strong segregation along the fault line behind the second partial dislocation. This segregation suggests that the fault structure after the SISF/CISF corresponds to an energy-lowered APB

are difficult to deduce from this post-deformation analysis; however, the most remarkable feature is between dislocations D1 and D2 in Fig. 4.8a. A higher-magnification atomic resolution STEM micrograph of the region around D2 is shown in Fig. 4.8b. To the left of this dislocation there is a stacking fault that could be either an SISF or CISF. To the right of dislocation D2 there is a region that

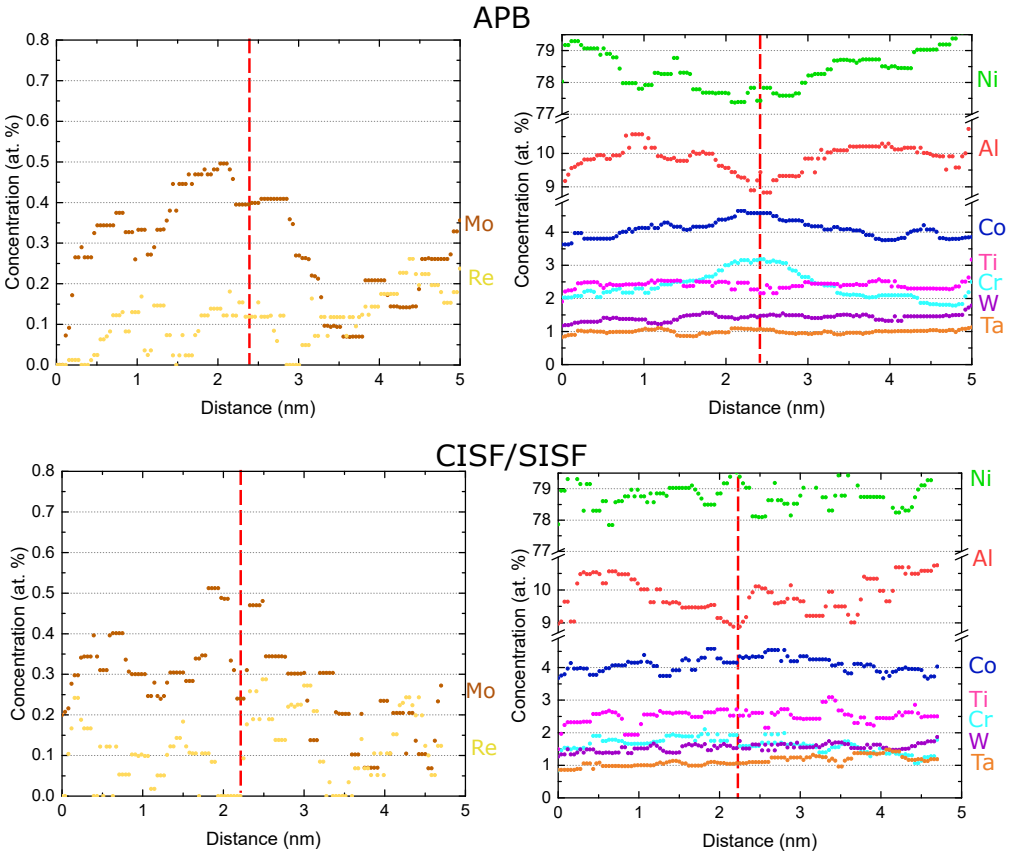

Figure 4.9 – Integrated EDX line scans of the APB and the SISF or CISF in Fig. 4.8.

apparently has perfect crystal stacking (i.e. no structural fault is present). However, closer inspection demonstrates that the higher intensity planes (corresponding to the higher atomic number, Ni-rich sublattice in the γ' structure) are actually offset by a $a/2\langle 110\rangle$ displacement in the vicinity of the $\{111\}$ plane that would project the stacking fault located to the left of D2. Note that the contrast from this superlattice fringe intensity is not uniform, and is only clearly observed in certain regions of the image. This lack of uniformity in contrast may be due to several factors, including the presence of surface contamination in these electropolished TEM foils, as well as local compositional fluctuations that may lead to a decrease in superlattice contrast. It is noted that a similar "patchiness" to the superlattice contrast is found in all regions investigated, as indicated for example in Fig. 4.2a.

The salient point is that this region to the right of D2 appears to have the structural attributes of an APB. Compositionally, it is also distinct from the perfect γ' regions as shown in the analysis of this region shown in the EDX maps of Fig. 4.8c. The elemental maps of the faults for Cr, Co and Al are presented here. The maps show that segregation of Cr is strongly localised to the APB and almost undetectable for the case of the CISF or SISF; the same phenomenon is observed for Co. Additionally, severe depletion of Al is observed for both, the APB and the CISF or SISF. Integrated concentration profiles of the detailed region were also computed for quantitative analysis and are presented in Fig. 4.9. The quantitative results confirm the strong segregation of Co and Cr to the APB. No segregation of Ta, Nb and W elements were observed in any of the faults.

4.5 Segregation-assisted plasticity in superalloys

In this section, focus is put on the diffusion mechanisms controlling the lengthening of the faults. Fig. 4.10a shows the growing tip STEM image of a CESF/SESF fault. The position of the dislocations at the ending tip is indicated approximately within 13 atomic planes in Fig 4.10b (dislocation space). The poor contrast around the twin tip nucleus makes it impossible to locate the partial dislocations precisely. However, the extrinsic nature of the fault is confirmed by the fact that the fault extends along two layers (ABC<u>B</u>ABC). A comparative analysis of the Cr concentration levels around fault tip is presented in the EDX elemental map of the same region presented in Fig. 4.10c. The dislocation space lines are also placed for comparative analysis. The region around dislocation core is surrounded by an enriched atmosphere of Cr. The wake of the solute atmosphere leaves behind a segregated trail of Cr solute. This is also extended to a lower extent to the Co EDX map in Fig. 4.11a.

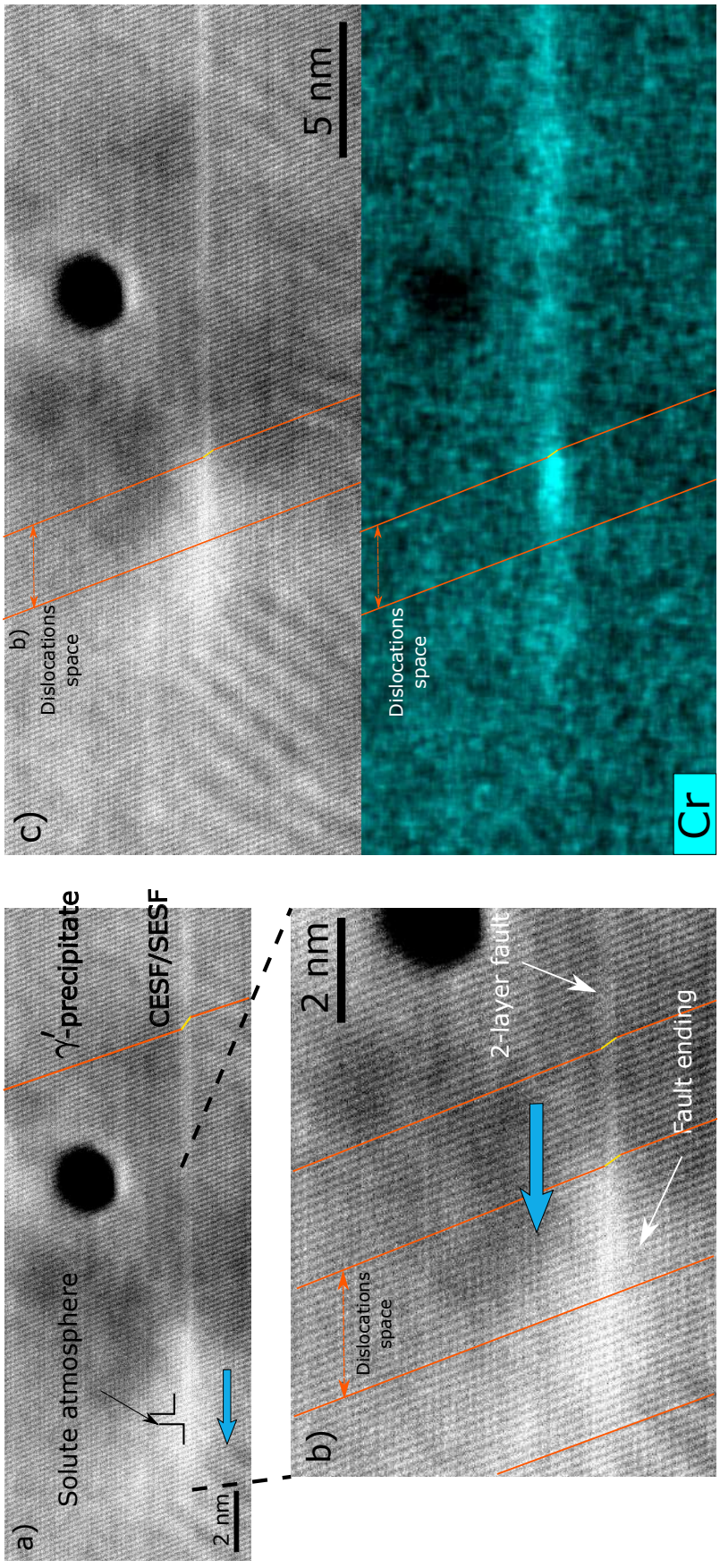

Figure 4.10 – a) Terminating CESF/SESF with higher intensity at the growing front (left) indicating the position of a solute atmosphere as indicated from the spatial comparison with the EDX Cr elemental map (right)

In contrast, both regions, fault tip and fault core show a pronounced depletion of Al. The chemical compositions of the solute atmosphere and the γ' precipitate are presented in Fig. 4.11b obtained by integration of the maps values indicated in Fig. 4.11a. The chemical shift is further confirmed by the EDX line scan along the extrinsic fault presented in Fig. 4.11c. These results show that the local elemental composition shifts from $\gamma' \rightarrow \gamma$ equilibrium chemistry.

This shift is further confirmed by the extended study presented in Fig. 4.12 for all the type of faults presented here. In this figure, the ratios of γ'- and γ-stabilisers with respect to the γ' phase values for the different faults are shown. These ratios were calculated as:

$$\gamma'\text{-stabilishers fraction} = \frac{(c_{\mathrm{Al}} + c_{\mathrm{Ta}} + c_{\mathrm{Ti}} + c_{\mathrm{Nb}})_{\mathrm{fault}}}{(c_{\mathrm{Al}} + c_{\mathrm{Ta}} + c_{\mathrm{Ti}} + c_{\mathrm{Nb}})_{\gamma'-\mathrm{phase}}} \tag{4.1}$$

$$\gamma\text{-stabilishers fraction} = \frac{(c_{\mathrm{Co}} + c_{\mathrm{Cr}} + c_{\mathrm{Mo}})_{\mathrm{fault}}}{(c_{\mathrm{Co}} + c_{\mathrm{Cr}} + c_{\mathrm{Mo}})_{\gamma'-\mathrm{phase}}} \tag{4.2}$$

The compositional values at the faults have been calculated from the integrated average between the mid-points of the concentration peaks. These results were averaged, if possible, from all analysed cases for each kind of fault. For all the faults, a loss of γ'-stabilisers and conversely, an increase of γ-stabilisers is observed. Similar results have been reported by Smith et al. [4] for the case of SESFs on the disk-type alloy ME3. The same phenomenon is generalised in this work for CISFs/SISFs and APBs.

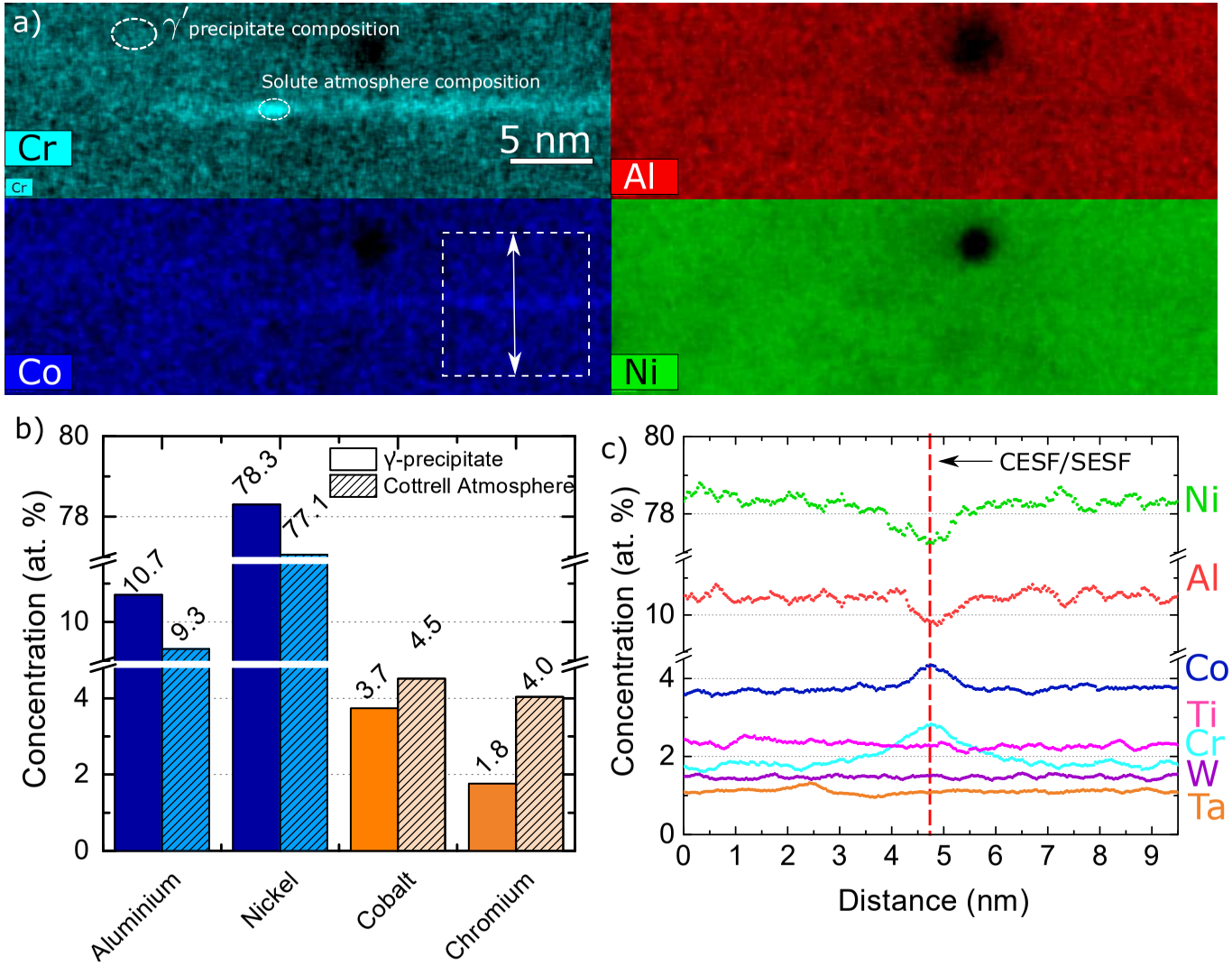

Figure 4.11 – a) EDX elemental maps showing segregation of Cr and Co along the fault, with a higher concentration solute atmosphere at the growing front; b) atomic composition of the Cottrell atmosphere at the growing front of the fault and comparison with γ' chemical composition. The composition at the fault tip is shifted locally to a γ-like structure; c) integrated EDX line scan along the SESF/CESF indicated in (a).

The results presented in Fig. 4.10 and in Fig. 4.11 indicate the presence of at least two diffusion processes taking place simultaneously during dislocation shearing:

- Segregation along the fault: the Cr and Co enrichment of the different faults with respect to the surrounding γ' precipitate composition requires of long-range diffusion from the bulk. For the case of the complex faults (CESFs-CISFs) and APBs, the diffusion flux is believed to be driven by the transformation of the high energy faults created by the dislocation shearing to low energy ones. This is achieved by stabilising locally a γ-like structure at the fault and thus, reducing the wrong-neighbours penalty. This process is illustrated schematically in Fig. 4.13 for the different faults observed. For the case of the lower energy faults (SISF-SESF), the segregation of solute species is believed to decrease the energy of these faults according to the published work in the literature [95, 31]. Obviating quantitative deviations of the different concentration levels, the segregation patterns reported show no qualitative distinction between faults. This implies that the same segregation mechanisms are likely to be present regardless of the kind of fault. The specific distinctions in terms of the concentration peaks might be related to the different bonding structures and in particular, their associated fault energies, as illustrated in Fig. 4.13.

- Solute atmosphere around the twin partials: the partials nuclei are surrounded by a solute cloud of Co and Cr of a few nm in size. The solute cloud presumably moves coupled with the partial dislocations as they shear the γ' precipitates. The enhanced enrichment of the dislocation core with respect to the fault might be driven by the reduction of the local strain energy associated with the dislocation. Additionally, this cloud can support, provisionally, the

stabilisation of the fault structure during the initial moments after the dislocation shearing and before the long-range diffusion segregation to the fault occurs.

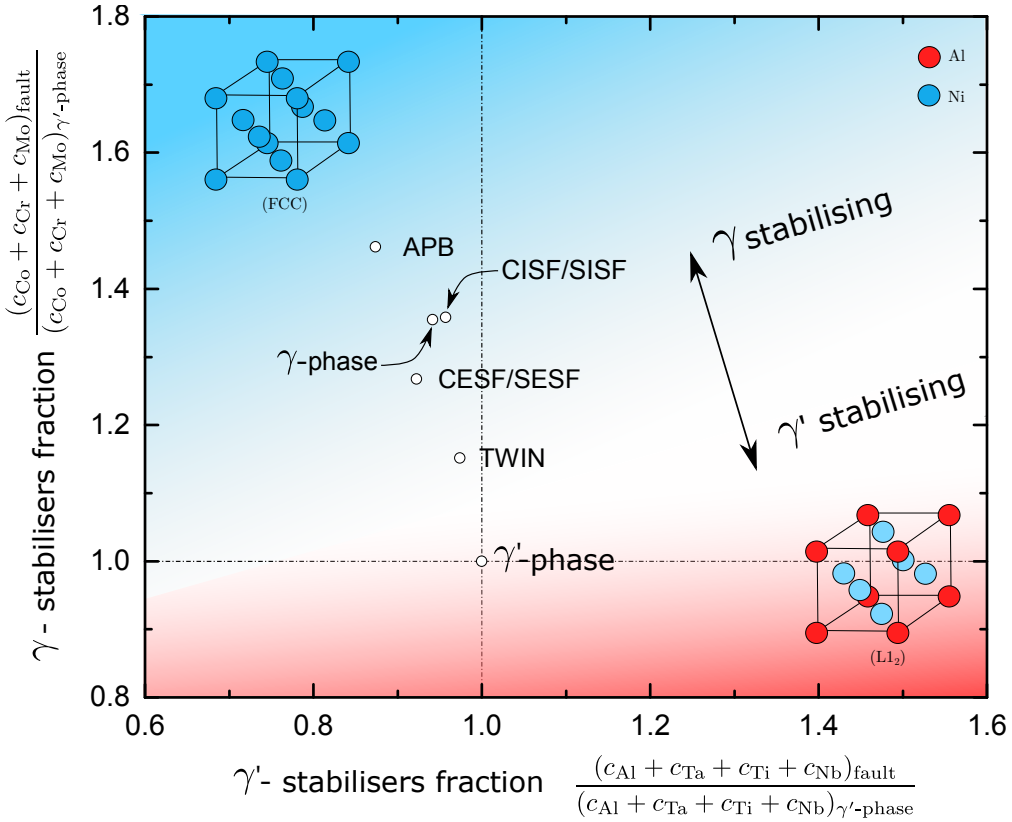

Figure 4.12 – Ratios of γ'- and γ-stabilisers for the different faults reported in this chapter. The ratios were calculated with respect to the γ' phase values. For all the faults, a loss of γ'-stabilisers and conversely, an increase of γ-stabilisers is observed. This fact is specially intense for the case of the APB.

Additionally, a third diffusion mechanism might be operative simultaneously for the case of SESFs and microtwins. This mechanism implies the short-range atomic reshuffling of the Ni and Al lattice sites at the fault line leading to the perfect SESF-twin structure [9, 10]. This third mechanism might be coupled with a lateral diffusion of the twin boundary segregation perpendicular to the boundary plane as the twin thickens. Further experimentation is needed to confirm this point.

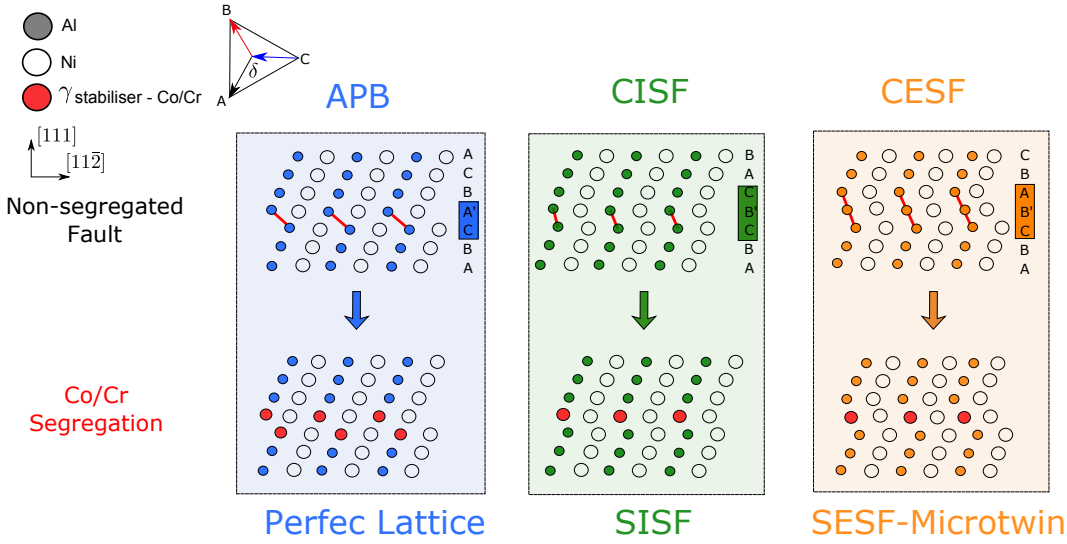

Figure 4.13 – Atomic structures of the different faults observed (APB, CISF and CESF-Microtwin). Red lines represent high energy wrong neighbour bondings in the unsegregated faults (top) which might be suppressed or at least lowered their energy by the segregation of Ni-like atoms such as Cr and Co (bottom).

Two different diffusion scales can be identified among the different diffusion mechanisms. For the latter case of the atomic reshuffling and the solute-atmosphere motion, the diffusion scale relative to the dislocation motion can be considered as short-range atomic movement. Nonetheless, the extended segregation events observed require long-range diffusion which, at the same time, implies much slower time scales. It is well known that when several mechanisms are coupled simultaneously, the slowest one is limiting [22]. Therefore, in the light of this, it seems reasonable to assume that as a first approximation, the lengthening of the different faults under these conditions (800°C and 650 MPa) is governed by the segregation of γ-stabilisers to the fault. This is further supported by the work of Smith et al. [96] where a comparative study of the lengthening rates for the different diffusion processes taking place is presented. The mechanistics of the plastic deformation observed here can be potentially extended to a range of medium-high temperatures. These ideas are further developed and incorporated into a mathematical model to

estimate the diffusion kinetics of the different faults in the following chapter.

4.6 Conclusions

The chemical changes associated with the microtwin formation and propagation have been studied on the single crystal superalloy MD2. The following conclusions can be extracted from the experimental results presented here:

1. HR-STEM at atomic resolution has been used to characterise the creep deformation mechanisms occurring in this material; these involve microtwins – in mature and embryo stages (SESFs/CESFs)– and other type of planar faults such as SISFs/CISFs or APBs.

2. All types of planar faults examined were enriched with γ-stabilisers – Cr, Co and Mo (to some extent) – with respect to the nominal γ' phase composition of this alloy. Concomitantly, a depletion of γ'-stabilisers at the faults has been observed. This produces a shift of the chemical structure from the γ' phase composition to the γ phase one. This shift is especially intense for the case of APBs.

3. When the planar faults evolved to mature microtwins, the segregation was confined to the twin/matrix boundaries, so that the nominal γ' phase composition inside the fault is recovered. This implies a contribution of diffusion within the twin to its growth.

4. The study has been extended to quantitative compositional analysis of the microtwins using correlative APT and TKD analysis. The Cr content was shown to increase by $\approx$2 at.% and Co by $\approx$1 at.% at the microtwin-parent interfaces. No chemical segregation was confirmed within the γ matrix.

These findings provide critical and important data to support the quantitative modelling of the microtwinning mechanism, and the dependence of its kinetics upon alloy composition.

5. The diffusion processes active during the planar fault shearing have been studied in detail. Two different diffusion scales have been identified: the long-range diffusion associated with the fault segregation process and the short-range scale of the solute cloud surrounding the dislocation core and also of the atomic-reordering.

5 Microscopic modelling of the microtwinning kinetics

5.1 Introduction

There is a clear similarity of the microtwinning mechanism observed in superalloys to classical deformation twinning [13], since there is a well-defined crystallography involving a twin plane and shear. On the other hand, some characteristics of a diffusional phase transition have been identified in the previous chapter. For instance, there is a need for diffusion in the vicinity of the twin/matrix interface and an enrichment with regard to solute atoms [97, 52, 10, 4]. Thus in some ways one should consider microtwins to form by a coupled diffusional/displacive mechanism of the type proposed for other alloy systems [98, 99, 100, 101, 102, 45].

In the previous chapters, multiple qualitative aspects of microtwinning have been identified, but many questions concerning the microtwinning mechanism remain unanswered. For instance, the rate-controlling processes needed for twin lengthening are still controversial. It is also not clear how these can be described mathematically and how they are related to the phenomena needed for twin thickening. The processes controlling the nucleation of the microtwins are still not fully understood. Neither is proven that the deformation on the microscale due to the microtwins

explain the macroscopically observed time-dependent response.

To this end, the present chapter proposes a mathematical model to describe the phase-transformation problem of microtwinning motivated by the experimental observations presented previously. The chapter is organised as follows. First, the underlying mechanisms – diffusion and shearing – are coupled in a phase transformation model using a physically faithful approach. The procedure includes the following steps: (i) the twin lengthening kinetics are modelled and the velocity of the microtwin dislocations are estimated; (ii) a homogenisation framework is developed to obtain the macroscopic strain rate from the calculated velocity. Then, the predictions are compared with the experimentally observed macroscopic behaviour. Second, a microtwin nucleation theory is proposed. This leads to a nucleation map dependent on the crystal orientation and the stress state where the influence of the fault energy is studied. Finally, the implications and ramifications of this work are discussed.

5.2 Kinetics of microtwin formation

The elemental segregation presented in the previous chapter indicates that a coupled displacive-diffusive transformation is operative during microtwinning. Following by these experimental observations, the following transformation model is proposed for the microtwin formation under $\langle 011 \rangle$ tension, see Fig. 5.1. First, a pair of complete $a/2\,[\bar{1}01]\,(111)$ dislocations on adjacent planes is constrained to the γ/γ' interface as the applied creep stress is insufficient to overcome the high energy APB energy created, see Fig. 5.1a. Second, these dislocations decorrelate into partial dislocations, see Fig. 5.1b, with differing Schmid factors:

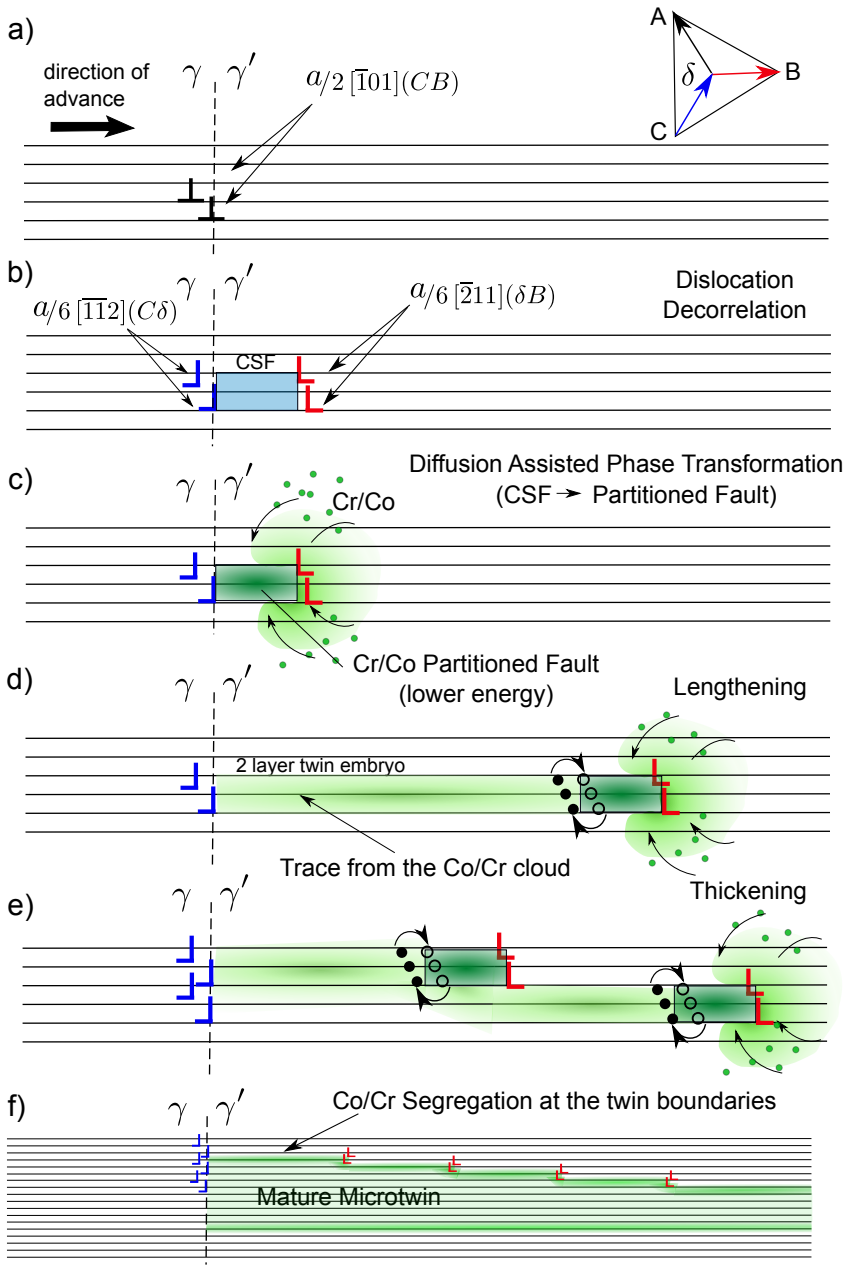

Figure 5.1 – Schematic illustration of the microtwinning mechanism: a) two perfect $a/2\,[\bar{1}01]$ dislocations get trapped at the γ/γ' phase boundary; b) partials $a/6\,[\bar{2}11]$ of higher Schmid factor (red) enter the precipitate creating a high energy CSF thus preventing their propagation; (c) Co and Cr enrichment at the fault transforms the CSF to a lower energy pseudo extrinsic stacking fault which represents a microtwin embryo; d) the leading partials can now continue shearing the precipitate leaving behind them traces of Co and Cr. Atomic reordering can still take place behind the partial dislocations; e) the partials shear on every consecutives planes thus thickening the microtwin; f) the mature microtwin contains segregation of Co and Cr at the microtwin-parent interfaces.

$$\begin{cases} \frac{a}{2}[\bar{1}10] \rightarrow \frac{a}{6}[\bar{1}2\bar{1}] + \frac{a}{6}[\bar{2}11] \\ \\ \frac{a}{2}[\bar{1}01] \rightarrow \frac{a}{6}[\bar{1}\bar{1}2] + \frac{a}{6}[\bar{2}11] \end{cases} \tag{5.1}$$

The partials $a/6\,[\bar{2}11]$ of higher Schmid factor enter the precipitate creating a high energy two layer complex stacking fault (CSF) behind it, thus preventing its extensive propagation into the γ'. This fault is similar to the ones described first by Kolbe [9] and later confirmed by Smith et al. [32]. Third, Co and Cr are partitioned to the leading partial, see Fig. 5.1c, thus transforming the CSF to a lower energy superlattice pseudo extrinsic stacking fault in a γ stabilised atmosphere which represents a microtwin embryo. At the same time the short range reordering after the fault leads to the twinned embryonic structure while the leading partials can now continue shearing the precipitate leaving behind them a trace of Co and Cr remnant from the shearing process, see Fig. 5.1d. This combined process will leave enough time for the necessary atomic reshuffling to occur in order to annihilate the wrong neighbours structure, thus enabling the lengthening of the twin. The segregation process involves long range diffusion and a continuous flux of Co and Cr to the advancing partials. The microtwin embryo thickens by a ledge mechanism, see Fig. 5.1e, in a similar way as the one proposed recently by Smith et al. [4]. The partials shearing on every consecutive planes benefit from the remnant Cr and Co enriched regions. Notably, it is expected that subsequent leading partials confer faster shear rates than might be expected by long range diffusion alone [90]. Plausibly, the mature microtwin arising from this mechanism possesses segregation of Co and Cr at the microtwin-parent interfaces only or within close vicinity of them, see Fig. 5.1f; there exists the possibility of slight enrichment of these elements inside the twin arising from the shearing partial

residue.

This process differs from the theory first introduced by Kolbe [9], for which no long range diffusion was assumed necessary. This long range diffusion process presented here is also supported by the work of Viswanathan et al. [90] which suggests that the movement of partials during planar fault growth is controlled instead by the diffusion rate of segregating elements. Furthermore, Smith et al. [32] proposed that the segregation has a localised stabilising effect, accomplished through the formation of a region of γ phase at the planar fault within the γ' precipitates. The localised microtwinning partitioning of Cr and Co presented in the previous chapter (known γ phase stabilising elements) supports this hypothesis. Therefore, in the light of the results from the previous chapter, it seems reasonable to assume that as a first approximation, the lengthening of the different faults under these conditions is governed by the segregation of γ-stabilisers to the fault. This is further supported by the work of Smith et al. [96] where a comparative study of the lengthening rates for the different diffusion processes taking place is presented, showing that the segregation of Co and Cr to the faults is the time limiting process. In order to model the twin growth kinetics, one may assume that the two diffusion processes are simultaneously controlling the shearing of the partials: (i) the partitioning of Co and Cr into the body of the fault, and (ii) the short range reordering events behind the leading partials.

5.2.1 A model for microtwin formation

A mathematical procedure derived from the work of Atkinson [103] is used here to model diffusion assisted twinning. It is assumed that growth is produced by the lateral movement of ledges.

The elements Cr and Co are assumed to control twin lengthening and thickening. The important aspect is to consider carefully the length scale associated with this. There are at least three possible scenarios of importance, see Fig. 5.2:

- Scenario 1: initially, the fault starts as a single thin plate of height h_t (equal to two atomic planes) growing within the matrix. Its lengthening is supported by long range diffusion of Co/Cr from the surrounding matrix. This scenario represents the twin embryo or SESF.

- Scenario 2: second, we consider the situation a little way back from the leading tip, just a few ledges away; here it can be anticipated that the twin is still remarkably thin such that there is a need to support significant long range bulk diffusion of Co/Cr from the surrounding matrix; this is because there is no substantial volume of twin to support a diffusional flux from it.

- Scenario 3: a third scenario relates to the situation far behind the leading tip when the twin is now much thicker; here, following the experimental observations, the bulk of the twin is no longer enriched with Cr/Co consistent with the need only for diffusion controlled migration of the ledges. Therefore, the ledge migrates but with a diffusion field which is now – to a first approximation – symmetrical across the twin/matrix interface. The above and, in particular, the velocity calculated is also potentially modified by the fact that the ledge can grow along a terrace ahead of it which is enriched with respect to Cr/Co, compared to the mean composition of those elements in the alloy.

We now proceed to analyse in detail the above scenarios with a particular emphasis on determining the ledge velocity for each case:

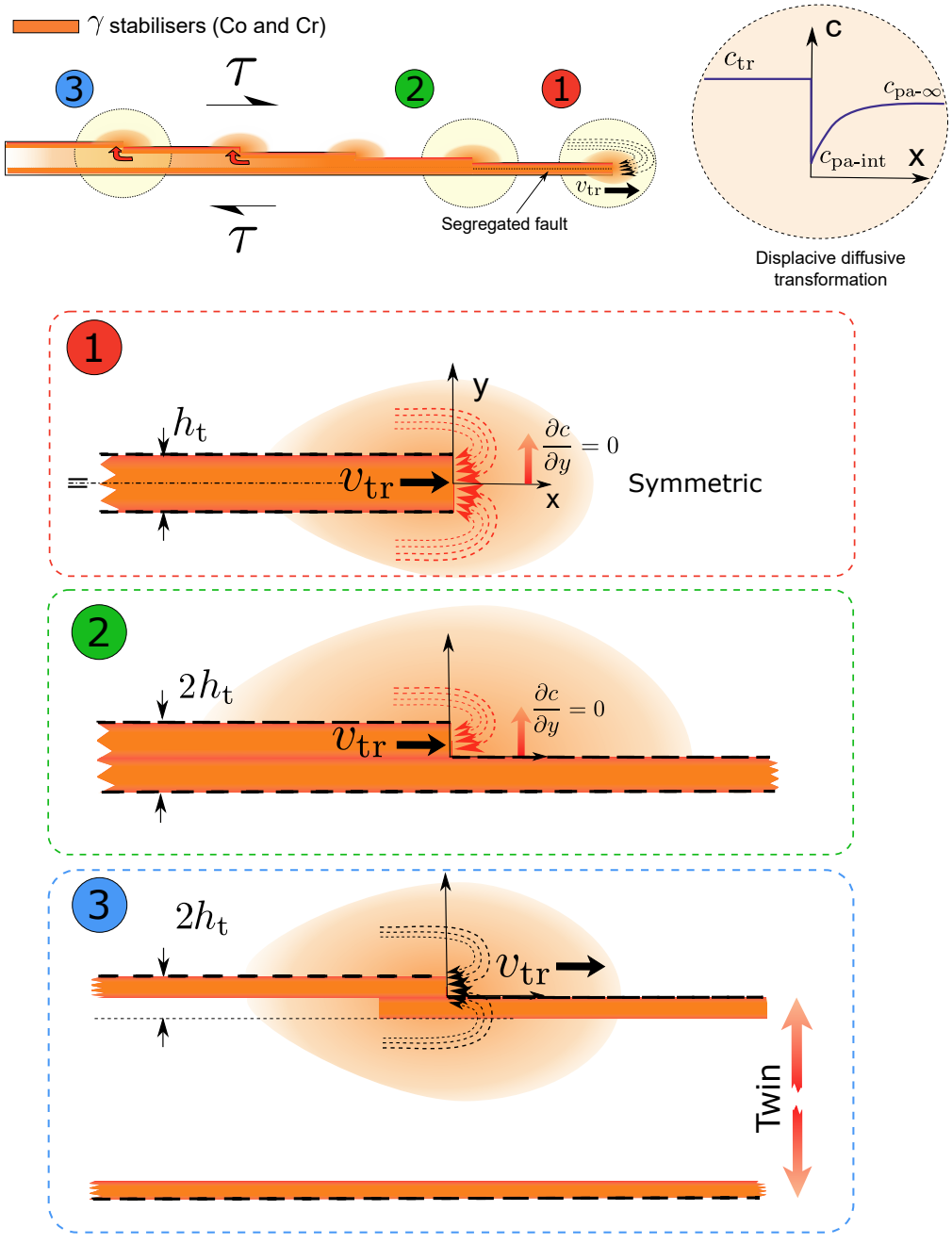

Figure 5.2 – Microtwin growing in the γ' phase by a ledge type mechanism (top). Three different diffusion scenarios can be identified along the twin: 1) growth of the twin tip in a virgin material with Co and Cr support exclusively from the surrounding material; 2) at the initial stage of growth, when the micotwin is still a few atomic planes thick and therefore the available Co an Cr to segregate is small, the additional Co an Cr for thickening might need to still be supported by bulk diffusion from the matrix; 3) once the twin thickens, the diffusion support of Co and Cr is not constrained anymore to the the matrix but also to the twin body.

Scenario 1

Initially, the twin tip advances supported by bulk diffusion, broadly similar to a plate growth like problem, see Fig. 5.2-scenario 1. For this case, the mathematical procedure developed by Atkinson [103] can be adapted assuming a no flux condition on the plane of symmetry ($\frac{\partial c}{\partial y} = 0$). Then, the problem is reduced to solving the concentration field in the upper half of the symmetry plane with a characteristic length of $l_{\text{char}} = h_{\text{t}}/2$, where h_{t} is the twin ledge height . At the leading edge, the Stefan condition must be satisfied to accomplish mass conservation [103]:

$$v_{\text{tr}} = D_{\text{eff}} \frac{\partial c}{\partial X}\bigg|_{\text{step}} (c_{\text{tr}} - c_{\text{pa-int}})^{-1} \tag{5.2}$$

where v_{tr} is the twin step transformation velocity, X is the absolute coordinate along the twin length, $D_{\text{eff}} = \frac{D_{\text{Co}}\, c_{\text{Co}} + D_{\text{Cr}}\, c_{\text{Cr}}}{c_{\text{Co}} + c_{\text{Cr}}}$ is the effective diffusivity of Co and Cr in the γ' parent phase and c_{tr} and $c_{\text{pa-int}}$ are the effective Co+Cr concentrations ($c = c_{\text{Cr}} + c_{\text{Co}}$) in the twin phase and in the parent phase at the twin step, respectively, see Fig. 5.3a. At this stage, the required support of solute for growth is exclusively bulk diffusion, so it seems reasonable to consider diffusion solely in the parent phase around the twin, governed by Fick's laws [104], whereas for simplicity, negligible diffusion occurs in the twin at this stage [103].

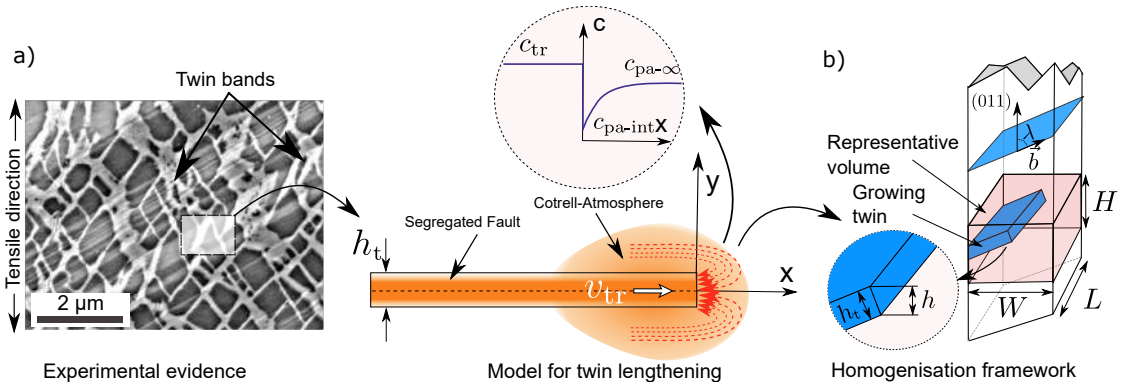

Figure 5.3 – a) Experimental evidence of microtwin bands and detailed diagram of the twin lengthening mathematical problem; b) geometrical diagram of the twin glide plane and the representative volume used in the homogenisation calculations.

The diffusion problem is formulated in a moving non-dimensional coordinate system, $x = 2\,(X - v_{\mathrm{tr}})/h_{\mathrm{t}}$ and $y = 2\,Y/h_{\mathrm{t}}$ (relative to stationary coordinates $X - Y$). Introducing the Péclet number $p = \frac{v_{\mathrm{tr}} h_{\mathrm{t}}}{4D}$, one has:

$$\begin{cases} \nabla^2 \Gamma\{x,y\} + 2p\frac{\partial \Gamma}{\partial x} = 0 \\ \frac{\partial \Gamma}{\partial y} = 0 \quad \text{on} \quad y = 1,\ x < 0 \\ \frac{\partial \Gamma}{\partial y} = 0 \quad \text{on} \quad y = 0,\ x > 0 \\ \frac{\partial \Gamma}{\partial x} = -\alpha^{-1}\{p\} \quad \text{on} \quad x = 0,\ 0 \leq y < 1 \end{cases} \tag{5.3}$$

where $\alpha\{p\} = -\left(\frac{\partial \Gamma}{\partial x}\Big|_{\mathrm{step}}\right)^{-1}$ is an unknown to be determined (assumed constant here) and the dimensionless concentration is defined by

$$\Gamma\{x,y\} = \frac{c\{x,y\} - c_{\text{pa-}\infty}}{c_{\mathrm{e}} - c_{\text{pa-}\infty}} \tag{5.4}$$

In addition to the diffusion problem around the step interface, there is also a short range atomic reordering at the interface which is necessary for the twin tip to advance, which limits the interface mobility. The mobility of the interface μ_o is approximated using the thermally activated dislocation theory [105, 106] in which the probability of a dislocation advancing along the glide direction is associated with the free energy change of the event ΔG, in this case with the atomic reshuffling. This energy change $\Delta G = \Delta G_0 - \tau V$ includes the work done by the external shear stress τ against the zero-stress energy barrier of the reshuffling processes ΔG_0, where V is the activation volume of the deformation mechanism defined as $V = -\left(\frac{\partial \Delta G}{\partial \tau}\right)_T$. The energy barrier ΔG_0 associated with these reordering events has been studied in detail by Kovarik et al. [10] and is used here. Hence, the

interface mobility can then be approximated as:

$$\mu_o = b\,\nu \exp\{-(\Delta G_0 - \tau\, V)/kT\} \tag{5.5}$$

where ν is the Debye frequency vibration of a reshuffled Ni atom [10], k is the Boltzmann constant, T is the absolute temperature and b is the Burgers vector norm of the twinning dislocation (and the distance progressed by the reaction in every successful attempt).

The effect of the interface reactions (short range reordering) on the twin kinetics is included by considering deviation from the equilibrium at the interface ($c_{\text{pa-int}} \neq c_{\text{e}}$) [103]. For this case, the extra-boundary condition needed is imposed by accounting for the interface mobility μ_0, which is controlled by short range atomic reshuffling:

$$v_{\text{tr}} = \mu_0(c_{\text{pa-int}} - c_{\text{e}}) \tag{5.6}$$

In case of large μ_0 the problem is diffusion controlled ($\mu_0 \to \infty$ implies $c_{\text{pa-int}} \to c_{\text{e}}$), whereas for small μ_0 the problem is interface controlled.

The approximated solution using Fourier transforms and perturbation theory proposed by Atkinson [103] leads to a set of two non-linear equations:

$$\begin{cases} \alpha\{p\} = \pi^{-1}[1 - C + \ln(2\pi/p)] \\ \Omega_0 = 2p\alpha\{p\} + (p/q)[1 - 2p\alpha\{p\}] \end{cases} \tag{5.7}$$

where $C = 0.5772...$ is the Euler constant and $q = \mu_0(c_{\text{tr}} - c_{\text{e}})(4D/h_{\text{t}})^{-1}$ is defined as a non-dimensional interface mobility. In this system, $\alpha\{p\}$ and p are the unknowns to be determined and Ω_0 is defined as the dimensionless normalised supersaturation

concentration $\Omega_0 = (c_\infty - c_\mathrm{e})/(c_\mathrm{tr} - c_\mathrm{e})$. Once this system is solved, the velocity of the twin ledge v_tr can be recovered from the definition of the Péclet number p. The concentration field far from the twin tip can be approximated by the zero order Bessel function K_0 following [103]

$$c\{x, y\} = \frac{\alpha}{p} K_0\{pr\} \exp\{-px\} \tag{5.8}$$

where $r = \sqrt{x^2 + y^2}$.

This process allows for the estimation of v_tr as a function of the geometry h_t, assuming D_eff and the concentration values.

Scenario 2

In this case, it is assumed that the microtwin is growing on a preformed twin. For the avoidance of doubt, the assumption made is that the main diffusion flux is still limited to the surrounding matrix based on the argument that the reservoir of Co/Cr of the embryonic twin is still not enough to support the necessary partitioning of these elements to the new ledge. As is apparent, this problem shares the same mathematical structure as the one detailed in scenario 1 with the only difference being that the characteristic length in this case is $l_\mathrm{char} = h_\mathrm{t}$, as indicated if Fig. 5.2-scenario 2. Therefore the velocity resulting from the analysis is half the one considered in the previous case. The non-dimensional quantities and Péclet number remain the same as in scenario 1.

Scenario 3

Now, the growing front is advancing in a region where the concentration differs from the nominal concentration of the matrix due to the already enriched terrace ahead of it, see Fig. 5.2-scenario 3. Once the twin thickens, the partitioned

Table 5.1 – Velocities and characteristic lengths for the three different scenarios formulated.

	Scenario 1 (Twin Tip)	Scenario 2 (Thin Twin)	Scenario 3 (Mature Twin)
Velocity	$\approx \frac{2D_{\text{eff}}}{h_{\text{t}}}$	$\approx \frac{D_{\text{eff}}}{h_{\text{t}}}$	$\approx \frac{2D_{\text{eff}}}{h_{\text{t}}}$
Characteristic length	$\frac{h_{\text{t}}}{2}$	h_{t}	$\frac{h_{\text{t}}}{2}$

region is now confined to the twin interfaces, leaving a region inside the twin with the same nominal concentration as the matrix. This problem resembles the one proposed in scenario 1, with a different concentration assumed ahead of the growing ledge ($c_{\text{pa-}\infty}$). But if it is assumed that the homogenised concentration ahead of the growing ledge (matrix + twin) is still close enough to the nominal matrix concentration ($\text{volume}_{\text{segregated}} << \text{volume}_{\text{non segregated}}$) the Péclet number for this scenario would be close to the one calculated for scenario 1. Therefore the velocity arising should be in the same order of magnitude ($v_{\text{case3}} \approx v_{\text{case1}} \approx \frac{2D_{\text{eff}}}{h_{\text{t}}}$).
The characteristic lengths and approximate velocities of the three different scenarios are summarised in Table 5.1. The analysis presented here shows that, regardless of the growing stage of the twin (scenarios 1, 2 or 3), the growth velocity of the dislocation front is approximately of order $v_{\text{t}} \approx \frac{D_{\text{eff}}}{h_{\text{t}}}$. Therefore, it seems reasonable to assume this estimation as a first approximation of the twin ledge velocity in Section 5.2.2.

The physical parameters ($c_{\text{pa-}\infty}$, c_{e}, c_{tr}, D_{eff}, h_{t}, ΔG_0 and V) involved in the problem need to be estimated based on experimental measurements and thermodynamic estimates. The Co and Cr concentrations in the γ' at infinity ($c_{\text{pa-}\infty}$) were extracted using the averaged APT concentrations in the γ' far field from the twin. The

compositions at the twin ledge interface (c_{tr}) were calculated by averaging the integrated concentration between mid-points of the concentration peaks of the APT analysis in Chapter 4. The concentration peaks from all the interfaces analysed here were considered. The γ' equilibrium composition (c_{e}) and the chemical diffusivities of Co and Cr (D_{Co} and D_{Cr}) were obtained using Thermo-Calc software (database TTNI8) and DICTRA (database MOBNI3) for equilibrium phase calculations and kinetics, respectively [107, 108]. The activation volume V was derived from the data in Fig. 3.9b, taking into account the tests where microtwinning was active at 800°C. The activation energy for the short range reordering (ΔG_0) was determined as the addition of migration and vacancy formation energies following the work

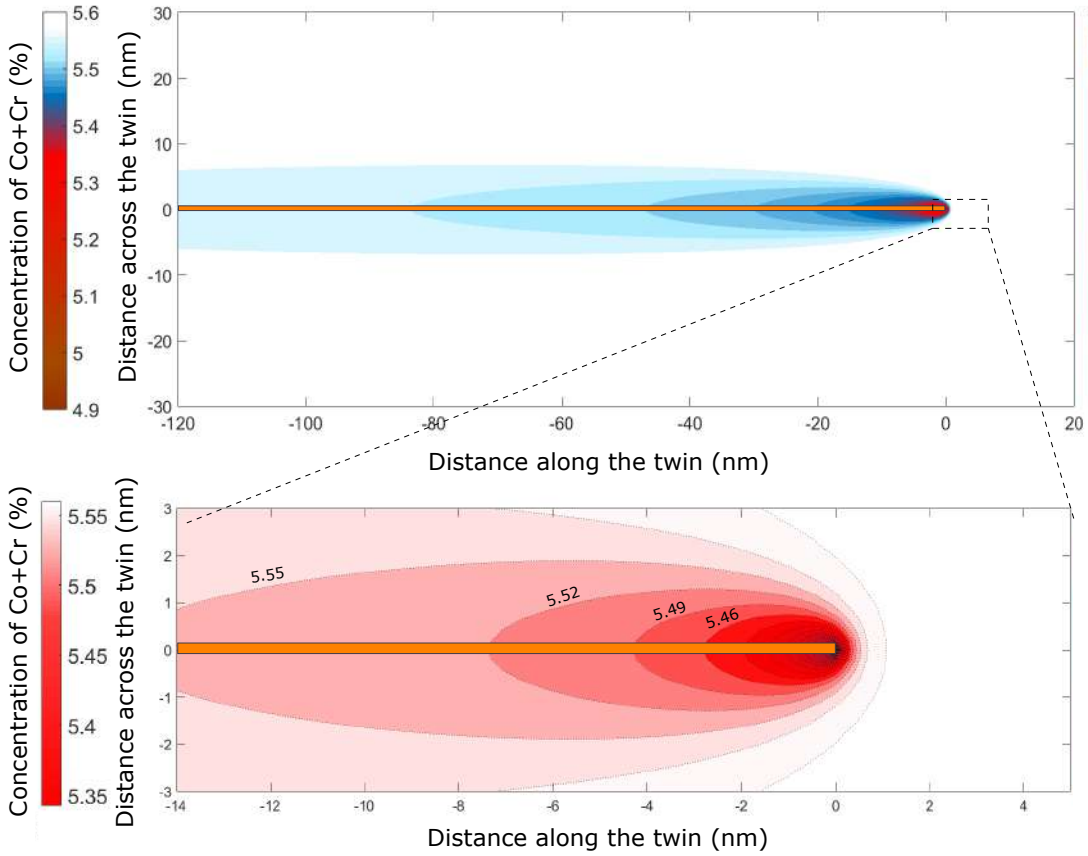

Figure 5.4 – Calculated Co+Cr concentration field for a leading twin tip growing at 800°C (top) and detailed view with concentration stream lines of the concentration field indicating the shape of the diffusion field (bottom).

Table 5.2 – Parameters used for calculating the twin dislocation velocities in MD2 Ni-based superalloy.

D_{Co} (m^2/s)	D_{Cr} (m^2/s)	D_{effe} (m^2/s)	$c_{\mathrm{pa}\text{-}\infty}(\%)$	$c_{\mathrm{tr}}(\%)$	$c_{\mathrm{e}}(\%)$
2.35×10^{-18}	1.77×10^{-18}	2.10×10^{-18}	5.62	6.35	4.99
ν (rad/s)	$a_{\gamma'}$ (m)	b (m)	$V(b^3)$	ΔG_0 (eV)	h_{t}(m)
9.66×10^{13}	3.5×10^{-10}	1.4×10^{-10}	266.8	2.27	$(7/3)\sqrt{3}\times10^{-10}$

of Kovarik et al. [10]. Finally, the height of the twin step was set to twice the {111} spacing for γ' ($h_{\mathrm{t}} = 2a_{\gamma'}/\sqrt{3}$, where the lattice parameter $a_{\gamma'}$ for MD2 was obtained from the measurements of Pyczak et al. [109] on the similar superalloy CMSX-4 using X-ray diffraction). The parameters used in the calculations of the diffusion field and dislocation velocities are given in Table 5.2.

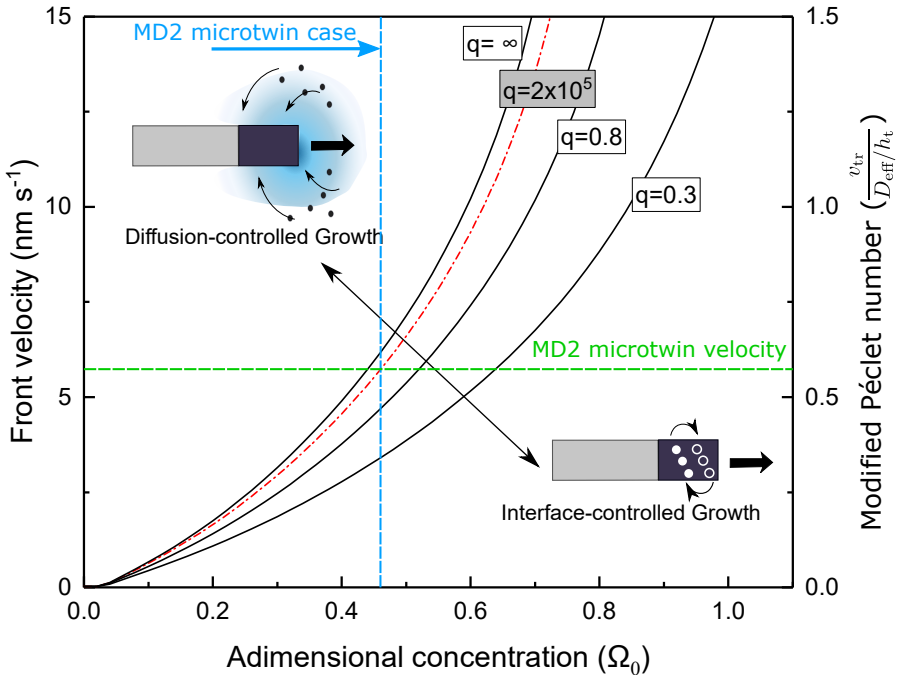

Figure 5.5 – Twin ledge growth velocity v_{tr} against the non-dimensional concentration $\Omega_0 = (c_{\mathrm{pa}\text{-}\infty} - c_{\mathrm{e}})/(c_{\mathrm{tr}} - c_{\mathrm{e}})$ for different non-dimensional interfaces mobilities $q = \mu_0(c_{\mathrm{tr}} - c_{\mathrm{e}})(2D_{\mathrm{eff}}/h_{\mathrm{t}})^{-1}$. The specific velocity curve for the case of microtwins growing at 650 MPa and 800°C is indicated in red. The specific value of Ω_0 obtained experimentally from APT measurements is indicated as a vertical blue line. Finally, the computed velocity for this specific case of the microtwins growing in MD2 at 650 MPa and 800°C is indicated as a horizontal green line.

The computed concentration field around a twin tip for the case of 800°C and 650 MPa is illustrated in Fig. 5.4. The iso-concentration surfaces around the twin tip are ellipsoidal in form. From these results, one deduces that the diffusion phenomena are not only constrained to a few atomic spacings but involve long range mass transport. From this concentration field, the twin ledge velocity is plotted in Fig. 5.5 as a function of the non-dimensional concentration and the non-dimensional interface mobility q. The specific case of 650 MPa and 800°C ($q = 2\times10^5$) is highlighted as a red line. The green line indicates the experimental value of adimensionalised concentration ($\Omega_0 = 0.46$) found for MD2. As a first approximation, the growth rate of the microtwin embryo is of order of magnitude $v_{\mathrm{tr}} \sim D_{\mathrm{eff}}/h_{\mathrm{t}}$ as observed from the green line indicating the computed velocity for the specific case of 650 MPa and 800°C. It is noticeable that this problem is analogous to the diffusion assisted shearing of other faults [31, 32] and therefore the study could be extended in principle to APBS, SISFs or SESFs.

5.2.2 Homogenisation of the microtwin kinetics

To compare the lengthening rates computed with the experimental results, a homogenisation approach is taken. The shearing rate $\dot{\gamma}$ produced by the microtwinning mechanism is extracted from the growth rate of the twinned phase:

$$\dot{\gamma} = \dot{f}_{\text{V-twin}}\, s \tag{5.9}$$

where $\dot{f}_{\text{V-twin}}$ is the rate of change with time of the twinned volumetric fraction and s is the twin shear. By assuming the previously introduced ledge growth

mechanism, the rate of change of volume fraction can be approximated as

$$\dot{f}_{\text{V-twin}} = \frac{n\, h_t\, l}{H\, L\, W}\, \overline{v}_{\text{tr}} \tag{5.10}$$

where n is the number of twins ledges in the reference volume, h_t and l are the growing front dimensions of each twin ledge, $\overline{v}_{\text{tr}}$ is the mean twin ledge transformation velocity and H, L, W are the height, length and width of the reference volume as indicated in Fig. 5.3b, respectively. In this expression, $f_{\text{twin}} = n\, h_{\text{t}}\, \cos\phi/H$ is the average twin fraction calculated from the tested specimens where $h_{\text{t}}\, \cos\phi$ is the projection of the twin height on the tensile axis. In this approach we assume that the twins are growing homogeneously during the test until the final twinned structure is formed. The mean twin ledge velocity $\overline{v}_{\text{tr}}$ corresponds to the averaged velocity across γ and γ', assuming instantaneous glide across the γ phase ($\overline{v}_{\text{tr}} = v_{\text{tr}}/f_{\gamma'}$, where $f_{\gamma'}$ is the γ' volume fraction). Taking this into account the overall creep rate can be rewritten as

$$\dot{\gamma} = \frac{f_{\text{twin}}(L+W)}{2\, L\, W\, f_{\gamma'}\, \cos\phi} v_{\text{tr}}\, s \tag{5.11}$$

where the twin front width l is approximated by the averaged section chord $l = (L+W)/2$. Finally, for the case of single crystal and assuming a single activated twin system, the Schmid angles (ϕ, λ) are used to relate the microscopic twinning shear strain rate $\dot{\gamma}_{\text{twin}}$ to the tensile macroscopic strain rate $\dot{\varepsilon}$ following [81]:

$$\dot{\varepsilon} = \frac{\mathrm{d}}{\mathrm{d}t}\sqrt{1 + \gamma_{\text{twin}}^2 \cos^2\phi + 2\gamma_{\text{twin}} \cos\phi \cos\lambda} \tag{5.12}$$

All the quantities involved here are known from the experiments $(f_{\text{twin}}, W, L, f_{\gamma'})$,

are geometrical relations (ϕ, λ, s) or calculated from the diffusion problem (v_{tr}). The twin fractions (f_{twin}) were obtained from image analysis on the micrographs cited in the previous subsection and presented in Fig. 3.11. The width and thickness of the sample, W and L, were set to 1.6 mm and 1 mm, respectively. The set of new parameters used in this homogenisation framework is given in Table 5.3.

Table 5.3 – Parameters used for calculating the homogenised microtwin strain rates in MD2.

W(m)	L(m)	ϕ	λ	$f_{\gamma'}$(%)
1.6×10^{-3}	1×10^{-3}	35.3°	54.7°	63

The calculated strain rates at 800°C produced by microtwin shearing for the three stress levels where this mechanism is active are indicated in Fig. 5.6. The strain rates calculated are found to be a good approximation of the experimental ones without any free parameter calibration. Moreover, the model captures reasonably well the observed strain rate dependence on the stress through the increase of the twin nucleation density (introduced by f_{twin}) and the assistance of the external stress on the interface reactions ($\Delta G = \Delta G_0 - \tau V$). The predicted values are always below the real strain rates. It is important to note that this is an approximate model constructed on the basis of the experimental information available, trying to avoid calibration or fitting. Therefore, several physical factors need to be considered that might influence the results:

- The twin volume growth rate may be larger in reality than the proposed approximation. This is due to several twin ledges advancing on the same shear plane, while in the model proposed here a single twin ledge was assumed per atomic plane.

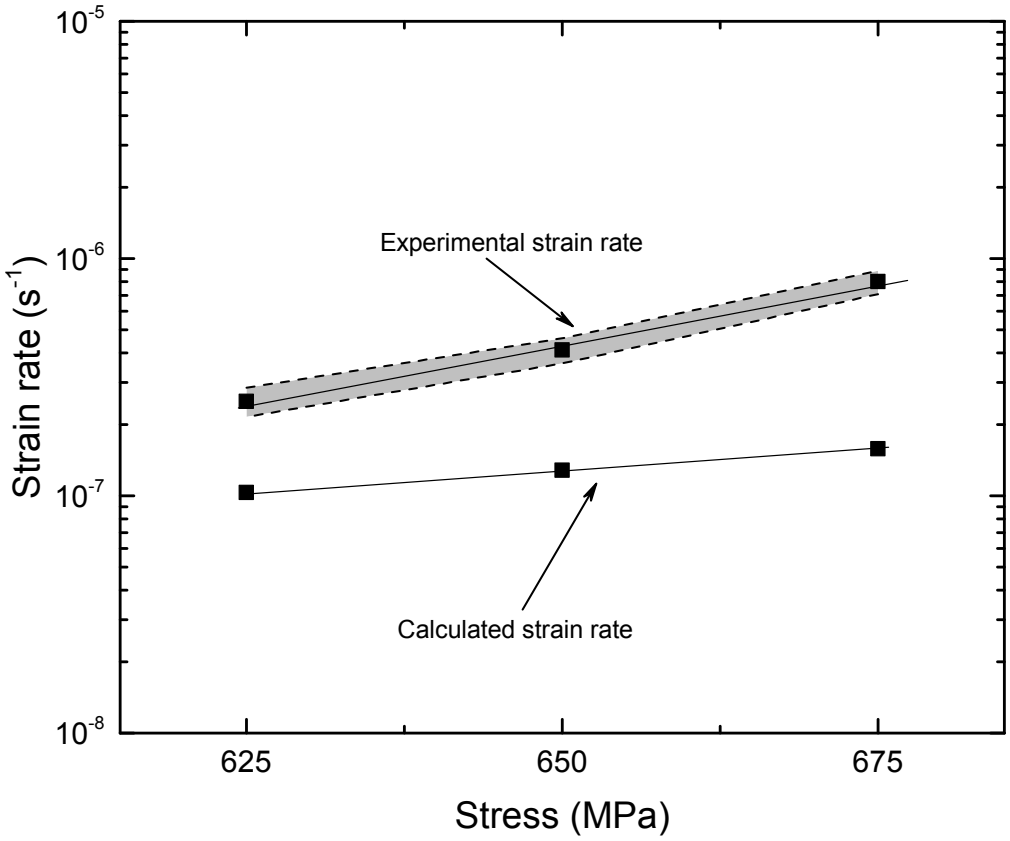

Figure 5.6 – Calculated and experimentally measured steady creep strain rates (with standard deviation) for MD2 single crystal superalloy at 800°C and several stresses.

- In the diffusion problem presented in the previous section, the twin ledge was assumed to grow in an infinite γ' with a fixed concentration. This is not the real case as the γ' precipitates have an approximate size of $\approx 1\mu$m. As a consequence, when the twin tip gets closer to the γ-γ' interface, the twin ledge can benefit from additional diffusion from the Cr- and Co-enriched γ. This is expected to increase the twin ledge velocity.

- Additionally, the effect of enhanced diffusion along the dislocation cores was not included in this model. This is expected to increase solute support rates and therefore the dislocation shearing rates.

- The shear rates calculated here are just the contribution of the microtwinning

mechanism to the overall deformation – other mechanisms may be operative thus increasing the overall creep rates.

5.3 Nucleation of microtwins

In this section, consideration is given to the factors determining microtwinning nucleation. In this regard, microtwin nucleation in Ni-based superalloys shares some similarities with twin formation in nanograined materials [110, 111, 112, 113, 114]. The γ/γ' interfaces in the superalloy work as partial dislocation sources analogous to grain boundaries in nanograined metals.

A microtwin embryo can form within the γ' phase by the glide of leading partial dislocations with identical Burgers vectors on consecutive upper or lower {111} planes. In competition, APB slip of γ' precipitates can occur when the leading partial dislocation is followed by a trailing partial dislocation on the same plane forming jointly a full type dislocation as indicated in Fig. 5.7a. Following the approach of McCabe et al. [112], the total force F_{partial} per unit length of dislocation l exerted on either the trailing partial or twin partial follows

$$\frac{F_{\text{partial}}}{l} = \frac{-F_{\text{rep}} + F_{\text{fault}} + F_{\tau}}{l} \tag{5.13}$$

where F_{rep} is the elastic repulsion due to the leading partial dislocation, F_{fault} is the contribution resulting from the change in fault energy due to the trailing partial and F_{τ} is the external force exerted by the shear stress. Here, we have assumed that the complex extrinsic stacking fault associated with the microtwin formation (CESF-2) can be treated as two consecutives complex intrinsic faults (CISFs) over two adjacent {111} planes [76]. Therefore, the term $F_{\text{fault}}/l = \gamma_{\text{CISF}} - \gamma_{\text{CESF-2}} \approx -\gamma_{\text{CISF}}$ for the

case of the microtwin and $F_{\text{fault}}/l = \gamma_{\text{CISF}} - \gamma_{\text{APB}}$ for the case of APB shearing as indicated in Fig. 5.7b. The external force is equal to $F_\tau/l = b\,\sigma\,\text{SF}$ where σ is the uniaxial applied stress stress and SF is the Schmid factor of the dislocation. The elastic repulsion component has been proven to be the same for both configuration of partials [112].

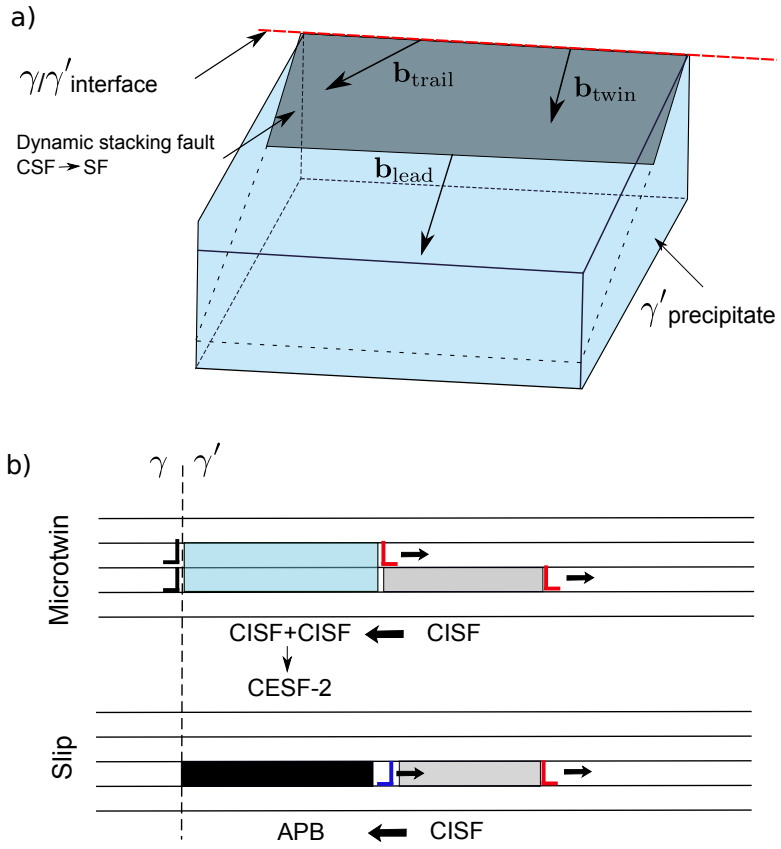

Figure 5.7 – a) Schematic diagram of the twin nucleation process for Ni-based superalloys. A leading partial dislocation is generated from the γ/γ' interface forming a faulted structure along the twin plane. At high temperatures, this fault structure is evolving as Cr and Co partition around the leading partial (CSF $\rightarrow$ SF); b) two cases can occur: a new twin partial enters the precipitate on a consecutive gliding plane leading to a twin embryo, or the already dissociated trailing slip partial on the same plane enters the precipitate leading to an APB. Whether the driving force for twinning or slip is preferred depends on the time available for transforming to a low energy SF determined by the dislocation velocity. Adapted from McCabe et al. [112].

Microtwinning becomes favourable when the driving force for nucleation of a twinning partial is greater than the driving force for gliding of a trailing partial ($F_{\text{twin}} - F_{\text{trailing}} > 0$). This criterion leads to the following critical stress for microtwin nucleation

$$\sigma_{\text{cri}} > \frac{2\,\gamma_{\text{CISF}} - \gamma_{\text{APB}}}{b\,(\text{SF}_{\text{twin}} - \text{SF}_{\text{trailing}})} \tag{5.14}$$

At the same time, the stress on the twin partial dislocation must be higher than the energy threshold for twin partial formation which can be approximated by: $\sigma_{\text{tw}} > \gamma_{\text{CISF}}/(b\,\text{SF}_{\text{twin}})$. The critical stress for microtwin nucleation satisfying both conditions is shown in Fig. 5.8 as a function of the crystal orientation. The tensile or compressive character of the required load is specified in Fig. 5.8a and the different stress levels are indicated in Fig. 5.8b for three different cases: first a completely unsegregated fault (CESF-2), second a partially partitioned/reordered fault with 50% of the original fault energy and finally the totally partitioned/reordered case where the fault might be identified with a perfect SESF. Fault energies used are $\gamma_{\text{APB}} = 147\,\text{mJ/m}^2$, $\gamma_{\text{CISF}} = 177\,\text{mJ/m}^2$ and $\gamma_{\text{SESF}} = 74\,\text{mJ/m}^2$ [76]. The energy reduction promoted by the segregation and the atomic reordering of the fault leads to twin nucleation with stresses below 700 MPa, comparable with the experimental observations. Further *ab initio* calculations of the influence of the partitioning phenomenon on the microtwin nucleation are required to obtain better estimates, but the tendency is clear: $\langle 011 \rangle$ and $\langle 001 \rangle$ crystal directions are the most prone orientations for creep twin formation followed by $\langle 111 \rangle$. This clearly coincides with the observations made in the literature which indicate that the $\langle 011 \rangle$ and $\langle 001 \rangle$ orientations are the most repeated for microtwinning [10, 97, 4, 32].

A new variable is hereby added to the complexity of the microtwin formation: a time dependent nucleation mechanism. At this point, some of the main aspects of

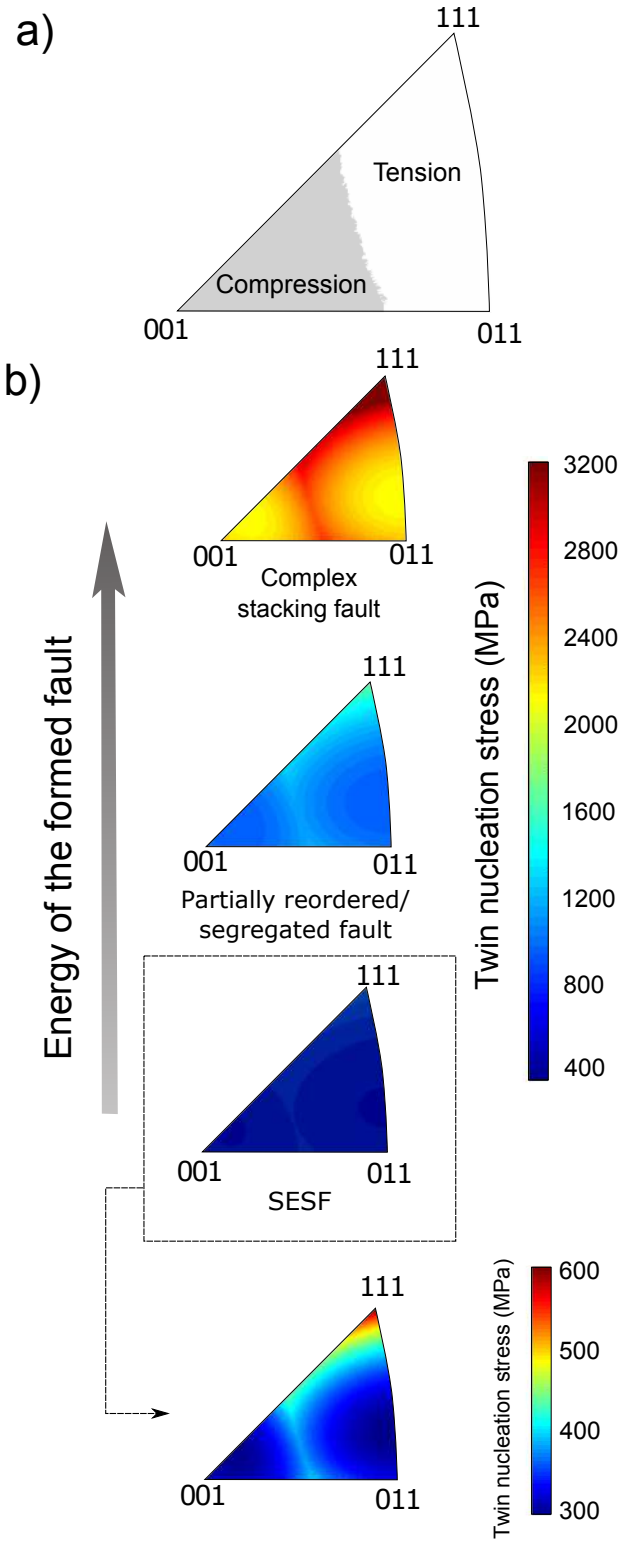

Figure 5.8 – Microtwin nucleation maps for a generalised Ni-based superalloy: a) tensile/compressive character of the critical twin stress; b) critical stress for microtwin nucleation for three cases of study: a completely unsegregated fault (top), a partially partitioned/reordered fault with 50% of the original fault energy (middle) and a totally partitioned/reordered SESF fault (bottom), middle. Fault energies assumed are $\gamma_{\mathrm{APB}} = 147\,\mathrm{mJ/m^2}$, $\gamma_{\mathrm{CISF}} = 177\,\mathrm{mJ/m^2}$ and $\gamma_{\mathrm{SESF}} = 74\,\mathrm{mJ/m^2}$ [76].

the formation of microtwins have been studied; however, the implications of this segregation assisted mode of plasticity on the mechanical behaviour of the alloy are still unclear. This is the focus of the next section.

5.4 Discussion

The segregation assisted dislocation shearing presented here might be crucial for understanding one of the still daunting aspects of the superalloys: the sudden drop of yield-strength properties at high temperatures ($T \approx> 800\,^{\circ}\mathrm{C}$). This concept is illustrated in Fig. 5.9 where the diffusivities of Cr and Co computed from Thermo-Calc [107] are shown against the yield stress along the $\langle 001 \rangle$ orientation of the commercial superalloy CMSX-4. This superalloy has a similar composition and mechanical behaviour to MD2. During plastic deformation at low temperatures ($T < 700\,^{\circ}\mathrm{C}$), the diffusion processes are still limited and the dislocations need to enter into the γ' precipitates without the assistance of segregation. This creates "full-energy" faults within the γ' precipitates which strengthen considerably the alloy. This regime is where the wide variety of standard athermal plasticity theories for superalloys are applicable [65, 66]. As the temperature increases, the diffusion processes gradually start to become more and more important during plastic deformation. The dislocation shearing within the γ' precipitates is now assisted by local changes in the chemistry and reordering processes, thus the classical strengthening mechanism for Ni-based superalloys (the high-energy faults shearing) vanishes. This provokes a reduction of the stress required to shear the γ' precipitates and, as a consequence, a sudden drop of the plastic-strength of the alloy can be observed in Fig. 5.9. At really high temperatures ($T > 900\,^{\circ}\mathrm{C}$), the dislocation climbing of γ' precipitates and the rafting processes becomes the dominating plastic

mechanisms degrading even more the mechanical strength of the alloy [45, 3, 39].

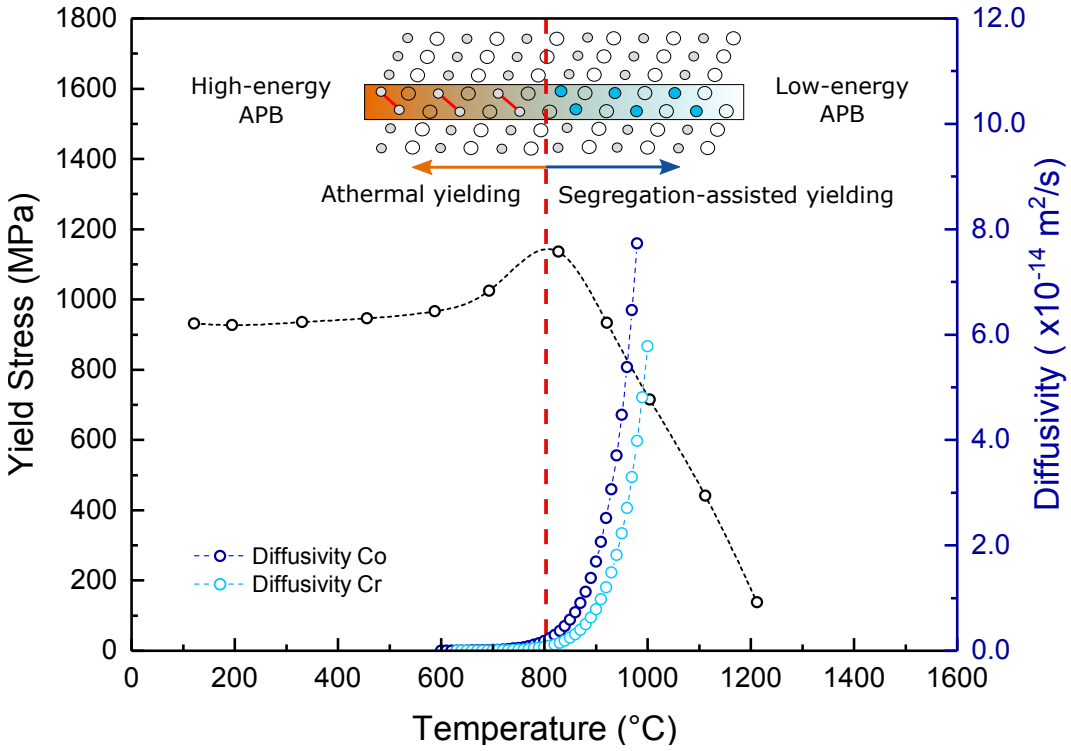

Figure 5.9 – Correlation between the evolution of the yield stress of the single crystal superalloy CMSX-4 [115] with temperature and the diffusivity of Cr and Co within the γ' precipitates. The results presented in this chapter suggest that at higher temperatures (T > 800°C) the segregation to the deformation faults (APBs, SESFs, SISFs or microtwins) controls the strength of the alloy by changing locally its composition and therefore the fault energies necessary for dislocation glide.

As a result, the strong effect of the local chemical changes on the creep and plastic strength must not be obviated in future models. One of the first experimental attempts to accomplish this purpose has been presented by Smith et al. [53], proposing the addition of certain elements (Ti, Ta and Nb) to block the effect of the γ-stabilisers and eventually strengthen the alloy. In order to push forward the temperature capabilities of these alloys, these segregation processes need to be fully integrated in multi-physics continuum models which potentially will allow the

dependence of the strength of the alloy on its chemical composition to be captured. This is the purpose of the next chapter.

5.5 Conclusions

Microtwinning in the single crystal superalloy MD2 has been modelled physically. The following specific conclusions can be drawn:

1. A dislocation-based mechanism based on the decorrelation of partials has been proposed for microtwin formation due to loading on the $\langle 011 \rangle$ direction. The twin partial configuration proposed is consistent with the 60° crystallographic rotation found by EBSD analysis.

2. The kinetics of the microtwinning process have been modelled using phase transformation theory to account for the effects of temperature, stress and alloying. Physical constants (diffusion coefficients, chemical concentrations and twin fractions) were determined from thermodynamic databases, atom probe tomography, microstructural analysis and physical insights into the process.

3. The modelling allowed for the recovery of the creep rate with reasonable accuracy. The stress dependence was also partially captured and compared with experimental results. At this scale, the acquired mechanistic knowledge of the microtwinning process allowed for a better understanding of the deformation modes occurring in these materials.

4. A criterion for microtwin nucleation has been introduced. Studying the influence of stress and segregation/reordering on the nucleation of microtwins revealed the necessity for chemical diffusion if microtwinning is to occur.

This finding emphasises the crucial role of the composition on microtwin nucleation kinetics.

5. The results presented here suggest that the chemical changes confined locally at the faults associated with the high temperature time-dependent plasticity contributes significantly to drop the strength of the superalloys. This phenomenon – which changes the stress necessary for plastic deformation – needs to be accounted for in future theories for the high temperature time-dependent plasticity of these materials ($T > 700\,^{\circ}C$).

6 Continuum modelling of segregation assisted plasticity in Ni-based superalloys

6.1 Introduction

The complex behaviour of superalloys in the range of temperatures of interest (600-850°C) makes it challenging to predict their mechanical response and performance required for optimising the efficiency of component design. The diffusion processes studied in the previous chapters are at the source of relevant plastic events: anomalous yielding, an extensive anisotropy and a non-Schmidian tensile/compressive asymmetric behaviour [116, 117, 118]. Therefore, reliable models able to describe the different aspects of high temperature deformation, including the effect of the chemical diffusion processes, are of both theoretical and practical interests.

Despite the abundant amount of research on the mechanical behaviour of superalloys at high temperature under creep, only a few studies focus on chemical changes during plastic deformation. These studies are usually limited to experimental reports of their existence [52, 119, 67]. Paradoxically, these changes have been proven to be crucial in the creep strength of the alloy by eliminating the classical

strengthening mechanism of high-energy fault shearing of γ' precipitates [120, 53]. This consideration is especially important above 600°C where the diffusion processes during deformation become dominant. A chemical-mechanical bridge between physical modelling at the mechanistic lower scale of the previous chapter and the continuum modelling at the higher scale is thus needed.

The work presented in this chapter aims at filling this gap. A general continuum modelling framework for phase transformations is proposed. This model is developed for finite deformation within a thermodynamically consistent framework. The model was developed consistently with the experimental observations after creep presented in the previous chapters. It couples the mechanics of the phase transformation with changes in the chemical composition and, therefore, diffusion between phases (parent and transformed phases). The diffusion problem is then particularised for creep microtwinning plasticity in Ni-based superalloys. The diffusion phase transformation theory is derived from Chapter 5.

6.2 Continuum mechanics framework

As presented in the previous chapters, the plastic deformation of superalloys in the studied range of temperatures (mainly due to stacking faults and microtwinning) is intimately linked with chemical fluctuations. These chemical fluctuations are observed within the plastic regions, evolving through a transformation process resembling a diffusional phase transition. These findings differ from the old fashioned static view of plastic flow, in which the crystal general structure (i.e., crystal rotations from twinning is still considered though) and the composition remain unchanged during deformation and where the material response is only dependent on the density of plastic sources or dislocations.

In this work, the irreversible part of the total deformation is assumed to be the combination of:

- Standard plastic slip: the flow rule is decomposed into elemental shear slips over the different slip systems of the crystal. The atomic structure of the material remains unaltered after deformation, and so does its elastic behaviour. Two different slip systems are considered herein, consistent with previous works in the literature [36, 38]: {111} octahedral slip and {001} cubic slip.

- Phase transformation induced deformation: in a general case, this term can consist not only of shear deformations but also of dilatational contributions associated with the phase transformation. In terms of the material structure, it can either change its atomic ordering (martensitic transformations) or its orientation (twinning). Generally, these change the elastic resistance of the material. With regards to the specific case treated in this manuscript, segregation assisted microtwinning is considered as a diffusional phase transformation that produces a reorientation of the lattice and no dilatation.

The model is represented by the rheological scheme shown in Fig. 6.1. The different deformation mechanisms are represented by three nonlinear viscous dashpots capturing the rate dependency of each mechanism. In the following, we adopt subscripts and superscripts “pa” and “tr” to indicate parent phase and transformed phase of the body, respectively. The different slip and twinning systems are presented in Table 6.1.

Furthermore, we assume that the parts of the body undergoing a phase transformation deform only elastically once the transformation occurs. The Cauchy stress $\boldsymbol{\sigma}$ of the homogenized body is the sum of the two phase contributions, i.e. the parent

phase resistance $\boldsymbol{\sigma}_{\mathrm{pa}}$ and the transformed phase resistance $\boldsymbol{\sigma}_{\mathrm{tr}}$:

$$\boldsymbol{\sigma} = \boldsymbol{\sigma}_{\mathrm{pa}} + \boldsymbol{\sigma}_{\mathrm{tr}} \tag{6.1}$$

Both stress tensors are characterized by linear elastic springs in Fig. 6.1. Their corresponding micromechanical phase activators control the contribution of each phase to the total stiffness as the material undergoes the phase transformation.

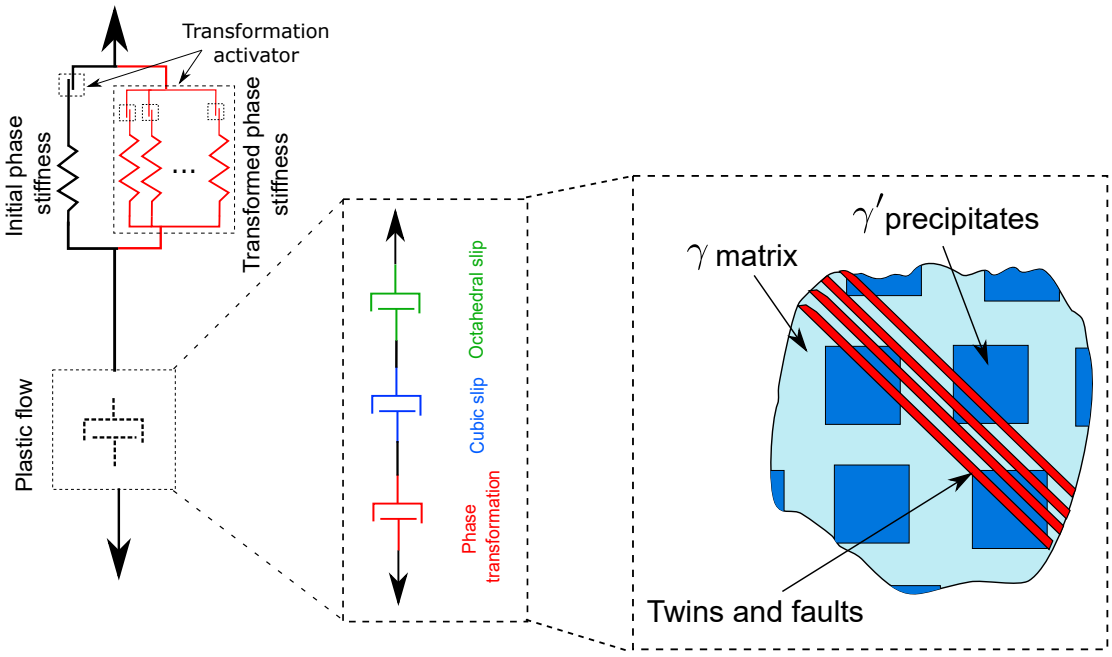

Figure 6.1 – Rheological scheme of the proposed constitutive model and microstructural diagram of a microtwinned structure for Ni-based superalloys.

The formation of stacking faults and microtwins has been observed to be triggered by local chemical changes [97, 53]. More specifically, the enrichment of Co and Cr in the new phase lower substantially its formation energy, and thus the required stress for the transformation. The dependence of the phase deformation resistance on the Co and Cr concentrations is included in the model through the definition of the free energy density of the new phase. This concentration is defined in the diffusion-assisted transformation problem. The solution to this diffusional problem

Table 6.1 – Slip and microtwin systems used in the crystal plasticity framework

Octahedral Slip	Cubic Slip	Microtwinning
$\pm(111)$-$[10\bar{1}]$	$\pm(001)$-$[110]$	$+(111)$-$[11\bar{2}]$
$\pm(111)$-$[1\bar{1}0]$	$\pm(001)$-$[1\bar{1}0]$	$+(111)$-$[1\bar{2}1]$
$\pm(111)$-$[0\bar{1}1]$	$\pm(100)$-$[0\bar{1}1]$	$+(111)$-$[\bar{2}11]$
$\pm(\bar{1}11)$-$[101]$	$\pm(100)$-$[011]$	$+(\bar{1}11)$-$[\bar{1}1\bar{2}]$
$\pm(\bar{1}11)$-$[110]$	$\pm(010)$-$[101]$	$+(\bar{1}11)$-$[\bar{1}2\bar{1}]$
$\pm(\bar{1}11)$-$[0\bar{1}1]$	$\pm(010)$-$[\bar{1}01]$	$+(\bar{1}11)$-$[211]$
$\pm(1\bar{1}1)$-$[10\bar{1}]$		$+(1\bar{1}1)$-$[1\bar{1}2]$
$\pm(1\bar{1}1)$-$[110]$		$+(1\bar{1}1)$-$[121]$
$\pm(1\bar{1}1)$-$[011]$		$+(1\bar{1}1)$-$[\bar{2}11]$
$\pm(11\bar{1})$-$[101]$		$+(11\bar{1})$-$[1\bar{2}1]$
$\pm(11\bar{1})$-$[1\bar{1}0]$		$+(11\bar{1})$-$[\bar{2}1\bar{1}]$
$\pm(11\bar{1})$-$[011]$		$+(11\bar{1})$-$[112]$

between both phases has been already presented in Chapter 5 and is used here within a continuum mechanics framework. In the present work, the heat terms are neglected as the body is assumed to deform under isothermal conditions. This assumption is consistent with the small heat produced by plastic deformation with respect to the thermal energy stored in the body at high temperatures. Heat terms can be incorporated trivially if needed.

It is noteworthy that the phase transformation theory described here can be also applied to other physical problems such as martensitic phase transitions in steels [121, 122] or growth problems in biological tissues [123, 124] where the material structure evolves with time and, therefore, the mechanical properties also change. In the next section, the kinematics, thermodynamics and constitutive details of the model are presented in detail.

6.2.1 Kinematics

Four configurations are considered to define the kinematics of the model, starting from an initial reference configuration Ω_0 to a final loaded or current configuration

Ω, see Fig. 6.2. Two intermediate configurations have been added to define the constitutive equations for the plastic mechanisms: slip plasticity and transformation plasticity. The first one is referred to as the intermediate transformed configuration $\overline{\Omega}$ in which only the phase transformation part of the deformation gradient tensor $\mathbf{F}^{\mathrm{p:tr}}$ is accounted for. The second one is referred to as the intermediate relaxed configuration $\overline{\overline{\Omega}}$ in which both phase transformation and slip shearing are considered. For an arbitrary material point $\mathbf{X}$ defined in the undeformed or reference configuration Ω_0, the current configuration Ω is reached through the mapping $\mathbf{x} = \varphi\{\mathbf{X}, t\}$, where φ is a mapping function and t is the time. The deformation gradient $\mathbf{F}$, velocity $\mathbf{v}$ and velocity gradient $\mathbf{l}$ tensor are derived as:

$$\begin{cases} \mathbf{F} = \nabla_{\mathbf{X}}\varphi \\ \mathbf{v} = \dot{\varphi} \\ \mathbf{l} = \nabla_x \mathbf{v} = \dot{\mathbf{F}}\mathbf{F}^{-1} \end{cases} \tag{6.2}$$

The total deformation gradient tensor $\mathbf{F}$ is multiplicatively decomposed into an elastic part $\mathbf{F}^{\mathrm{e}}$, which includes the crystal lattice distortion and local rigid rotations, and a plastic part $\mathbf{F}^{\mathrm{p}}$ [61]:

$$\mathbf{F} = \mathbf{F}^{\mathrm{e}}\mathbf{F}^{\mathrm{p}} = \mathbf{F}^{\mathrm{e}}\mathbf{F}^{\mathrm{p:s}}\mathbf{F}^{\mathrm{p:tr}} \tag{6.3}$$

The plastic deformation gradient tensor $\mathbf{F}^{\mathrm{p}}$ is decomposed into the contributions of the phase transformation $\mathbf{F}^{\mathrm{p:tr}}$ and the slip shearing $\mathbf{F}^{\mathrm{p:s}}$. The Jacobian associated with the slip shearing retains the unimodal property $J^{\mathrm{p:s}} = \det\{\mathbf{F}^{\mathrm{p:s}}\} = 1$, while a dilatational component $J^{\mathrm{p:tr}} = \det\{\mathbf{F}^{\mathrm{p:tr}}\} \neq 1$ can be expected in the case of the phase transformation.

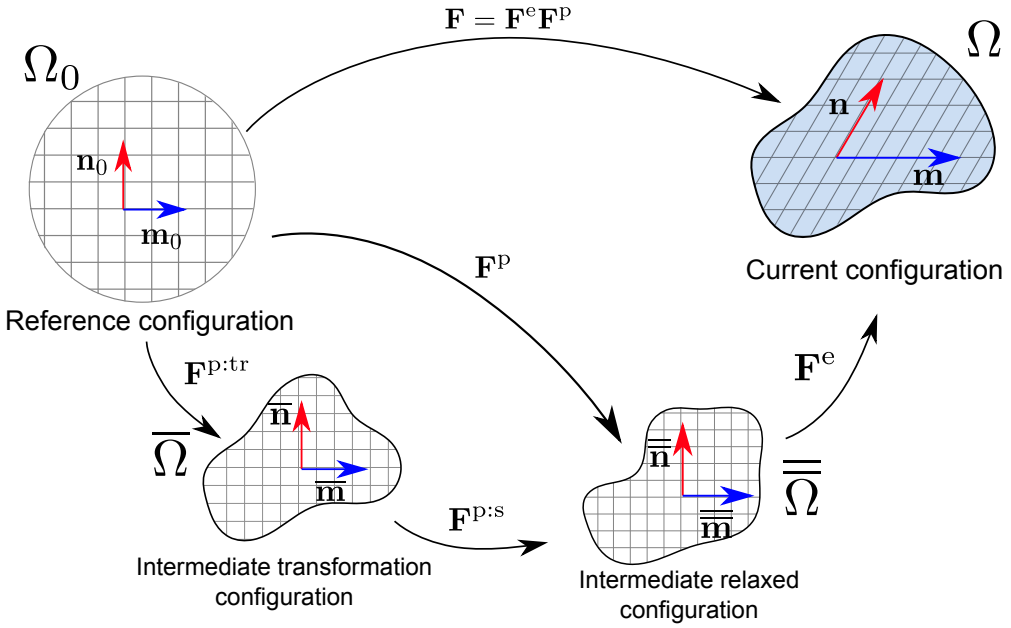

Figure 6.2 – Kinematics of the proposed model showing the reference or initial configuration Ω_0, the intermediate transformation configuration $\overline{\Omega}$, the intermediate relaxed configuration $\overline{\overline{\Omega}}$, and the current or loaded configuration Ω.

The velocity gradient of the unified branch can be obtained by time-differentiating Eq. (6.3) as (see Appendix A for more details):

$$\mathbf{l} = \dot{\mathbf{F}}\mathbf{F}^{-1} = \mathbf{l}^{e} + \mathbf{F}^{e}\overline{\overline{\mathbf{L}}}^{p:s}\mathbf{F}^{-e} + \mathbf{F}^{e}\overline{\overline{\mathbf{L}}}^{p:tr}\mathbf{F}^{-e} \tag{6.4}$$

where $\mathbf{l}^{e}$ is the elastic contribution to the velocity gradient in the current configuration Ω, $\overline{\overline{\mathbf{L}}}^{p:s}$ is the plastic component associated with standard slip and $\overline{\overline{\mathbf{L}}}^{p:tr}$ is the contribution of the irreversible phase transformation, both in the intermediate configuration $\overline{\overline{\Omega}}$:

$$\begin{cases} \mathbf{l}^{e} = \dot{\mathbf{F}}^{e}\mathbf{F}^{-e} \\ \overline{\overline{\mathbf{L}}}^{p:s} = \dot{\mathbf{F}}^{p:s}\mathbf{F}^{-p:s} \\ \overline{\overline{\mathbf{L}}}^{p:tr} = \mathbf{F}^{p:s}\dot{\mathbf{F}}^{p:tr}\mathbf{F}^{-p:tr}\mathbf{F}^{-p:s} \end{cases} \tag{6.5}$$

These velocity gradients can be broken down into their symmetric ($\mathbf{d}^{\mathrm{e}}$, $\overline{\overline{\mathbf{D}}}^{\mathrm{p:s}}$ and $\overline{\overline{\mathbf{D}}}^{\mathrm{p:tr}}$) and skew parts ($\mathbf{w}^{\mathrm{e}}$, $\overline{\overline{\mathbf{W}}}^{\mathrm{p:s}}$ and $\overline{\overline{\mathbf{W}}}^{\mathrm{p:tr}}$):

$$\begin{cases} \mathbf{l}^{\mathrm{e}} = \mathbf{d}^{\mathrm{e}} + \mathbf{w}^{\mathrm{e}} \\ \overline{\overline{\mathbf{L}}}^{\mathrm{p:s}} = \overline{\overline{\mathbf{D}}}^{\mathrm{p:s}} + \overline{\overline{\mathbf{W}}}^{\mathrm{p:s}} \\ \overline{\overline{\mathbf{L}}}^{\mathrm{p:tr}} = \overline{\overline{\mathbf{D}}}^{\mathrm{p:tr}} + \overline{\overline{\mathbf{W}}}^{\mathrm{p:tr}} \end{cases} \tag{6.6}$$

expressed in Ω_0 for the elastic terms and in $\overline{\overline{\Omega}}$ for the plastic terms.

6.2.2 Thermodynamics

In this section, the First and Second Principles of Thermodynamics are taken as the starting point in order to derive the thermomechanical forces for the different deformation modes (elastic, slip and phase transformation), the elastic response of each phase and to verify the thermodynamical consistency of the constitutive model developed herein. To this end, the Thermodynamic Principles and the free energy function ψ_0 are expressed in the reference configuration Ω_0, since the evolution of the transformed phase is tracked in this configuration. However, the plastic terms are expressed in the dilated configuration $\overline{\overline{\Omega}}$ where the flow rules are usually defined [125]. The reduced global form of energy balance expressed in Ω is postulated as [34]

$$\frac{\mathrm{d}}{\mathrm{d}t}\int_{\Omega} e\,\mathrm{d}V = \int_{\Omega}(\boldsymbol{\sigma} : \mathbf{d} - \nabla_{\mathbf{x}}\,\mathbf{q} + r)\,\mathrm{d}V \tag{6.7}$$

where e is the specific internal energy per unit volume, $\boldsymbol{\sigma} : \mathbf{d}$ is the stress power per unit volume, $\mathbf{q}$ is the heat flow into the body per unit area and r is the internal heat production, i.e. chemical reactions or radiation, all of these being defined in the current configuration Ω. This energy balance can be rewritten in the reference

configuration using $\mathrm{d}V = J\mathrm{d}V_0$ as:

$$\int_{\Omega_0} \dot{e}_0 \, \mathrm{d}V_0 = \int_{\Omega_0} (\boldsymbol{\sigma} : \mathbf{d} - \nabla_{\mathbf{x}} \mathbf{q} + r) J \, \mathrm{d}V_0 \tag{6.8}$$

where $\dot{e}_0$ is the rate of specific internal energy e_0 per unit reference volume.

The stress power $\boldsymbol{\sigma} : \mathbf{d}$ can be additionally decomposed into the elastic and plastic contributions by using Eq. (6.4):

$$\boldsymbol{\sigma} : \mathbf{d} = \boldsymbol{\sigma} : \mathbf{l}^{\mathrm{e}} + \boldsymbol{\sigma} : \mathbf{F}^{\mathrm{e}} \overline{\overline{\mathbf{L}}}^{\mathrm{p:tr}} \mathbf{F}^{-\mathrm{e}} + \boldsymbol{\sigma} : \mathbf{F}^{\mathrm{e}} \overline{\overline{\mathbf{L}}}^{\mathrm{p:s}} \mathbf{F}^{-\mathrm{e}} \tag{6.9}$$

The first term stands for the elastic power; the second term is the contribution of the transformation deformation; and the last term is the standard plastic contribution. Rearranging and expressing each term in its relevant configuration (dilated configuration $\overline{\overline{\Omega}}$ for slip and phase transformation terms and current configuration Ω for elastic terms), Eq. (6.9) can be expressed as (see Appendix A for more details):

$$\boldsymbol{\sigma} : \mathbf{d} = J^{-\mathrm{e}} \Big(\overline{\overline{\mathbf{M}}} : \overline{\overline{\mathbf{L}}}^{\mathrm{p:s}} + \overline{\overline{\mathbf{M}}} : \overline{\overline{\mathbf{L}}}^{\mathrm{p:tr}} \Big) + J^{-1} \Big(\mathbf{S}_0 : \mathbf{F}^T \mathbf{d}^{\mathrm{e}} \mathbf{F} \Big) \tag{6.10}$$

where $\mathbf{S}_0 = J\mathbf{F}^{-1}\boldsymbol{\sigma}\mathbf{F}^{-T}$ is the second Piola-Kirchhoff stress of the homogenized system resistance (parent + transformed phase) in the reference configuration, and $\overline{\overline{\mathbf{M}}} = \mathbf{F}^{\mathrm{e}T}\mathbf{F}^{\mathrm{e}}\overline{\overline{\mathbf{S}}}$ is the Mandel stress tensor in $\overline{\overline{\Omega}}$, with $\overline{\overline{\mathbf{S}}} = J^{\mathrm{e}}\mathbf{F}^{\mathrm{e}-1}\boldsymbol{\sigma}\mathbf{F}^{\mathrm{e}-T}$ being the second Piola-Kirchhoff stress in $\overline{\overline{\Omega}}$.

The First Principle of Thermodynamics can be expressed in its local form in Ω_0 by

substituting Eq. (6.10) into Eq. (6.8):

$$\dot{e}_0 = \left(\overline{\overline{\mathbf{M}}} : \overline{\overline{\mathbf{L}}}^{\mathrm{p:s}} + \overline{\overline{\mathbf{M}}} : \overline{\overline{\mathbf{L}}}^{\mathrm{p:tr}}\right) J^{\mathrm{p}} + \mathbf{S}_0 : \mathbf{F}^T \mathbf{d}^{\mathrm{e}} \mathbf{F} \tag{6.11}$$

Note that heating effects are neglected assuming constant and uniform temperature T within the body.

The Second Principle of Thermodynamics reads:

$$\frac{\mathrm{d}}{\mathrm{d}t} \int_\Omega \eta \, \mathrm{d}V + \int_\Omega \nabla_{\mathbf{x}} \frac{\mathbf{q}}{T} - \frac{r}{T} \, \mathrm{d}V \geq 0 \tag{6.12}$$

where η is the specific internal entropy per unit of deformed volume. In a similar way to the first Principle, the second Principle can be expressed in the reference configuration Ω_0 in its local form as:

$$\dot{\eta}_0 \geq 0 \tag{6.13}$$

As in the first Principle, the heating effects are also neglected here.

The specific internal entropy η_0 and the specific internal energy e_0 are both linked by the definition of the Helmholtz specific free energy $\psi_0 = e_o - T\eta_0$, where T is the absolute temperature.

The combination of the First and the Second Principles of Thermodynamics (Eqs. (6.11) and (6.13)) along with the free energy rate $\dot{\psi}_0 = \dot{e}_o - \dot{T}\eta_0 - T\dot{\eta}_0$ leads to the following expression of the Clausius-Duhem inequality (assuming constant temperature):

$$-\dot{\psi}_0 + J^{\mathrm{p}}\left(\overline{\overline{\mathbf{M}}} : \overline{\overline{\mathbf{L}}}^{\mathrm{p:s}} + \overline{\overline{\mathbf{M}}} : \overline{\overline{\mathbf{L}}}^{\mathrm{p:tr}}\right) + \mathbf{S}_0 : \mathbf{F}^T \mathbf{d}^{\mathrm{e}} \mathbf{F} \geq 0 \tag{6.14}$$

where the left-hand side term represents the dissipation rate per unit reference volume.

The Helmholtz free energy function of the homogenized material ψ_0 is assumed to be the combination of the contribution associated with the parent domain ψ_0^{pa} and the transformed domain ψ_0^{tr}:

$$\psi_0 = (1 - f_0)\psi_0^{\mathrm{pa}} + f_0\psi_0^{\mathrm{tr}} \tag{6.15}$$

where f_0 is the volume fraction of material that has undergone the phase transformation in the reference configuration Ω_0 and corresponds to the joint addition of the contributions of all the phase transformation systems or twin systems $f_0 = \sum_\beta f_{0:\beta}$. The free energy function $\psi_0^i\{\mathbf{C}^{\mathrm{e}}, c_i\}$ for each phase i is assumed to be a function of the elastic right Cauchy-Green tensor $\mathbf{C}^{\mathrm{e}} = \mathbf{F}^{\mathrm{e}\,T}\mathbf{F}^{\mathrm{e}}$ and the mass concentration of the studied elements (Co and Cr) in each phase, c_{pa} and c_{tr}. These are defined as mass of solute per total mass ($c_{\mathrm{sol}} = \frac{m_{\mathrm{sol}}}{m_{\mathrm{tot}}}$). Please note that $c_{\mathrm{pa}} = c_{\mathrm{pa}-\infty}$ from Chapter 5. The total mass of these solute elements within both phases reads:

$$m_{\mathrm{Co+Cr}} = V_0\Big((1 - f_0)\rho_{0:\mathrm{pa}}\, c_{\mathrm{pa}} + f_0\rho_{0:\mathrm{tr}}\, c_{\mathrm{tr}}\Big) \tag{6.16}$$

Supported by experimental observations [97, 4, 53], the concentration differences are small enough (1% to 2%) to assume that the density of both phases is approximately the same in the reference configuration ($\rho_{0:\mathrm{pa}} \approx \rho_{0:\mathrm{tr}}$). Taking this into account, time deriving Eq. (6.16) and assuming mass conservation of the diffusive species ($\dot{m}_{\mathrm{Co+Cr}} = 0$), one reaches:

$$(1 - f_0)\dot{c}_{\mathrm{pa}} = -f_0\dot{c}_{\mathrm{tr}} - \dot{f}_0(c_{\mathrm{tr}} - c_{\mathrm{pa}}) \tag{6.17}$$

The time derivative of ψ_0 defined in Eq.(6.15) combined with Eq. (6.17) then reads

$$\dot{\psi}_0 = \left[(1-f_0)\frac{\partial \psi_0^{\mathrm{pa}}}{\partial \mathbf{C}^{\mathrm{e}}} + f_0 \frac{\partial \psi_0^{\mathrm{tr}}}{\partial \mathbf{C}^{\mathrm{e}}}\right] : \dot{\mathbf{C}}^{\mathrm{e}} - \psi_0^{\mathrm{pa}}\dot{f}_0 + \psi_0^{\mathrm{tr}}\dot{f}_0 + f_0\frac{\partial \psi_0^{\mathrm{tr}}}{\partial c_{\mathrm{tr}}}\dot{c}_{\mathrm{tr}} - f_0\frac{\partial \psi_0^{\mathrm{pa}}}{\partial c_{\mathrm{pa}}}\dot{c}_{\mathrm{tr}} - \dot{f}_0(c_{\mathrm{tr}} - c_{\mathrm{pa}})\frac{\partial \psi_0^{\mathrm{pa}}}{\partial c_{\mathrm{pa}}} \quad (6.18)$$

Substituting the definition of the right Cauchy-Green deformation tensor $\mathbf{C}^{\mathrm{e}}$ and rearranging, the term $\frac{\partial \psi_0^i}{\partial \mathbf{C}^{\mathrm{e}}} : \dot{\mathbf{C}}^{\mathrm{e}}$ (where i stands for the parent phase or the transformed phase) can be rewritten as:

$$\frac{\partial \psi_0^i}{\partial \mathbf{C}^{\mathrm{e}}} : \dot{\mathbf{C}}^{\mathrm{e}} = 2\frac{\partial \psi_0^i}{\partial \mathbf{C}^{\mathrm{e}}} : \mathbf{F}^{\mathrm{e}\,T}\mathbf{d}^{\mathrm{e}}\mathbf{F}^{\mathrm{e}} \quad (6.19)$$

Introducing this in Eq. (6.18) and substituting this expression for $\dot{\psi}_0$ into Eq. (6.14), the Clausius-Duhem inequality reads

$$\underbrace{\left(\mathbf{F}^{\mathrm{p}}\mathbf{S}_0\mathbf{F}^{\mathrm{p}T} - 2\left[(1-f_0)\frac{\partial \psi_0^{\mathrm{pa}}}{\partial \mathbf{C}^{\mathrm{e}}} + f_0\frac{\partial \psi_0^{\mathrm{tr}}}{\partial \mathbf{C}^{\mathrm{e}}}\right]\right) : \mathbf{F}^{\mathrm{e}T}\mathbf{d}^{\mathrm{e}}\mathbf{F}^{\mathrm{e}}}_{\text{elastic}} + \underbrace{J^{\mathrm{p}}\left(\overline{\overline{\mathbf{M}}} : \overline{\overline{\mathbf{L}}}^{\mathrm{p:s}}\right)}_{\text{slip}}$$
$$+ \underbrace{J^{\mathrm{p}}\left(\overline{\overline{\mathbf{M}}} : \overline{\overline{\mathbf{L}}}^{\mathrm{p:tr}}\right) + \left(\psi_0^{\mathrm{pa}} - \psi_0^{\mathrm{tr}} + (c_{\mathrm{tr}} - c_{\mathrm{pa}})\frac{\partial \psi_0^{\mathrm{pa}}}{\partial c_{\mathrm{pa}}}\right)\dot{f}_0}_{\text{transformation}} + \underbrace{f_0\left(\frac{\partial \psi_0^{\mathrm{pa}}}{\partial c_{\mathrm{pa}}} - \frac{\partial \psi_0^{\mathrm{tr}}}{\partial c_{\mathrm{tr}}}\right)\dot{c}_{\mathrm{tr}}}_{\text{diffusion}} \geq 0 \quad (6.20)$$

Here, the transformation term $(c_{\mathrm{tr}} - c_{\mathrm{pa}})\frac{\partial \psi_0^{\mathrm{pa}}}{\partial c_{\mathrm{pa}}}$ is small compared to the other high energy transformation terms if the parent phase does not contain any high energy defect or is near equilibrium ($(c_{\mathrm{tr}} - c_{\mathrm{pa}})\frac{\partial \psi_0^{\mathrm{pa}}}{\partial c_{\mathrm{pa}}} \ll \psi_0^{\mathrm{pa}} - \psi_0^{\mathrm{tr}}$). This assumption is valid for the present work and, therefore, the transformation term can be omitted:

$$\underbrace{\left(\mathbf{F}^{\mathrm{p}}\mathbf{S}_0\mathbf{F}^{\mathrm{p}T} - 2\left[(1-f_0)\frac{\partial\psi_0^{\mathrm{pa}}}{\partial\mathbf{C}^{\mathrm{e}}} + f_0\frac{\partial\psi_0^{\mathrm{tr}}}{\partial\mathbf{C}^{\mathrm{e}}}\right]\right) : \mathbf{F}^{\mathrm{e}T}\mathbf{d}^{\mathrm{e}}\mathbf{F}^{\mathrm{e}}}_{\text{elastic}} + \underbrace{J^{\mathrm{p}}\left(\overline{\overline{\mathbf{M}}} : \overline{\overline{\mathbf{L}}}^{\mathrm{p:s}}\right)}_{\text{slip}}$$
$$+ \underbrace{J^{\mathrm{p}}\left(\overline{\overline{\mathbf{M}}} : \overline{\overline{\mathbf{L}}}^{\mathrm{p:tr}}\right) + (\psi_0^{\mathrm{pa}} - \psi_0^{\mathrm{tr}})\dot{f}_0}_{\text{transformation}} + \underbrace{f_0\left(\frac{\partial\psi_0^{\mathrm{pa}}}{\partial c_{\mathrm{pa}}} - \frac{\partial\psi_0^{\mathrm{tr}}}{\partial c_{\mathrm{tr}}}\right)\dot{c}_{\mathrm{tr}}}_{\text{diffusion}} \geq 0 \quad (6.21)$$

The Coleman and Noll method [126] establishes that the fundamental inequality presented in Eq. (6.21) must be satisfied for every admissible thermodynamic process. Accordingly, the elastic term must be equal to zero for any $\mathbf{F}^{\mathrm{e}T}\mathbf{d}^{\mathrm{e}}\mathbf{F}^{\mathrm{e}}$, leading to the constitutive equation:

$$\overline{\overline{\mathbf{S}}} = 2J^{p-1}\left[(1-f_0)\frac{\partial\psi_0^{\mathrm{pa}}}{\partial\mathbf{C}^{\mathrm{e}}} + f_0\frac{\partial\psi_0^{\mathrm{tr}}}{\partial\mathbf{C}^{\mathrm{e}}}\right] \quad (6.22)$$

Introducing this expression into Eq. (6.21) reduces the Clausius-Duhem inequality to:

$$\underbrace{J^{\mathrm{p}}\left(\overline{\overline{\mathbf{M}}} : \overline{\overline{\mathbf{L}}}^{\mathrm{p:s}}\right)}_{\text{slip}} + \underbrace{J^{\mathrm{p}}\left(\overline{\overline{\mathbf{M}}} : \overline{\overline{\mathbf{L}}}^{\mathrm{p:tr}}\right) + (\psi_0^{\mathrm{pa}} - \psi_0^{\mathrm{tr}})\dot{f}_0}_{\text{transformation}} + \underbrace{f_0\left(\frac{\partial\psi_0^{\mathrm{pa}}}{\partial c_{\mathrm{pa}}} - \frac{\partial\psi_0^{\mathrm{tr}}}{\partial c_{\mathrm{tr}}}\right)\dot{c}_{\mathrm{tr}}}_{\text{diffusion}} \geq 0 \quad (6.23)$$

where, as stated by the Second Principle of Thermodynamics, the left-hand side of this equation represents the rate of internal entropy production $\dot{\eta}_0$ and is equal to the dissipation rate per unit reference volume $\dot{\mathcal{D}}$. The first term in Eq. (6.23) is the dissipation associated with the plastic deformation due to slip, the second term comes from the dissipation produced by the plastic transformation and the third term is the dissipation associated to the concentration change of the body driven by the diffusion between phases.

6.2.3 Constitutive model

6.2.3.1 Elastic behaviour

The Helmholtz free energy of each phase i is assumed to be additively decomposed into a mechanical term $\psi^i_{0:\text{mech}}\{\mathbf{E}^\text{e}\}$ dependent only on the elastic strain $\mathbf{E}^\text{e}$ and a chemical term $\psi_{0:\text{chem}}\{c_i\}$ dependent on the concentration of Co+Cr in each phase:

$$\psi^i_0 = \psi^i_{0:\text{mech}}\{\mathbf{E}^\text{e}\} + \psi^i_{0:\text{chem}}\{c_i\} \tag{6.24}$$

Deformation in metals usually leads to infinitesimal elastic strains and the mechanical part of the elastic strain energy can be defined as a quadratic function of the elastic strain:

$$\psi^i_{0:\text{mech}} = \frac{1}{2}\mathbb{C}_i :: (\mathbf{E}^\text{e} \otimes \mathbf{E}^\text{e}) \tag{6.25}$$

where $\mathbb{C}_i$ represents the fourth-order elasticity tensor of phase i and $\mathbf{E}^\text{e} = \frac{1}{2}(\mathbf{C}^\text{e} - \mathbf{I})$ is the Green-Lagrange elastic strain. Using this expression in Eq. (6.22), the second Piola-Kirchhoff stress tensor reads:

$$\overline{\overline{\mathbf{S}}} = J^{p-1}\Big[(1-f_0)\mathbb{C}_\text{pa} + f_0\,\mathbb{C}_\text{tr}\Big] : \mathbf{E}^\text{e} \tag{6.26}$$

The fourth-order matrix elasticity tensor $\mathbb{C}_i$ can be formulated in crystal principal axes as:

$$\mathbb{C}_\text{pa} = \mathbf{R}_{\text{crys}\to\Omega_0}\mathbf{R}_{\text{crys}\to\Omega_0}\,\mathbb{C}_\text{crys}\,\mathbf{R}^T_{\text{crys}\to\Omega_0}\mathbf{R}^T_{\text{crys}\to\Omega_0} \tag{6.27}$$

where $\mathbb{C}_\text{crys}$ is the stiffness matrix in the principal crystal axes and $\mathbf{R}_{\text{crys}\to\Omega_0}$ is the rotation matrix between the principal crystal configuration and the reference

configuration. $\mathbb{C}_{\text{tr}}$ is related to $\mathbb{C}_{\text{crys}}$ by:

$$\mathbb{C}_{\text{tr}} = \mathbf{R}_{\text{crys}\to\Omega_0}\mathbf{R}_{\text{crys}\to\Omega_0}\mathbf{R}_{\text{twin}}\mathbf{R}_{\text{twin}}\mathbb{C}_{\text{crys}}\mathbf{R}^T_{\text{twin}}\mathbf{R}^T_{\text{twin}}\mathbf{R}^T_{\text{crys}\to\Omega_0}\mathbf{R}^T_{\text{crys}\to\Omega_0} \tag{6.28}$$

where $\mathbf{R}_{\text{twin}}$ represents the transformation matrix between the lattice orientation in the matrix and the lattice orientation in the twinned region. The rotation matrix $\mathbf{R}_{\text{twin}}$ is defined for the case of compound type twins in FCC by [56]:

$$\mathbf{R}_{\text{twin}} = 2(\overline{\overline{\mathbf{m}}}_\beta \otimes \overline{\overline{\mathbf{m}}}_\beta) - \mathbf{I} \tag{6.29}$$

where $\overline{\overline{\mathbf{m}}}_\beta$ represents the glide direction of the twin system β in the relaxed configuration $\overline{\overline{\Omega}}$.

The free energy for stacking faults in metals is usually expressed in terms of the stacking fault energy γ_{SF} defined as [105]:

$$\gamma_{\text{SF}} = \frac{\partial \Psi}{\partial A_{\text{f}}} = h_{\text{t}}\left(\psi^{\text{tr}}_{0:\text{chem}} - \psi^{\text{pa}}_{0:\text{chem}}\right) \tag{6.30}$$

where Ψ is the extensive free energy, A_{f} is the area of fault and h_{t} the height of an individual fault or twin ledge.

Finally, the stacking fault energy γ_{SF} of the new phase needs to be defined as a function of its concentration and therefore, of its growth rate. For this purpose, the model presented in Chapter 5 is used here. As a summary, the growth velocity of the fault ledge is obtained by solving locally the diffusion problem in its surrounding with the concentration of the fault as a boundary condition. The energy profile considered in this work for the growing fault as a function of the Co+Cr concentration c is presented in Fig. 6.3a. The fault concentration profile as

a function of the fault growing rate is presented in Fig. 6.3b. This profile is obtained by solving the diffusion model in Chapter 4 for different fault concentrations.

Here, three different scenarios can be identified from Fig. 6.3a-b. First, when the strain rates are high compared to the characteristic diffusion rate of the problem, the chemical problem can be considered as static and, therefore, the new phase is growing with the same concentration as the parent phase. This implies that the fault is growing unsegregated with a high stacking fault energy corresponding to a complex stacking fault ($\gamma_{\mathrm{SF}} = \gamma_{\mathrm{2xCISF}} = 354\,\mathrm{mJ/m^2}$ [76]). This is indicated as scenario A in Fig. 6.3a-b. The concentration threshold for scenario A is considered to be the parent concentration experimentally found by APT for MD2 in the previous chapter. On the other hand, if the phase transformation occurs slowly enough, the fault can be considered to be in fully segregated equilibrium, therefore, with a low energy corresponding to a standard SESF ($\gamma_{\mathrm{SF}} = \gamma_{\mathrm{SESF}} = 74\,\mathrm{mJ/m^2}$ [76]). This is indicated as scenario C in Fig. 6.3a-b. The concentration threshold for scenario C is assumed to be the fault concentration found in the previous

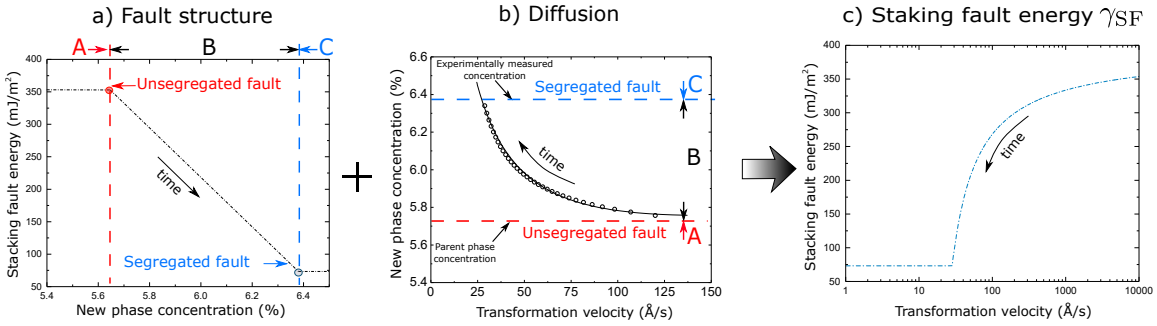

Figure 6.3 – a) Fault concentration of the new phase c_{tr} as a function of the transformation velocity v_{tr} obtained from the diffusion model of Barba et al. [51]. Points are the exact solution for the diffusion problem; b) stacking fault energy $\gamma_{\mathbf{SF}}$ as a function fo the concentration of the new phase. Energies for the perfect CSF (unsegregated fault) and SESF (segregated fault) are obtained from Voronstov et al. [76]; c) the combination of the functions presented in a) and b) leads to the stacking fault energy for the phase transformation problem vs. its fault growth rate.

chapter by APT. Between these two extreme cases, the growing fault is partially in equilibrium and the staking fault energy is assumed to follow a linear relation with the Co+Cr concentration of the fault as indicated in scenario B [76]. Bringing together both functions in Fig. 6.3a-b leads to the definition of the new phase staking fault energy depending on the fault lengthening rate, see Fig. 6.3c.

6.2.3.2 Plastic relations

Plastic slip flow

From the kinematics of dislocation motion, the plastic velocity gradient $\overline{\overline{\mathbf{L}}}^{\mathrm{p:s}}$ is of the form [127]:

$$\overline{\overline{\mathbf{L}}}^{\mathrm{p:s}} = \sum_{\alpha} \dot{\gamma}_{\alpha} \overline{\overline{\mathbf{m}}}_{\alpha} \otimes \overline{\overline{\mathbf{n}}}_{\alpha} \tag{6.31}$$

where $\dot{\gamma}_{\alpha}$ is the shear rate of the slip system α and $\overline{\overline{\mathbf{n}}}_{\alpha}$ is the corresponding slip plane normal defined in the relaxed configuration $\overline{\overline{\Omega}}$ ($\overline{\overline{\mathbf{m}}}_{\alpha}$ is the same as in Eq. (6.29)).

The plastic flow described in (6.31) is defined by the plastic multiplier $\dot{\gamma}_{\alpha}$. The evolution of the plastic multipliers is governed by the conjugate thermodynamic forces for each mechanism which can be identified from the expression of the mechanical dissipation sources in Eq. (6.23). The driving force for slip shearing per unit of volume in the intermediate configuration $\overline{\overline{\Omega}}$ can be rewritten as:

$$\dot{\overline{\overline{\mathcal{D}}}}_{\mathrm{slip}} = \overline{\overline{\mathbf{M}}} : \overline{\overline{\mathbf{L}}}^{\mathrm{p:s}} = \sum_{\alpha} \overline{\overline{\mathbf{M}}} : (\overline{\overline{\mathbf{m}}}_{\alpha} \otimes \overline{\overline{\mathbf{n}}}_{\alpha}) \dot{\gamma}_{\alpha} = \sum_{\alpha} \tau_{\alpha} \dot{\gamma}_{\alpha} \tag{6.32}$$

where $\tau_{\alpha} = \overline{\overline{\mathbf{M}}} : (\overline{\overline{\mathbf{m}}}_{\alpha} \otimes \overline{\overline{\mathbf{n}}}_{\alpha})$ is the slip resolved shear stress on slip system α and corresponds to the driving force for slip shearing.

The evolution of the plastic multiplier $\dot{\gamma}_{\alpha}$ can be described by viscous flow rules

dependent on the conjugate thermodynamic force τ_α. While more complex relationships exist, e.g. [128], they can be linked through a simple power-law [129, 130]:

$$\dot{\gamma}_\alpha = \dot{\gamma}_0 \left(\frac{\tau_\alpha}{s_\alpha} \right)^{1/m_\alpha} \tag{6.33}$$

where $\frac{1}{m_\alpha} \approx \frac{Q_{\text{act}}}{k_B T}$, with k_B as the Boltzmann constant, T is the absolute temperature and Q_{act} is the activation energy of the deformation mechanism. Non-explicit yielding is considered in this model. If $\tau_\alpha > 0$, the material is always plastically deforming along the slip plane following the positive direction of τ_α. This approach has been used successfully before in other creep models [131, 132, 133].

Phase transformation flow

Extending the same approach to the phase transformation, $\mathbf{F}^{\text{p:tr}}$ accounts for two contributions associated with each phase transformation system β:

- Shear strain γ_{tr} that follows a slip direction $\overline{\overline{\mathbf{m}}}_\beta$ and is associated with the Schmid tensor $\overline{\overline{\mathbf{m}}}_\beta \otimes \overline{\overline{\mathbf{n}}}_\beta$, where $\overline{\overline{\mathbf{n}}}_\beta$ is the corresponding transformation plane normal.

- Volumetric strain $\delta_{\text{tr}:\beta} = J^{\text{tr}} - 1$ where $J^{\text{tr}} = \det\{\mathbf{F}^{\text{tr}}\}$. This transformation can be expressed as a function of a unit-modulus tensor $\mathbf{F}_{\Delta V}$ that determines the volumetric part of the phase transformation gradient and is escalated by the volumetric multiplier $\delta_{\text{tr}:\beta}$.

The transformation velocity gradient then reads [134]:

$$\overline{\overline{\mathbf{L}}}^{\text{p:tr}} = \sum_\beta \dot{f}_{0:\beta} \Big[(\gamma_{\text{tr}} (\overline{\overline{\mathbf{m}}}_\beta \otimes \overline{\overline{\mathbf{n}}}_\beta) + \delta_{\text{tr}:\beta} \mathbf{F}_{\Delta V} \Big] \tag{6.34}$$

where $\dot{f}_{0:\beta}$ is the fraction rate of transformed phase β.

For the case of microtwins and stacking faults in superalloys, where the transformation consists of a simple shear, the dilatational term is negligible ($\delta_{\mathrm{tr}:\beta} = J^{\mathrm{tr}} - 1 = J^{\mathrm{p}} - 1 = 0$) and, therefore, $\dot{f}_{\beta} = \dot{f}_{0:\beta}$ is assumed from this point onwards [4, 9]. Thus, the velocity gradient $\overline{\overline{\mathbf{L}}}^{\mathrm{p:tr}}$ reduces to:

$$\overline{\overline{\mathbf{L}}}^{\mathrm{p:tr}} = \sum_{\beta} \dot{\gamma}_{\beta} (\overline{\overline{\mathbf{m}}}_{\beta} \otimes \overline{\overline{\mathbf{n}}}_{\beta}) \tag{6.35}$$

where the plastic multiplier $\dot{\gamma}_{\beta}$ is related to the transformation fraction rate $\dot{f}_{0:\beta}$ by:

$$\dot{\gamma}_{\beta} = \dot{f}_{0:\beta} \gamma_{\mathrm{tr}} \tag{6.36}$$

Similar to slip, the driving force for phase transformation per unit volume in the intermediate configuration $\overline{\overline{\Omega}}$ can be extracted from the dissipation rate:

$$\begin{aligned} &\dot{\overline{\overline{\mathcal{D}}}}_{\mathrm{transformation}} = \overline{\overline{\mathbf{M}}} : \overline{\overline{\mathbf{L}}}^{\mathrm{p:tr}} + J^{-\mathrm{p}} (\psi_0^{\mathrm{pa}} - \psi_0^{\mathrm{tr}}) \dot{f}_0 = \\ &\sum_{\beta} \left[\overline{\overline{\mathbf{M}}} : (\overline{\overline{\mathbf{m}}}_{\beta} \otimes \overline{\overline{\mathbf{n}}}_{\beta}) \, \gamma_{\mathrm{tr}} + J^{-\mathrm{p}} (\psi_0^{\mathrm{pa}} - \psi_0^{\mathrm{tr}}) \right] \dot{f}_{0:\beta} = \sum_{\beta} \left[\tau_{\beta} + J^{-\mathrm{p}} \frac{\psi_0^{\mathrm{pa}} - \psi_0^{\mathrm{tr}}}{\gamma_{\mathrm{tr}:\beta}} \right] \dot{\gamma}_{\beta} \end{aligned} \tag{6.37}$$

where $\tau_{\beta} = \overline{\overline{\mathbf{M}}} : (\overline{\overline{\mathbf{m}}}_{\beta} \otimes \overline{\overline{\mathbf{n}}}_{\beta})$ is the phase transformation resolved shear stress of the phase transformation system β. The driving force for phase transformation assuming plastic isochoricity ($J^{\mathrm{p}} = 1$) is then defined as $\tau_{\beta} + \frac{\psi_0^{\mathrm{pa}} - \psi_0^{\mathrm{tr}}}{\gamma_{\mathrm{tr}}}$. Making use of the free energy split into elastic $\psi_{0:\mathrm{mech}}$ and chemical contributions $\psi_{0:\mathrm{chem}}$, we can express this driving force in terms of the elastic strain $\mathbf{E}^{\mathrm{e}}$ and the stacking fault energy Γ_{SF} from Eqs. (6.30), (6.24) and (6.25) as:

$$\tau_{\beta} + \frac{\psi_0^{\mathrm{pa}} - \psi_0^{\mathrm{tr}}}{\gamma_{\mathrm{tr}}} = \tau_{\beta} - \frac{\Gamma_{\mathrm{SF}:\beta}}{\gamma_{\mathrm{tr}} \, h_{\mathrm{t}}} - \frac{1}{2 \, \gamma_{\mathrm{tr}}} \Big(\mathbb{C}_{\mathrm{tr}} - \mathbb{C}_{\mathrm{pa}} \Big) :: (\mathbf{E}^{\mathrm{e}} \otimes \mathbf{E}^{\mathrm{e}}) \tag{6.38}$$

Following the procedure introduced by Mareau et al. [130] for magnesium and Meric et al. [129] for FCC materials, this driving force can be introduced in the numerator term of the power law in Eq. (6.33). The flow rule for the plastic multiplier $\dot{\gamma}_\beta$ follows

$$\begin{cases} \dot{\gamma}_\beta = \dot{\gamma}_0 \left(\dfrac{\tau_\beta - \frac{\Gamma_{\mathrm{SF}:\beta}}{\gamma_{\mathrm{tr}}\, h_{\mathrm{t}}} - \frac{1}{2\,\gamma_{\mathrm{tr}}} \Big(\mathbb{C}_{\mathrm{tr}} - \mathbb{C}_{\mathrm{pa}} \Big) :: (\mathbf{E}^{\mathrm{e}} \otimes \mathbf{E}^{\mathrm{e}})}{s_\beta} \right)^{1/m_\beta}, \\ \qquad\qquad \text{if } \tau_\beta - \dfrac{\Gamma_{\mathrm{SF}:\beta}}{\gamma_{\mathrm{tr}}\, h_{\mathrm{t}}} - \dfrac{1}{2\,\gamma_{\mathrm{tr}}} \Big(\mathbb{C}_{\mathrm{tr}} - \mathbb{C}_{\mathrm{pa}} \Big) :: (\mathbf{E}^{\mathrm{e}} \otimes \mathbf{E}^{\mathrm{e}}) > 0 \\ \dot{\gamma}_\beta = 0, \\ \qquad\qquad \text{if } \tau_\beta - \dfrac{\Gamma_{\mathrm{SF}:\beta}}{\gamma_{\mathrm{tr}}\, h_{\mathrm{t}}} - \dfrac{1}{2\,\gamma_{\mathrm{tr}}} \Big(\mathbb{C}_{\mathrm{tr}} - \mathbb{C}_{\mathrm{pa}} \Big) :: (\mathbf{E}^{\mathrm{e}} \otimes \mathbf{E}^{\mathrm{e}}) \leq 0 \end{cases} \tag{6.39}$$

where m_β is the rate dependency coefficient defined as in the slip case. The plastic flow rule associated with the phase transformation is assumed to be unidirectional. Indeed, as detwinning is unlikely to happen under uniaxial loading conditions, it is not considered in this work, as done elsewhere [135, 136].

Hardening laws

The strain hardening of the viscous resistance parameters $\dot{s}_i$ for each slip/twin system i is defined by the generalized rate equation:

$$\dot{s}_i = \sum_j h_{ij} \dot{\gamma}_j \tag{6.40}$$

where h_{ij} are the hardening moduli. The sum ranges over all the deformation mechanisms (slip+twin). The hardening moduli evolution is defined as [137]:

$$h_{ij} = (q + (1-q)\,\delta_{ij})\, h_0\, \mathrm{sech}^2 \left\{ \frac{h_0\, \gamma_i}{s_s - s_0} \right\} \left(1 + \sum_{i \neq j} f_{ij} \tanh\{\gamma_j / \gamma_0\} \right) \tag{6.41}$$

where q is the cross hardening parameter, δ_{ij} is the Kronecker symbol, h_0 is the hardening modulus, s_0 is the initial shear resistance, s_s is the breakthrough stress at which the large plastic flow initiates, γ_0 is the amount of shear strain after which the interaction between the shear systems reaches a peak strength and f_{ij} represents the degree of interaction between deformation mechanisms. For the sake of simplicity, only the strong hardening interaction of the twin bands on the other non-coplanar twin/slip systems is considered ($f_{ij} \neq 0$ if $j \in$ twin systems and i and j are not coplanar). This is believed to be the strongest hardening mechanism because of its high effectiveness in reducing the free path for dislocations. Hardening between the coplanar slip or twin systems is not considered.

As a summary, Fig. 6.4 presents the proposed multiscale approach for the phase transformation problem. First, the viscous growth rate for the phase transformation $\dot{f}_0$ is defined in terms of the free energy function $\psi_{\text{tr}} - \psi_{\text{pa}}$ using the Principles of Thermodynamics. Then, the free energy change is linked with the concentration of the new phase c_{tr} using atomistic data from the literature [76]. Linear evolution of the fault energy with respect to the concentration is assumed. Finally, the concentration of the new phase is defined as a function of its growth rate using diffusion theory [51]. The set of nonlinear diffusion equations are coupled with the mechanics of the constitutive problem and thus need to be solved simultaneously. The set of diffusion equations linking the fault concentration and its growth rate are detailed in Eqs. (5.7) in Chapter 5. This set of nonlinear diffusion equations is coupled to the mechanics of the constitutive problem through the strain rate – stacking fault energy relationship in Eq. (6.39) and thus need to be solved simultaneously.

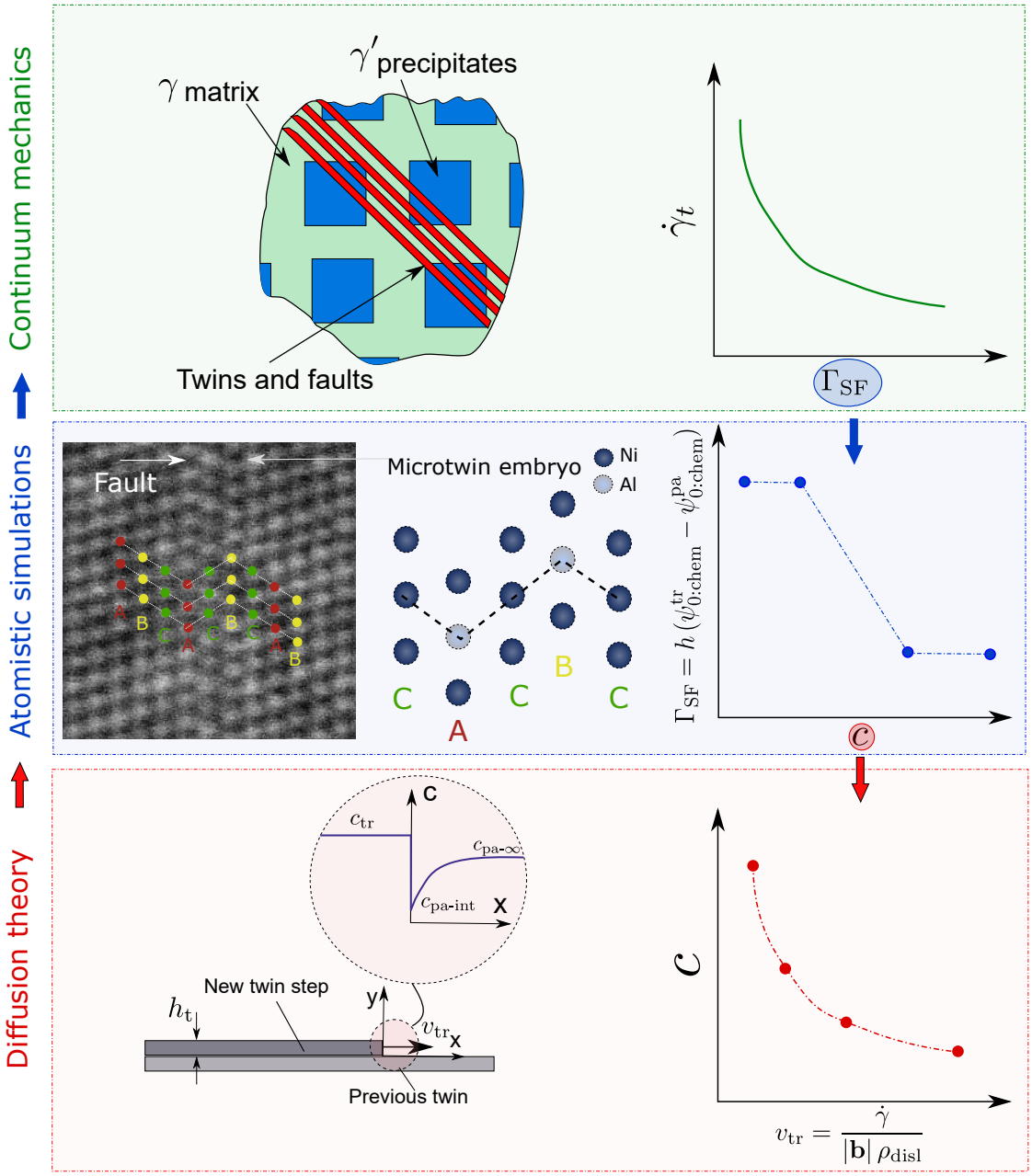

Figure 6.4 – Multiscale diagram of the proposed constitutive model for the diffusion-assisted microtwinning formation: (bottom) diffusion theory links growth velocity with Co and Cr concentration at the twin [51]; (center) concentration is associated with stacking fault energy of growing fault by means of atomistic simulations [76]; (top) finally, stacking fault energy (or equivalently free energy) is connected with the macroscopic strain rate.

6.3 Thermodynamic consistency of the model

The thermodynamic consistency of the phase transformation model is studied here. In order for the process to be fully thermodynamically consistent, the Clausius-Duhem inequality must be satisfied for any arbitrary variation of the state of the system (elastic deformation, slip deformation, phase transformation or chemical concentration changes in this case):

$$\underbrace{J^{\mathrm{p}}\left(\overline{\overline{\mathbf{M}}}:\overline{\overline{\mathbf{L}}}^{\mathrm{p:s}}\right)}_{\text{slip}}+\underbrace{J^{\mathrm{p}}\left(\overline{\overline{\mathbf{M}}}:\overline{\overline{\mathbf{L}}}^{\mathrm{p:tr}}\right)+(\psi_0^{\mathrm{pa}}-\psi_0^{\mathrm{tr}})\dot{f}_0}_{\text{transformation}}+\underbrace{f_0\Big(\frac{\partial\psi_0^{\mathrm{pa}}}{\partial c_{\mathrm{pa}}}-\frac{\partial\psi_0^{\mathrm{tr}}}{\partial c_{\mathrm{tr}}}\Big)\dot{c}_{\mathrm{tr}}}_{\text{diffusion}}\geq 0 \quad (6.42)$$

Following the Coleman and Noll [126] method, we aim at satisfying the positive or zero condition for each of the terms to assure the thermodynamical consistency of the model.

The first term associated with the slip dissipation can be expressed in the intermediate configuration $\overline{\overline{\Omega}}$ as a function of the slip plastic multipliers $\dot{\gamma}_\alpha$ and the projected stress τ_α:

$$\overline{\overline{\mathbf{M}}}:\overline{\overline{\mathbf{L}}}^{\mathrm{p:s}}=\sum_\alpha\overline{\overline{\mathbf{M}}}:(\overline{\overline{\mathbf{m}}}_\alpha\otimes\overline{\overline{\mathbf{n}}}_\alpha)\dot{\gamma}_\alpha=\sum_\alpha\tau_\alpha\dot{\gamma}_\alpha\geq 0 \quad (6.43)$$

where the consistency is obtained implicitly from the flow rule definition in Eq. (6.33), where the same direction for stress τ_α and the plastic multiplier $\dot{\gamma}_\alpha$ is imposed ($\tau_\alpha\dot{\gamma}_\alpha\geq 0$).

Similarly, the second term associated with the transformation dissipation can be rearranged in the intermediate configuration $\overline{\overline{\Omega}}$ using the definition of the plastic flow in Eq. (6.34), the definition of the projected stress τ_β and the relation in Eq.

(6.36) as:

$$\overline{\overline{\mathbf{M}}} : \overline{\overline{\mathbf{L}}}^{\mathrm{p:tr}} + (\psi_0^{\mathrm{pa}} - \psi_0^{\mathrm{tr}})\dot{f}_0 = \sum_\beta \Big[\overline{\overline{\mathbf{M}}} : (\overline{\overline{\mathbf{b}}}_\beta \otimes \overline{\mathbf{n}}_\beta)\,\gamma_{\mathrm{tr}} + (\psi_0^{\mathrm{pa}} - \psi_0^{\mathrm{tr}})\Big]\dot{f}_{0:\beta} = \sum_\beta \Big[\tau_\beta + \frac{\psi_0^{\mathrm{pa}} - \psi_0^{\mathrm{tr}}}{\gamma_{\mathrm{tr}}}\Big]\dot{\gamma}_\beta \geq 0 \quad (6.44)$$

where again the consistency is obtained implicitly from the flow rule definition in Eq. (6.39), where the same direction for the driving force and the plastic multiplier $\dot{\gamma}_\beta$ is imposed ($\Big[\tau_\beta + \frac{\psi_0^{\mathrm{pa}} - \psi_0^{\mathrm{tr}}}{\gamma_{\mathrm{tr}}}\Big]\dot{\gamma}_\beta \geq 0$).

The third term is associated with the driving force for diffusion between the parent phase and the transformed phase. This is driven by a reduction of the Gibbs free energy per unit volume $\delta G = \delta\psi + \delta p + \eta\delta T$ of the biphasic system, where ψ and p, are respectively the Helmholtz free energy and the pressure of the system. In isothermal solid-solid transformations, the term associated with the pressure p is small and can be ignored leading to $\delta\psi = \delta G$ [105]. By introducing the definition of the chemical potential ($\mu = \frac{\partial G}{\partial c} = \frac{\partial \psi}{\partial c}$), the transformation dissipation term reads:

$$f_0\Big(\frac{\partial \psi_0^{\mathrm{pa}}}{\partial c_{\mathrm{pa}}} - \frac{\partial \psi_0^{\mathrm{tr}}}{\partial c_{\mathrm{tr}}}\Big)\dot{c}_{\mathrm{tr}} = f_0(\mu_{\mathrm{pa}} - \mu_{\mathrm{tr}})\dot{c}_{\mathrm{tr}} \geq 0 \quad (6.45)$$

If we assume a closed system including parent and transformed phase (see Fig. 6.5) the sign of this term can be expressed as:

$$\mathrm{sign}\{\dot{c}_{\mathrm{tr}}\} = \mathrm{sign}\{\delta c_{\mathrm{tr}}|_{\delta t}\} = \mathrm{sign}\{\delta m_{\mathrm{tr}}|_{\delta t}\} = -\mathrm{sign}\{\mathcal{J}\} \quad (6.46)$$

where $\delta c|_{\delta t}$ and $\delta m|_{\delta t}$ are an infinitesimal concentration increment and a mass increment for an infinitesimal time increment δt, and $\mathcal{J}$ is the mass flux across the interface of both phases relative to the new phase (positive as indicated in Fig.

6.5). Introducing the generalized first Fick's law at the interface $\mathcal{J} \propto (\mu_{\text{tr}} - \mu_{\text{pa}})$ [138], the sign of the dissipation term can be expressed as:

$$\text{sign}\{(\mu_{\text{pa}} - \mu_{\text{tr}})\dot{c}_{\text{tr}}\} = -\text{sign}\{\mu_{\text{pa}} - \mu_{\text{tr}}\}\,\text{sign}\{\mathcal{J}\} = \text{sign}\{\mu_{\text{pa}} - \mu_{\text{tr}}\}\text{sign}\{\mu_{\text{pa}} - \mu_{\text{tr}}\} \geq 0 \quad (6.47)$$

which proves that the transformation dissipation term in Eq. (6.42) is always positive during non-equilibrium ($\dot{c}_{\text{tr}} \neq 0$) or zero at equilibrium ($\mu_{\text{pa}} = \mu_{\text{tr}}$).

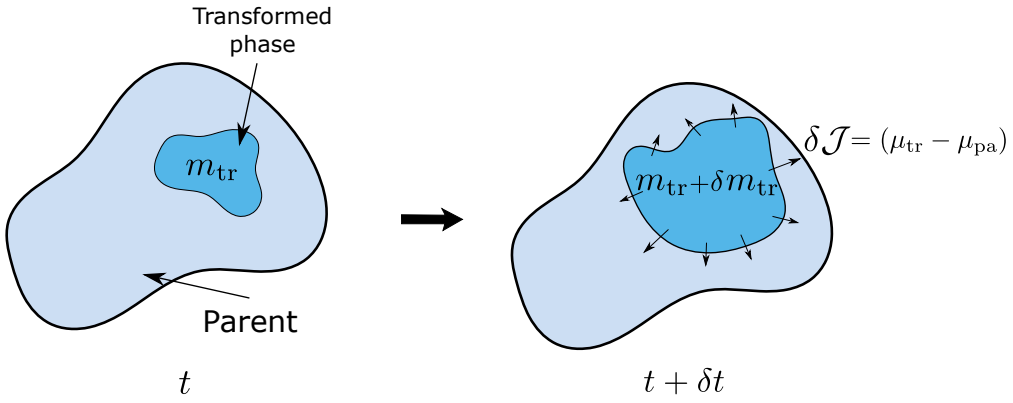

Figure 6.5 – Diagram of the fluxes present in the mass diffusion problem for the case of phase transformation.

6.4 Conclusions

This chapter analyses the phenomenon of segregation assisted plasticity in Ni-based superalloys using phase-transformation diffusion theory and crystal plasticity theory. The following contributions can be extracted from this work:

- On the basis of the experimental observations, a mechanical constitutive model for Ni-based superalloys has been developed accounting for the three main mechanisms observed in these alloys between 700 and 800°C: octahedral slip, cubic slip and microtwinning. The microtwinning mechanism has been

modelled as a phase transformation phenomenon.

- The flow rules for the three mechanisms have been developed from the dissipation rates derived from the application of the First and Second Principles of Thermodynamics. Finite deformation is assumed. The thermodynamic consistency of the model has been proven.

- The flow rule for the phase transformation includes the proposed model for the diffusion-assisted growth introduced in the previous chapter.

- The driving force for the phase transformation includes the free energy change introduced by the change of atomic structure through the stacking fault energy. It also includes the discrepancy between the stiffness of the parent phase and the transformed phase.

7 Numerical modelling of mid-temperature creep in Ni-based superalloys

7.1 Introduction

The continuum framework developed in the previous chapter is now used to study the mechanical behaviour of Ni-based superalloys in the mid-temperature range. The model described was implemented in a user material subroutine UMAT for the FE program ABAQUS/Standard [139]. The implicit integration of the crystal plasticity equations was done following the methodology of the work of Huang [140] and Kysar [141]. The plastic relationships (plastic-flow rules) developed in the previous chapter were implemented in the original user subroutine maintaining the Newton-Raphson structure of the code. The main additional difficulty appearing from the new plastic flow relations is that, for each Newton-Raphson iteration, the strain-rate evaluation of the microtwinning systems using Eq. (6.39) is coupled to diffusion equations in Eqs. (5.7). These diffusion equations are solved all together iteratively in an inner loop using the bisection method.

The constitutive model has been calibrated for MD2 superalloy. Once calibrated

the model is used to study the effect of microtwinning on the mechanical behaviour of this alloy. First, the orientation dependent behaviour of the single crystal superalloy at 800°C is studied computationally. The results are compared with the experimental data reported in Chapter 3. Second, the model is extended to study the simultaneous activities of different plastic mechanisms in the polycrystalline superalloy MD2-CC and their influence on the mechanical behaviour. Both single crystal and polycrystal applications demonstrate the critical role of the diffusion-assisted microtwinning mechanism in providing the high antisymmetric behaviour observed in superalloys.

7.2 Simulations of creep in single crystal MD2 Ni-based superalloy

The calibrated model results for $\langle 001 \rangle$, $\langle 011 \rangle$ and $\langle 111 \rangle$ compression tests are shown in Fig. 7.1. The compression creep tests for MD2 superalloy indicated in Table 3.3 were used here to calibrate the constitutive model. The elastic constants (C_{11},C_{12} and C_{44}) for MD2 superalloy were obtained from literature data [142]. The shear induced by microtwinning γ_{tr} was obtained from geometrical relations [51]. The identification process to obtain the rest of the plastic model parameters was carried out by an inverse optimization approach. To this end, the uniaxial creep strain-time curves for compression along $\langle 001 \rangle$, $\langle 011 \rangle$ and $\langle 111 \rangle$ directions shown in Fig. 3.2 were used as input data. The optimization problem was solved using a genetic algorithm within the constitutive framework implemented in Matlab [143]

for uniaxial testing conditions. The residual R is given by

$$R = \frac{1}{n}\sum_{i=1}^{n}(\varepsilon_i^{\text{exp}} - \varepsilon_i^{\text{num}})^2 \tag{7.1}$$

where n is the number of data points compared and ε^{exp} and ε^{num} represent the experimental and numerical values of the creep strain, respectively. The final stages of deformation were excluded from the optimization process as, during the tertiary creep, the damage mechanisms are dominant and their effect is not included in this model.

The elastic and geometrical constants and the calibrated model parameters for the three deformation modes considered are presented in Table 7.1. The application of the model to predict the plastic behaviour of single crystals is presented next.

Table 7.1 – Crystal plasticity constitutive parameters for MD2 Ni-based superalloy. The parameters marked with an asterisk * has been optimised using the creep response of the material while the rest have been obtained from the literature or geometric considerations.

Elastic Properties							
C_{11} (GPa)	C_{22} (GPa)	C_{44} (GPa)	$\gamma_{\text{tr:}\beta}$ (-)	h_{t} (m)			
230	150	90	$\sqrt{2}/2$	$7/3\sqrt{3}\times10^{-10}$			
Octahedral Slip							
γ_0^* (1/s)	m^*(-)	s_0^* (MPa)	τ_s^* (MPa)	h_0^* (MPa)	f_{ij}^* (-)	γ_0^* (-)	q^* (-)
1.68×10^{-8}	0.098	235	237	949	1.04	0.02	2.51
Cubic Slip							
γ_0^* (1/s)	m^*(-)	s_0^* (MPa)	τ_s^* (MPa)	h_0^* (MPa)	f_{ij}^* (-)	γ_0^* (-)	q^* (-)
5.7×10^{-7}	0.098	302	290	951	1.04	0.02	2.51
Twinning							
γ_0^* (1/s)	m^*(-)	s_0^* (MPa)	τ_s^* (MPa)	h_0^* (MPa)	f_{ij}^* (-)	γ_0^* (-)	q^* (-)
1.16×10^{-6}	0.3	52	76	841	1.04	0.02	2.51

7.2.1 Macroscopic creep behaviour

Numerical models with the dimensions of the specimens employed in the uniaxial compression and tension tests described in Chapter 3 were developed in

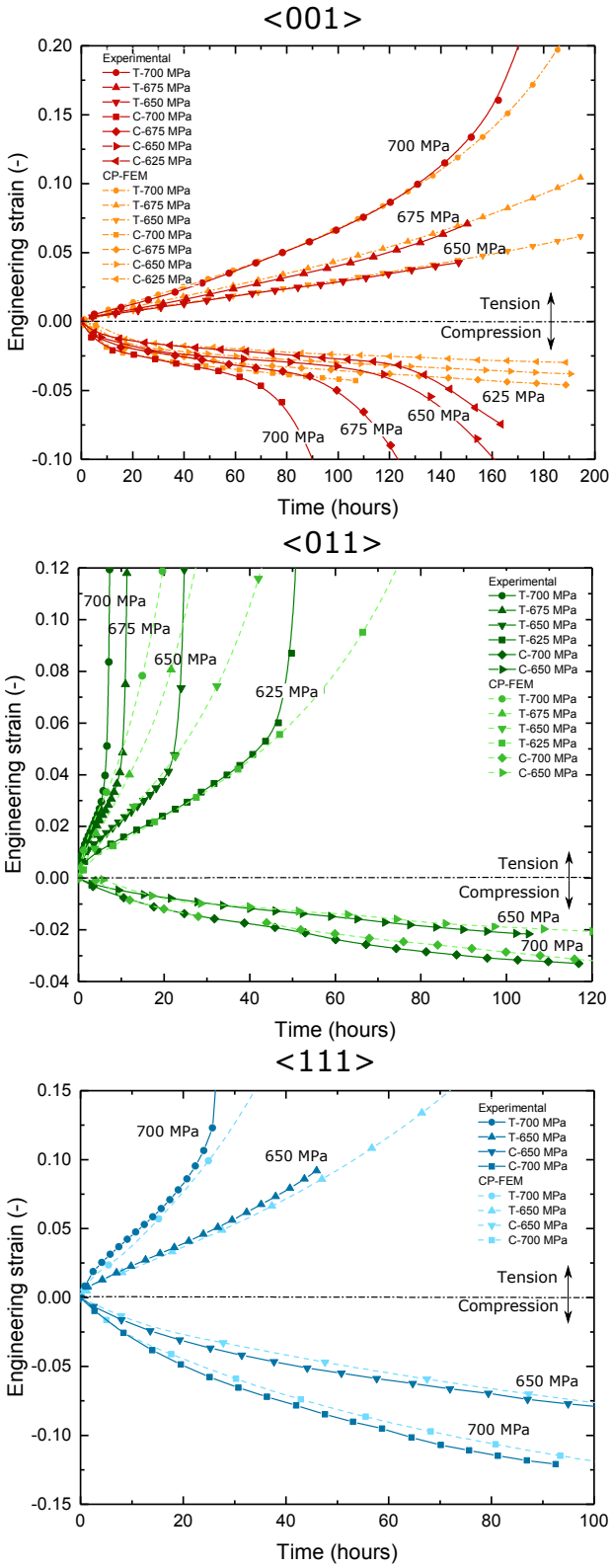

Figure 7.1 – Strain-time experimental curves of MD2-single crystal superalloy at 800 °C for different stresses vs. model predictions.

ABAQUS/Standard. The models were meshed with C3D8 elements. The boundary conditions of the experimental setup were reproduced accordingly. The specific crystal orientations used in the models were extracted from the EBSD measurements given in Table 3.2.

The measured and predicted creep strain-time curves for the tension creep tests along $\langle 001 \rangle$, $\langle 011 \rangle$ and $\langle 111 \rangle$ are shown in Fig. 7.1. In all three tensile crystal directions, the macroscopic responses were predicted with reasonable accuracy. For the testing directions where microtwinning was active ($\langle 001 \rangle$-compression and $\langle 011 \rangle$-tension) the model underestimates the plastic strain of the final stage of the creep test. This can be explained in terms of specific damage mechanisms (not accounted for in the model) associated with the microtwin boundaries introduced in Chapter 3, where an embrittlement of the samples developing tensile twins was reported. As a summary, an increase of dislocation densities in the parent phase at the microtwin boundaries was observed. These pile-ups were presumably formed by the abrupt change of Schmid factors between twin and parent phases; the microtwins acted as dislocation barriers. As the parent phase deforms plastically on different slip/twin systems than the principal twin system, the dislocations become increasingly trapped, producing stress concentrations and promoting damage. In the present work, the same phenomenon was observed for the case $\langle 001 \rangle$-compression testing when microtwinning is activated, leading to a final stage with accelerated strain rates, see Fig. 7.1. This damage process could be added in future developments of the constitutive framework presented here. For example, one could limit the amount of plastic deformation that the parent phase can accommodate when the slip and twin systems are different from the main one [110]. If this plastic deformation would reaches a critical value, catastrophic failure can occur, as observed experimentally.

The increasing strain rates observed in this work in the computational curves are due to the cross-sectional area reduction due to plastic elongation and the fact that both models and experiments are carried out under constant engineering stress.

7.2.2 Mechanisms activity

The activity fraction for each slip (octahedral and cubic) and twin mechanism ($f_{\text{oct}}, f_{\text{cub}}, f_{\text{twin}}$) is defined as:

$$f_i = \frac{\gamma_i}{\gamma_{\text{total}}} \tag{7.2}$$

where $i \in$\{oct,cub,twin\} and $\gamma_{\text{total}} = \gamma_{\text{oct}} + \gamma_{\text{cub}} + \gamma_{\text{twin}}$.

The values obtained for each orientation are plotted in Fig. 7.2 for 800°C and 650 MPa under both tension and compression conditions. The asymmetric behaviours observed in the creep curves correlates well with the type of deformation mechanism activated, especially for ⟨001⟩ and ⟨011⟩ orientations. Twinning is active and responsible for most of the creep plastic deformation for ⟨001⟩-compression and for ⟨011⟩-tension. This is in agreement with previous experimental studies where microtwinning was found to account for most of the plastic deformation during creep (up to $\approx 90\%$) for ⟨011⟩-tension [24, 51, 53]. For ⟨111⟩ specimens, no change of mechanism is found due to the dominant role of cubic slip in this direction and the symmetry of this mechanism. This could explain the reduced asymmetric behaviour in this direction when compared with ⟨001⟩ and ⟨011⟩. The activity study presented here was generalized for the whole set of possible single crystal orientations in Fig. 7.3 for tension and compression cases. Although only the microtwinning mechanism is antisymmetric in terms of its kinematics, the high asymmetry is also extended to the other two mechanisms. The directions in the lower part of the inverse pole figure, along the ⟨001⟩-⟨110⟩ pole line present a high

asymmetry in terms of activity between tension and compression cases (e.g. the twin and octahedral regions swap). In the upper part of the inverse pole figure, the deformation along the cubic systems is preferred over the two other mechanisms both in tension and compression. The mechanism symmetry also leads to a higher symmetric creep behaviour.

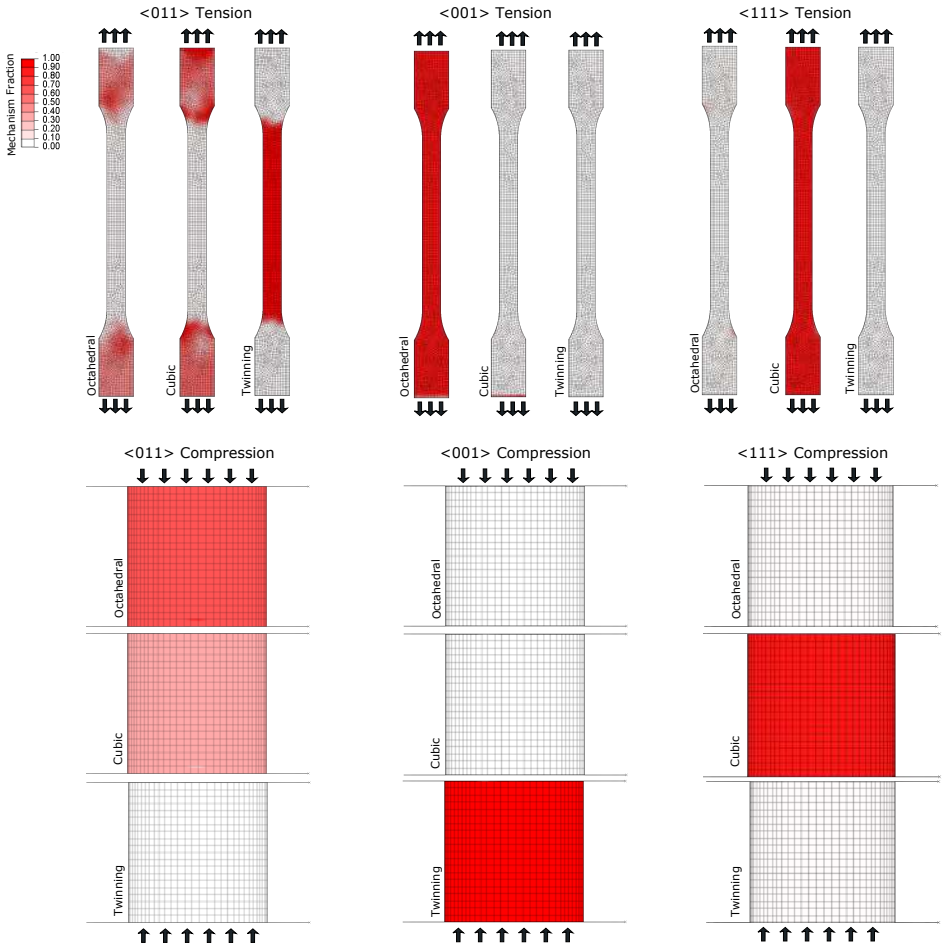

Figure 7.2 – Shear contribution to the total one for each deformation mechanism for simulations performed at 650 MPa and 800°C. The mechanism fraction is defined as $f_{\text{oct,cub,twin}} = \frac{\gamma_{\text{oct,cub,twin}}}{\gamma_{\text{total}}}$

Another crucial point regarding the creep deformation of single crystals is the rotation of the lattice during the test, as it has a great influence on the creep life [7, 24, 78, 144]. This rotation is produced when the deformation is limited to

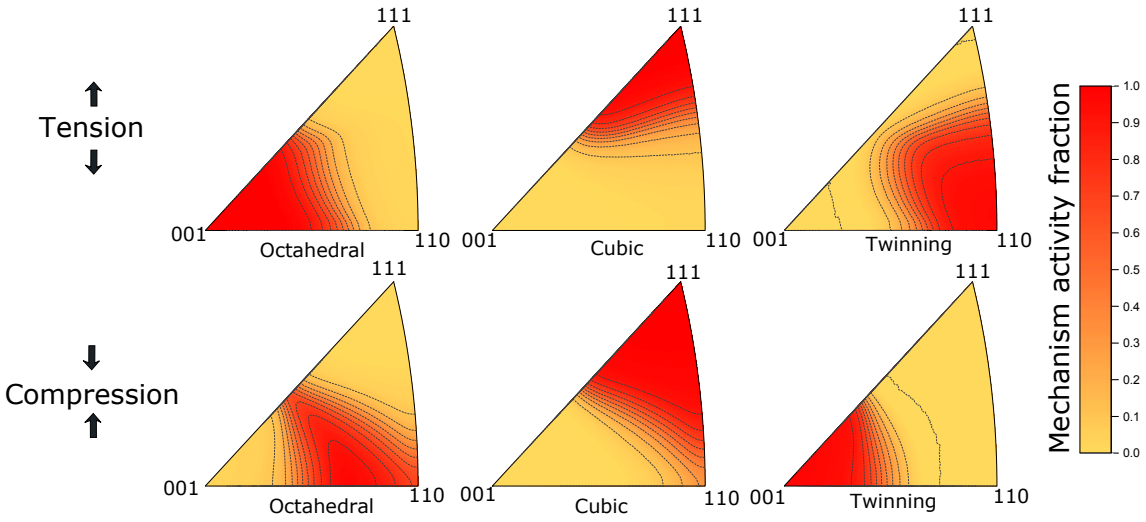

Figure 7.3 – Mechanism activity fraction inverse pole figures for octahedral slip, cubic slip and twinning for both tension and compression cases at 650 MPa and 800°C. The activity fraction is defined as: $f_{\text{oct,cub,twin}} = \frac{\gamma_{\text{oct,cub,twin}}}{\gamma_{\text{total}}}$

only one shear system and the tensile axis is constrained by the loading machine. This phenomenon is defined as "single slip" [145]. When several slip systems are activated (standard slip or twinning), the rotations of the lattice are less pronounced as the rotations of slip systems counteract each other.

The rotations for the different loading directions are presented in Fig. 7.4a for the 800°C-650 MPa cases. The tension and compression cases along the ⟨111⟩ direction and the tension case along the ⟨011⟩ direction show the greatest lattice rotation after testing. This is in agreement with the slip system activities presented in Fig. 7.4b for the six different loading conditions. It can be observed that for the cases with large rotations, only one shear system is active. The deformation is constrained to shear along (111)-[11$\bar{2}$] twin system for the case of ⟨011⟩ in tension and (100)-[011] for the case ⟨111⟩ in tension and compression. For the tension cases, the loading axis rotates towards the single slip direction while for the compression case, it rotates towards the single slip plane normal, in agreement with CP theory

[145]. The time at which 2% of plastic strain is experimentally reached for each orientation (see Fig. 7.4) is shown in Table 7.2. The time-to-rupture is in agreement with other creep orientation dependence studies [146]. This and Fig. 7.4 indicate a correlation between the single slip cases and the conditions with higher creep rates ($\langle 111 \rangle$ tension and compression and $\langle 011 \rangle$ tension). This correlation can also be extended to the time to rupture for the tension cases in Fig. 7.1. These observations are in agreement with previous experimental studies showing that conditions in which only one deformation shear system is active present the worst creep responses and are thus not desirable [36, 7, 2]. A physical explanation for this can be proposed by comparing the two testing conditions with microtwins presented in Fig. 3.5b ($\langle 110 \rangle$-tension and $\langle 001 \rangle$-compression). For $\langle 110 \rangle$-tension, only one system of twin bands is observed in agreement with the simulations presented in Fig. 7.4b. In such a condition, the shearing distance free path for new gliding dislocations in the single slip mode is not affected by the formation of new twins as the partial dislocations run parallel to the preformed twins. However, for $\langle 001 \rangle$ compression, the twin band network extends along two different twin planes reducing drastically the mean free path of the gliding dislocations and thus considerably hardening the alloy. Therefore, it can be inferred that loading cases where more than one system is active should present lower minimum creep rates and higher creep life than when multiple systems are active. This effect is included in the constitutive model by the cross-hardening term f_{ij} between different slip planes.

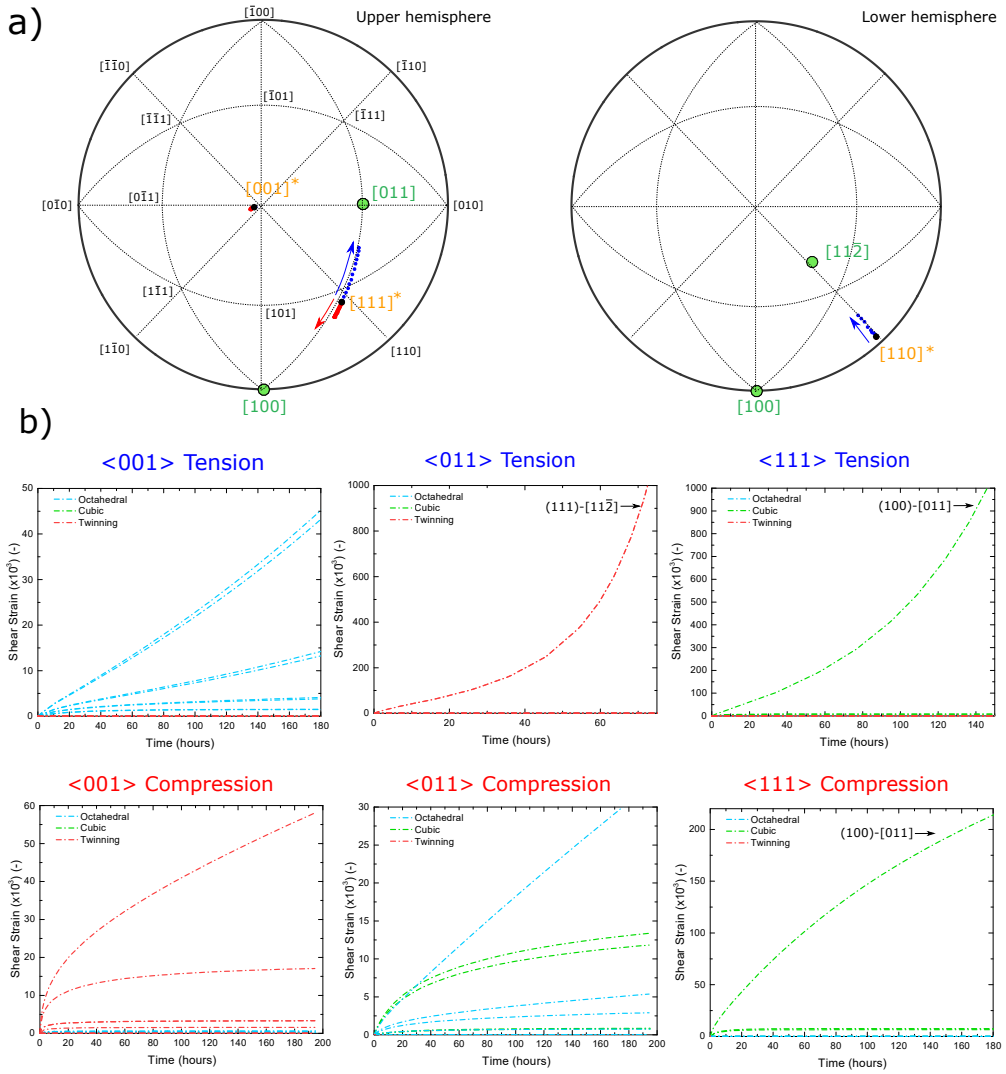

Figure 7.4 – a) Inverse pole figure showing the rotations of the crystal lattice obtained from the single crystal numerical simulations at 800°C and 650 MPa. In orange and marked with * the tested crystal orientations and in green the slip direction and normals. Blue is for the rotations of tensile cases and red is for the rotations of compression cases. The whole orientation plane is shown due to the non-symmetric character of microtwinning; b) shear strains of the different deformation systems for the three different tested orientations. Blue is for octahedral slip, green is for cubic slip, and red is for microtwinning.

7.3 Mid-temperature creep of polycrystalline aggregates

In this section, the model is used to demonstrate its predictive capability for creep of Ni-based superalloys polycrystalline aggregates. A series of polycrystalline

Table 7.2 – Creep times for reaching 2% plastic strain for each orientation and loading case.

	⟨001⟩	⟨011⟩	⟨111⟩
Tension	37.2 h	3.2 h	6.0 h
Compression	14.1 h	51.3 h	3.1 h

compression creep tests of MD2-CC superalloy was used to validate the proposed constitutive model. The study is then extended to analyse the tension/compression differences at the micromechanical level during high temperature deformation of polycrystalline superallloys.

7.3.1 Experimental campaign

A polycrystalline version of the single crystal superalloy MD2 presented in the previous chapters is used in this analysis. Cylinders of 5 mm diameter for 5 mm length were machined, see Fig. 3.1b. A series of compression creep tests at 800°C and 650-700 MPa were performed. The tests were run for 150 hours. The strain was measured from the displacement of the grips using digital image correlation. An image of the experimental setup is presented in Fig. 7.5a. Compression tests were selected in this study to minimize grain boundary sliding, the formation of cavities at the grain boundaries and premature failure of the material.

7.3.2 Numerical setup

A numerical model simulating the alloy microstructure was constructed from a series of grain measurements, see Fig. 7.5b. The measured statistical grain size distributions were fitted to a normal distribution and included in the computational model using the grain-aggregates generator tool Neper [147]. Fig. 7.5c shows an example of the polycrystalline model used here. The orientation information was

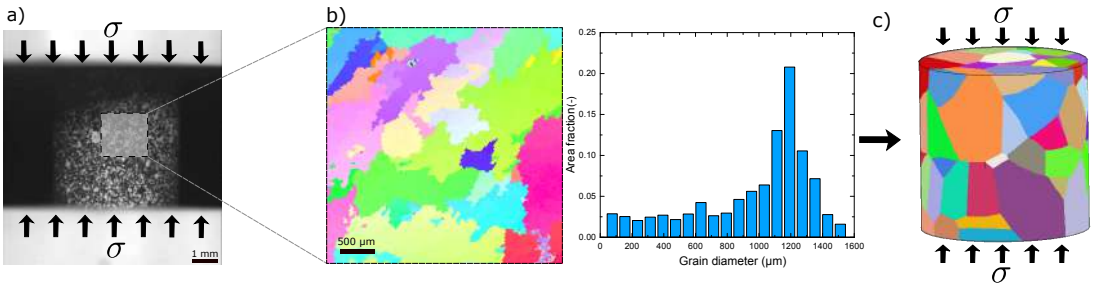

Figure 7.5 – a) Experimental set-up for the polycrystalline compression creep tests; b) characteristic EBSD micrograph of polycrystalline MD2-CC superalloy (left) and statistical grain diameter distribution (right); c) synthetic polycrystalline model used for the numerical simulations. The information obtained from the statistical grain size distribution was used to construct the computational model.

extracted from the EBSD measurements of the pre-tested sample and matched with the grain distribution in the computational model.

Compression and tension conditions were both simulated: the former to validate the model against the experimental results and the latter to study the tension-compression behaviour of the polycrystalline superalloy. The boundary conditions for the compression cases were the same as for the single crystal. For the tension cases, the bottom face of the cylinder was fixed in the loading direction and the top was pulled to maintain the coherence with the compression case. The final FE model contains 103 grains with a total of 5,427 tetrahedral elements and was run using ABAQUS/Standard [139].

7.3.3 Mechanisms activity

The numerical results provided by the polycrystalline model were compared with the experimental data for the compression loading, see Fig. 7.6. A good correlation was found between the experimental and computational curves, especially in the secondary creep region. The curves slightly differ during the initial primary creep region for 650 MPa, but are still in the expected scatter of the creep results.

This demonstrates the ability of the model to faithfully reproduce the mechanical behaviour of polycrystalline materials from single crystal properties.

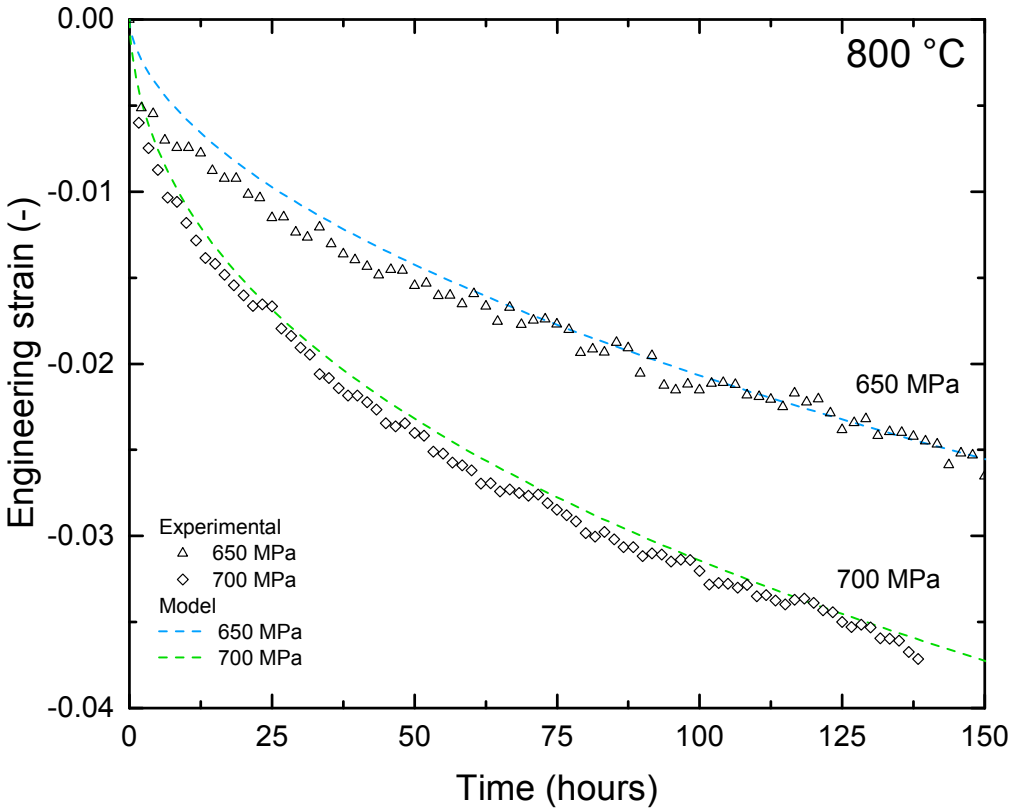

Figure 7.6 – Creep strain vs. time curves used for validation purposes for the polycrystalline superalloy MD2-CC tested at 800°C under compression stresses of 650 MPa and 700 MPa.

In Fig. 7.7a-b, a comparison between the tensile and compression creep cases is presented. In Fig. 7.7a, simulations exhibit an antisymmetric behaviour between tension and compression cases with an inferior creep strength for tension. This might be exclusive for the case studied here due to the large grain size of the alloy. The results are further analysed in Fig. 7.7b where the activities of the different mechanisms are computed. The activity is defined as the ratio of shear strain produced by each mechanism to the total activity, see Eq. (7.2). The results show that in most grains, a single deformation mechanism is dominant

per grain rather than a mix of several ones. Near to the grain boundaries, the strain incompatibilities between grains produce non-homogeneous complex stress states different from the uniaxial ones controlling the deformation within the core of the grains. This leads to a mix of deformation mechanisms different from the hegemony observed inside the grains. This is the cause of the unfilled regions in the combined graph in Fig. 7.7b. For compression, octahedral and cubic slips are more common than microtwinning, while in tension the contributions of all mechanisms are comparable. This might be explained again by the large grain size of the alloy being therefore a specific phenomenon of the combination of grains and orientations studied here. The change in mechanism between tension and compression extends along the whole aggregate as observed in the combined activity diagram in Fig. 7.7b (right). These changes in mechanism are caused by the unidirectionality of the microtwinning shearing and they explain the asymmetric strength observed in Fig. 7.7a as grains deform by mechanisms with differing creep strengths for the different loading conditions. This difference in creep strength is expected to vanish as the testing volume increases or the mean grain size gets smaller. The role of the microtwinning mechanism on the creep strength is further supported by previous observations in Chapter 3 linking the formation of microtwins to a premature failure of the alloy. The local promotion of stress concentrations due to microtwinning was observed to lead to an important damage of the microstructure for single crystal alloys. In the present work, the experimental observations presented in Fig. 7.8 confirm the extension of this phenomenon to polycrystalline alloys. Here, a grain orientation map was obtained from the fracture surface of a MD2-CC sample after tensile creep testing at 750°C and 550 MPa. The deformation marks observed in Fig. 7.8a at the end point of the crack surface were analysed in detail. Here,

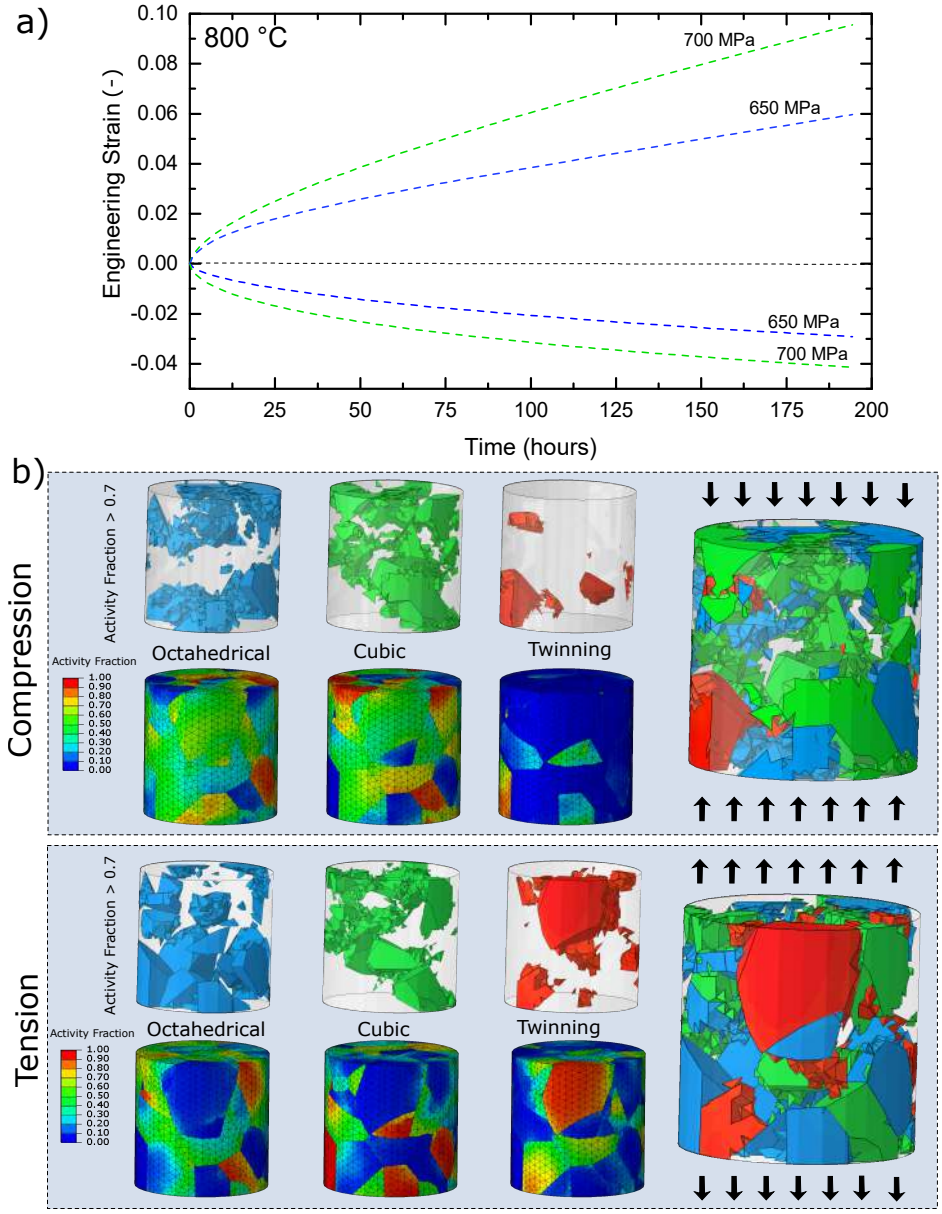

Figure 7.7 – a) Numerical curves for polycrystal simulations at 800°C and stresses indicated in tension and compression; b) deformation mechanisms activity analysis for tension and compression simulations under 700 MPa and 800°C. The mechanism activity is calculated as $f_{\mathrm{oct,cub,twin}} = \frac{\gamma_{\mathrm{oct,cub,twin}}}{\gamma_{\mathrm{total}}}$.

microtwins were found to extend along grain 1 but not grain 2. In the former grain, two twin systems are active, one of them parallel to the crack surface. This is in agreement with the grain activity analysis presented in Fig. 7.8b-c, where the potential active mechanism for each grain was deduced from their Schmid factors.

The different active mechanisms for each grain are intimately linked with the crack propagation path. The crack is found to extend from the sample surface following the microtwin bands from one of the systems and advancing transgranularly as indicated by the red line. When the crack path encounters the grain boundary in its way to untwinned grain 2, it changes from transgranular to intergranular. The fact that the crack starts propagating along the microtwinned grains is crucial for the life prediction. This can be due to the lack of strengthening mechanisms in microtwins boundaries, differing from the preformed grain boundaries which are carefully strengthened during the alloying process. In this case, it was found that even though the twinned grains represent only around $\approx 5\%$ of the total number of grains, their role on the failure mechanism is not negligible. These results are further proof of the crucial role of microtwinning on the mechanical behaviour of Ni-based superalloys at high temperatures.

Although the proposed constitutive framework has been particularized for the case of MD2 superalloy in this thesis, the formulation remains general. If another alloy is to be modelled, the whole framework is still valid but further calibration and experimental measurements would be needed. These include:

- Direct atom probe tomography measurements of Co and Cr (or other) concentrations in the γ' phase and at the microtwins for the given alloy.
- Thermodynamic calculations of the alloy diffusivities using CALPHAD.
- Calibration of the properties indicated with a "*" symbol in Table 7.1 and the elastic constants (C_{11},C_{22} and C_{44})

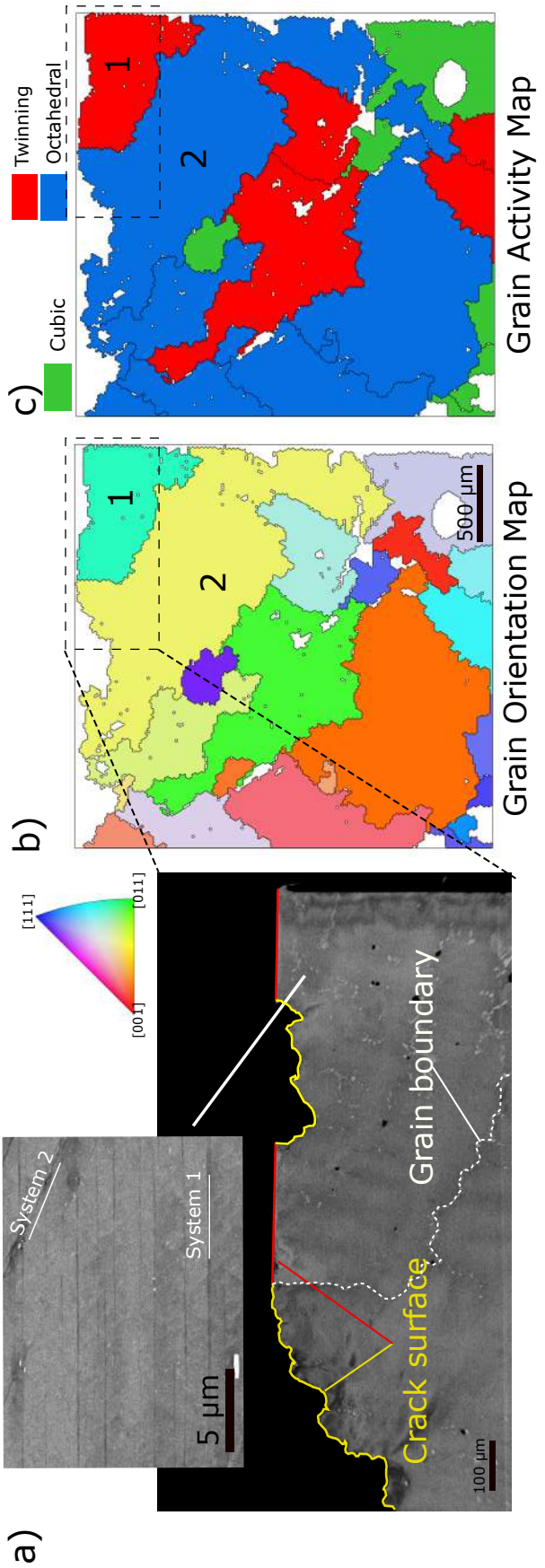

Figure 7.8 – a) fracture surface with microtwins after testing polycrystalline MD2-CC at 750°C and tensile stress of 550 MPa. The grain containing a flat fracture surface is found to be replete of microtwins; b) grain orientation map of the region indicated in (a); c) grain activity map of the same region.

7.4 Conclusions

In this chapter, the mechanical behaviour of Ni-based superalloys at 800°C has been rationalised using FE and CP modelling. The numerical results presented here lead to the following conclusions:

- The constitutive model developed in the previous chapter has been implemented in a FE code and its parameters have been identified for the MD2 single crystal superalloy from experimental data obtained in Chapter 3.

- A wide range of stress conditions and orientations has been covered, in both tension and compression states. Good agreement between numerical predictions and experimental data was found in terms of the strain-time curves depending on crystal orientation and stress level.

- The activation of the different deformation mechanisms correlates well with the ones observed experimentally. A strong connection between the high anisotropy of superalloys and the activation of microtwinnning has been found.

- Moreover, the observed relations between elastic rotations during deformation, number of active slip systems and creep life of the specimen have been rationalised. The results show that the prevalence of only one active shear system produces large rotations, softens the material due to the lack of hardening mechanisms and thus reduces the creep life of the alloy.

- The single crystal constitutive model has been extended into a polycrystalline framework in order to study the high temperature behaviour of polycrystalline alloy MD2-CC. The numerical creep curves show good correlation with the

experimental tests extending the validation of the model for polycrystalline alloys.

- The different active mechanisms between tension and compression showed that microtwinning asymmetry provokes significant changes on the other two mechanisms.

- Finally, an experimental correlation has been found between the active deformation mechanism within a grain and the different crack propagation modes in the grains for polycrystalline alloys. Microtwinning is observed to promote transgranular crack paths which might lead to premature initiation of failure, thus reducing the life of the turbine components.

The results presented in this chapter demonstrate the capacity of the model proposed to predict the mechanical behaviour of Ni-based superalloys at high temperatures. In addition, the importance of taking into account the coupling between chemistry and plasticity within this temperature range is highlighted.

8 Conclusions and future work

8.1 Concluding remarks

This thesis presented a structured experimental and computational study aimed at providing a deeper understanding of the microtwinning mechanism in Ni-based superalloys.

First, the activation of the microtwins depending on crystal orientation, stress and temperature was studied. A systematic series of creep tests varying these three conditions separately was performed. Results from post-mortem examination were used to construct an activity map for microtwinning. The crystal orientation analysis showed that microtwinning is active for $\langle 001 \rangle$ under compression and $\langle 011 \rangle$ under tension. The tension-compression mechanical asymmetry found for these directions was found to correlate with the appearance of microtwins. In terms of temperature and stresses, for $\langle 011 \rangle$ crystals under tension, microtwinning was found to be active under stresses between 625-675 MPa and within the temperature interval 800-825°C. The formation of these microtwins produced a brittle fracture of the material. Dislocation density measurements showed that pile-ups of dislocations at the microtwin boundaries produce stress concentrations thus creating preferable

paths for crack propagation.

Second, the underlying diffusion processes was studied using combined transmission electron microscopy and atom probe tomography. The results revealed chemical changes at the core of the growing microtwins and other types of faults (CISFs/SISFs, CESFs/SESFs and APBs). These consist of solute clouds of Co and Cr at the fault tip and segregation of the same elements to the fault interfaces. This phenomenon was observed only within the γ' precipitates where the energy of the faults is expected higher. This segregation results in a shift of the chemical structure of the fault from γ' to γ like chemical composition. This chemical shift was rationalised in terms of the energy reduction for the complex stacking faults created.

Third, these findings were used to construct a phase transformation model consistent with the diffusion processes observed experimentally. The model takes into account the long range diffusion supporting the growing fault and the required short range reordering at the interface. The output of the model is the fault growth rate. The results showed only a small influence of the interface reactions under the studied conditions. The computed growth rates were used in an homogenisation framework to obtain the macroscopic creep rates. The framework allowed for the recovery of the creep rate with reasonable accuracy. A criterion for microtwin nucleation was also proposed. The nucleation stresses obtained for unsegregated and segregated faults revealed a need for diffusion if microtwinning is to occur. These results imply that the chemical changes confined locally at faults associated with the high temperature time-dependent plasticity might contribute significantly to the drop of the strength observed in the superalloys above 700°C.

Fourth, the gained understanding was translated into a thermodynamic consistent model for phase transformations. The model accounts for plasticity in the form of

cubic and octahedral slip and microtwinning. The latter is treated as a coupled displacive-diffusive phase transformation by linking the previous diffusion model with plasticity thermodynamics. The time-dependency of the stacking fault energy for microtwinning is accounted for. The framework was developed under the assumptions of finite deformation.

Finally, the continuum framework was used to study the creep behaviour of single crystal superalloy MD2 at 800°C. The model parameters were calibrated against compression creep tests and validated with tensile conditions for $\langle 001 \rangle$, $\langle 011 \rangle$ and $\langle 111 \rangle$ crystals. The model captured the high anisotropy and tension compression asymmetry observed in the experiments. The activation of the microtwinning for the different loading conditions correlated with the experimental cases. The model was then extended to study the polycrystalline MD2-CC. The microstructural information of the alloy was introduced through the statistical distribution of grain sizes and crystal orientations. The numerical creep behaviour showed good agreement with the experimental results. The results showed that the asymmetric mechanism activity of single crystals is also present within the grains in the polycrystalline version.

The future development of superalloys needs to include the effect of this new plastic mechanisms into account. Designing against the segregation-assisted plasticity presented in this thesis will be critical for the next generation of turbine-disk alloy and possibly for the high-stressed regions of the single crystal blades. Future improvements of the work presented in this thesis is presented next.

8.2 Future work

The future developments motivated from this study fall into the following categories:

- Increasing understanding of mechanism changes in Ni-based superalloys during the yield stress drop by atomic resolution studies.
- Extension of the model to include more physical dependencies (temperature, dislocation densities, non-local diffusion and damage)
- Application of the gained knowledge to the computational design of a new generation of creep resistant alloys.

8.2.1 TEM study of the yield stress drop region

The temperature region between 700-850°C in Ni-based superalloys is still a controversial topic. The factors leading to softening beyond 800°C are not well understood [9] and further systematic experimentation is needed to understand the softening effects arising in this temperature range. The faults study presented in Chapter 4 using TEM could be extended to other temperatures in the range of interest (700-850°C). This would allow to study systematically the changes of chemistry and dislocation systems that lead to the strength drop in these alloys. An increasing role of the coupling between dislocation plasticity and segregation with temperature is expected.

8.2.2 Extension of the model to include temperature dependence and other types of faults

The model developed in this thesis was calibrated at isothermal condition of 800°C. The temperature dependence could be added to the constitutive model by adding a pre-exponential factor of Arrhenius type [148]. Further tests on $\langle 001 \rangle$ and $\langle 111 \rangle$ crystal directions are needed to calibrate this term (activation energy) for cubic slip and octahedral slip. Additionally for the case of microtwinning, the diffusivity used

in the low scale phase transformation problem is also dependent on the temperature. Additionally, the phase transformation theory developed for microtwinning could be extended to other types of faults. In order to extend the framework, further chemical atomic analysis of the different faults is needed. Additionally, for the case of segregation assisted APB shearing, a modification of the phase transformation model is required. This is due to the fact that for APBs, the segregated region is constant during the shearing process and thus no further mass of γ stabilisers is needed once the APB core is segregated.

8.2.3 A dislocation-based crystal plasticity model

The constitutive model presented here could be enhanced by the introduction of the dislocation densities as an internal state variable. As presented before, for Ni-based superalloys, the different classes of partial dislocations originate from different types of dissociations and recombinations of full dislocations during the secondary creep stage, see Fig. 8.1a. This makes the interdependence between the different slip and twin systems not solely limited to the hardening interaction but also to the dislocation reaction kinetics. Several authors have included the partial nucleation reactions in their models [149, 150] using simplified formulations (Boolean models). The combination of the reaction laws with physical models for nucleation kinetics (see Fig. 8.1b) would complete the formulation of the stacking fault problem in Ni-based superalloys.

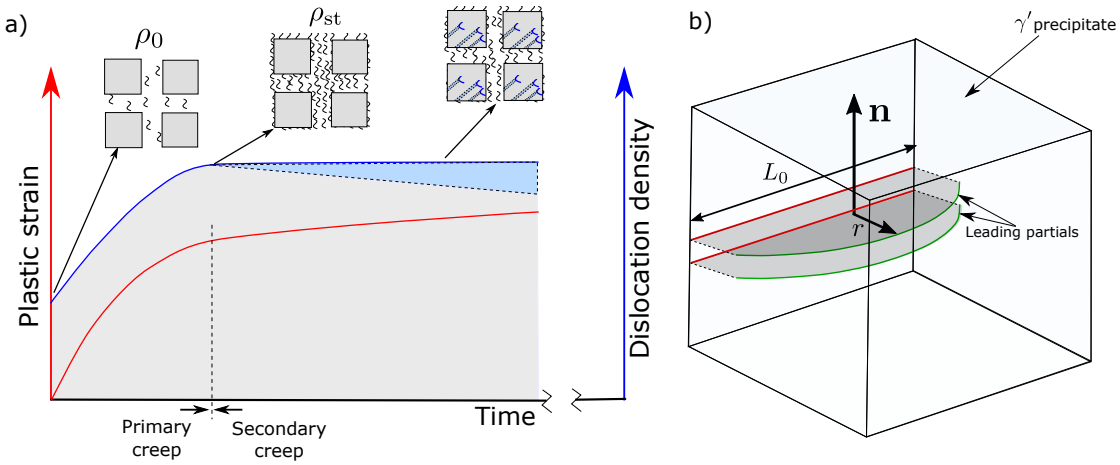

Figure 8.1 – a) Schematics of the dislocation density evolution during a creep test for Ni-based superalloy in the mid-temperature range (650-850°C); b) nucleation diagram for a set of twin partial dislocations at the γ-γ' interface.

8.2.4 Coupled diffusion-mechanical FE framework for explicit problems

In the continuum framework proposed here, the diffusion field was assumed to be contained within the element. This means that the concentration of the new growing fault was treated as an internal variable even when obtained locally from the solution of the diffusion field around the stacking fault. This assumption is accurate for element sizes much larger than the stacking fault height. However, it is of scientific interest to study explicitly the growth of microtwins at a lower scale, see Fig. 8.2. This would help understand the role of stress, temperature or strain rate on determine the characteristic twin thickness and twin fraction. For these studies, the diffusion field around the twin ledge is larger than the characteristic element size and the concentration field needs to be solved coupled with the displacement field [151].

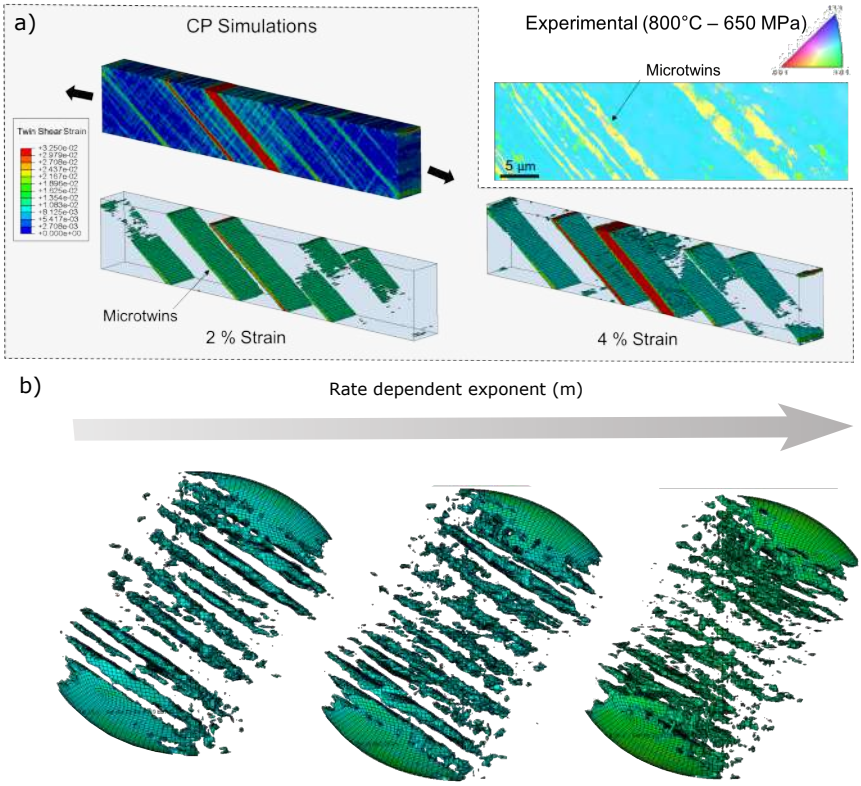

Figure 8.2 – a) Explicit study of the twin growth under tensile deformation for different levels of plastic strain and comparison with the experimental results; b) study of the influence of the viscous parameter m of the rate dependency power law in (6.33) on the twin growth during compression deformation.

8.2.5 Modelling of damage for the microtwin interfaces

The observed enhanced damage associated with the microtwin formation is crucial for the turbine component integrity. In order to include this critical aspect in the computational design of the component, a damage model needs to be included in the framework. Two sources of damage can be identified: non-local dislocation pile-up and intrinsic twin boundary weakening. From a computational point of view, two approaches could be followed: continuum damage or explicit damage frameworks. The former refers to the kind of models that accounts for the damage in the constitutive equations as an internal variable [148]. The latter requires

FE models of higher complexity to define explicitly the crack track and damage propagation [152].

8.2.6 Coupling engineering and alloy-by-design

The findings reported in this thesis provide a deep understanding of the mechanisms that produce creep deformation in a critical design range for superalloys (650-850°C). This can be used in combination with thermodynamical databases to propose novel alloys compositions with better creep properties for a given component, see Fig. 8.3. The mechanical behaviour of the component to optimise is calculated in a dual scale model where the chemical dependence is taken into account by the phase transformation theory. Then this component behaviour is associated with a merit index for each alloy composition. Optimal alloys can therefore be selected and tested for different priority requirements: cost, creep life, formability, etc.

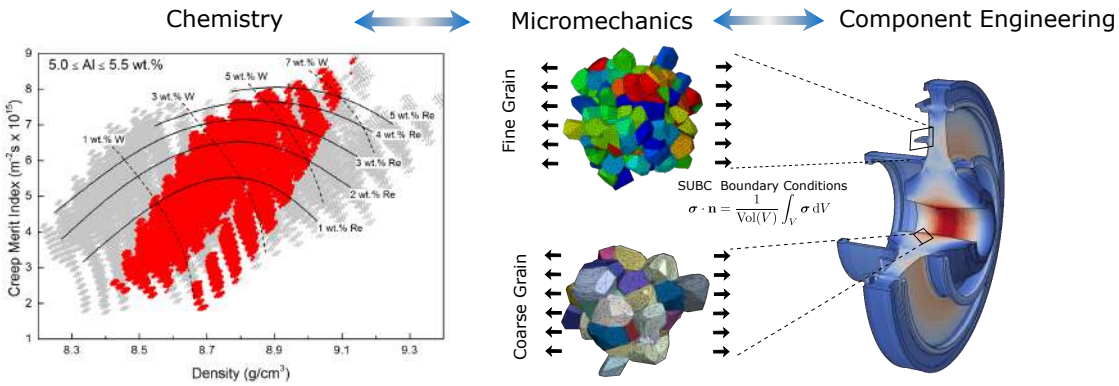

Figure 8.3 – Multiscale framework proposed for coupling chemical composition and component design. The critical conditions for the component are calculated in a two scale model connected by stress boundary conditions. The lower scale contains the chemical and microstructural information. Then a merit index map built on the basis of the component performance can be designed. Chemistry map from Zhu et al. [153]

A Details on the mathematical formulation

A.1 Velocity gradient (l)

The velocity gradient $\mathbf{l}$ in the current configuration Ω is defined as:

$$\mathbf{l} = \nabla_{\mathbf{x}}\mathbf{v} = \dot{\mathbf{F}}\mathbf{F}^{-1} \tag{A.1}$$

where each of the terms $\dot{\mathbf{F}}$ and $\mathbf{F}^{-1}$ can be expressed from the definition of the deformation gradient $\mathbf{F} = \mathbf{F}^{\mathrm{e}}\mathbf{F}^{\mathrm{p}} = \mathbf{F}^{\mathrm{e}}\mathbf{F}^{\mathbf{p:s}}\mathbf{F}^{\mathrm{p:tr}}$ as:

$$\begin{cases} \dot{\mathbf{F}} = \dot{\mathbf{F}}^{\mathrm{e}}\mathbf{F}^{\mathrm{p:s}}\mathbf{F}^{\mathrm{p:tr}} + \mathbf{F}^{\mathrm{e}}\dot{\mathbf{F}}^{\mathrm{p:s}}\mathbf{F}^{\mathrm{p:tr}} + \mathbf{F}^{\mathrm{e}}\mathbf{F}^{\mathrm{p:s}}\dot{\mathbf{F}}^{\mathrm{p:tr}} \\ \mathbf{F}^{-1} = \mathbf{F}^{-\mathrm{p:tr}}\mathbf{F}^{-\mathrm{p:s}}\mathbf{F}^{-\mathrm{e}} \end{cases} \tag{A.2}$$

and introducing this in Eq. A.1:

$$\mathbf{l} = \dot{\mathbf{F}}^{\mathrm{e}}\mathbf{F}^{\mathrm{p:s}}\mathbf{F}^{\mathrm{p:tr}}\mathbf{F}^{-\mathrm{p:tr}}\mathbf{F}^{-\mathrm{p:s}}\mathbf{F}^{-\mathrm{e}} + \mathbf{F}^{\mathrm{e}}\dot{\mathbf{F}}^{\mathrm{p:s}}\mathbf{F}^{\mathrm{p:tr}}\mathbf{F}^{-\mathrm{p:tr}}\mathbf{F}^{-\mathrm{p:s}}\mathbf{F}^{-\mathrm{e}} + \mathbf{F}^{\mathrm{e}}\mathbf{F}^{\mathrm{p:s}}\dot{\mathbf{F}}^{\mathrm{p:tr}}\mathbf{F}^{-\mathrm{p:tr}}\mathbf{F}^{-\mathrm{p:s}}\mathbf{F}^{-\mathrm{e}} \tag{A.3}$$

The simplification of this expression leads to:

$$\begin{cases} \mathbf{l} = \dot{\mathbf{F}}^{\mathrm{e}}\mathbf{F}^{\mathrm{p:s}}\mathbf{F}^{\mathrm{p:tr}}\mathbf{F}^{-\mathrm{p:tr}}\mathbf{F}^{-\mathrm{p:s}}\mathbf{F}^{-\mathrm{e}} + \mathbf{F}^{\mathrm{e}}\dot{\mathbf{F}}^{\mathrm{p:s}}\mathbf{F}^{\mathrm{p:tr}}\mathbf{F}^{-\mathrm{p:tr}}\mathbf{F}^{-\mathrm{p:s}}\mathbf{F}^{-\mathrm{e}} + \mathbf{F}^{\mathrm{e}}\mathbf{F}^{\mathrm{p:s}}\dot{\mathbf{F}}^{\mathrm{p:tr}}\mathbf{F}^{-\mathrm{p:tr}}\mathbf{F}^{-\mathrm{p:s}}\mathbf{F}^{-\mathrm{e}} \\ \Rightarrow \mathbf{l} = \underbrace{\dot{\mathbf{F}}^{\mathrm{e}}\mathbf{F}^{-\mathrm{e}}}_{\mathbf{l}^{\mathrm{e}}} + \mathbf{F}^{\mathrm{e}}\underbrace{\dot{\mathbf{F}}^{\mathrm{p:s}}\mathbf{F}^{-\mathrm{p:s}}}_{\overline{\overline{\mathbf{L}}}^{\mathrm{p:s}}}\mathbf{F}^{-\mathrm{e}} + \mathbf{F}^{\mathrm{e}}\underbrace{\mathbf{F}^{\mathrm{p:s}}\dot{\mathbf{F}}^{\mathrm{p:tr}}\mathbf{F}^{-\mathrm{p:tr}}\mathbf{F}^{-\mathrm{p:s}}}_{\overline{\overline{\mathbf{L}}}^{\mathrm{p:tr}}}\mathbf{F}^{-\mathrm{e}} \\ \Rightarrow \mathbf{l} = \mathbf{l}^{\mathrm{e}} + \mathbf{F}^{\mathrm{e}}\overline{\overline{\mathbf{L}}}^{\mathrm{p:s}}\mathbf{F}^{-\mathrm{e}} + \mathbf{F}^{\mathrm{e}}\overline{\overline{\mathbf{L}}}^{\mathrm{p:tr}}\mathbf{F}^{-\mathrm{e}} \end{cases} \tag{A.4}$$

where $\mathbf{l}^{\mathrm{e}}$ is the elastic contribution to the velocity gradient in the current configuration, $\overline{\overline{\mathbf{L}}}^{\mathrm{p:s}}$ is the plastic component associated with standard slip and $\overline{\overline{\mathbf{L}}}^{\mathrm{p:tr}}$ is the contribution of irreversible phase transformations to the velocity gradient both in the intermediate relaxed configuration $\overline{\overline{\Omega}}$.

A.2 Stress power ($\boldsymbol{\sigma} : \mathbf{d}$)

The stress power $\boldsymbol{\sigma} : \mathbf{d}$ can be additionally decomposed into the elastic and plastic contributions by using Eq. A.4:

$$\boldsymbol{\sigma} : \mathbf{d} \xrightarrow[\boldsymbol{\sigma}:\mathbf{w}^{\mathrm{e}}=0]{\mathbf{l}^{\mathrm{e}}=\mathbf{d}^{\mathrm{e}}+\mathbf{w}^{\mathrm{e}}} \underbrace{\boldsymbol{\sigma} : \mathbf{d}^{\mathrm{e}}}_{1} + \underbrace{\boldsymbol{\sigma} : \mathbf{F}^{\mathrm{e}}\overline{\overline{\mathbf{L}}}^{\mathrm{p:s}}\mathbf{F}^{-\mathrm{e}}}_{2} + \underbrace{\boldsymbol{\sigma} : \mathbf{F}^{\mathrm{e}}\overline{\overline{\mathbf{L}}}^{\mathrm{p:tr}}\mathbf{F}^{-\mathrm{e}}}_{3} \tag{A.5}$$

where the symmetry of the cauchy stress tensor has been used ($\boldsymbol{\sigma} : \mathbf{w} = 0$) [34]. The first term stands for the elastic power, the second term is the contribution of the the standard slip deformation and the last term is the transformation deformation contribution. In order to define each term in the most convenient configuration, the elastic term can be conveniently expressed in Ω_0 and the plastic terms in $\overline{\overline{\Omega}}$. The terms in Eq. A.5 can be rearranged using the mathematical expressions in Section A.3 :

- (1) $\boldsymbol{\sigma} : \mathbf{d}^{\mathrm{e}} \xrightarrow{\boldsymbol{\sigma}=J^{-1}\mathbf{F}\mathbf{S}_0\mathbf{F}^T} J^{-1}(\underbrace{\mathbf{F}}_{A}\underbrace{\mathbf{S}_0\mathbf{F}^T}_{B}) : \underbrace{\mathbf{d}^{\mathrm{e}}}_{C} \xrightarrow{(\mathbf{AB}):\mathbf{C}=\mathbf{B}:(\mathbf{A}^T\mathbf{C})} J^{-1}(\underbrace{\mathbf{S}_0}_{A}\underbrace{\mathbf{F}^T}_{B}) : \underbrace{(\mathbf{F}^T\mathbf{d}^{\mathrm{e}})}_{C} \xrightarrow{(\mathbf{AB}):\mathbf{C}=\mathbf{A}:(\mathbf{C}\mathbf{B}^T)} J^{-1}\mathbf{S}_0 : (\mathbf{F}^T\mathbf{d}^{\mathrm{e}}\mathbf{F})$

- (2) $\boldsymbol{\sigma} : (\mathbf{F}^{\mathrm{e}}\overline{\overline{\mathbf{L}}}^{\mathrm{p:s}}\mathbf{F}^{-\mathrm{e}}) \xrightarrow{\boldsymbol{\sigma}=J^{-\mathrm{e}}\mathbf{F}^{-\mathrm{e}T}\overline{\overline{\mathbf{M}}}\mathbf{F}^{\mathrm{e}T}} J^{-\mathrm{e}}(\underbrace{\mathbf{F}^{-\mathrm{e}T}\overline{\overline{\mathbf{M}}}\mathbf{F}^{\mathrm{e}T}}_{A}) : (\underbrace{\mathbf{F}^{\mathrm{e}}\overline{\overline{\mathbf{L}}}^{\mathrm{p:s}}}_{B}\underbrace{\mathbf{F}^{-\mathrm{e}}}_{C}) \xrightarrow{\mathbf{A}:(\mathbf{BC})=(\mathbf{A}\mathbf{C}^T):\mathbf{B}}$
  $J^{-\mathrm{e}}(\underbrace{\mathbf{F}^{-\mathrm{e}T}}_{A}\underbrace{\overline{\overline{\mathbf{M}}}\cancel{\mathbf{F}^{\mathrm{e}T}\mathbf{F}^{-\mathrm{e}T}}}_{B}) : (\underbrace{\mathbf{F}^{\mathrm{e}}\overline{\overline{\mathbf{L}}}^{\mathrm{p:s}}}_{C}) \xrightarrow{(\mathbf{AB}):\mathbf{C}=\mathbf{B}:(\mathbf{A}^T\mathbf{C})} J^{-\mathrm{e}}\overline{\overline{\mathbf{M}}} : (\cancel{\mathbf{F}^{-\mathrm{e}}\mathbf{F}^{\mathrm{e}}}\overline{\overline{\mathbf{L}}}^{\mathrm{p:s}}) \rightarrow$
  $J^{-\mathrm{e}}\overline{\overline{\mathbf{M}}} : \overline{\overline{\mathbf{L}}}^{\mathrm{p:s}}$

- (3) $\boldsymbol{\sigma} : (\mathbf{F}^{\mathrm{e}}\overline{\overline{\mathbf{L}}}^{\mathrm{p:tr}}\mathbf{F}^{-\mathrm{e}}) \xrightarrow{\boldsymbol{\sigma}=J^{-\mathrm{e}}\mathbf{F}^{-\mathrm{e}T}\overline{\overline{\mathbf{M}}}\mathbf{F}^{\mathrm{e}T}} J^{-\mathrm{e}}(\underbrace{\mathbf{F}^{-\mathrm{e}T}\overline{\overline{\mathbf{M}}}\mathbf{F}^{\mathrm{e}T}}_{A}) : (\underbrace{\mathbf{F}^{\mathrm{e}}\overline{\overline{\mathbf{L}}}^{\mathrm{p:tr}}}_{B}\underbrace{\mathbf{F}^{-\mathrm{e}}}_{C}) \xrightarrow{\mathbf{A}:(\mathbf{BC})=(\mathbf{A}\mathbf{C}^T):\mathbf{B}}$
  $J^{-\mathrm{e}}(\underbrace{\mathbf{F}^{-\mathrm{e}T}}_{A}\underbrace{\overline{\overline{\mathbf{M}}}\cancel{\mathbf{F}^{\mathrm{e}T}\mathbf{F}^{-\mathrm{e}T}}}_{B}) : (\underbrace{\mathbf{F}^{\mathrm{e}}\overline{\overline{\mathbf{L}}}^{\mathrm{p:tr}}}_{C}) \xrightarrow{(\mathbf{AB}):\mathbf{C}=\mathbf{B}:(\mathbf{A}^T\mathbf{C})} J^{-\mathrm{e}}\overline{\overline{\mathbf{M}}} : (\cancel{\mathbf{F}^{-\mathrm{e}}\mathbf{F}^{\mathrm{e}}}\overline{\overline{\mathbf{L}}}^{\mathrm{p:tr}}) \rightarrow$
  $J^{-\mathrm{e}}\overline{\overline{\mathbf{M}}} : \overline{\overline{\mathbf{L}}}^{\mathrm{p:tr}}$

where $\overline{\overline{\mathbf{M}}}$ is the Mandel stress tensors in $\overline{\overline{\Omega}}$. Substituting these terms in Eq. 6.8 leads to:

$$\boldsymbol{\sigma} : \mathbf{d} = J^{-1}(J^{\mathrm{p}}\overline{\overline{\mathbf{M}}} : \overline{\overline{\mathbf{L}}}^{\mathrm{p:s}} + J^{\mathrm{p}}\overline{\overline{\mathbf{M}}} : \overline{\overline{\mathbf{L}}}^{\mathrm{p:tr}} + \mathbf{S}_0 : \mathbf{F}\mathbf{d}^{\mathrm{e}}\mathbf{F}) \tag{A.6}$$

A.3 Proof of mathematical relationships

- $\boxed{\mathbf{A} : (\mathbf{BC}) = (\mathbf{B}^T\mathbf{A}) : \mathbf{C}}$

  $\mathbf{A} : (\mathbf{BC}) = A_{ij}B_{kl}C_{mn}\delta_{lm}\delta_{ik}\delta_{jn} = A_{ij}B_{il}C_{lj}$

  $(\mathbf{B}^T\mathbf{A}) : \mathbf{C} = B_{ij}A_{kl}C_{mn}\delta_{ik}\delta_{jm}\delta_{ln} = B_{ij}A_{il}C_{jl} = A_{il}B_{ij}C_{jl} = A_{ij}B_{il}C_{lj}$

- $\boxed{\mathbf{A} : (\mathbf{BC}) = (\mathbf{A}\mathbf{C}^T) : \mathbf{B}}$

  $\mathbf{A} : (\mathbf{BC}) = A_{ij}B_{kl}C_{mn}\delta_{lm}\delta_{ik}\delta_{jn} = A_{ij}B_{il}C_{lj}$

  $(\mathbf{A}\mathbf{C}^T) : \mathbf{B} = A_{ij}C_{kl}B_{mn}\delta_{jl}\delta_{im}\delta_{kn} = A_{ij}C_{kj}B_{ik} = A_{ij}B_{ik}C_{kj} = A_{ij}B_{il}C_{lj}$

- $\boxed{(\mathbf{AB}) : \mathbf{C} = \mathbf{B} : (\mathbf{A}^T\mathbf{C}))}$

  $(\mathbf{AB}) : \mathbf{C} = A_{ij}B_{kl}C_{mn}\delta_{jk}\delta_{im}\delta_{ln} = A_{ij}B_{jl}C_{il}$

$$\mathbf{B} : (\mathbf{A}^T\mathbf{C}) = B_{ij}A_{kl}C_{mn}\delta_{km}\delta_{il}\delta_{jn} = B_{ij}A_{ki}C_{kj} = A_{ki}B_{ij}C_{kj} = A_{ij}B_{jl}C_{il}$$

Bibliography

[1] Rolls Royce Company. The jet engine. Technical report, Rolls Royce, 1986.

[2] R.C. Reed. *The superalloys: fundamentals and applications*. Cambridge, 2006.

[3] R.C. Reed and C.M.F. Rae. 22 - Physical metallurgy of the nickel-based superalloys. In D.E. Laughlin and K. Hono, editors, *Physical Metallurgy (Fifth Edition)*, pages 2215–2290. Elsevier, Oxford, 2014.

[4] T.M. Smith, R.R. Unocic, H. Deutchman, and M.J. Mills. Creep deformation mechanism mapping in nickel base disk superalloys. *Materials at High Temperatures*, 33(33):1–12, 2016.

[5] I. Alvarez, A.C. Picasso, and A.J. Marzocca. Cross-slip and dislocation climb in nickel-base superalloys. *Materials Science & Engineering, A*, 236:7–10, 1997.

[6] G.B. Viswanathan, P.M. Sarosi, M.F. Henry, D.D. Whitis, W.W. Milligan, and M.J. Mills. Investigation of creep deformation mechanisms at intermediate temperatures in René 88 DT. *Acta Materialia*, 53(10):3041–3057, 2005.

[7] C.M.F. Rae, N. Matan, and R.C. Reed. The role of stacking fault shear in the primary creep of [001] - oriented single crystal superalloys at 750°C and 750 MPa. *Materials Science and Engineering A*, 300(1-2):125–134, 2001.

[8] J. Zhang, T. Jin, Y. Xu, and Z. Hu. Antiphase boundary Strengthening in a Single Crystal Nickel-base Superalloy. *Journal of Materials Science & Technology*, 18(2):159–162, 2002.

[9] M. Kolbe. The high temperature decrease of the critical resolved shear stress in nickel-base superalloys. *Progress in Materials Science*, A319-321:383–387, 2001.

[10] L. Kovarik, R.R. Unocic, J. Li, P. Sarosi, C. Shen, Y. Wang, and M. J.J. Mills. Microtwinning and other shearing mechanisms at intermediate temperatures in Ni-based superalloys. *Progress in Materials Science*, 54:839–873, 2009.

[11] G.B. Viswanathan, S. Karthikeyan, P.M. Sarosi, R.R. Unocic, and M.J. Mills. Microtwinning during intermediate temperature creep of polycrystalline Ni-based superalloys: mechanisms and modelling. *Philosophical Magazine*, 86:4823–4840, 2006.

[12] M.R. Barnett. *Twinning and its role in wrought magnesium alloys.* Woodhead Publishing, 2012.

[13] J.W. Christian and S. Mahajan. Deformation twinning. *Progress in Materials Science*, 39(1):1–157, 1995.

[14] R.W.K. Honeycombe. The plastic deformation of metals. *Crystal Research and Technology*, 20(5):634–634, 1985.

[15] E Orowan. Zur kristallplastizität. *Zeitschrift für Physik A Hadrons and Nuclei*, 89(9):634–659, 1934.

[16] G.I. Taylor. Plastic strain in metals. *The Institute of Metals*, 800:307–325, 1938.

[17] A. Kelly, G.W. Groves, and P. Kidd. *Crystallography and crystal defects*. Wiley, 2000.

[18] T.L Altshuler and J.W. Christian. Low temperature twinning in pure iron. *Acta Metallurgica*, 14(7):903–908, 1966.

[19] P.R. Thornton and T.E. Mitchell. Deformation twinning in alloys at low temperatures. *Philosophical Magazine*, 7(75):361–375, 1962.

[20] A. Cottrell. *An introduction to metallurgy*. Universities Press (India) Pvt. Limited, 1990.

[21] F.R.N. Nabarro and J.P. Hirth. *Dislocations in solids (Chapter 75 dislocations and twinning in face centred cubic crystals)*. Elsevier Science, 2007.

[22] D. Caillard and J.L. Martin. In D. Caillard and J.L. Martin, editors, *Thermally Activated Mechanisms in Crystal Plasticity*, volume 8 of *Pergamon Materials Series*, pages vii – viii. Pergamon, 2003.

[23] B. Kear and J. Oblak. Deformation modes γ' precipitation hardened Ni-base superalloy. *Journal de Physique Colloques*, 35:35–45, 1974.

[24] M.G. Ardakani, M. McLean, and B.A. Shollock. Twin formation during creep in single crystals of nickel-based superalloys. *Acta Materialia*, 47:2593–2602, 1999.

[25] D.M. Knowles and Q.Z. Chen. Superlattice stacking faul formation and twinning during creep in γ/γ' single crystal superalloy CMSX-4. *Materials Science and Engineering A*, 340:88–102, 2003.

[26] D.M. Knowles and S. Gunturi. The role of $\langle 112 \rangle$ $\{111\}$ slip in the asymmetric nature of creep of single crystal superalloy CMSX-4. *Materials Science and Engineering: A*, 328:223–237, 2002.

[27] C. Tian, G. Han, C. Cui, and X. Sun. Effects of stacking fault energy on the creep behaviors of Ni-base superalloy. *Materials & Design*, 64:316–323, 2014.

[28] R.R. Unocic, G.B. Viswanathan, P.M. Sarosi, S. Karthikeyan, J. Li, and M.J. Mills. Mechanisms of creep deformation in polycrystalline Ni-base disk superalloys. In R.C. Reed, K.A. Green, P. Caron, T. Gabb, M.G. Fahrmann, E.S. Huron, and S.A. Woodard, editors, *Superalloys 2008*, pages 25–32. The Minerals, Metals and Materials Society, 2008.

[29] R.R. Unocic, N. Zhou, L. Kovarik, C. Shen, Y. Wang, and M.J. Mills. Dislocation decorrelation and relationship to deformation microtwins during creep of a γ' precipitate strengthened Ni-based superalloy. *Acta Materialia*, 59(19):7325–7339, 2011.

[30] M. Legros, N. Clement, P. Caron, and A. Coujou. In-situ observation of deformation micromechanisms in a rafted γ/γ' superalloy at 850 °C. *Materials Science and Engineering: A*, 337:160–169, 2002.

[31] M.S. Titus, A. Mottura, G.B. Viswanathan, A. Suzuki, M.J. Mills, and T.M. Pollock. High resolution energy dispersive spectroscopy mapping of planar

defects in $L1_2$-containing Co-base superalloys. *Acta Materialia*, 89:423–437, 2015.

[32] T.M. Smith, B.D. Esser, N. Antolin, G.B. Viswanathan, T. Hanlon, A. Wessman, D. Mourer, W. Windl, D.W. McComb, and M.J. Mills. Segregation and η phase formation along stacking faults during creep at intermediate temperatures in a Ni-based superalloy. *Acta Materialia*, 100:19–31, 2015.

[33] S. Karthikeyan, R.R. Unocic, P.M. Sarosi, G.B. Viswanathan, D.D. Whitis, and M.J. Mills. Modeling microtwinning during creep in Ni-based superalloys. *Scripta Materialia*, 54(6):1157–1162, 2006.

[34] G.A. Holzapfel. Nonlinear solid mechanics: A continuum approach for engineering science. *Meccanica*, 37(4):489–490, 2002.

[35] F. Roters, P. Eisenlohr, L. Hantcherli, D.D. Tjahjanto, T.R. Bieler, and D. Raabe. Overview of constitutive laws, kinematics, homogenization and multiscale methods in crystal plasticity finite-element modeling: Theory, experiments, applications. *Acta Materialia*, 58(4):1152–1211, 2010.

[36] R.N. Ghosh, R.V. Curtis, and M. McLean. Creep deformation of single crystal superalloys — modelling the crystallographic anisotropy. *Acta Metallurgica et Materialia*, 38(10):1977–1992, 1990.

[37] D.W. MacLachlan and D.M. Knowles. Creep-behavior modeling of the single-crystal superalloy CMSX-4. *Metallurgical and Materials Transactions A*, 31(5):1401–1411, 2000.

[38] S. Keshavarz, A.C.E. Ghosh, S.and Reid, and S.A. Langer. A non-Schmid crystal plasticity finite element approach to multi-scale modeling of nickel-based superalloys. *Acta Materialia*, 114:106–115, 2016.

[39] A. Ma, D. Dye, and R.C. Reed. A model for the creep deformation behaviour of single-crystal superalloy CMSX-4. *Acta Materialia*, 56(8):1657–1670, 2008.

[40] H. Brehm and U. Glatzel. Material model describing the orientation dependent creep behavior of single crystals based on dislocation densities of slip systems. *International Journal of Plasticity*, 15(3):285–298, 1999.

[41] E. P. Busso, F. T. Meissonnier, and N. P. O'Dowd. Gradient-dependent deformation of two-phase single crystals. *Journal of the Mechanics and Physics of Solids*, 48(11):2333–2361, 2000.

[42] L.G. Zhao, N.P. O'Dowd, and E.P. Busso. A coupled kinetic-constitutive approach to the study of high temperature crack initiation in single crystal nickel-base superalloys. *Journal of the Mechanics and Physics of Solids*, 54(2):288 – 309, 2006.

[43] K. Yashiro, M. Naito, and Y. Tomita. Molecular dynamics simulation of edge dislocation piled at cuboidal precipitate in Ni-based superalloy. *Transactions of the Japan Society of Mechanical Engineers Series A*, 69(677):210–217, 2003.

[44] M. Shenoy, Y. Tjiptowidjojo, and D. McDowell. Microstructure-sensitive modelling of polycrystalline IN 100. *International Journal of Plasticity*, 24:1694–1730, 2008.

[45] Y.M. Zhu, A.J. Morton, and J.F. Nie. Growth and transformation mechanisms of 18R and 14H in Mg–Y–Zn alloys. *Acta Materialia*, 60(19):6562–6572, 2012.

[46] Y.K. Kim, D. Kim, H.K. Kim, C.S. Oh, and B.J. Lee. An intermediate temperature creep model for Ni-based superalloys. *International Journal of Plasticity*, 79:153–175, 2016.

[47] W.J.J. Vorster and F.P.E. Dunne. Crystal plasticity and multiscale modelling of superalloy creep. *Philosophical Magazine*, 92(February 2015):830–848, 2012.

[48] S. Keshavarz and S. Ghosh. Multi-scale crystal plasticity finite element model approach to modeling nickel-based superalloys. *Acta Materialia*, 61(17):6549–6561, 2013.

[49] S. Keshavarz and S. Ghosh. Hierarchical crystal plasticity FE model for nickel-based superalloys: Sub-grain microstructures to polycrystalline aggregates. *International Journal of Solids and Structures*, 2014.

[50] S. Keshavarz and S. Ghosh. A crystal plasticity finite element model for flow stress anomalies in Ni_3Al single crystals. *Philosophical Magazine*, 95:1–22, 2015.

[51] D. Barba, D. Pedrazzini, A. Collins, A.J. Wilkinson, M.P. Moody, P.A.J. Bagot, A. Jérusalem, and R.C. Reed. On the microtwinning mechanism in a single crystal superalloy. *Acta Materialia*, 127:37–40, 2017.

[52] L.P. Freund, Olivier M.D.M. Messé, J.S. Barnard, M. Göken, S. Neumeier, and C.M.F. Rae. Segregation assisted microtwinning during creep of a

polycrystalline L12-hardened Co-base superalloy. *Acta Materialia*, 123:295–304, 2017.

[53] T.M Smith, B.D Esser, N. Antolin, A. Carlsson, R.E.A. Williams, A. Wessman, T. Hanlon, H.L. Fraser, W. Windl, D.W. McComb, and M.J. Mills. Phase transformation strengthening of high-temperature superalloys. *Nature Communications*, 7:13434, 2016.

[54] D. Peirce, R.J. Asaro, and A. Needleman. Material rate dependence and localized deformation in crystalline solids. *Acta Metallurgica*, (31):1951–1976, 1983.

[55] R.J. Asaro and A. Needleman. Texture development and strain hardening in rate dependent polycrystals. *Acta Metallurgica*, (33):923–953, 1985.

[56] P. Van-Houtte. Simulation of the rolling and shear texture of brass by the Taylor theory adapted for mechanical twinning. *Acta Metallurgica*, 26(4):591–604, 1978.

[57] A.V. Staroselsky. *Crystal plasticity due to slip and twinning.* PhD thesis, Massachusetts Institute of Technology, 1988.

[58] A.V. Staroselsky and L. Anand. A constitutive model for HCP materials deforming by slip and twinning: application to magnesium alloy AZ31B. *International Journal of Plasticity*, 19(10):1843 – 1864, 2003.

[59] R. Lebensohn and C. Tomé. A self-consistent anisotropic approach for the simulation of plastic deformation and texture development of polycrystals: Application to zirconium alloys. *Acta Metallurgica et Materialia*, 41(9):2611 – 2624, 1993.

[60] G. Proust, C. Tomé, and G.C. Kaschner. Modeling texture, twinning and hardening evolution during deformation of hexagonal materials. *Acta Materialia*, 55(6):2137 – 2148, 2007.

[61] S.R. Kalidindi, C.A. Bronkhorst, and L. Anand. Crystallographic texture evolution in bulk deformation processing of FCC metals. *Journal of the Mechanics and Physics of Solids*, 40(3):537–569, 1992.

[62] C.D. Allen. *Plasticity of nickel-based single crystal superalloy.* PhD thesis, Massachusetts Institute of Technology, 1995.

[63] M. McLean, G.A. Webster, F.R.N. Nabarro, and A. Cottrell. Nickel-base superalloys: current status and potential. *Philosophical Transactions: Physical Sciences and Engineering*, 351(1697):419–433, 1995.

[64] T.M. Pollock and A.S. Argon. Creep resistance of CMSX-3 nickel base superalloy single crystals. *Acta Metallurgica et Materialia*, 40(1):1–30, 1992.

[65] D.J. Crudden, A. Mottura, N. Warnken, B. Raeisinia, and R.C. Reed. Modelling of the influence of alloy composition on flow stress in high-strength nickel-based superalloys. *Acta Materialia*, 75:356–370, 2014.

[66] E.I. Galindo-Nava, L.D. Connor, and C.M.F. Rae. On the prediction of the yield stress of unimodal and multimodal γ' Nickel-base superalloys. *Acta Materialia*, 98:377–390, 2015.

[67] Y.M. Eggeler, J. Müller, M.S. Titus, A. Suzuki, T.M. Pollock, and E. Spiecker. Planar defect formation in the γ' phase during high temperature creep in single crystal coni-base superalloys. *Acta Materialia*, 113:335–349, 2016.

[68] R.R. Unocic, L. Kovarik, C. Shen, P.M. Sarosi, Y. Wang, J. Li, S. Ghosh, and M.J. Mills. Deformation mechanisms in Ni-base disk superalloys at higher temperatures. In R.C. Reed, K.A. Green, P. Caron, T. Gabb, M.G. Fahrmann, E.S. Huron, and S.A. Woodard, editors, *Superalloys 2008*, pages 377–385. The Minerals, Metals and Materials Society, 2008.

[69] V.A. Vorontsov, L. Kovarik, M.J. Mills, and C.M.F. Rae. High-resolution electron microscopy of dislocation ribbons in a CMSX-4 superalloy single crystal. *Acta Materialia*, 60(12):4866–4878, 2012.

[70] V.A. Vorontsov, R.E. Voskoboinikov, and C.M.F. Rae. Prediction of mechanical behaviour in Ni-base superalloys using the phase field model of dislocations. *Advanced Materials Research*, 278:150–155, 2011.

[71] P.M. Sarosi, G.B. Viswanathan, and M.J. Mills. Direct observation of an extended complex stacking fault in the γ' phase of a Ni-base superalloy. *Scripta Materialia*, 55:727–730, 2006.

[72] B. Roebuck, D.C. Cox, and R.C. Reed. An innovative device for the mechanical testing of miniature specimens of superalloys. In K.A. Green, H. Harada, T.E. Howson, T.M. Pollock, R.C. Reed, J.J. Schirra, and S. Walston, editors, *Superalloys 2004*, pages 523–528. The Minerals, Metals and Materials Society, 2004.

[73] A.J. Wilkinson, G. Meaden, and D.J. Dingley. High-resolution elastic strain measurement from electron backscatter diffraction patterns: New levels of sensitivity. *Ultramicroscopy*, 106(4–5):307–313, 2006.

[74] A.J. Wilkinson, E.E. Clarke, T.B. Britton, P. Littlewood, and P.S. Karamched. High-resolution electron backscatter diffraction: An emerging tool for studying local deformation. *The Journal of Strain Analysis for Engineering Design*, 45:365–376, 2010.

[75] W.S. Rasband. *ImageJ*. U. S. National Institutes of Health, Bethesda, Maryland, USA, 1997-2016.

[76] V.A. Vorontsov, R.E. Voskoboinikov, and C.M.F. Rae. Shearing of γ' precipitates in Ni-base superalloys: a phase field study incorporating the effective γ-surface. *Philosophical Magazine*, 92(5):608–634, 2012.

[77] M. Yamashita and K. Kakehi. Tension/compression asymmetry in yield and creep strengths of ni-based superalloy with a high amount of tantalum. *Scripta Materialia*, 55(2):139 – 142, 2006.

[78] K. Kakehi. Tension/compression asymmetry in creep behavior of a Ni-based superalloy. *Scripta Materialia*, 41(5):461–465, 1999.

[79] G.L. Drew, R.C. Reed, K. Kakehi, and C.M.F. Rae. Single crystal superalloys: the transition from primary to secondary creep. In K.A. Green, H. Harada, T.E. Howson, T.M. Pollock, R.C. Reed, J.J. Schirra, and S. Walston, editors, *Superalloys 2004*. The Minerals, Metals and Materials Society, 2004.

[80] J. Svoboda and P. Lukis. Activation energy of creep in <001>-orientated superalloy CMSX-4 single crystals. *Materials Science and Engineering A*, 234-236(97):173–176, 1997.

[81] C.N. Reid and W.S. Owen. *Deformation geometry for materials scientists*. Pergamon Press, Oxford, 1973.

[82] H.U. Hong, B.G. Choi, I.S. Kim, Y.S. Yoo, and C.Y. Jo. Deformation behavior during thermo-mechanical fatigue of a nickel-based single crystal superalloy. *Procedia Engineering*, 10:281–286, 2011.

[83] J. Kanesund, J.J. Moverare, and S. Johansson. Deformation and damage mechanisms in IN792 during thermomechanical fatigue. *Materials Science and Engineering A*, 528(13-14):4658–4668, 2011.

[84] X.Z. Lv, J.X. Zhang, and H. Harada. Twin-dislocation and twin-twin interactions during cyclic deformation of a nickel-base single crystal TMS-82 superalloy. *International Journal of Fatigue*, 66:246–251, 2014.

[85] J.J. Moverare, S. Johansson, and R.C. Reed. Deformation and damage mechanisms during thermal-mechanical fatigue of a single-crystal superalloy. *Acta Materialia*, 57(7):2266–2276, 2009.

[86] F. Sun, J. Zhang, and H. Harada. Deformation twinning and twinning-related fracture in nickel-base single-crystal superalloys during thermomechanical fatigue cycling. *Acta Materialia*, 67:45–57, 2014.

[87] A. Pineau, A.A. Benzerga, and T. Pardoen. Failure of metals I: Brittle and ductile fracture. *Acta Materialia*, 107:424–483, 2016.

[88] N. Zhou, C. Shen, M.J. Mills, J. Li, and Y. Wang. Modeling displacive-diffusional coupled dislocation shearing of γ' precipitates in Ni-base superalloys. *Acta Materialia*, 59:3484–3497, 2011.

[89] J.F. Nie, Y.M. Zhu, J.Z. Liu, and X.Y. Fang. Periodic segregation of solute atoms in fully coherent twin boundaries. *Science*, 340(6135):957–960, 2013.

[90] G.B. Viswanathan, R. Shi, A. Genc, V.A. Vorontsov, L. Kovarik, C.M.F. Rae, and M.J. Mills. Segregation at stacking faults within the γ' phase of two Ni-base superalloys following intermediate temperature creep. *Scripta Materialia*, 94:5–8, 2014.

[91] H. Hoeft and P. Schwaab. Investigations towards optimizing EDS analysis by the cliff-lorimer method in scanning transmission electron microscopy. *X-Ray Spectrometry*, 17(5):201–208, 1988.

[92] M. Herbig, M. Kuzmina, C. Haase, R. K. W. Marceau, I. Gutierrez-Urrutia, D. Haley, D. A. Molodov, P. Choi, and D. Raabe. Grain boundary segregation in Fe–Mn–C twinning-induced plasticity steels studied by correlative electron backscatter diffraction and atom probe tomography. *Acta Materialia*, 83:37–47, 2015.

[93] P.J. Felfer, B. Gault, G. Sha, L. Stephenson, S.P. Ringer, and J.M. Cairney. A new approach to the determination of concentration profiles in atom probe tomography. *Microscopy and Microanalysis*, 18:359–364, 2012.

[94] T.M. Smith. *Orientation and alloying effects on creep strength in Ni-based superalloys*. PhD thesis, The Ohio State University, 2016.

[95] A. Breidi, J. Allen, and A. Mottura. First-principles modeling of superlattice intrinsic stacking fault energies in Ni 3 Al based alloys. *Acta Materialia*, 145:97–108, 2018.

[96] T.M. Smith, Y. Rao, Y. Wang, M. Ghazisaeidi, and M.J. Mills. Diffusion Processes During Creep at Intermediate Temperatures in a Ni-based Superalloy. *Acta Mater.*, 141:261–272, 2017.

[97] D. Barba, S. Pedrazzini, A. Vilalta-Clemente, A.J. Wilkinson, M.P. Moody, P.A.J. Bagot, A. Jérusalem, and R.C. Reed. On the composition of microtwins in a single crystal nickel-based superalloy. *Scripta Materialia*, 127:37–40, 2017.

[98] H.K.D.H. Bhadeshia. Diffusional and displacive transformations. *Scripta Metallurgica*, 21(8):1017–1022, 1987.

[99] G.J. Jones and R.K. Trivedi. Lateral growth in solid-solid phase transformations. *Journal of Applied Physics*, 42(11):4299–4304, 1971.

[100] Y. Li and G. Purdy. On the growth of Widmänstatten precipitates in an Al-Cu alloy. *Acta Materialia*, 56(3):364–368, 2008.

[101] S.A. Mujahid and H.K.D.H. Bhadeshia. Coupled diffusional/displacive transformations: Effect of carbon concentration. *Acta Metallurgica et Materialia*, 41(3):967–973, 1993.

[102] G.B. Olson, H.K.D.H. Bhadeshia, and M. Cohen. Coupled diffusional/displacive transformations. *Acta Metallurgica*, 37(2):381–390, 1989.

[103] C. Atkinson. The growth kinetics of individual ledges during solid/solid phase transformations. *Proceedings of the Royal Society of London*, pages 351–368, 1981.

[104] A. Fick. On liquid diffusion. *The London, Edinburgh,and Dublin Philosophical Magazine and Journal of Science*, 10:30–39, 1855.

[105] J.P. Hirth and W.D. Nix. An analysis of the thermodynamics of dislocation glide. *Physica Status Solidi (b)*, 35(1):177–188, 1969.

[106] G. Schoeck. The activation energy of dislocation movement. *Physica Status Solidi (b)*, 8(2):499–507, 1965.

[107] J.O. Andersson, T. Helander, L. Höglund, P. Shi, and B. Sundman. Thermo-Calc & DICTRA, Computational tools for materials science. *Calphad*, 26(2):273–312, 2002.

[108] -Thermotech Ni-based superalloys database v8.0, Accessed January 2015.

[109] F. Pyczak, B. Devrient, and H. Mughrabi. The effects of different alloying elements on the thermal expansion coefficients, lattice constants and misfit of nickel-based superalloys investigated by X-Ray diffraction. In K.A. Green, H. Harada, T.E. Howson, T.M. Pollock, R.C. Reed, J.J. Schirra, and S. Walston, editors, *Superalloys 2004*, pages 827–836. The Minerals, Metals and Materials Society, 2004.

[110] A. Jérusalem, M. Dao, S. Suresh, and R. Radovitzky. Three-dimensional model of strength and ductility of polycrystalline copper containing nanoscale twins. *Acta Materialia*, 56(17):4647–4657, 2008.

[111] L. Li and C. Ortiz. Pervasive nanoscale deformation twinning as a catalyst for efficient energy dissipation in a bioceramic armour. *Nature materials*, 13(5):501–7, 2014.

[112] R.J. McCabe, I.J. Beyerlein, J.S. Carpenter, and N.A. Mara. The critical role of grain orientation and applied stress in nanoscale twinning. *Nature communications*, 5(May):3806, 2014.

[113] F. Wu, Y.T. Zhu, and J. Narayan. Macroscopic twinning strain in nanocrystalline Cu. *Materials Research Letters*, 2(2):63–69, 2014.

[114] Y.T. Zhu, X.Z. Liao, S.G. Srinivasan, and E.J. Lavernia. Nucleation of deformation twins in nanocrystalline face-centered-cubic metals processed by severe plastic deformation. *Journal of Applied Physics*, 98(3):1–8, 2005.

[115] A. Sengupta, S.K. Putatunda, L. Bartosiewicz, J. Hangas, P.J. Nailos, M. Peputapeck, and F.E. Alberts. Tensile behavior of a new single-crystal nickel-based superalloy (CMSX-4) at room and elevated temperatures. *Journal of Materials Engineering and Performance*, 3(1):73–81, 1994.

[116] Q. Qin and J.L. Bassani. Non-associated plastic flow in single crystals. *Journal of the Mechanics and Physics of Solids*, 40(4):835–862, 1992.

[117] Q. Qin and J.L. Bassani. Non-Schmid yield behavior in single crystals. *Journal of the Mechanics and Physics of Solids*, 40(4):813–833, 1992.

[118] N. Tsuno, S. Shimabayashi, K. Kakehi, C.M.F. Rae, and R.C. Reed. Tension/-compression asymmetry in yield and creep strengths of Ni based superalloys. *Superalloys 2008*, pages 433–442, 2008.

[119] Paraskevas Kontis, Zhuangming Li, David M. Collins, Jonathan Cormier, Dierk Raabe, and Baptiste Gault. The effect of chromium and cobalt segregation at dislocations on nickel-based superalloys. *Scripta Materialia*, 145(Supplement C):76 – 80, 2018.

[120] D. Barba, T.M. Smith, J. Miao, M.J. Mills, and R.C. Reed. Segregation-assisted plasticity in ni-based superalloys. Metallurgical and Materials Transactions A, 2018.

[121] L. Schemmann, S. Zaefferer, D. Raabe, F. Friedel, and D. Mattissen. Alloying effects on microstructure formation of dual phase steels. *Acta Materialia*, 95:386–398, 2015.

[122] S.L. Wong, M. Madivala, U. Prahl, F. Roters, and D. Raabe. A crystal plasticity model for twinning- and transformation-induced plasticity. *Acta Materialia*, 118:140–151, 2016.

[123] S. Budday, P. Steinmann, and E. Kuhl. The role of mechanics during brain development. *Journal of the Mechanics and Physics of Solids*, 72:75–92, 2014.

[124] P.C.W Davies, L. Demetrius, and J.A. Tuszynski. Cancer as a dynamical phase transition. *Theoretical biology & medical modelling*, 8:30, 2011.

[125] A.M. Cuitino and M. Ortiz. Computational modelling of single crystals. *Materials Science and Engineering*, 1(3):225–263, 1993.

[126] B.D. Coleman and M.E. Gurtin. Thermodynamics with internal state variables. *The Journal of Chemical Physics*, 47(2):597–613, 1967.

[127] J.R. Rice. Inelastic constitutive relations for solids: An internal-variable theory and its application to metal plasticity. *Journal of the Mechanics and Physics of Solids*, 19(6):433–455, 1971.

[128] U.F. Kocks, A.S. Argon, and M.F. Ashby. *Thermodynamics and kinetics of slip*. Number v. 19 in International Series of Monographs in Natural Philosophy. Pergamon Press, 1975.

[129] L. Méric and G. Cailletaud. Single crystal modeling for structural calculations: part 2—finite element implementation. *Journal of Engineering Materials and Technology*, 113(1):171–182, 1991.

[130] C. Mareau and M.R. Daymond. Micromechanical modelling of twinning in polycrystalline materials: Application to magnesium. *International Journal of Plasticity*, 85:156–171, 2016.

[131] Esteban P. Busso, David W. Dean, and David Linkens. On the effects of loading conditions and geometry on time-dependent singular crack tip fields. *Engineering Fracture Mechanics*, 50(2):231 – 247, 1995.

[132] Dhyanjyoti Deka, Deepu S. Joseph, Somnath Ghosh, and Michael J. Mills. Crystal plasticity modeling of deformation and creep in polycrystalline ti-6242. *Metallurgical and Materials Transactions A*, 37(5):1371–1388, May 2006.

[133] M.K. Samal and S. Ghosh. Evaluation of creep deformation and mechanical properties of nickel-based superalloys through fe analysis based on crystal plasticity models. *Procedia Engineering*, 55(Supplement C):342 – 347, 2013. 6th International Conference on Creep, Fatigue and Creep-Fatigue Interaction.

[134] J.D. Clayton. A continuum description of nonlinear elasticity, slip and twinning, with application to sapphire. *Proceedings of the Royal Society A: Mathematical, Physical and Engineering Science*, 465(2101):307 LP – 334, 2009.

[135] Milan Ardeljan, Irene J. Beyerlein, and Marko Knezevic. Effect of dislocation density-twin interactions on twin growth in az31 as revealed by explicit crystal plasticity finite element modeling. *International Journal of Plasticity*, 99(Supplement C):81 – 101, 2017.

[136] Yuichi Tadano, Yui Yoshihara, and Seiya Hagihara. A crystal plasticity modeling considering volume fraction of deformation twinning. *International Journal of Plasticity*, 84(Supplement C):88 – 101, 2016.

[137] J.L Bassani and T.Y. Wu. Latent hardening in single crystals II. Analytical characterization and predictions. *Proceedings of the Royal Society of London. Series A: Mathematical and Physical Sciences*, 435(1893):21–41, 1991.

[138] L. Onsager. Irreversible processes. *Physical Reviews*, 37:237–241, 1931.

[139] Dassault Systémes. *Abaqus/Implicit*, 2010.

[140] Y Huang. A user-material subroutine incorporating single crystal plasticity in the abaqus finite element program, mech report 178. Technical report, Division of Engineering and Applied Sciences, Harvard University, Cambridge, Massachusetts, 1991.

[141] J. W. Kysar. Addendum to 'a user-material subroutine incorporating single crystal plasticity in the abaqus finite element program, mech report 178. Technical report, Division of Engineering and Applied Sciences, Harvard University, Cambridge, Massachusetts., 1997.

[142] D. Leidermark, J.J. Moverare, S. Johansson, K. Simonsson, and S. Sjöström. Tension/compression asymmetry of a single-crystal superalloy in virgin and degraded condition. *Acta Materialia*, 58:4986–4997, 2010.

[143] The MathWorks Inc., Natick, M.A. *MATLAB*, 2000.

[144] Toru Inoue, Katsushi Tanaka, Hiroki Adachi, Kyosuke Kishida, Norihiko L. Okamoto, Haruyuki Inui, Tadaharu Yokokawa, and Hiroshi Harada. Evolution

of orientation distributions of γ and γ' phases during creep deformation of ni-base single crystal superalloys. *Acta Materialia*, 57(4):1078 – 1085, 2009.

[145] A.S. Khan and S. Huang. *Continuum theory of plasticity*. Wiley-Interscience publication. Wiley, 1995.

[146] P.E. McHugh and R. Mohrmann. Modelling of creep in a ni base superalloy using a single crystal plasticity model. *Computational Materials Science*, 9(1):134 – 140, 1997. Selected papers of the Sixth International Workshop on Computational Mechanics of Materials.

[147] R. Quey, P.R. Dawson, and F. Barbe. Large-scale 3D random polycrystals for the finite element method: Generation, meshing and remeshing. *Computational Methods Applied to Mechanical Engineering*, 200:1729–1745, 2011.

[148] E. Alabort, D. Putman, and R.C. Reed. Superplasticity in Ti–6Al–4V: Characterisation, modelling and applications. *Acta Materialia*, 95(Supplement C):428 – 442, 2015.

[149] Y.S. Choi, T.A. Parthasarathy, C. Woodward, D.M. Dimiduk, and M.D. Uchic. Constitutive model for anisotropic creep behaviors of single-crystal ni-base superalloys in the low-temperature, high-stress regime. *Metallurgical and Materials Transactions A*, 43(6):1861–1869, 2012.

[150] C.M.F. Rae and R.C. Reed. Primary creep in single crystal superalloys: Origins, mechanisms and effects. *Acta Materialia*, 55(3):1067 – 1081, 2007.

[151] O. Barrera, E. Tarleton, H.W. Tang, and A.C.F. Cocks. Modelling the coupling between hydrogen diffusion and the mechanical behaviour of metals. *Computational Materials Science*, 122:219–228, 2016.

[152] G. Vigueras, F. Sket, C. Samaniego, L. Wu, L. Noels, D. Tjahjanto, E. Casoni, G. Houzeaux, A. Makradi, J.M. Molina-Aldareguia, M. Vázquez, and A. Jérusalem. An xfem/czm implementation for massively parallel simulations of composites fracture. *Composite Structures*, 125(Supplement C):542 – 557, 2015.

[153] Z. Zhu, L. Höglund, H. Larsson, and R.C. Reed. Isolation of optimal compositions of single crystal superalloys by mapping of a material's genome. *Acta Materialia*, 90:330–343, 2015.